University of Southampton

Faculty of Engineering and Physical Sciences

School of Engineering Sciences

3-Dimensional Imaging and Mathematical Modelling of Human Pulmonary Lymphatics

by

Stephanie Katherine Robinson, BSc.

ORCID ID 0000-0001-5436-2929

Thesis For The Degree Of Doctor Of Philosophy

June 2021

University of Southampton

Abstract

Faculty of Engineering and Physical Sciences

School of Engineering Sciences

Thesis For The Degree Of Doctor Of Philosophy

3-Dimensional Imaging and Mathematical Modelling of Human Pulmonary Lymphatics

by

Stephanie Katherine Robinson, BSc.

Lymphatics drain fluid, cells, and essential metabolites back to the circulatory system to maintain fluid homoeostasis. The fluid balance is critical for normal tissue function and is often disturbed in lung diseases such as COPD, asthma, and lung cancer. Although 6.5 million people in the UK are undergoing active treatment for these diseases, little is known about how lymphatics influence lung fluid dynamics.

This study developed and applied a methodology to assess the anatomical structure and predict the function of the 3D lymphatic network in healthy and diseased peripheral human lung tissue.

High-resolution X-ray micro-computed tomography (μCT) provided the 3D structural blueprint of the lung samples down to a voxel size of 5 μm. The pulmonary lymphatic network was subsequently identified and segmented within the same tissue using immunohistochemistry and anti-podoplanin antibodies (D240 and LP21). These micrographs were used to manually segment the lymphatic structures within the μCT dataset alongside the blood vessels, airways and lung parenchyma.

A physiologically accurate image-based mathematical model was established using these geometries. Flow in the blood and microlymphatics are described using the Stokes equations and flow through the interstitium using Darcy's law. Starling's law describes flow across the blood and lymphatic vessel walls, with a uni-directional restraint given to the lymphatic vessel wall to represent the primary valve condition. In addition to changes in input geometry, the model shows sensitivity to pulmonary blood vessel pressure and vessel flow velocities.

To validate the methodology, ten formalin-fixed, paraffin-embedded peripheral lung biopsies were used, four controls, four from patients with acute respiratory injury or inflammation and two with severe COPD disease. Inter- and intra-sample lymphatic heterogeneity was assessed by vessel volume, vessel surface area, network branch and junction number, vessel tortuosity and fractal dimension.

Two hierarchical lymphatic populations were identified; precollecting lymphatics and microlymphatics. Three microlymphatic subpopulations were also defined based on their structural heterogeneity and anatomical location in the lung: intralobular(IL); subpleural (SP) and bronchovascular(BVB). This suggested pulmonary fluid dynamics may vary in different anatomical locations. In the active disease group, five of the six microlymphatic measures were distinct to both the COPD and control groups ($P<0.0001$). Whereas, no morphological differences were seen between the control and COPD sample groups, suggesting fluid dynamics in the control and COPD samples would be similar, whilst those in the active disease sample would be different.

To test the predictions from the morphometry assessment, a finite element mesh was created for the lymphatics, blood vessels and parenchyma in five random volumes from the IL, SP and BVB regions in the control group, and IL region of the acute disease and COPD samples. Using COMSOL Multiphysics ©, finite element simulation software and the mathematical model, fluid flow within the lung geometries were then simulated and compared.

Modelling results predict fluid drainage does vary between anatomical areas of the peripheral lung but in the IL region, the COPD geometries drain fluid less efficiently than the control (0.0015 $ml.min^{-1}/mm^3$ lymphatic volume and 0.0024 $ml.min^{-1}/mm^3$ lymphatic volume respectively). The model considers both blood vessel and interstitial structural variation and their proximity to the lymphatics in 3D space. This more sophisticated analysis accounts for some of the discrepancies between the morphometry assessment and the modelling predictions. This highlights the benefit of incorporating image-based modelling into biological systems to provide higher-level consideration of structure-function relationships of the whole tissue.

Table of Contents

Table of Tables

Table of Figures

Table of Figures

Table of Figures

Research Thesis: Declaration of Authorship

I, Stephanie Katherine Robinson, declare that this thesis "**3-Dimensional Imaging and Mathematical Modelling of Human Pulmonary Lymphatics",** and the work presented in it are my own and has been generated by me as the result of my own original research.

I confirm that:

- This work was done wholly or mainly while in candidature for a research degree at this University;
- Where any part of this thesis has previously been submitted for a degree or any other qualification at this University or any other institution, this has been clearly stated;
- Where I have consulted the published work of others, this is always clearly attributed;
- Where I have quoted from the work of others, the source is always given. With the exception of such quotations, this thesis is entirely my own work;
- I have acknowledged all main sources of help;
- Where the thesis is based on work done by myself jointly with others, I have made clear exactly what was done by others and what I have contributed myself;
- Parts of this work have been published as:

Robinson, Stephanie K, Jonathan J Ramsden, Jane Warner, and Peter M Lackie. 2019. "Correlative 3D Imaging and Microfluidic Modelling of Human Pulmonary Lymphatics Using Immunohistochemistry and High- Resolution μ CT." Scientific Reports 9 (6415): 1–14. https://doi.org/10.1038/s41598-019-42794-7.

Signed: .....

Date: .....

Acknowledgements

I would first like to acknowledge the considerable advice and support my two supervisors, Professor Tiina Roose and Dr Peter Lackie, have provided throughout the production and writing of this thesis. Especially in allowing me the freedom to take this work in whichever direction I felt was warranted.

I would like to also thank the staff in the Biomedical Imaging Unit, Histochemical Research Facility and the Mu-VIS group. They made my work fun as well as rewarding, even in difficult times. A special word should be given to Mat Lawson, my PhD partner in crime within the imaging unit for the last 4 years.

Importantly, the EPSRC and the Kerkut Charitable Trust also deserve recognition for funding this work and my time.

Finally, I would like to thank my parents Jackie and David Robinson, and my husband, Neil Smyth. Their continual support has enabled me to complete this thesis during times of ill health when I thought I may not be able.

List of Abbreviations

2D	2-Dimensional
3D	3-Dimensional
BVB	Broncho-vascular Bundle
CAT	Computer Axial Tomography
CD31	Cluster of Differentiation-31
CD4	Cluster of Differentiation-4
CD8	Cluster of Differentiation-8
CPU	Central Processing Unit
DAB	3,3'-Diaminobenzidine
ECM	Extracellular matrix
EDTA	Ethylenediaminetetraacetic acid
eNOS	Endothelial nitric oxide synthase
FD	Fractal Dimension
FFPE	Formalin Fixed Paraffin Embedded
GB	Gigabyte
GFP	Green Fluorescent Protein
GOLD	Global initiative for chronic Obstructive Lung Disease
iBALT	inducible Bronchus Associated Lymphoid Tissue
IBMM	Image-Based Mathematical Modelling
IHC	Immunohistochemistry
IL	Intra-Lobular
IPF	Idiopathic Pulmonary Fibrosis
IS	Intra-Septa
LEC	Lympahtic Endothelial Cells
LP21	Lp-mab-21
LYVE-1	Lymphatic Vessel Endothelial Hyaluronan Receptor 1
MRI	Magnetic Resonance Imaging
NSEs	Navier-Stokes Equations
PCK	Pan Cytokeratin
PECAM	Platelet Endothelial Cell Adhesion Molecule-1
PLAG	Platelet Aggregation
RAM	Random Access Memory
RNA	Ribonucleic acid
ROI	Region of Interest
RTP	Room Temperature and Pressure
SARS	Severe Acute Respiratory Syndrome

SEM	Scanning Electron Microscopy
SMCs	Smooth Muscle Cells
SP	Subpleural
T1 Cells	Type-1 Alveolar Cells
TB	Terabyte
TBS	Tris-Buffered Saline
TEM	Transmission Electron Microscopy
TNFα	Tumour Necrosis Factor Alpha
VECs	Vascular Endothelial Cells
VEGF-C	Vascular Endothelial Growth Factor-C
VEGFR-2	Vascular Endothelial Growth Factor Recptor-2
VOI	Volume of Interest
αSMA	Alpha Smooth Muscle Actin
µCT	X-ray Micro-computed Tomography

Chapter 1 **Introduction and Aims**

1.1 The Lymphatic System

1.1.1 Introduction to the Lymphatic System

The study of the lymphatic system has an extensive history, with important contributions made in the field from as early as the 16th century (Loukas *et al.*, 2011). Despite this, it has only been in the last half a century where lymphatic research has really accelerated (Loukas *et al.*, 2011). This growing interest could be as a result of the relatively recent technological developments for improving the ease of mapping lymph drainage, or, the system's newly recognised importance in clinical fields such as cancer, oedema, nutrition, endocrinology, surgery, and the immune response (Guyton & Hall, 2010).

The study of the lymphatic system was consolidated in 1966 by the founding of the International Society of Lymphology during the first international symposium of lymphology in Zurich of the same year (Sheilds, 2001). The newly termed study of "Lymphology" was split into four separate yet cooperative components. These components were the system's transported medium (known as lymph), the cells which are suspended within the lymph (known as lymphocytes), the vessels (lymphatics) that transport these components and the organised lymphoid tissues or organs that the lymphatics innervate. The focus of this work is the lymphatic vessels, the transport links on which the whole system is built; therefore, this section will focus on only this division of the lymphatic system.

There are two main physiological functions of the lymphatics. Phylogenetic research shows the lymphatics evolved when multicellular organisms required a system to remove fluids and proteins from tissues and return them to the bloodstream (Olszewski, 1991). Therefore it acts as a drainage system returning water, proteins and metabolites within tissue lymph to the circulatory system; thus, oversees the maintenance of fluid homoeostasis within the body (Oliver & Detmar, 2002).

The lymphatics also allow rapid transport of lymphocytes and other cell signalling molecules throughout the body via specialised lymphoid tissues. Only relatively recently have scientists proven that the immune system cannot function normally if the lymphatics are absent. As such, the lymphatic system is classified as a part of the immune system. Advancements in oncology and autoimmunity have also highlighted the clinical interest for fully understanding the cellular

transport within the lymphatic system (Alitalo, Tammela & Petrova, 2005), especially in a pathological setting (Mansel, 2000).

Although the desire for knowledge for this system has increased dramatically over the past half-century, the understanding of the systems function is still naive. Research has accentuated extreme variations between and within a species, and even within individuals. It has been suggested that these observations are possibly due to functional differences between species, natural variation within a species, and the system's dynamic characteristics within a non-homeostatic individual (Skandalakis, 2007). This discrepancy has resulted in a limited number of statistically reliable studies being published, and even fewer studies being consolidated. Those that have been published are biased towards animal studies which for many clinicians, have questionable relevance.

The methods available for imaging the system have also been limited, thus raising a difficulty for studying the system (Oliver & Detmar, 2002). In human tissue biopsies, particularly if necrotic, the smaller lymphatics are indistinguishable from the blood capillaries when using conventional histology (Oliver & Detmar, 2002). Therefore, the lymphatics are often absent from histological reporting of disease, and, as a consequence, thought of as secondary to the circulatory system. It was not until the 1990s when specific molecular markers were identified for lymphatic capillaries which enabled large-scale imaging and characterisation of tissue lymphatics in health and disease (Kaipainen *et al.*, 1995).

1.1.2 Structure of the Lymphatics

The lymphatic system is one of the few body systems where the network structure and distribution is still yet to be fully and confidently mapped in all tissue types (Cueni & Detmar, 2008). The generalised structure of the system, however, has been consistently observed in animal models, and to date, human studies have not grossly contradicted these findings (Cueni & Detmar, 2008).

As mentioned above, it has only been since 1990 that lymphatic specific molecular markers became available to discriminate cells comprising the lymphatic network from those in the blood vasculature (Kaipainen *et al.*, 1995). As such, the nomenclature used for the different types of conduits that make up the lymphatic network has not been standardised. Due to this, the research that exists detailing the structure of these conduits can be easily misinterpreted as multiple terms have been used interchangeably within and between species studied. The terminology used in this work will be best suited to the structure it describes. Once stated, the

use of this term will be consistent throughout. Initially, however, the extent of this variation will be demonstrated with the introduction of each conduit level.

The hierarchical structure of the lymphatic network as a whole has been compared to the venous half of the circulatory system by the fact that that they are both low-pressure vessel-based systems, with the smallest vessels intercalating back to the larger vessels which eventually terminate in ducts near the heart (Ohtani, 2008). One research group has shown that mammalian lymphatic endothelial cells are derived directly from the cardinal vein which supports the theory of lymphatic development initially proposed by Sabin in 1902 (Srinivasan et al. 2007,Sabin F.R 1902).

There are, however, several key differences that make the lymphatic network unique. Compared to veins of a similar size lymphatics have thinner walls, contain more valves, and have much greater variation in their calibre. Also, lymph vessels are considerably more numerous than veins, often connected by short anastomotic branches (Haagensen, 1972). The network as a whole differs from the venous system as it has now been experimentally determined that there are structures of lower complexity and structures of higher complexity that are non-existent in the venous system, both of which will be subsequently described. The variation of network structures and their distribution also seems to differ significantly between different tissues compared to the circulatory system (Ohtani, 2008).

The venous system is usually divided into venous capillaries, venules, and veins depending on which part of the system is being described. Similarly, the lymphatic vessel network can be split into the primary and secondary lymphatics. The primary lymphatics are those that consist of prelymphatics, and microlymphatics and are the simple structures of the smallest size that function simply to uptake or absorb fluid from the interstitium, thus creating lymph. The secondary lymphatics consist of highly structured vessels, trunks, and ducts. These larger sized structures collect lymph from the primary lymphatics and propel the lymph centrally to allow the interaction of lymph with the lymphatic organs and the circulatory system (see Figure 1.1). The detailed structure of all primary lymphatics and the smallest of the secondary lymphatics will now be discussed.

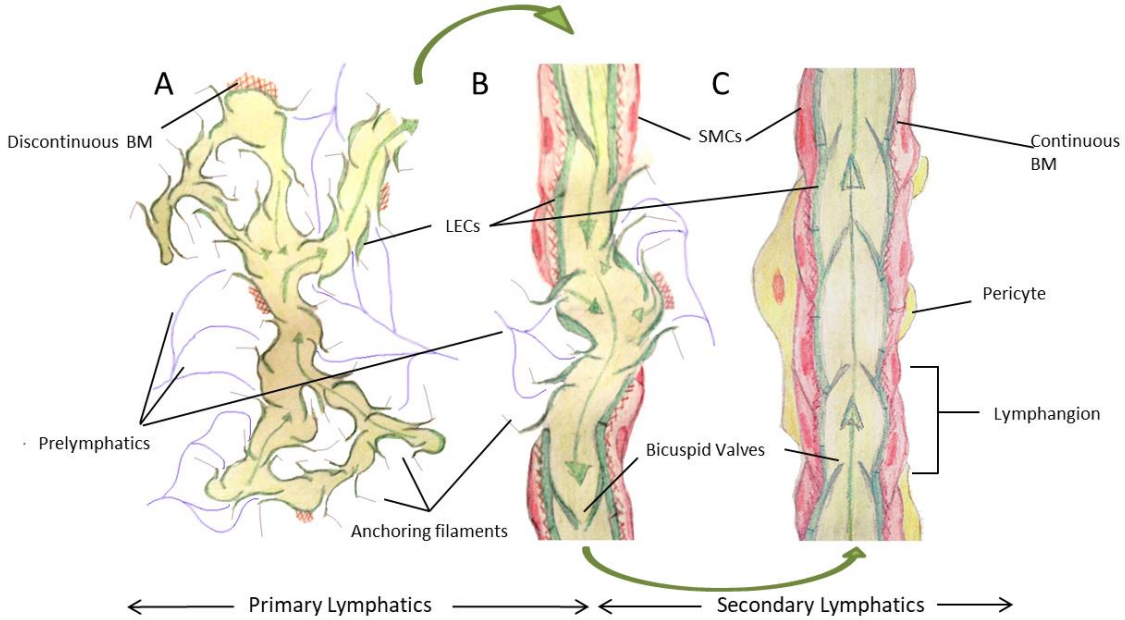

Figure 1.1 Comparison of Lymphatic vessels. **a** Microlymphatics range in diameter from 15-75 µm and have a lymphatic endothelium (LECs) specialised to uptake fluid from the prelymphatics (blue lines). They are anchored to the surrounding connective tissue by anchoring filaments to prevent the low internal vessel pressures causing collapse. **b** Precollecting lymphatics have a total diameter range from 35-500 µm and are fed by the microlymphatics. They act both to propel lymph by the use of smooth muscle cells (SMCs: pink) and to uptake lymph from the tissue via prelymphatics. **c** Collecting lymphatics are of a similar size to, and receive lymph from, the precollecting lymphatics. They function solely to propel lymph fluid centrally by the use of SMCs and pericytes (yellow). N.B This diagram is not to scale. BM =Basement membrane, green arrow= direction of lymph flow.

1.1.3 Prelymphatics (Primary Lymphatics)

At the periphery of the system, the lymphatics form a functional entity with non-endothelialized interstitial tissue channels (see Figure 1.1 a and b), which in most tissues are termed the prelymphatics (Casley-Smith, 1979). These structures are not considered vessel structures at all but have been accepted as the structures that initiate the formation of lymph by supplying tissue fluid and content for microlymphatic uptake (Rovenska, 2011). The basement membrane presents a hindrance, particularly to the larger macromolecules, at high flow rates thus the prelymphatics are probably the paths that enable macromolecule suspensions to pass from the interstitial space to the lymphatics (Casley-Smith, 1976). The prelymphatics were first described by the use of electron microscopy in 1980 by Casley-Smith (Casley-Smith, 1980). These channels were shown to range from 0.1-2 µm in diameter depending on the type and state of the innervated tissue. They form an interconnecting network which, from current understanding, is now thought to infiltrate all the cell masses of the body. The findings of this study suggested the previously described (and in some papers still described) “blind-ended” nature of the lymphatic capillaries is an artefact from the retrograde filling methods used in morphometric studies (Rovenska, 2011). Therefore,

from current knowledge, the most peripheral part of the lymphatic system is now described as a completely open system of tissue channels.

It should be noted that the majority of the work that measured and characterised these channels was carried out in the 1970s/80s before unequivocal lymphatic detection was available, thus, could well be deemed out of date. Currently, however, there seems not to be any evidence to contradict these findings. Therefore, there are grounds to review the extent of the prelymphatics considering the availability of modern and more advanced imaging methods.

1.1.4 Microlymphatics (Primary Lymphatics)

Prelymphatics are drained by the collectively described 'microlymphatics', 'initial lymphatics', 'terminal lymphatics', or 'lymphatic capillaries'(Scallan *et al.*, 2010). As the 'lymphatic capillaries' may be much larger than traditional blood capillaries (15-75 µm and 5-10 µm respectively (Leak & Jamuar, 1983)) and the presence of prelymphatics render the 'terminal lymphatics' and 'initial lymphatics' descriptions ambiguous, these three phrases will be hereafter avoided. Figure.1a shows the microlymphatics structure.

The microlymphatics do not always loop back upon themselves and thus, as previously stated, are commonly described as blind-ended vessels (Swartz, 2001). In contrast to blood vessels and secondary lymphatics, microlymphatics are not invested by pericytes, and they are generally irregularly contoured as they are low pressured structures of little mechanical strength (Swartz, 2001). They are often observed in human studies in a partially or fully collapsed state (Schmid-Schönbein 1990, Aukland & Reed 1993). They are also sometimes termed 'bulbous' which may seem contradictory to the previous statement. This description comes from animal studies which ensure lymphatic visualisation by inducing localised oedema (increased tissue fluid), this increases the hydrostatic pressure difference between the interstitium and vessel resulting in the swelling of microlymphatic structures. In this dilated form, they tend to lose their tubular appearance (Schraufnagel, 2010).

The microlymphatics are comprised of a single highly attenuated layer of nonfenestrated cells known as lymphatic endothelial cells (LECs) which, except for the microlymphatics in the bat's wing, are noncontractile (Leak 1976, Hogan & Unthank 1986). The use of transmission electron microscopy (TEM) in 1966 revealed that specialised inter-endothelial junctions play a significant role in the draining function of microlymphatics. Later work showed that discontinuous 'button-like' junctions anchor the LEC's together either side of the mutually overlapping endothelial extensions (Baluk *et al.*, 2007). These rounded extensions give rise to the LEC typical oak-leaf shape (Schraufnagel, 2010). The endothelial projections on the external side of the vessels do not

possess any intercellular adhesive junctions but attach directly to the framework of the extracellular matrix (ECM) by elastic fibres termed 'anchoring filaments' (Leak & Burke, 1968). When interstitial fluid pressure rises, the anchoring filaments are put under strain. Thus, they pull back the external endothelial projection permitting the easy passage of fluid and particles into the vessel (Schulte-Merker, Sabine & Petrova, 2011). These filaments are also thought to help preserve the functionality of lymphatics by preventing vessel collapse when lymphatic capacity reaches a maximum (Pullinger & Florey, 1935). The internal endothelial projections are completely unattached and act like a micro-valve. As fluid enters the lumen and the pressure differences across the vessel wall reverse, the anchoring filaments loosen, and the internal 'micro-valves' begin to close, preventing retrograde flow back into the interstitium (Pullinger & Florey, 1935). These 'micro-valves' are also termed primary valves (Trzewik *et al.*, 2001).

1.1.5 Precollecting Lymphatics (Secondary Lymphatics)

The precollecting lymphatics connect the primary lymphatic network to the secondary lymphatic network (see Figure 1.1b). Although the precollectors have now been considered to be a distinct lymphatic vessel, their definition is ambiguous because precollectors have features of both microlymphatics and collecting vessels (Yang & Oliver, 2014). They have fully developed bicuspid valves, but unlike the collecting vessels, which the valves are located at regular intervals, their distribution is more irregular and may comprise of a single leaflet (Tretbar *et al.*, 1992, Sacchi *et al.*, 1997). The precollectors contain one or more discontinuous layers of smooth muscle cells (SMC) outside the LEC layer which are not related to the valve position (Comparini, 1962). These cells are arranged helicoidally and are capable of performing spontaneous phasic contractions needed to propel lymph (Zawieja, 2009). Within the sections lacking muscle, the endothelial layer is similar to that of microlymphatics with a discontinuous basement membrane and observable anchoring filaments. These structural features suggest these sections absorb fluid and therefore, pre-collecting lymphatics have a dual role: uptake and propulsion of lymph (Sacchi *et al.*, 1997). The presence and absence of an SMC layer may explain the extremes in the lumen shape. The precollector lumen can differ from ovoidal to slit or even star-like in different serial sections of the same vessel, thus, their diameter can range from 35 to 150 μm or even 300 μm in some cases (Sacchi *et al.*, 1997).

1.1.6 Collecting Lymphatics (Secondary Lymphatics)

The collecting lymphatics, graphically shown in Figure 1c, drain the precollectors and are denoted either pre-nodal or post-nodal by their anatomical location only; no morphological or structural differences exist between the two (Scallan *et al.*, 2010). The wall structure is similar to that of

blood vessels. Three layers can be identified, the intima, media, and adventitia, composed of LEC's, SMC's and collagen fibres, respectively (Boggon & Palfrey, 1973). They are no larger than the precollectors with a diameter ranging from 35-300 µm and like the precollectors, the muscle bundles are arranged in a helicoidal manner, but in contrast, the SMC layer and the basement membrane are continuous (Sacchi *et al.*, 1997). Collecting lymphatics display many swellings and strictures along their course due to the presence of regularly placed bicuspid valves (Pan *et al.*, 2010). An Immunofluorescence study gave evidence for the lack of microvalves within these vessels as the LEC of the collecting lymphatics possessed zipper-like junctions and button-like junctions were not evident (Baluk *et al.*, 2007).

The section of the vessel that is encompassed by two valves is known as a lymphangion (Loukas *et al.*, 2011). Lymph propulsion is regulated by the cyclical compression and expansion of lymphatic vessels by surrounding tissues and intrinsic pump forces generated by the spontaneous phasic contraction of SMCs (Zawieja, 2009). Different anatomical sites possess different lymphangion diameter to length ratios being generally highest in the legs or organs with high hydrostatic pressure (Földi *et al.*, 2006). Lymphangions have also been reported to double or triple their diameter during diastole (Benoit et al. 1989, Nisimaru 1982). This observation can pose a limitation to the lumped modelling of lymph flow within these vessels (Margaris & Black, 2012) (see section 1.4.2).

1.2 The Human Lung and Pulmonary Lymphatics

Like the rest of the body, lymphatics are essential for lung fluid homeostasis, inflammatory and immune responses (Schraufnagel, 2010). They are imperative in the lung as fluid can be more difficult to control in comparison to other tissues, and excess interstitial tissue fluid can have more physiological consequences (Miserocchi *et al.*, 2001).

The lungs have one of the most extensive blood capillary beds in the body as half of the circulating blood needs to pass through this organ at any one time (Guyton & Hall, 2010). The lung's interstitial space and thin epithelium are therefore constantly exposed to large variations in osmotic, hydrostatic, and hydrodynamic forces and must adapt rapidly to a constant movement of fluid, protein, and cells (Sozio *et al.*, 2012).

The lungs also have to respond to inhaled environmental insults such as bacteria, viruses and air pollutants (Negrini & Passi, 2007). The mobilisation of lymphocytes and other defensive mechanisms to and from the site is, therefore, vital to prevent infection or tissue damage (Miserocchi *et al.*, 2001).

In addition to these well-known functions, the pulmonary lymphatics are vital in aiding the adaptation of fetal breathing at birth and possibly influential in tissue repair and fibrosis and human chronic diseases (Kulkarni et al. 2011, Ebina 2008, El-Chemaly et al. 2009, Yamashita et al. 2009, Mori et al. 2013).

1.2.1 Structural Features of the Peripheral Lung

To understand the distribution and function of peripheral pulmonary lymphatics, knowledge of the pulmonary anatomy is vital. An overview of the basic respiratory anatomy is given below and graphically shown in Figure 1.2. This detail is well summarised in a recent review article (Hsia, Hyde & Weibel, 2016).

The secondary lobule, defined as the smallest structural unit of the lung, is marginated by a connective tissue septum termed the interlobular septa. This lobule is supplied by a centrally located bronchiole and pulmonary artery branch. These two structures form the bronchovascular bundle, which is encircled by a small amount of supporting connective tissue termed the centrilobular interstitium.

The central bronchiole divides into the terminal bronchioles which have a continuous wall and the respiratory bronchioles which terminate into alveolar ducts and the alveoli. These airways are accompanied by small bronchial arteries, derived from the thoracic aorta, which supplies the bronchiole wall with oxygen and nutrients. The small bronchial veins drain into the central pulmonary veins. The connective tissue surrounding the bronchial and the alveolar structures is termed the intralobular interstitium, and the tissue space between alveolar sacs where gas exchange occurs is usually termed the interalveolar septa.

The pulmonary artery branch gives rise to the smaller arterioles, which in turn feed a dense capillary network in the intralobular interstitium and interalveolar septa. Small venules carry the newly oxygenated blood towards the periphery of the lobule, which subsequently merge into the pulmonary vein branches located in the interlobular septa.

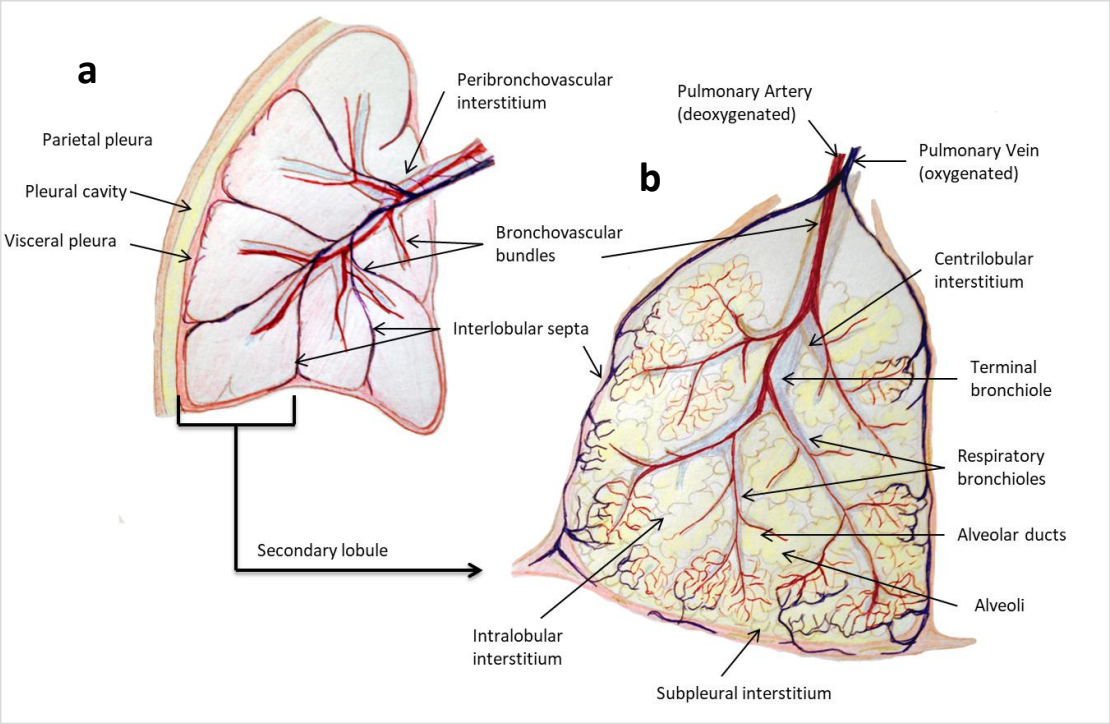

Figure 1.2 Human Lung Anatomy and Terminology. **a** A simplified structure of one of the five lobes of the human lung made up of secondary lobules of ~ 1cm in diameter. Each secondary lobule is supplied by a bronchovascular bundle comprised of a bronchiole and a pulmonary artery branch. These bundles are surrounded by their specific connective tissue termed the peribronchovascular interstitium. **b** A close-up image of the secondary lobule also termed the respiratory unit of the lung. The arteries accompany the bronchi, whereas the veins travel through the interlobular septa. A respiratory bronchiole with all its associated structures is also known as the pulmonary acinus or primary lobule. N.B. Not all of the capillary beds are detailed; every alveolus is densely covered in a blood vessel network to enable oxygen exchange to occur.

1.2.2 Drainage of the Pulmonary Lymphatics

Although debated, the drainage of the pulmonary lymphatics are generally thought to take two routes: the more peripheral lymph vessels drain towards the subpleural interstitium and subsequently return to the hilum via the interlobular septal vessels; the central lymphatics drain directly towards the hilum (Leak & Jamuar, 1983). The pleural flow is more efficient than the central flow, which explains the “butterfly pattern” of an acute pulmonary oedema radiograph in human patients (Fleischner, 1967). The butterfly pattern refers to the bilateral perihilar distribution of opacity upon the frontal chest radiograph (Gluecker *et al.*, 1999).

It has been shown that gravity and respiratory movement also affect lymph flow as the lower lobes have been shown to clear lymph four times faster than the upper lobes (Staub 1974) (Negrini & Passi, 2007).

1.2.3 History of Structural Pulmonary Lymphatic Studies

Historically, the study of the pulmonary lymphatic anatomy has been limited to lymphangiography, TEM or, more recently, scanning electron microscopy (SEM) of *ex vivo* casts due to a lack of reliable morphological markers and reagents *in vivo* (Ohtani 2008, Leak & Jamuar 1983, Schraufnagel 2010). The 20th-century studies suggested that lung lymphatic vessels exist within the connective tissue sheets surrounding the large airways and blood vessels, the parietal and visceral pleura, and the interlobular septa (Lauweryns & Baert 1977, Marchetti et al. 1994, Leak & Jamuar 1983). Much of this work confirmed that the lung contains microlymphatics and collecting lymphatics (defined by their ultrastructure as previously described), although their distribution within the lung is not uniform (Leak & Jamuar, 1983).

1.2.4 Lymphatic Biomarkers Within the Human Lung

The recent identification of specific lymphatic biomarkers, coupled with the availability of antibodies for visualisation, has enabled a greater understanding of the pulmonary lymphatic morphology and function (Kahn et al. 2002, Scavelli et al. 2004, Kato et al. 2006).

Lymphatic vessel endothelial hyaluronan receptor 1 (LYVE-1) is one of the first markers of LECs to be identified (Jackson, 2004). It is strongly expressed on the entire luminal and abluminal surface of LECs, even on fine filopodia of growing vessels during lymphangiogenesis. However, LVYE-1 is less strongly expressed on collecting lymphatics than on microlymphatics and expression of LYVE-1 can be downregulated by cytokines, such as TNFα in some inflammatory conditions (Johnson et al. 2007, Baluk & McDonald 2008). LYVE-1 has been shown to be expressed by pulmonary capillaries, and pulmonary arteries and some macrophages in the lung (Baluk et al. 2005, Favre et al. 2003, Cho et al. 2007).

The transcription factor Prox-1 is also expressed in LECs from the early stages of embryonic development (E9.5 in mouse). Prox-1 is believed to be a master control gene inducing the expression of other lymphatic markers and is a convenient marker of the nuclei of LECs (Wilting *et al.*, 2002).

Podoplanin is a platelet aggregation-inducing type I transmembrane sialoglycoprotein, highly expressed in LECs and involved in tumour invasion and metastasis (Oki *et al.*, 2015). Its mass varies from 38 to 50 kDa due to the extent of the sialylation of its extracellular domain(Pula *et al.*, 2013). In the context of the lung, podoplanin deficient mice die at birth on account of respiratory failure and lymphatic defects (Schacht *et al.*, 2003). However, in mice, rats and humans, the species-specific glycoprotein is also expressed in type I epithelial cells (T1 cells) as well as LECs.

(Gonzalez & Dobbs, 1998). In rats and humans, podoplanin is up-regulated in T1 cells upon acute lung injury and infection (Mcelroy & Kasper 2004, Newman et al. 2000, Tyrrell et al. 2012). To date, two isoforms of podoplanin have been discovered which are probably a product of alternative splicing, but their biological significance is not yet known (Pula *et al.*, 2013).

The monoclonal antibody, D240, is presently the most widely used anti-human podoplanin antibody, with antibody NZ-1 also being frequently used, for both therapeutic targeting and molecular imaging (Ogasawara *et al.*, 2008). Both recognise an amino acid epitope within the three PLAG (platelet aggregation) domains in the extracellular region of the protein (see Figure 1.3). All currently characterised monoclonal antibodies raised against human podoplanin (shown in Figure 1.3) have shown staining of T1 cells when used for imaging except for LpMab-21 (LP21) (Kaneko *et al.*, 2017). LP21 has a conformational epitope that includes an O-linked glycosylation moiety, whereas D240's, NZ-1's, and LpMab-17's epitopes are solely amino acid-based (Ogasawara *et al.*, 2008). Although LpMab-12 is also targeted against an O-linked glycosylation moiety, it still demonstrated T1 cell staining.

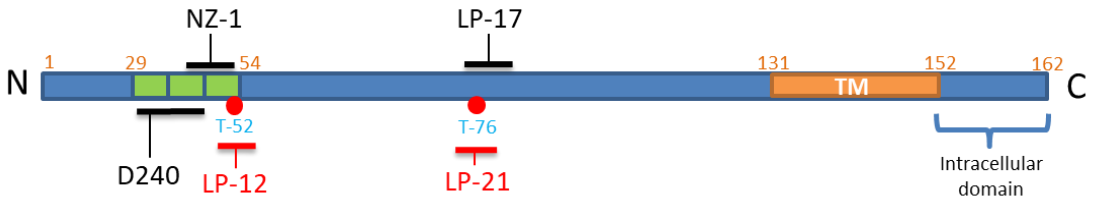

.

Figure 1.3 The Binding Sites of Characterised Antibodies Raised Against Human Podoplanin. Diagrammatic representation of the polypeptide transcript of human podoplanin. The red circles indicate two of the multiple threonine (blue text) O-linked glycosylation sites known to exist in the extracellular region of human podoplanin. The names of the antibodies in black have peptide epitopes, whereas those in red have epitopes that include the sugar moiety. Amino acid numbers indicated by the orange text. Orange domain =transmembrane domain, green domains= platelet aggregation (PLAG) domains.

1.2.5 Current Understanding of Peripheral Pulmonary Lymphatics

Work done by Schraufnagel in 2010 detected the existence of prelymphatics within the healthy animal lung (Schraufnagel, 2010) and, along with his colleagues, had previously shown how lymphatics could expand after pulmonary tissue insult (Schraufnagel et al. 1994).

El-Chemaly et al. (2009) and Yamashita et al. (2009) were amongst the first to detail the 2D morphology of peripheral human pulmonary lymphatics using anti-podoplanin antibodies (D240). They compared the morphometry of healthy peripheral pulmonary lymphatics to lymphatics present in idopathic pulmonary fibrotic (IPF) tissue and tissue with diffuse alveolar damage. In healthy lung controls, both groups observed lymphatic structures only in the interlobular septa,

the visceral pleura and the bronchovascular bundle as historical studies suggest (Lauweryns & Baert 1977, Marchetti et al. 1994, Leak & Jamuar 1983).

Within the same year, this finding was contradicted as it was demonstrated that human lymphatic vessels extend beyond the bronchovascular bundle, following intralobular arteries deep inside the secondary lobule and that some are present independent of blood capillaries in the interalveolar septa (Kambouchner & Bernaudin, 2009). This study only characterised the vessels according to their diameter as the paper mainly concerned their existence and validity of the D240 antibody.

Detailed morphological characteristics, lymphatics distribution and lymphatic patterning associated with the entire healthy human secondary lobule was first reported in 2012 (Sozio *et al.*, 2012). This paper showed that the size of the lymphatic vessels decreased when moving towards the periphery, and can be split into three distinct populations defined by their vicinity to other tissue structures and characterised by their morphometric parameters.

Lymphatics associated with the bronchovascular bundle, subpleural space and interlobular septa were shown to have long and thin profiles as if cut longitudinally along their length.

Peripheral lymphatics associated with arteries and arterioles only were shown to be much smaller structures but of a greater quantity than the other populations. This observation was attributed to the fact that the arterial wall (both the endothelium and SMCs) expresses the main lymphangiogenic factor, vascular endothelial growth factor C (VEGF-C) (Partanen et al. 2000).

Few lymphatics were observed in the interalveolar septa independent of blood vessels; thus, they could not be described as a fourth population distinct from the perivascular lymphatics. However, they suggest that interalveolar lymphatics probably do not play a significant role in the interstitial drainage of the lung under normal conditions due to their size and number. The finding of intraalveolar lymphatics in the healthy human peripheral lung was supported in 2013 (Mori *et al.*, 2013). Mori et al. (2013) showed that the typical interalveolar lymphatic structures do not alter their morphology in Chronic Obstructive Pulmonary Disease (COPD) patient lung samples; however this does not rule out modulation of these structures in other pulmonary disease states.

The research as mentioned above has detailed the morphometry and distribution of pulmonary lymphatics in healthy tissue. However, although much detail is inferred, the work is limited by the use of 2D data which has the potential to miss crucial morphological features of the lymphatics. For example, vessels which appear to be separate in 2D could be parts of the same complex 3D structure. Only two known studies, from the same group (Tohoku University, Japan) have attempted to image features of the peripheral human pulmonary lymphatics in 3D (Yamashita *et al.*, 2009) (Ebina *et al.*, 2010). In both studies, the authors used serial sections of D240+ stained

lung tissue (maximum 50 sections (200 μm)) and imaged each stained section at the same location. They aligned and then reconstructed these 2D images into a 3D image of the D240+ structures in the lung tissue. Both of these studies were demonstrating methods, rather than experimental study; therefore, no statistical conclusions were made on the structure of the pulmonary lymphatics. It should be noted that microtome sectioning for histological staining is known to create cutting artefacts such as lost sections, section compression or stretching which over a series of 50 sections may have considerable effects on the obtained 3D structure (Mega *et al.*, 1997; Scott *et al.*, 2015).

1.3 X-Ray Micro-Computed Tomography (μCT)

X-Ray Micro-Computed Tomography (μCT) is a 3D imaging technique that detects the attenuation of an X-ray beam transmitted through a rotating sample and measures the samples internal structure to micrometre spatial resolution.

1.3.1 Basic Setup

Micro-focus X-ray Computed Tomography (μCT) is closely related to the Computerized Axial Tomography (CAT or CT) scans that have been used for medical imaging for nearly 50 years (Landis & Keane, 2010). Within the μCT scanner, an electron beam is focused onto a micrometre-sized spot on an elemental metal target, generating an X-ray source at that particular point. The sample, placed between the X-ray source and detector, selectively absorbs X-rays leaving only those that penetrate through the sample to reach the detector. The sample is rotated by a small angle, producing a series of 2D radiographs of the object, analogous to the radiographs captured by rotating the X-ray source(s) and detector(s) around the patient in a medical CT scanner. Moving the sample relative to the source and detector allows for the optimization of geometric magnification, spatial resolution and sample focusing by adjusting the source to sample and sample to detector distances. The standard set up for a laboratory-based μCT scanner is shown in Figure 1.4.

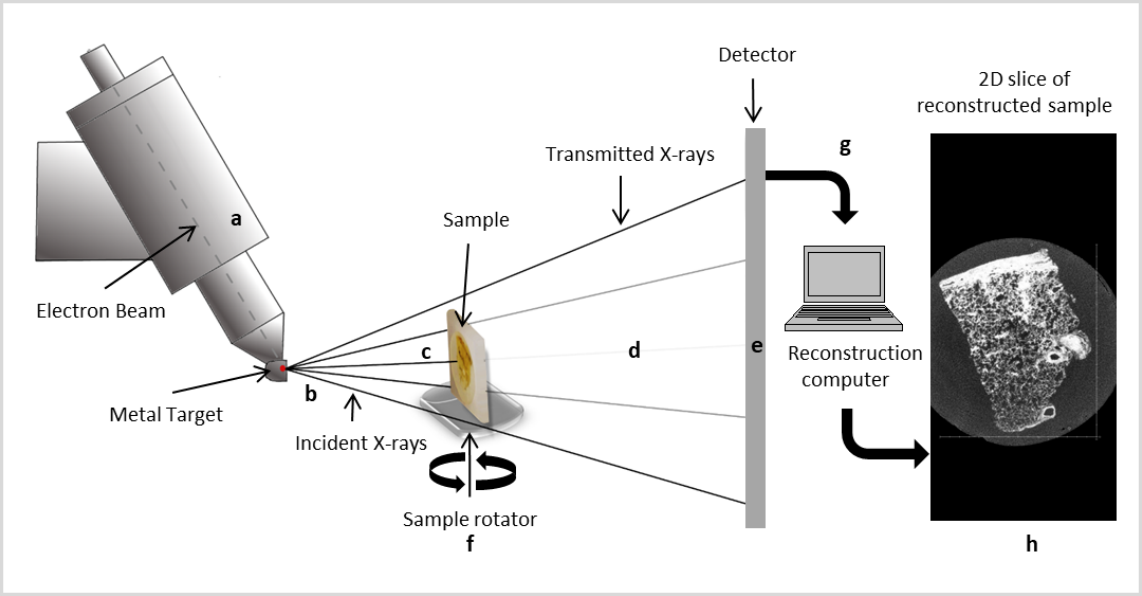

Figure 1.4 A Diagram of a Standard Absorbance X-ray µCT Scanner. An electron beam (**a**) is accelerated and focused onto typically a tungsten or molybdenum target metal with a spot size of ~1 µm(**b**). X-rays are produced from the target in a scattered "cone-beam" shape (**c**). These incident X-rays hit the sample and get absorbed in numbers dependent on the sample density. The transmitted (**d**) X-rays continue in a trajectory towards the X-ray detector (**e**) which collects the number of photons hitting each part of the detector, termed a radiograph. The distance the detector is away from the sample changes the amount of geometric magnification achieved. This process is repeated at increments throughout a 360°rotation (**f**). All radiographs are sent to a reconstruction computer to assemble the data into a 3D volumetric image (**g**). This image can be viewed as a density map in 3D or as a 2D slice at any orientation through the volume (**h**).

In radiographs, features can only be identified within the 2D plane of the image projection. A feature can be lost if it overlaps with other features through the depth of the projection. Using algorithms developed from applied mathematics and computer science, a series of 2D radiographs are reconstructed into a 3D digital image where each voxel (3D pixel) represents the X-ray absorption at a single point in 3D space (Flannery *et al.*, 1987). As X-ray absorption is related to material density, the 3D internal structure can be inferred from the images, and internal features can be uniquely positioned. Following the convention used in the display of 2D radiographs, parts of the sample that absorb more incident X-rays appear whiter, with the background (typically air) and less X-ray absorbing regions appear darker.

1.3.2 Increasing X-ray Contrast in Samples

Imaging with greater detail is achieved when samples have inherent or added X-ray contrast. Imaging contrast is often achieved either by using or generating, air interfaces within the tissue or by chemical enhancement of the tissue using stains, or filling agents that highly absorb X-rays. Many of these highly absorbing stains are those that contain heavy metals such as osmium,

phosphotungstic acid, and barium, or non-metal stains that contain elements of a relatively high atomic number such as iodine.

As well as providing basic contrast in the image, increasing the X-ray attenuation of tissues allows faster µCT scans. Faster scans reduce the likely extent of biological sample movement during the scan, minimising the pixel shift between each radiograph taken. Simple tomographic reconstruction relies on the assumption that the samples are physically stable and do not move as they are rotated, therefore, the likelihood of movement artefacts is reduced.

1.3.3 Diagnostic Sample Preparation Methods

Traditional diagnostic imaging methods require soft tissues, once excised, to be preserved to prevent tissue degradation, and a level of structural rigidity introduced to the tissue to allow sectioning.

The most commonly used preservation method is chemical fixation, where the biochemical processes, which cause tissue degradation and decay, are stopped through protein crosslinking or denaturing. The use of ethanol is used to dehydrate the tissue to enable embedding of the tissue into hydrophobic resin or wax. The added rigidity which the resin or wax provides is essential for mechanical sectioning for 2D imaging and staining.

Although fresh, hydrated tissues can be imaged using µCT, due to the lack of contrast achieved, the high prevalence of movement artefacts and the incompatibility with correlative imaging, it is very rarely undertaken. Therefore, standard tissue preservation and immobilisation methods are often ideal for high resolution µCT imaging. Tissue immobilization stops movement artefacts, while a density interface is created between the tissue and the embedding medium, which improves imaging contrast (Scott *et al.*, 2015; Katsamenis *et al.*, 2019).

As standard, clinical samples undergo resin or paraffin embedding protocols to facilitate sectioning for diagnostic light or electron microscopy. A plethora of archived human biopsies, collected over many decades are stored in clinical archives, therefore, provide an almost unlimited supply of human samples to study a wide range of disease conditions. The non-destructive nature of µCT allows imaging of these samples without compromising them.

Resin-embedded sample blocks for research or diagnosis are mainly prepared for ultramicrotomy and transmission electron microscopy. Thus, blocks are often no larger than 1-2 mm^3 and include heavy metal stains which increases X-ray absorption contrast but has inherent limitations as mentioned above. Resins also partially inhibit photo-switching of fluorophores, thus preventing correlative fluorescent imaging techniques (Kim *et al.*, 2015).

Our group has assessed the use of paraffin wax as an immobilising and contrast medium for µCT through the use of archived human lung biopsy samples. This work showed that it is possible to image blood vessels and lung parenchyma without the need for contrast stains or cast formers if the µCT imaging is optimised (Scott *et al.*, 2015). Last year our group demonstrated how a laboratory µCT scanner had been optimised for soft tissue imaging using standard X-ray absorbance techniques. Figure 1.5 shows an example image taken of formalin-fixed, paraffin-embedded (FFPE) human lung tissue (Katsamenis *et al.*, 2019). With the use of µCT it is now possible, therefore, to assess human lung samples provided from tissue banks or provided by biopsy/ lobectomy specimens taken during surgical interventions (Jones *et al.*, 2016; Scott *et al.*, 2015; Hogg *et al.*, 2009; Hogg, McDonough & Suzuki, 2013; Verleden *et al.*, 2014; Tanabe *et al.*, 2018; Boon *et al.*, 2016; Litzlbauer *et al.*, 2010; Watz *et al.*, 2005; Katsamenis *et al.*, 2019).

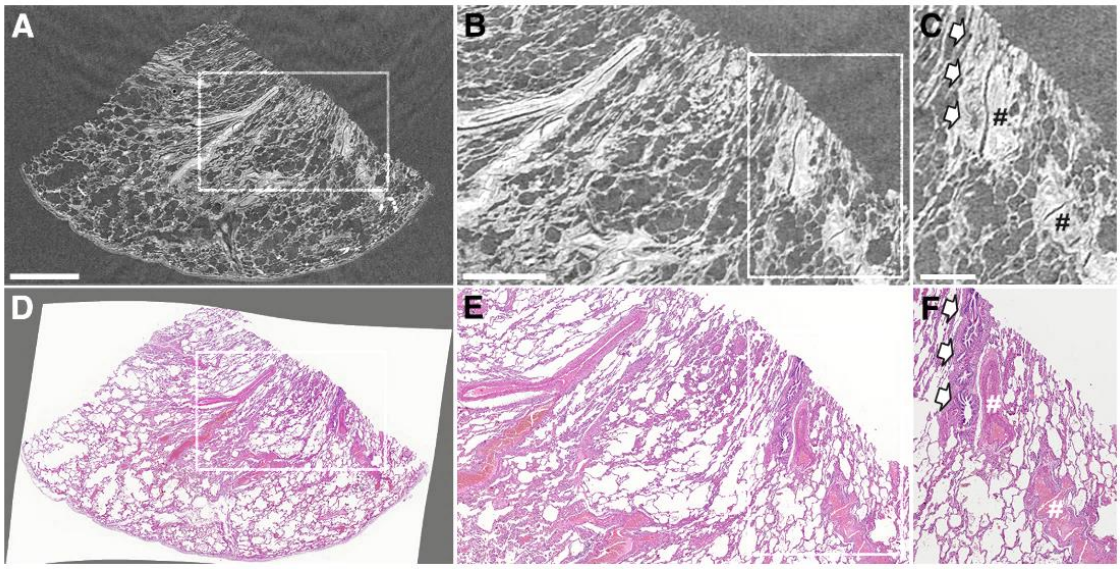

Figure 1.5 Correlative µCT and Histology Imaging of a Formalin-Fixed Paraffin-embedded Clinical Sample (from Figure 3, Katsamenis *et al.*, 2019). Comparison between lung tissue imaged by µCT and light microscopy for conventional histology. The lung biopsy sample has been taken from a non-involved site from a patient with lung cancer. A-C: The µCT slice is provided. D-F: Digitized images of the histology slide. D: The histology image is intentionally presented against a grey background to highlight the degree to which the image had to be unwrapped to fit its non-distorted state (i.e., before sectioning). The comparison shows that tissue lung microstructure is clearly visible in the µCT data set at high image contrast levels, which is because of the newly developed µCT scanner that is optimized for soft tissue imaging at high spatial resolutions. Boxed areas are shown at higher magnification to the right. B, C, E, and F: Higher-magnification images for comparison of µCT imaging to the higher-resolution light microscopy histology. C and F: Arrows indicate an airway; hash marks, a blood vessel, respectively. Scale bars: 2 mm (A); 1 mm (B); 500 mm(C) (Katsamenis *et al.*, 2019).

These diagnostic tissue preparation processes (predominantly the use of ethanol for dehydration) can shrink the tissue up to 50% of its original volume (Senter-zapata *et al.*, 2016; Schneider & Ochs, 2014a). Extreme care must, therefore, be taken when analysing quantitive morphometry, as is the case with all forms of standard histological imaging methods.

Snap freezing using liquid nitrogen or dry ice is also commonly used to immobilise the tissue for sectioning if chemical fixation is undesired. Examples of this are when the biomolecular analysis is desired post-imaging, or your chosen antibody is not compatible with formalin-fixed, paraffin-embedded sample preparation. In standard protocols, samples are often snap-frozen in O.C.T (optimal cutting temperature) compounds which are made up of water-soluble glycols and resins to maintain a consistent microtome cutting density. Due to the lack of contrast, this method is, therefore, is not advantageous to µCT imaging. However, for tissue samples that have open structures like the lung, snap- freezing in its native state can provide good contrast for µCT imaging due to the frozen tissue- air interface.

Despite this, any form of snap freezing adds complexity for µCT imaging as maintenance of the frozen state, without any deformation, is difficult. However, work performed by Kantor et al. (2002) demonstrated an application of a liquid nitrogen-based cooling rig (cyrostatic chamber) for laboratory µCT imaging. Movement of Iodine based contrast agent across a section of porcine arterial vascular wall was visualised and quantified, tracing the 3D movement of the iodine into tissue volume of up to 2 cm^3 to monitor trans-vascular fluid dynamics. Work performed in 2003 showed a cryogenic µCT scanning technique that produced 3D images of bone architecture before RNA isolation and gene expression analysis of human iliac crest bone biopsies (Maran *et al.*, 2003).

Critical point drying is another tissue preparation technique that can induce high contrast between tissue and air interfaces. It avoids the creation of damaging surface tension forces associated with oven drying by bringing liquid in the sample to the gas phase without crossing the liquid-gas phase boundary. Critical point drying of a primate's eye has shown that the contrast gained using critical point drying was qualitatively similar to those obtained in air-contrast enhancement. Of particular interest, this work also showed that post µCT imaging histological imaging was possible (Zysk *et al.*, 2012).

As with FFPE samples, critical point drying requires fixation and alcohol dehydration of the sample therefore, shrinking-artefacts are a common problem. Work in 2012, specific for whole lung imaging, demonstrated a method to eliminate sample preparation shrinkage artefacts (Vasilescu *et al.*, 2012). They showed that using a combination of perfusion fixation techniques and oven drying while the lungs were maintained at physiological pressures, only a +8.95% lung volume change occurred from the *in-vivo* µCT scan to one-day post-fixation and drying. Less than -4.90% volume change was measured 70 days post-fixation and drying. Histological analysis post sample preparation and µCT imaging demonstrated smooth blood vessel wall structures and open capillaries at 20 x magnification. It was also reported that no broken alveolar walls were apparent.

1.3.4 The Value of µCT as an Individual Technique

Using µCT to image the lung and other soft tissues allow the characterization of the topology, connectivity and micro-architecture of anatomical structures in 3D. Of particular importance for lung research, is the ability to assess connectivity of structures such as branching airways, blood vessels and fibrotic plaques. It is possible to image tissue volumes from cm^3 down to μm^3 on the same tissue sample with a laboratory µCT, thus achieving an overview of the structural context and detailed local tissue assessment.

To identify specific volumes or areas of interest within tissue samples, or to assess tissue heterogeneity, using traditional techniques has involved sectioning, staining and 2D microscopy to determine whether the area of interest has been exposed. A typical search can involve 20 or more such cycles per sample (Lewandowski *et al.*, 2016). Volumetric imaging by µCT before subsequent sectioning enables a more informed decision about the depth cutting required to reach the region of interest, potentially saving considerable time and effort.

The 3D volumes obtained by µCT provide a digital 3D density map of the sample that can be easily resliced in any of the x, y or z orthogonal planes and viewed as an "orthoslice". The µCT sectioning plane can further be adjusted to any plane selected by the user, allowing for 2D assessment of features from any direction or angle. The whole sample volume can then simply be viewed as slices parallel to the plane of choice by scrolling through images from the top to bottom of the sample. Most visualization software programmes allow the three orthogonal planes to be viewed and scrolled through at the same time. The viewer can then easily assess if a feature identified one 2D section is consistently seen in the surrounding tissue, allowing rapid assessment of heterogeneity within a sample. Imaging samples at a microscopic level by µCT has been referred to as 3D X-ray histology (Katsamenis *et al.*, 2019; Khimchenko *et al.*, 2016) or " 3D virtual histology" (Missbach-Guentner *et al.*, 2018; Busse *et al.*, 2018; Johnson *et al.*, 2006; Dudak *et al.*, 2016; Saccomano *et al.*, 2018). Simple volume rendering and differential thresholding of X-ray absorption values allow further examination of the 3D structure of the samples. More sophisticated segmentation of specific structures and networks within the tissue is increasingly becoming feasible and greatly facilitate quantitative analysis and modelling as will be discussed later.

As mentioned above, compared to conventional histology, µCT imaging eliminates cutting artefacts and errors such as lost sections, section compression or stretching (Mega et al., 1997, Scott *et al.*, 2015). It non-destructively generates isotropic image data for the whole sample that would be impractical or impossible to obtain by physical sectioning. As lung tissue is particularly prone to deformations during processing and mechanical sectioning, the benefit of µCT in lung

research is apparent in fields where the tissue morphometry is closely linked with disease diagnosis and progression such as in cancer or IPF (Jones, Milthorpe & Howlett, 1994).

1.3.5 Using µCT as a Correlative Tool

The non-destructive nature of µCT allows correlative and multimodal imaging approaches suited to the research area of interest. If *ex-vivo* samples are used, 3D µCT reconstructions can reach resolutions approaching that used for light microscopic histology on the same volume of lung tissue. This better resolution has enabled correlative studies between these two imaging techniques to be undertaken. Cellular detail and biomarkers, identified through histology and immunohistochemistry techniques, can be registered and located within the 3D µCT image data set of the same sample. This potential for 3D data sets to enhance traditional histopathology methods is nicely demonstrated in studies that use µCT to examine human lung tissues before sectioning and microscopy take place.

The effectiveness of combining µCT imaging with a human clinical sample processed routinely for diagnostic histology was first demonstrated by Scott and colleagues (Scott et al., 2015). Within the same unstained human lung tissue sample, the optimization of methods for µCT imaging and correlating µCT with histology were described, enabling high-resolution 3D imaging of the small airways and blood vessels in peripheral human lung tissue with high-fidelity.

Further to this work, the 3D interconnectivity between fibroblastic foci in lung samples taken from patients with idiopathic pulmonary fibrosis has been investigated (see Figure 1.6). Fibroblastic foci are an important diagnostic feature of some interstitial lung diseases. The µCT imaging data were correlated to Movat's pentachrome–stained sections of the same tissue. This correlative imaging approach demonstrated that using µCT alongside traditional histology enables accurate 3D analyses of the relationship between cellular and micro-architectural features of fibrotic lung diseases (Jones *et al.*, 2016).

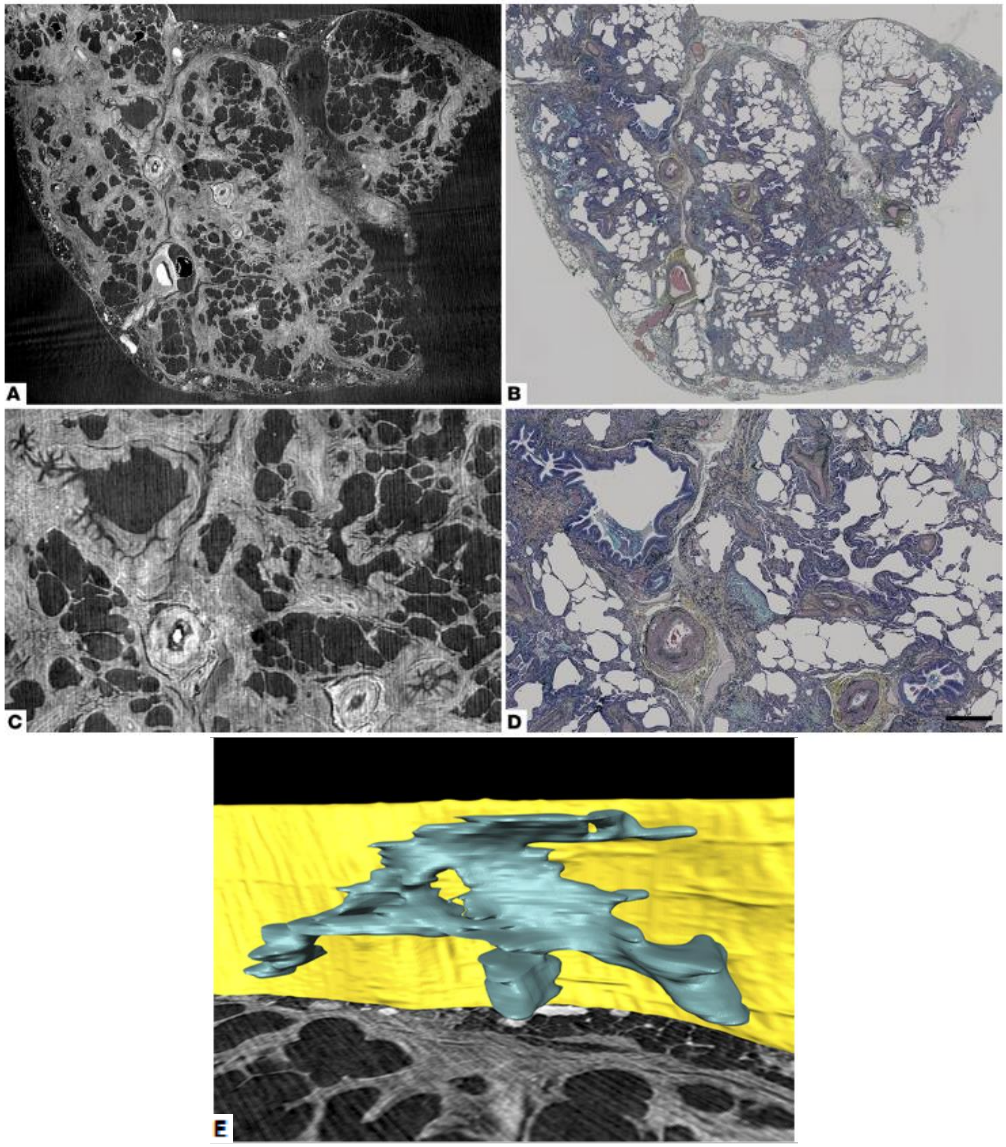

Figure 1.6 Use of µCT to Image 3D Connectivity of Fibroblastic Foci in IPF (from Figures 2 and 4, (Jones *et al.*, 2016). (A and B) Registration-based image matching of a micro-CT cross-sectional image to a histological section of usual interstitial pneumonia/idiopathic pulmonary fibrosis tissue stained with Movat's Pentachrome respectively . Images in C and D are subareas of A and B. Scale bar: 1,400 µm (A and B); 500 µm (C and D). (E) A computer-generated 3D surface view rendering of one fibroblast focus from micro-CT segmentation identifies that fibroblast foci are locally complex structures in 3D. The focus is blue, and for reference, the pleural surface is visualized in yellow (height 1 mm) with a micro-CT slice shown inferiorly (Jones *et al.*, 2016).

The number of conducting terminal bronchioles and transitional respiratory bronchioles in patients across all grades of COPD has been extensively studied with the use of µCT(McDonough *et al.*, 2012; Koo *et al.*, 2018). Using correlative µCT and histology on unstained FFPE samples, a study in 2018 showed the first direct evidence that the smallest airways within the lung are significantly lost in the lungs of patients with mild (Global Initiative for Chronic Obstructive Lung Disease (GOLD) level 1) and moderate (GOLD level 2) COPD (Koo *et al.*, 2018). This study also compared diseased samples with age-matched smokers with normal lung function. This loss was shown to occur in lung tissue in which no emphysematous destruction was present, indicating

small airways disease is an early pathological feature of mild and moderate COPD. The use of correlative histology demonstrated the remaining airways in COPD patients had thickened walls and marked fibrosis present. The use of μCT enabled these airways to be efficiently examined along their branch lengths and showed they are often entirely obstructed by fibrotic tissue, which confirmed traditional 2D studies (Hogg *et al.*, 2004; O'Shaughnessy *et al.*, 1997; Di Stefano *et al.*, 1996). Biomarkers of various immune cells such as CD8+ and CD4+ T cells, Neutrophil, B-cells and macrophages have also now been identified and mapped in patients with COPD using μCT and immunohistochemistry (IHC) (Tanabe *et al.*, 2018).

1.4 Mathematical Modeling of Lymph Flow

1.4.1 Introduction of Mathematical Modelling

Mathematical modelling is a process that simulates mechanical or chemical processes inside a given system using high powered computation. To be able to do this, input parameters (variables), constant parameters (non-variables) and physical laws (dictating the process described in mathematical terms) are required. As previously described, the lymphatic system is a highly complex dynamic system. This, when combined with the relative lack of reliable anatomical and physiological data, highlights the difficulty of analytically or numerically, modelling this system using mathematical methods. As such mathematical modelling of the lymphatic system is very much in its infancy.

The current models within the literature can be classified into two main categories, lumped models and continuum models. In the context, and for the simplicity of this work a lumped model refers to a model that is described by ordinary differential or algebraic equations as the system's dependent variables are assumed uniform over finite regions of space. In continuum modelling, these dependent variables are assumed uniform over infinitesimal regions of space and are therefore described by partial differential equations (Margaris & Black, 2012).

There are only a small number of existing models detailing the lymphatics compared to the blood circulation. The arterial tree has at least 30 models cited in the literature to date (Martin et al. 2012, Müller et al. 2016). As the majority of the lymphatic models are one-dimensional, models of higher dimensions are even more limited; it seems only two 3D models of lymph flow through a single lymphangion (with the valves neglected) and of a lymph node, has been published (Rahbar & Moore 2011, Cooper et al. 2015).

Most of the modelling work achieved for the lymphatics relates to the collecting lymphatics, more specifically the function of the lymphangion (Drake et al. 1986, Macdonald et al. 2008, Quick et

al. 2008, Venugopal et al. 2010, Bertram et al. 2011). A handful of microlymphatic models have been developed as well, but due to the relative lack of anatomical and physiological data, these are of even fewer numbers and detail (Elhay & Casley-Smith 1976, Reddy & Patel 1995, Mendoza et al. 2003, Galie & Spilker 2009, Roose & Swartz 2012).

Due to a lack of morphometric data, to date, no pulmonary specific lymphatic models have been created. Fortunately, a lot of experimental data has been obtained from pulmonary studies, giving confidence in input parameters and constants needed for modelling (Miserocchi et al. 2001, Moriondo et al. 2005, Negrini & Passi 2007). There have been some models of interstitial fluid, drug and protein movement in the lung; however, these do not include fluid uptake into the lymphatics (Roselli et al. 1987, Reichold et al. 2012).

The first model of the lymphatic system can be attributed to Reddy in 1974 (Reddy, 1974). His work was a simplified one-dimensional model of the entire lymphatic network, and it was based on fundamentals of fluid mechanics, predominately the Navier–Stokes equations (NSEs). Due to a lack of anatomical detail, this pioneering model excluded major parts of the lymphatic network; however, it remains the only model that attempts to detail the whole of the lymphatic circulation.

1.4.2 Lumped Models of the Collecting Lymphatics

Lumped models can be used to model lymphatics by reducing a continuous system to a discrete one (Margaris & Black, 2012). A discrete system is made up of discrete variables which can only take on a single value, whereas continuous variables can take on any value between two specified values in space. Therefore, the simple models of this type concerning the lymphatic system are of lymphangion unit modelling. An advantage of this approach is that usually, these models are simple, and the mathematical complications and computational simulation times are kept to a minimum. Although they can yield useful insight into the behaviour of a system under investigation, they cannot yield a comprehensive description of the flow.

As mentioned above, Reddy was the first to develop a model to describe the one-dimensional flow along a succession of lymphangions through the lymphatic network, each of which is modelled as a single computational node (Reddy, Krouskop & Newell, 1977). The governing equations of the fluid mechanics of the laminar flow of lymph fluid are described by the NSEs:

$$\nabla \cdot \underline{u} = 0, \tag{1.1a}$$

$$\frac{\partial \underline{u}}{\partial t} + \underline{u} \cdot \nabla \underline{u} = -\frac{1}{\rho} \nabla P^L + \nu \nabla^2 \underline{u}\,, \tag{1.1b}$$

where the velocity is denoted as $\underline{u}$, time as t, density as ρ, pressure as P^L, and viscosity as ν.

A simplification was made to assume the collecting lymphatics retain a cylindrical shape, and an average of the spatial pressure was used for each lymphangion. By doing so, the NSEs were reduced to ordinary differential equations, and hence, this can be described as a lumped model (Reddy et al. 1977, Reddy & Kesavan 1989). They denote Q^L, the volumetric flow rate, pressure P^L, and the radius, r, of the vessel as dependent variables, and applying the simplification stated above could rewrite the NSEs at equilibrium, including the volume conservation equation as the following:

$$\frac{\partial Q^L}{\partial x} = -2\pi r^L \frac{\partial r}{\partial t}, \tag{1.2a}$$

$$\frac{\partial \boldsymbol{Q^L}}{\partial \boldsymbol{t}} = -\frac{\boldsymbol{\pi r^2}}{\boldsymbol{\rho}} \frac{\boldsymbol{\partial}}{\boldsymbol{\partial x}} [\boldsymbol{P^L} - \boldsymbol{\rho g z}] + \frac{\boldsymbol{2\pi r}}{\boldsymbol{\rho}} \boldsymbol{\tau} \Big|_{\boldsymbol{r_c = r,}} \tag{1.2b}$$

where $\tau = \mu\ (\partial u/\partial r)$ is the stress term (stress at a point within the material that can be attributed to the rate at which the material is deforming around that point) calculated at the wall of the cylindrical vessel, $\rho g z$ is the pressure head (a fluid's internal energy due to the pressure exerted on its container), x is the distance along the vessel, and r_c is the radial coordinate. Since the flow is now laminar, this can be evaluated from Poiseuille's law. Considering the influence of an elastic wall on the pressure inside the lymphangion enabled the closure of these equations,thus a further equation was added connecting the radius of the vessel, r, and the internal lymphatic vessel pressure, P^L (Reddy, Krouskop & Newell, 1977). The authors stated this in the following form:

$$P^L = P + \frac{h}{r}[\sigma^{hoop} + \sigma^{act}], \tag{1.3}$$

with the interstitial pressure, P, the wall thickness, h, and the stresses in the wall, σ^{hoop}(the passive elasticity of the wall) and σ^{act}(the active contraction of the wall).

After deriving the equations describing the fluid flow and momentum transport within a single lymphangion, Reddy along with his co-workers proceeded to assemble them into a network model of the whole system (Krouskop et al. 1975, Reddy et al. 1977). As expected, many more simplifications and assumptions were necessary. The microlymphatics were considered to be lumped, and the nodes were not included at all since information on the microfluidics inside them was not available at that time. The results, according to the authors, were in agreement with experimental observations in sheep, and they suggested this extrapolated to humans (Hall, Morris & Woolley, 1965). However, this approach was questioned in terms of its validity by Olszewski & Engeset, who did experimental work on human leg lymphatics (Olszewski & Engeset, 1980).

In 1986, an electrical analogue model of lymphatic vessels was created by Drake et al. (1986). The lymphatic vessel was modelled as a resistance and a voltage source to take into account the respective flow resistance and pumping action of the vessel. The authors used the Thevenin theorem in their analysis, which requires the pressure–flow rate relationship to be linear.

Depending on the species and the size of the lymphatic vessel being considered, this relationship, in general, is highly nonlinear (Ohhashi, Azuma & Sakaguchi, 1980). Hence, the applicability of such models is questionable (Drake et al. 1991, Eisenhoffer et al. 1993).

The Drake et al. group produced a model that took both passive and active lymph flow into account and regardless of its simplicity, the model was useful as it demonstrated that when the pressure gradient is negative (when outflow pressure is greater than inflow pressure), flow is a result of active contractions, but when the pressure gradient becomes positive, the flow is due to mostly passive factors (Drake et al. 1991, Drake et al. 1996). This conclusion was later experimentally backed up by Gashev et al. (2002).

More recently, Quick et al. (2008) developed a lumped lymphangion model by using a model initially developed for the ventricles of the heart, termed the time-varying elastance approach (Sunagawa *et al.*, 1983), combined with a more complex lumped model, previously derived by Quick and co-workers (Quick et al. 2007, Venugopal et al. 2007). This model was described also using the linearised Navier–Stokes equations of fluid flow like Reddy (Krouskop, Newell & Reddy, 1975). The authors claimed that the simplification of their model (by neglecting inertia and the viscosity effect) to a simple algebraic equation is justifiable and the error introduced in mean flow is small. However, it has been shown that in the vicinity of the valves, the inertial terms are expected to be dominant, which suggests that this assumption may not be valid (Reddy & Kesavan, 1989).

The time-varying elastance model was advanced in 2010 by Venugopal et al. who implemented a bilinear transform for the pressure-volume relationship (Venugopal *et al.*, 2010). As a result of this work, they proposed that lymphangions change their contractile behaviour depending on the magnitude of the transmural pressure. At higher transmural pressures, lymphangions no longer respond dynamically to pressure changes and maintain a constant stroke volume.

Bertram et al. furthered this work by modelling a chain of lymphangions, concentrating on their pumping behaviour(Bertram *et al.*, 2011). As with all lumped models, a peristaltic wave of contraction cannot be modelled without multiple lumped components. This model was unique as it was the first model to add a pressure-dependent valve resistance (Margaris & Black, 2012). A constitutive equation of the vessel wall included passive elasticity and active contraction terms to allow wall stiffening at high internal pressures and the loss of compliance at high external ones. The resulting nonlinear ordinary differential equations yielded a complex behaviour, which depended on the parameters and the number of lymphangions in a chain.

The simple approaches such as the work by Quick et al. (2007) and Venugopal et al. (2007) have shown to be useful and can provide useful insight into the physiological function of the lymphatic system, such as the detail of the lymphatic response to pressure changes. However, these models should be used with caution, and their limitations should not be overlooked. For example, there are obvious differences in the behaviour of lymphangions and heart ventricles and the time-varying elastance model has been criticized as insufficient to describe the ventricle dynamics for which it was initially developed (Venugopal et al. 2010, Deserranno et al. 2007, Danielsen & Ottesen 2001).

Some lumped models can yield a very complicated behaviour as shown by studies mentioned above, but are still not able to resolve space-dependent flow characteristics unless additional lumped components are included as shown by Bertram et al. (2011). This is why more advanced computational models can have an advantage if the computing power is available for such simulations.

1.4.3 Continuum Models of the Collecting Lymphatics

Continuum models of the lymphatic system are limited in number. In 2008, Reddy's original mathematical model was adapted by adding two terms to the transmural pressure equation: a tension and damping term (Macdonald *et al.*, 2008). Moreover, the spatial pressures were not averaged, thus retaining the continuum nature of the governing equations. Another notable difference was that the contraction of the vessel wall was modelled by a change in Young's modulus where the data used to obtain parameters such as the Young modulus and damping terms were experimentally derived by the use of bovine mesenteric lymphatics. It should be noted that the properties measured had considerable variation owing to uncertainties in vessel diameter and wall thickness measurements (Macdonald *et al.*, 2008).

More recently, Rahbar and Moore progressed into the higher dimension of fluid flow modelling by developing a computational model of a contracting lymphangion in 3D (Rahbar & Moore, 2011). This model did not, however, include valves and inertial effects, and still assumed a relatively narrow vessel with an aspect ratio of 3.75.

1.4.4 Modelling of Primary Lymphatics

The models discussed to this point portray the lymphatic system as a network of lymphangions and are therefore only describing the functionality of the collecting lymphatics. These models are not concerned with the microlymphatics function. The few models that exist to attempt to

describe the function of the microlymphatics or the process of lymph formation will now be discussed.

Lymph formation, or the uptake of interstitial fluid into microlymphatics, has been a controversial topic, and much data has been gathered over the last few decades, along with a small number of mathematical models to support four main theories: hydraulic pressure gradients; osmotic pressure gradients; vesicular transport; and suction from collecting lymphatics (Reddy & Patel 1995, Elhay & Casley-Smith 1976, Dixon et al. 2009). A comprehensive review was made in 1993 from the literature at the time which concluded that the hydraulic mechanism for microlymphatic filling is most widely accepted and interstitial pressure is the primary determinant of lymph flow (Aukland & Reed, 1993). There have been more experimental and theoretical studies that have confirmed this theory since (Negrini & Del Fabbro 1999, Negrini et al. 2004, Moriondo et al. 2005).

One of the first mathematical models produced for the filling of the microlymphatics was produced in 1976 in support of the osmotic pressure gradient theory that one of the authors, Casley-Smith had previously advocated (Elhay & Casley-Smith 1976 and Casley-Smith 1975). The next more comprehensive model should probably be attributed to Reddy & Patel which came in 1995 (Reddy & Patel, 1995). The flow was described as being axisymmetric and as commonly thought, driven by a pressure gradient between the tissue space and the lymphatic vessel. To take into account of the anchoring filaments, the LECs were assumed to be supported by an elastic spring. Although the capacity of the LECs to produce circumferential stress is not generally accepted (Baluk et al., 2005), hoop stress was added to the momentum equation of the vessel wall. This model estimated that by increasing the amplitude of pressure pulses in the collecting vessel, the flow rate in the microlymphatic vessel increased which gave support to the hypothesis that suction from collecting vessels facilitates lymph uptake by the microlymphatics. The model also showed that the changes in interstitial fluid pressure affected the filling of the microlymphatics, which is also in agreement with the hydraulic mechanism of lymph formation. This model suffered from a lack of reliable data regarding the morphometry and parametric of the microlymphatics, and therefore, these inputs had to be estimated from the properties of blood vessels.

The microlymphatics have not only been modelled to investigate the mechanisms behind lymph formation, but the characterisation of the optimal structure for the microlymphatic network to carry lymph was the focus of a study by Roose & Swartz (2012). Using homogenization theory, these authors developed a model to understand how the microstructure of the microlymphatic network may affect macro-scale tissue drainage. Their model proved that a hexagonal network is

optimal to drain fluid away from tissue and gives a reason as to why this structural pattern is observed in the mouse tail and human skin.

Mendoza & Schmid-Schonbein also developed a model of the microlymphatics but focused more on the primary valve function, formed by the overlapping of LECs (Mendoza, Schmid-Schönbein & Schmid-Schonbein, 2003). The LECs were modelled as elastic beams by coupling the governing equations for fluid mechanics, the NSEs, directly to the deflection of the beam (see Figure 1.7).

To simplify the NSEs mentioned above, the authors of that study assumed that all inertial effects (creeping flow) and velocity in the y-direction were negligible, and the pressure acted only in the x-direction so that:

$$0 = -\frac{\partial P}{\partial x} + \mu \frac{\partial^2 v_x}{\partial y^2}, \qquad \textbf{(1.1)}$$

where *P i*s the fluid pressure, μ is the viscosity coefficient*,* v_x is the velocity in the x-direction (Mendoza, Schmid-Schönbein & Schmid-Schonbein, 2003) Since this equation is dependent upon the deflection of the LECs (defined as *w(x)* in this model), the authors coupled the above equation with a one-dimensional beam deflection equation written as:

$$\frac{d^4 w(x)}{dx^4} = \frac{1}{EI} \Delta P(x), \qquad \textbf{(1.2)}$$

where *ΔP(x)* is the transendothelial pressure drop, defined as the difference in the pressure between the basal side of the endothelial cell and the lumen of the vessel (as a function of the x coordinate), *E* is Young's modulus for endothelial cells and *I* is the area moment of inertia of the cell cross-section (Mendoza, Schmid-Schönbein & Schmid-Schonbein, 2003). To solve the coupled equation, this model assumes that the transendothelial pressure drop is constant for the nonoverlapping portion of the deforming cell and reduced to zero at the tip of the cell when P(x)=P(3 μm)=0. The deformable portion of the cell is considered cantilevered to the portion anchored by fibrillin fibres. Therefore with these boundary and initial conditions, the coupled equation can be used to calculate the displacement *w(x)* as a function of *x* (Mendoza, Schmid-Schönbein & Schmid-Schonbein, 2003).

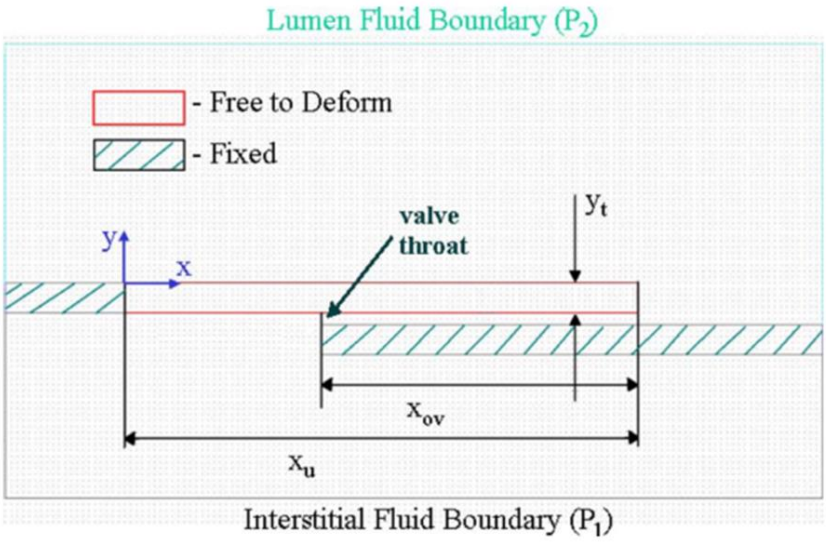

Figure 1.7 Geometric Representation of the Primary Lymphatic Valve. The portions of the LEC fixed to the extracellular matrix are distinguished from the "internal flaps "of the LEC that can deform. The location of the transmural pressure boundary condition Δp=p1−p2 is indicated above and below the diagram and x_u and x_{ov} represent the lengths of the LEC that is free to deform, and overlap, respectively. The thickness of the cell y_t is set to 0.25 microns (reproduced from Mendoza et al. 2003).

A more elaborate model produced six years later assumed two-dimensional flow (Galie & Spilker, 2009). The interstitial space was described as a porous medium, and by neglecting deformations, the flow was modelled using Brinkman's equations with appropriate no-slip boundary conditions. The authors concluded that adaptations made to the original model affected the results as the calculated LEC deflections were greater, and this was predominantly due to the inclusion of a porous media domain. It should be noted that both models still lack appropriate material properties for lymphatic cells as the authors still had to use data from VECs owing to the lack of data for the LECs.

It was later shown by Heppell et al. (2013 and 2015) that this mechanism of action was unlikely to represent the true mechanics behind how primary lymphatic valves function. The authors described the valves function by a sliding mechanism which better fits the known ultrastructure of the microlymphatics valves, which do not have as large overlaps as what is assumed in Mendoza et al. (2003)and Galie & Spilker's(2009) models.

1.4.5 Using X-ray µCT for Image-Based Mathematical Modelling in Lung

The vast amount of µCT imaging research since its conception has been in metrology and quality control for mechanical engineering applications as a consequence of the truly representative and isotropic nature of the imaging technique. As a result of its imaging accuracy, µCT imaging is now being used to obtain the 3D images required for 3D image-based mathematical modelling (IBMM). It should be noted that other imaging systems such as MRI are also used for IBMM in the

lung, detailed in an excellent review by Clark, Kumar and Burrowes, (2017)who also discuss the complexity of modelling the pulmonary system at different scales and dimensions.

In IBMM, in addition to the input parameters, constant parameters and physical laws, an accurate geometry of the system is also required. Length scales play such an essential role in the mechanics of a system that without precise geometries, as well as simulations being inaccurate, they often fail. 3D IBMM further advances this to simulate processes within a given 3D geometry, and as computational capacity is increasing, this form of IBMM is becoming more common.

Particularly in the biological field, the benefits of being able to perform IBMM lie in its hypothesis-generating capacity. Even with incomplete system knowledge, IBMM can simulate multiple mechanical and chemical processes in time, to examine how an extremely complex system may function with numerical and visual outputs. This form of analysis is of particular interest if it is not possible to generate an experimental system to create data to test the model's prediction, often the case for human physiology or pathology. As detailed in section 1.3, it is now possible to utilise µCT imaging capability in the biological field. As a result, 3D IBMM is growing rapidly in the biological and medical fields.

In lung biology, µCT imaging has helped evaluate micro-level airflow dynamics both directly and indirectly through 3D IBMM (Kumar *et al.*, 2013; Sera *et al.*, 2013). These techniques have shown how 3D microscopic changes in alveolar structure relate to changes in lung inflation, and it's efficiency. Kumar *et al.*, (2013) showed by that in contradiction to other models at the time that the expansion of the acinus is accompanied by an increase in both surface area and volume in such a way that the surface to volume ratio is not significantly altered, raising a question over the mechanics of the respiratory unit. This study was a registration driven model from two scans at driven pressures rather than a mathematical simulation; however, is of significant note nevertheless. Sera *et al.*, (2015) simulated the airflow and particle deposition numerically in a pulmonary acinar model based on absorptive synchrotron µCT of the mammalian lung.

One of the first micro-scale IBMM of lung tissue mechanics used the 2D topology of SEM images of mouse lung parenchyma as a geometrical input into a 2D model. This representative 2D of the alveolar sac was subjected to mathematical simulations biaxial loading due to uniformly distributed stresses (Gefen, Elad & Shiner, 1999). Since this time, owing to the technological advance of 3D imaging, synchrotron-based µCT has been used to generate real alveolar geometries of the rat alveolar network and performed IBMM to apply a three-dimensional strain state to the alveolar wall (Rausch *et al.*, 2011). In this study, they showed that the local strain in the alveolar wall could reach up to four times as high the value of the global strain. Also, thin structures cause hotspots that are especially at risk of overstretching and as a consequence

tearing. This work is of particular of interest in the application of clinical mechanical ventilation (Rausch *et al.*, 2011).

Studies performing IBMM on the pulmonary vasculature are lacking. A geometry of pulmonary artery branching, obtained through μCT imaging in combination with high-resolution dynamic projection imaging, has provided new information about the re-modelling capacity of pulmonary arterial anatomy after hypoxic exposure in the rat on the macro-scale. Transit time and other characteristics of pulmonary blood flow along the pulmonary arterial tree were shown to be different between rats exposed to hypoxic conditions and the controls (Molthen, Karau & Dawson, 2004).

At the microscale to date, no vascular IBMM studies using μCT have been performed in the lung. This is because discriminating hierarchal vasculature networks from each other, and often from the lung parenchyma, is, at present, impossible with μCT systems alone (Mansoor *et al.*, 2015).

1.4.6 Summary of Mathematical Modelling of Lymphatics and Lung

In summary, if a mathematical model agrees with experimentally defined facts and a hypothetical mechanism, this in itself does not imply that this mechanism is correct. However, its agreement can lend weight to the evidence in favour of the hypothesis, just as the model's failure to accord can seriously detract from it. It has been shown that creating a mathematical model by combining physical laws, quantitative morphology, and observational physiology, yields very important information about the functioning of a system which cannot be obtained from any of these approaches on their own, nor by a combination of just two of them.

Advancing IBMM simulations into the 3D in lung research has permitted the beginnings of sophisticated personalised mechanical modelling of health and disease in the lung. Currently, most of this work is at the macro-scale which, while giving valuable information about flow dynamics in the upper respiratory tract, is neglecting the physiology or sometimes pathology occurring in the respiratory unit of the lung.

1.5 Research Aims

1. To develop a method for imaging human pulmonary lymphatics and associated structural features in 3D with the use of X-ray μCT and IHC.
2. To design and apply a mathematical model, describing pulmonary physiological processes to real 3D geometries of healthy and diseased human tissue using finite-element modelling techniques.
3. To further current scientific knowledge of peripheral human lung lymphatics by describing 3D morphology of peripheral pulmonary lymphatics in archived biopsies of clinical lung tissue in states of health and disease.
4. To evaluate the effect of structural changes in the pulmonary lymphatics, vasculature and parenchymal geometry on the functional mechanics of pulmonary fluid movement in health and disease.

Foreword for Chapters 2 and 3

A major focus of this study is producing a replicable workflow for future large-scale research. Due to the size of the following section of work, it has been necessary to split the development of methods into two chapters. Chapter 2 will focus on the method development for identifying, imaging and analysing pulmonary lymphatics and other lung features in 3D. Chapter 3 will focus on the necessary steps to optimise the image geometries being used for 3D image-based mathematical modelling presented alongside the mathematical model design.

These chapters have been split for ease of reading. Some decisions taken in the methods for lymphatic imaging and analysis were made in the knowledge that mathematical modelling of these structures will follow.

In addition, many decisions to change a part of the methodology were made because of the results from the previous step in the methodology. Chapters 2 and 3 will therefore be written in a chronological order. The methods, results and discussion for developing and justifying each part of the methodology will be given before progressing onto the next step in the methodology.

Last year, a large proportion of the following two chapters were published as a peer-reviewed original article as a proof of principle study using two of the FFPE human lung samples (Robinson *et al.*, 2019).

Chapter 2 Development of Methods for Imaging and Characterising Human Pulmonary Lymphatics

This chapter details the materials and methods for identifying, imaging and analysing pulmonary lymphatics and other lung features in 3D. Where necessary, the chronological development of parts of this methodology will be discussed and the final methods justified.

2.1 Tissue Sample Extraction and Preparation

Archived FFPE human lung tissue samples were used in this study. Lung tissue samples were obtained from patients undergoing therapeutic resection surgery for diagnostic or therapeutic purposes at Southampton University Hospital Trust (UK) with signed informed consent. For research purposes, full ethical approval was granted from the National Research Ethics Service Committee (South Central—Southampton A, number 08/H0502/3). All tissues were fixed in formalin for 48 hours and mounted in paraffin wax following routine histology protocols.

22 archived lung samples were used for the whole study, selected to be no bigger than 1.5cm^3 and known to be taken near the periphery of the lung as they contained a visceral pleural surface.

All samples were placed into three categories; Control samples; Active disease samples or COPD samples. The samples in the control group (n=11) were either taken from the margin of cancer resected tissue, or from diagnostic biopsies of young patients following a spontaneous pneumothorax event. The active disease samples (n=9) were taken from patients either undertaking activity known to induce lung damage, such as smoking, or the patients had comorbidities that are known induce lung tissue stress, such as pulmonary hypertension (Faight *et al.*, 2017). Finally, the last two samples (n=2) were both clinically classified as having COPD at the GOLD classification level 3 which is the 2nd highest level of classification for this disease (Rabe *et al.*, 2007).

A full list of all the tissue sample ID numbers and anonymised patient data information is given in Appendix A.

2.2 Methods for Human Lung Immunohistochemistry

The IHC methods detailed in this section were performed at the beginning of the study before any 3D imaging or correlative work was started. This was to ensure identifying the lymphatics within lung tissue in 2D was possible before full 3D imaging was undertaken.

2.2.1 Optimisation of Primary Antibody Staining

Optimisation experiments were performed to find the IHC protocol that gave the most specific antigen binding and largest stain to background contrast for each antibody. Commercial primary antibodies targeted against proteins in airway epithelium (PCK and Aquaporin-5), blood vasculature (CD31 and αSMA) and the lymphatic vasculature (D240, LP21, LYVE-1 and Prox-1) underwent pre-treatment and titration testing. The primary antibodies used, their target antigen, where each antibody was acquired is shown in Table 2.1.

Table 2.1 Primary Antibody Properties

Primary Antibody	Species and clone	Cell Target	Organelle Target	Protein Target (Epitope)	Commercial source and Code	Working dilution (from Source)	Antigen Retrieval Method
D240	Mouse-Monoclonal	Lymphatic Endothelium	Cell Membrane	Podoplanin (Glu33-Gly45) (Ogasawara *et al.*, 2008)	Abcam[1] ab77854	1:80	None
LP21	Mouse-Monoclonal	Lymphatic Endothelium	Cell Membrane	Podoplanin (Thr76 (gly)–Arg79) (Kaneko *et al.*, 2017)	Courtesy of Professor Yukinari Kato[2]	1:80	None
LYVE-1	Rabbit-Polyclonal	Endothelium	Plasma Membrane /TGN	Hyaluronan transporter	Abcam[1] ab14917	1:1500	None
Prox-1	Mouse-Monoclonal	Differentiating cells	Nuclei	Transcription factor	Abcam[1] ab33219	1:50	Heat Mediated (Citrate buffer)
CD31	Rabbit-Polyclonal	Endothelium	Cell membrane (junctions)	PECAM1 (C-terminal)	Abcam[1] ab38264	1:100	Heat Mediated (Citrate buffer)
αSMA	Mouse-Monoclonal	Smooth muscle	Whole cell	Actin (Cytoskeletal)	Sigma-Aldrich[3] A-2547	1:100000	None
PCK	Mouse-Monoclonal Mix	Epithelium	Whole cell	Cytokeratins 1,4,5,6,8,10,13,18, and 19	Sigma-Aldrich[3] C-2562	1:4000	Pronase

[1] Abcam, Cambridge UK; [2] University of Texas M.D. Houston, TX 77030; [3] Sigma-Aldrich Company Ltd., Dorset, UK.

A tissue section series (sixteen serial sections) was cut using a paraffin-wax microtome from one formalin-fixed paraffin-embedded lung tissue sample for each antibody to be tested. All tissue sections used in this study were cut 5 µm thick.

Four dilutions of each antibody stock (starting at the recommend dilution from the commercial source) were tested using the IHC protocol (section 2.2.2). As well as omitting any antigen

retrieval step, the following three antigen retrieval methods were tested for each primary antibody dilution:

- Heat mediated antigen retrieval in a 10mM sodium-citrate buffer solution (pH 6.0). Microwave at 50% power for 25 mins. Buffer composition: 2.1g citric acid, 25 ml 1M sodium hydroxide, 1L distilled water.
- Heat mediated antigen retrieval in a 1mM sodium-EDTA (Ethylenediaminetetraacetic acid) buffer solution (pH 8.0). Microwave at 50% power for 25 mins. Buffer composition: 0.037g EDTA, 8 ml 0.1M sodium hydroxide , 1L distilled water.
- Enzyme mediated. Incubate with pronase solution at room temperature and pressure (RTP) for 10 minutes. Solution composition: 0.1 ml 1% pronase stock (Dako, Agilent Pathology Solutions, Stockport, UK), 1.9 ml of Tris Buffered Saline (TBS) (pH 7.6).

Table 2.1 shows the determined working concentration and the antigen retrieval method (if necessary) required to produce the strongest staining signal against the target antigen for each antibody tested in FFPE human lung tissue.

2.2.2 Immunohistochemistry Protocol

All tissue sections for IHC underwent the following protocol. All steps performed at RTP unless otherwise stated.

1. Deparaffinise in clearene (solvent) for (2x 10 mins)
2. Rehydrate through graded alcohols: ABS, 90%, 70%, (5 mins/concentration).
3. Apply 0.05% hydrogen peroxide solution in methanol (10 minutes). Solution: 0.1 ml 30% hydrogen peroxide stock (Sigma) in 5.9 ml of Methanol.
4. Wash in TBS for 3 x 2 mins.
5. Perform antigen retrieval step of necessary (see section 2.2.1).
6. Apply avidin (20 mins) from a pre-made avidin/biotin blocking kit (Vector Laboratories LTD, Peterborough, UK).
7. Wash in TBS (3 x 2 mins).
8. Repeat steps 6 and 7 with biotin instead of avidin.
9. Block using culture medium for 20 mins. Culture media consisted of Dulbecco's modified eagles medium (Sigma); foetal calf serum, 10% v/v (PAA, Cell Culture Company, Yeovil, UK) and 1% bovine serum albumin (Sigma). Drain medium, do not wash off.
10. Apply primary antibodies at optimised dilution (see Table 2.1) and store at 4°C overnight.
11. Allow sections to reach RTP. Wash with TBS (3x 5 mins).

12. Apply biotinylated secondary antibodies (30 mins). Goat anti-mouse (Vector: BA-9200) at a 1:800 dilution; goat anti-rabbit (Vector: BA-1000) at a 1:400 dilution.
13. Wash in TBS for (3x 5 mins).
14. Apply a pre-made "ABC" complex of streptavidin (A), biotinylated horseradish peroxidase (B) (Vector) and TBS (1: 1: 75) (30 mins). Make up complex 30 mins before application.
15. Wash in TBS (3x 5 mins).
16. Apply a diaminobenzidine (DAB) chromogen solution (BioGenex, Fremont, CA, USA) (5 mins).DAB chromagen: DAB buffer: 15% sodium azide in a 16:500:25 ratio. Rinse immediately with TBS.
17. Place in running tap water (5 mins).
18. Counterstain with Mayer's haematoxylin (20 seconds).
19. Place in running tap water (5 mins).
20. Dehydrate through graded alcohols: 70%, 95%, ABS (5 mins/concentration).
21. Clear in clearene (solvent) for (2x 10 mins).
22. Mount glass coverslips using Pertex.

Across all IHC assays, including titrations, a section of human lung tissue was used as a negative control (omitting primary antibody) for each antigen retrieval method used in each staining assay undertaken.

2.2.3 Comparison of Primary Antibodies

Twenty serial sections were taken from one formalin-fixed paraffin-embedded lung sample. Three serial section were used to confirm if the commercial antibodies PCK, CD31 and D240 selectively stained the airways, blood vessels and lymphatic vessels respectively, and the antibody staining patterns didn't overlap. These antibodies were chosen as they gave highest signal and least cross-reactivity in the titration assays.

The PCK antibody stained the airway epithelium strongly with occasional single cell staining throughout the parenchymal tissue (see Figure 2.1 a). The CD31 antibody stained vascular endothelial cells (VECs) with occasional weak staining of airway epithelium (see Figure 2.1c). CD31 staining was specific for VECs with staining intensity variable yet discernible in vessels up to a diameter of 300 μm where the staining is lost. Both of these observations confirmed previous studies which used CD31 in the human lung (Müller et al. 2002, Pusztaszeri et al. 2006).

The D240 antibody strongly stained structures that are consistent with lumens of lymphatic vessels where LECS are present (see Figure 2.1b). Weak D240+ staining was apparent on alveolar wall surfaces. This is assumed to be T1 cell staining as podoplanin is known to be expressed in

these cells in Human lung (Gonzalez & Dobbs, 1998; Mcelroy & Kasper, 2004; Newman *et al.*, 2000; Tyrrell *et al.*, 2012).There was no evidence of D240 cross-reactivity with either CD31 or PCK antigens as the D240+ staining pattern was distinct (see Figure 2.1).

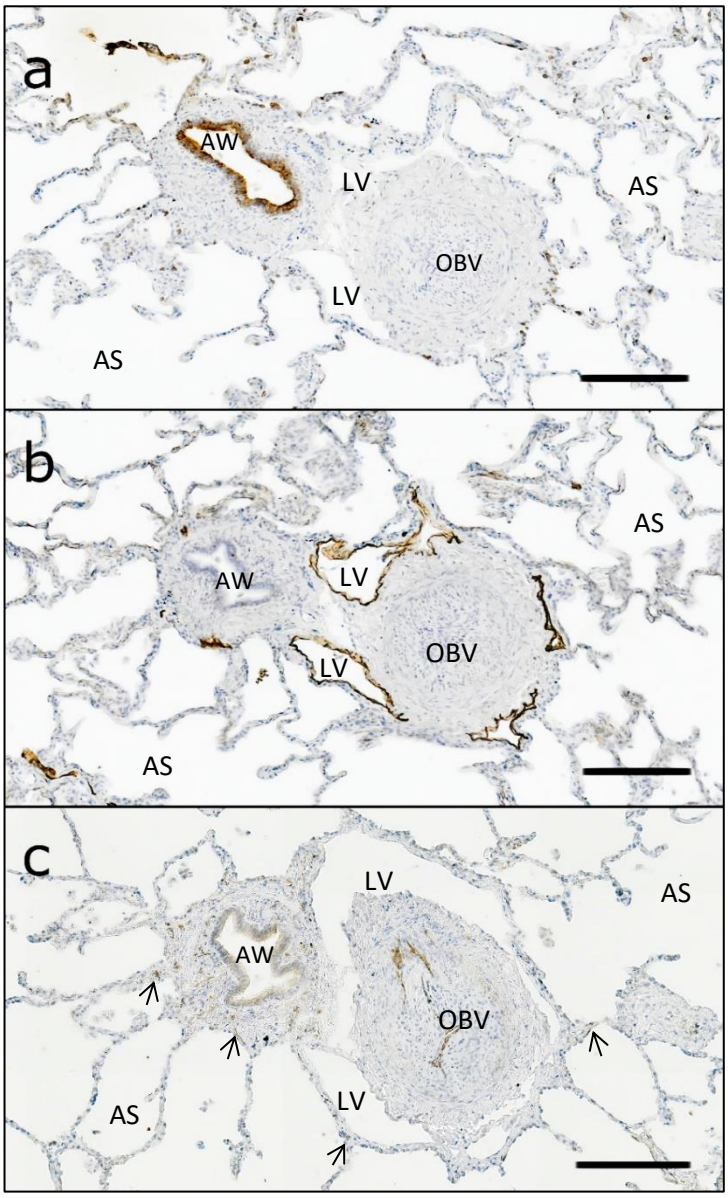

Figure 2.1 Staining Quality of Antibodies Raised Against Human Lung Proteins. a Immunostaining with PCK against the epithelial lining of the airways (AW) within a bronchovascular bundle of a healthy human lung tissue sample. **b** Immunostaining using D240 against the LECs within a bronchovascular bundle (LV=Larger Lymphatic vessel lumen). **c** Immunostaining with CD31 against the blood vessels (occluded blood vessel (OBV) and select capillaries (arrows)) within a bronchovascular bundle. Scale Bars = 200 µm. Alveolar Sacs (AS)

2.2.4 Comparison of Primary Antibodies Raised Against Lymphatic Endothelium

Using the same tissue series as in section 2.2.3, four serial sections were used to compare the specificity and staining quality of the three candidate antibodies raised against LECs that have

been traditionally used for lymphatic IHC; D240, Prox-1 and LYVE-1. The last section was stained with CD31 to see if the anti-LEC antibodies showed any staining of vascular endothelial cells.

LYVE-1 showed weak diffuse staining in a similar location to that of D240, but D240 staining was more defined for staining LECs in the specific tissue sample used. Some T1 cell staining was observed using both antibodies (see Figure 2.2 a and b). Poor LYVE-1 staining of LECs in human lung tissue has been previously noted due to the fact LYVE-1 was initially developed and optimised for the mouse (Schraufnagel 2010, Baluk et al. 2005, Pusztaszeri et al. 2006). Due to the lack of human studies to date, and the apparent success of D240 in most human tissues, a good quality anti-hyaluronic-acid receptor antibody, such as LYVE-1 has not been required.

Prox-1 stained nuclei in multiple cell types throughout the tissue section (see Figure 2.2c) confirming studies which have previously reported Prox-1 as a poor antibody for IHC use (Jakus *et al.*, 2014; Davis *et al.*, 2013). CD31 staining showed that LYVE-1 and D240 did not stain VECs whereas it was unclear if Prox-1 stained nuclei of VECs (Figure 2.2d).

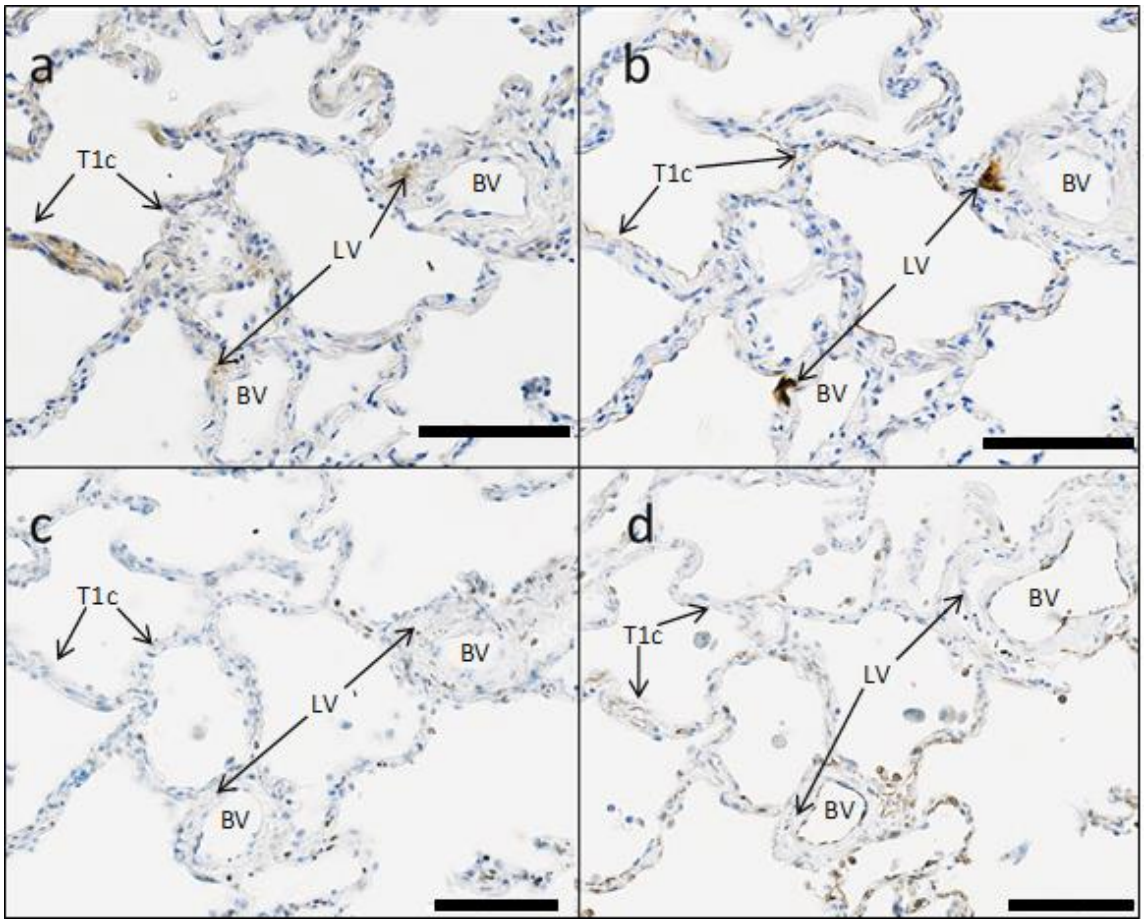

Figure 2.2 Staining Quality of Commercial Antibodies Raised Against Human Lung LECs. a Immunostaining with LYVE-1 against LECs within peripheral healthy human lung tissue. **b** Immunostaining using D240 against LEC within peripheral healthy human lung tissue. Lymphatic vessels (LV). **c** Immunostaining with PROX-1 against the nuclei of LEC within peripheral healthy

human lung tissue. **d** Immunostaining with CD31 against the blood vessels (BV) within peripheral healthy human lung tissue. T1 cells (T1c). Scale Bars =200 μm.

2.2.5 Comparison of Anti-podoplanin Primary Antibodies

Finally, a tissue series of five serial sections were taken from all 22 candidate samples used in the study. Two adjacent sections underwent the IHC protocol (2.2.2) using D240 and the donated LP21 antibody (see Table 2.1). This assay was to assess both antibodies' staining quality and consistency against LECs and their level of T1 cell cross-reactivity in different human samples.

In the sections stained with D240, four of the tissue samples had clear staining of LECs on all lumens visible with no other structures stained (see Figure 2.3a). Two tissue samples had clearly stained lymphatic vessels with faint and intermittent T1 cell staining, and sixteen had a strong lymphatic vessel stain and modest to extreme T1 cell staining (see Figure 2.3c,e). Across all tissue samples, LP21 showed high-quality, strong staining of LECs with no T1 cell staining (see Figure 2.3 b,d,f).

The finding that D240 stains T1 cells in human lung frequently and strongly contradicts histochemical studies which have previously used D240 to image human pulmonary lymphatics. Most papers imaging the lymphatics in 2D have not mentioned staining of T1 cells and report D240 as a specific LEC marker (Yamashita et al. 2009, Kambouchner & Bernaudin 2009, Sozio et al. 2012, Ebina et al. 2010). The only exception is Mori et al. 2013 who describe T1 cell staining weaker to that of LEC staining.

Despite these reports of D240 success, as detailed in section 1.2.4, human podoplanin is known as a T1 cell marker and has shown to be upregulated in lung damage or injury (Schacht *et al.*, 2005). Here, patient samples which were taken due to spontaneous pneumothorax were shown to have the strongest T1 cell staining. Some forms of tissue resections (e.g., lobectomies) are not routinely immersed in fixative in the operation theatre. Therefore, there is potential for upregulation of podoplanin in the T1 cells from the trauma of the surgery itself before the tissue is fixed. As archived tissue samples were used, it is impossible to know this with certainty; however, all tissues studied taken by using this type of tissue resection showed stronger staining of T1 cells by D240.

There were a number of large conduits (average diameterF of >50 μm) where their luminal wall was strongly stained by D240 and where LP21 staining was very faint. In two samples, no LP21 staining was apparent. The shape of these lumens which had a thicker-walled structure were consistent with 2D precollecting lymphatic morphology. In tissue samples where staining using D240 was strong for LECs and weak for T1 cells (as seen in Figure 2.3a), lumens of these large

conduit structures were very heavily stained. This observation reduces the possibility of these structures being mistaken for alveolar walls and thus the staining mistaken for T1 cell cross-reactivity.

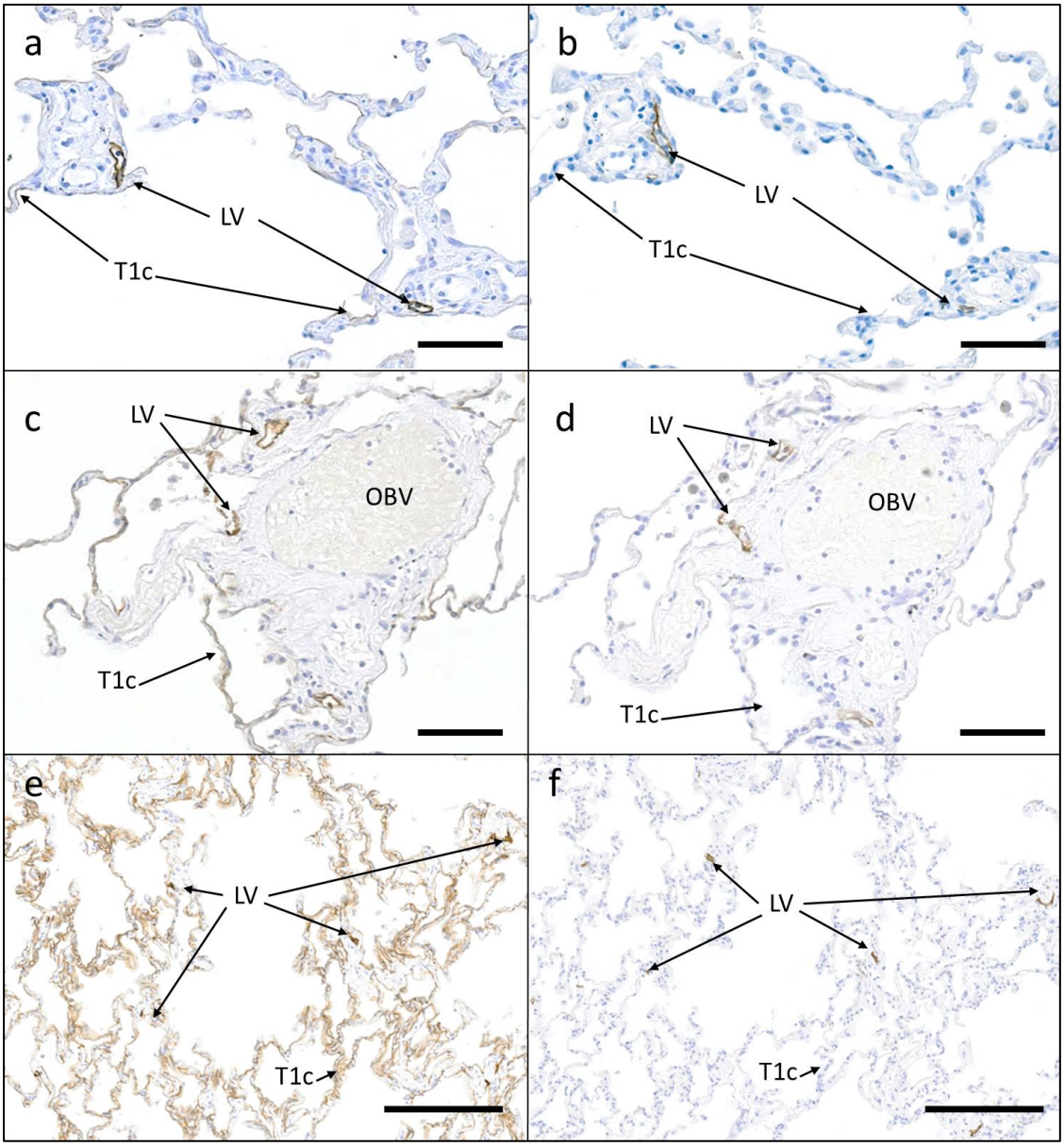

Figure 2.3 IHC Staining of Different Lung Samples to Show the Staining Quality of D240 and LP21. IHC on a two-section series of an active disease sample using **a** D240 **b** LP21. IHC on a two-section series of a COPD sample using **c** D240 **d** LP21. IHC on a two-section series of a spontaneous pneumothorax control sample using **e** D240 **f** LP21. Example Lymphatic Vessels (LV), Occluded Blood vessels (OBV), Example T1 cells (T1c). Scale bars for **a,b,c,d** = 100 µm, **e,f** =200 µm.

2.3 Correlative 2D and 3D Imaging of Pulmonary Lymphatics and Associated Structures

IHC development showed that the lymphatics, blood vessel and airways can be clearly identified in the human lung in 2D. The next section of the methodology focuses on the 3D study and its application. These methods detail how to first obtain the human lung samples' 3D structure before the IHC protocol is performed. Finally, the methods for combining the µCT data and IHC data of the same sample will be detailed.

To enable fair comparisons, the lung samples used in the application of the 3D workflow needed to be from the same location in the lung with no significant artefacts present. 12 of 22 samples were therefore removed from the study due to their 2D IHC sections (taken from the previous antibody validation assays) not meeting the following criteria:

- Samples must contain a pleural surface and have sufficient tissue depth (>3mm) from the pleural surface.
- Samples should have no signs of gross tissue damage such as scissor or puncture wounds.
- Samples should have no evidence of inadequate tissue preparation or fixation.
- Samples should have no evidence of surgical artefacts such as staples.
- Samples should not have extensively collapsed or deformed tissue (see Figure 2.4 as an example).
- Samples should not have extensive immune cell infiltration (see Figure 2.4 as an example).

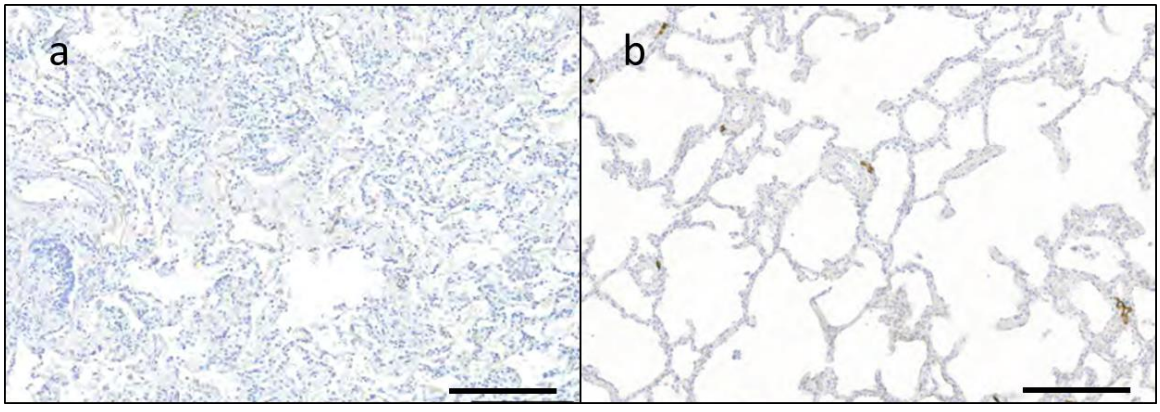

Figure 2.4 Sample Compression Artefacts. a D240+IHC image (following protocol in section 1.2.2) of a sample excluded from the 3D study due to extensive tissue compression and immune cell infiltration. **b** D240+IHC image of a sample taken into the 3D study showing good tissue preservation with an open lung structure.

Of the ten samples that met the criteria for 3D analysis, four were of the control group, four were of the active disease group and two were of the COPD group.

A second tissue series of ten serial sections was taken further into the 10 samples (~ 250 µm). The same IHC assay as in section 1.2.5 (D240 and LP21 comparison) was repeated to confirm staining consistency of the two antibodies within each sample. This assay showed an identical staining pattern of D240 and LP21 staining for each lung sample as was seen in the first assay confirming there was no variation in the quality of the antibody within a tissue sample.

2.3.1 X-ray µCT Scanning Protocol and Volume Reconstruction

The µCT machine used, and the voxel resolution achieved for each sample can be viewed in Appendix B. Technical details of the scanning protocol followed those of Scott & colleagues (Scott *et al.*, 2015).

A Nikon Metrology µCT scanner (MED-X, Nikon Metrology, Tring Herts, UK), with a 225kV micro-focused X-ray source and a high sensitivity cesium iodide scintillator, was used to scan the tissue samples. This machine was designed for soft tissue imaging. A Perkin-Elmer 1621 AN flat panel detector recorded the X-ray penetration through each sample while the samples were rotated through 360°. The resulting radiographs were digitally processed using a filtered-back-projection algorithm which generated a 32-bit float 3D volume file at a sample dependent voxel resolution. Each tissue sample was taken off its diagnostic ID cassette to enable the sample to be closer to the x-ray source to achieve a better voxel resolution of the reconstructed volume.

One sample used in this study was scanned on a µCT machine not designed for soft tissue imaging before the arrival of the MED-X machine. An example orthoslice (digital 2D slices through the µCT volume) of one human lung tissue sample scanned using the non-optimised µCT machine, and one and using the MED-X machine are shown in Figure 2.5.

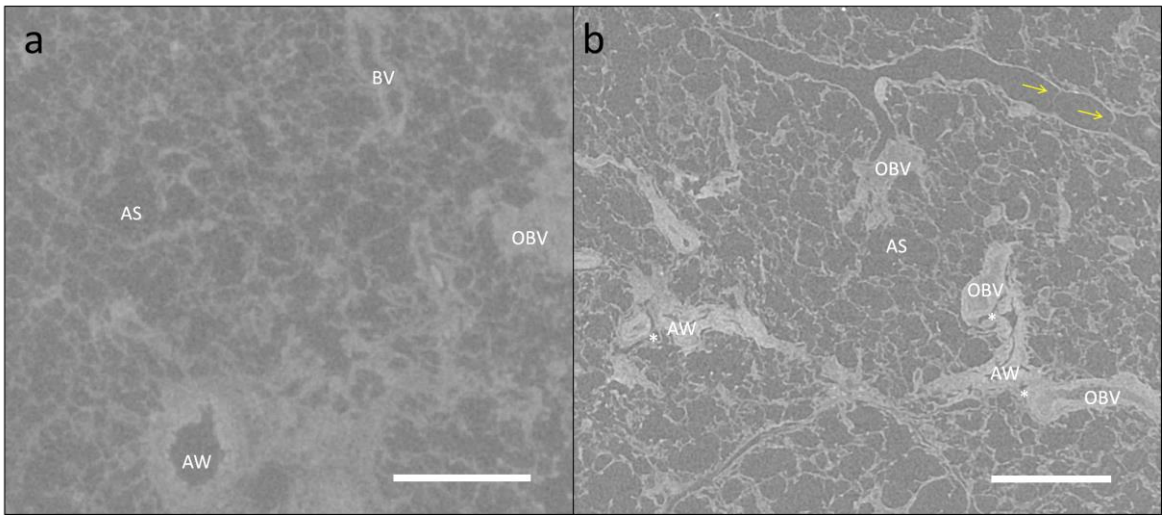

Figure 2.5 2D µCT Orthoslices of Human Lung Tissue Using Different µCT Machines. a A orthoslice of a human lung sample scanned using a µCT machine not designed for soft-tissue

imaging (achieving 13 µm resolution) **b** A orthoslice of a human lung sample scanned using the MED-X machine designed for soft-tissue imaging (achieving 6 µm resolution). AW= airway, AS= alveolar sac, BV=blood vessel, OBV=occluded vessel, yellow arrows = valves, asterisk= conduits encirculating blood vessels, Both scale bars= 1 mm.

The 3D image of the tissue sample scanned by the µCT machine not designed for soft tissue imaging achieved 13.2 µm voxel resolution. Although this enabled visualisation of the basic parenchymal architecture, the alveolar walls were not in sharp focus (see Figure 2.5a). Larger airways are identifiable by their collapsed star-like appearance (greater than 150 µm in diameter at the widest part of their star-like appearance). Large blood vessels with a patent lumen were also distinguishable in vessels with a lumen diameter greater than 40 µm. However, the lumen surfaces of occluded blood vessels of similar size were not distinguishable from the vessel wall and surrounding extracellular matrix.

The tissue sample scanned by the MED-X achieved 6 µm voxel resolution of the µCT image example given in Figure 2.5b. This ranged from 5 µm to 8.5 µm across the other 8 lung samples due to slight differences in their size. Using the MED-X µCT machine resulted in sharper imaging of the basic parenchymal architecture compared to µCT scan of human lung tissue taken on the non-optimised µCT machine (see Figure 2.5a). All blood vessel structures, occluded or patent were distinguishable down to a dimeter of approximately 25 µm. Valves were seen to be present within the lumen of some larger conduits (yellow arrows in Figure 2.5b). These valves were only distinguishable from the background noise due to the resolution and quality of the µCT scan. Finally, the resolution in this scan enabled the visualisation of conduit structures surrounding blood vessels which may have been missed in scans of poorer resolutions (see asterisks in Figure 2.5b).

2.3.2 Tissue Sectioning

A tissue section series of between 100-125 sections were taken from all tissue samples after being imaged by µCT resulting in a minimum sampling depth of 500 µm into the tissue. These sections were mounted onto pre-treated X-tra® adhesive glass slides (Leica Biosystems, Milton Keynes UK). The location of this sampling depth in the µCT scan volume, and the tissue section series is henceforth referred to as a tissue sample's "subvolume". Two subvolumes were taken from each sample. See Figure 2.6 for an overview of the sampling strategy of this work. The number of tissue sections taken to make each subvolume are detailed in Appendix B.

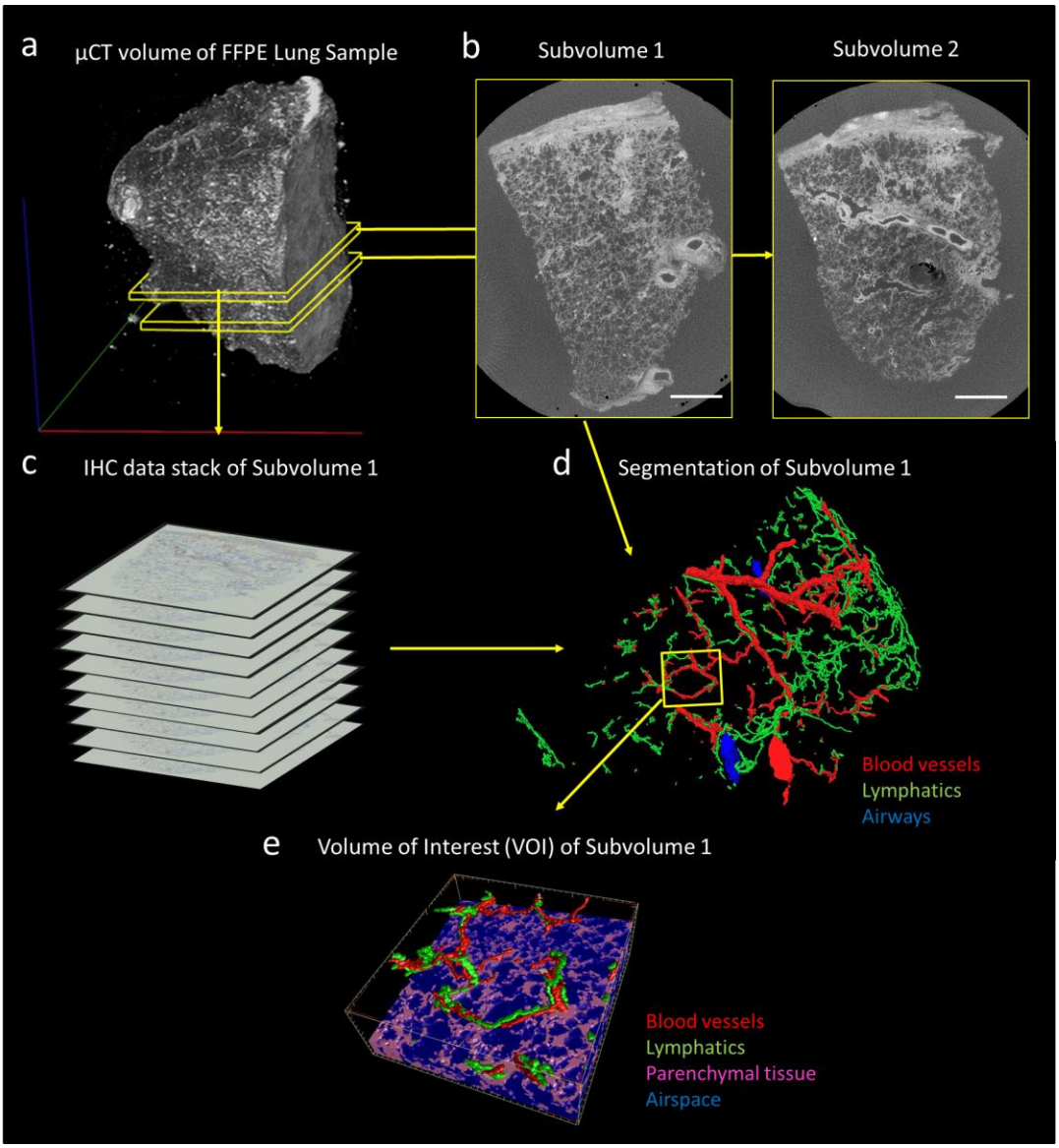

Figure 2.6 Overview of Human Lung Tissue Sampling. a Volume rendering of the µCT scan of a formalin-fixed paraffin-embedded lung sample and the locations of the two subvolumes (yellow)shown within the volume. **b** A 2D µCT orthoslice within each of the two subvolumes. Both scale bars = 1.5 mm **c** A representation of the 2D immunohistochemistry (IHC) image stack of subvolume 1 **d** Segmentation data of subvolume 1 made using the µCT dataset and the IHC dataset (Parenchymal tissue data not shown). A sampling volume of interest (VOI) is shown in yellow. **e** Volume rendering of the segmentation data in the VOI of Subvolume 1. Only bottom half of parenchymal tissue and airspace rendering are shown

A subvolume from one control lung sample was used to find the number of tissue sections in the subvolume's series that needed to be IHC stained to enable feature segmentation from the µCT dataset. In the 125-section series of this subvolume the 1st 2nd, 3rd and 4th were stained with PCK, CD31, αSMA and D240 respectively using the IHC protocol (section 2.2.2). This staining series was repeated every 10 sections in the series until the 100th section. D240 was used here instead of LP21 as in this sample D240 stained all lymphatic vessels in 2D, including the large conduits with no T1-cell staining.

2.3.3 Immunohistochemistry Slide Digitalisation

A user directed “Olympus dotslide” (Olympus, Southend-on-Sea, UK) system acquired digital images of the positively stained IHC slides at 20X magnification across the whole tissue section with the resulting image being saved as a VSI file. OlyVia software (Olympus) was used to view the slide images during all aspects of image analysis.

2.3.4 Registration of Immunohistochemistry Sections and X-ray µCT Volumes

A 3D software platform; Amira 6.0, standard edition (FEI, Eindhoven, The Netherlands) was used to align one of the digital IHC stained sections to a corresponding “floating” 2D digital slice of the µCT data set) using the Amira ”slice” module. The µCT data set was then resampled by a Lanczos filter in the “resample” module using the aligned µCT slice as a reference. Lanczos resampling smoothly interpolates the value of a digital signal in the defined sampling plane. The result was that every X-Y plane through the µCT dataset now resembled each cut section from the subvolume’s series.

2.3.5 Segmentation of Structures Within the µCT Dataset

The TrakEM2 plugin of the open source image software Fiji (Schindelin *et al.*, 2012).was used for µCT feature segmentation of the registered µCT datasets.

Lymphatic vessel staining patterns were manually segmented across the whole tissue face in the X-Y plane by reference to the IHC data (see Figure 2.7a and b). The blood vessel networks were also manually segmented by a combination of µCT morphology (larger vessels) and by reference to the IHC data (arterioles, venules). The segmentation area of all vessels included the interlumenal space and the walls of the vessels. Due to the damage during heat mediated antigen retrieval, it was not possible to determine the exact position of the capillaries within the alveolar wall, thus no capillary structures were included in the segmented blood vessel datasets. Picking up cut tissue sections onto coated slides with different charge strengths were tested, but with no improvement to results.

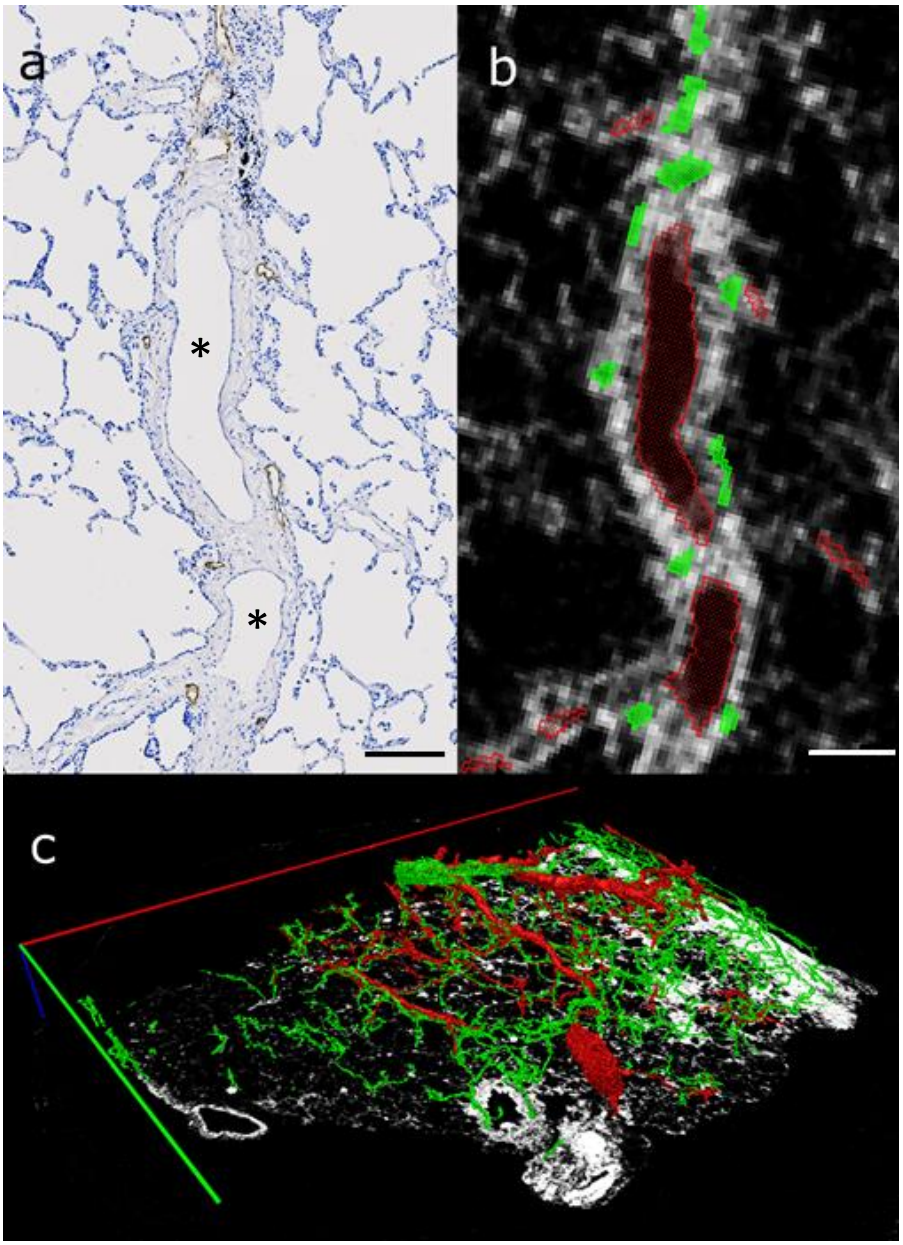

Figure 2.7 Feature Segmentation. **a** A region of interest (ROI) of the digitalised IHC section of a control lung tissue stained in blue (acidic stain) and the lymphatic vessels outlined in brown (anti-podoplanin antibody (D240)- DAB conjugate). A blood vessel is identifiable in the centre of the image by the dense connective tissue surrounding a smooth lumen (*). Scale bar=200 µm. **b**: The corresponding µCT ROI to panel **a** with the segmented lymphatic vessels outlined in green and the blood vessel marked in red. Scale bar=200 µm. **c** A rendered 3D image of segmented features within the subvolume of a control lung sample (500 µm depth). Scale bars are 10 mm (red); 8 mm (green);0.5 mm(blue). Lymphatics segmentation - Green, Blood vessels segmentation- Red, and Interstitial tissue segmentation (one µCT slice)- white.

The µCT orthoslices that were not segmented by histology correspondence were manually interpolated to join up the segmented features in the Z-axis to a depth of 500 µm (total subvolume size) to make a 3D image as shown in Figure 2.7c.

Greyscale value thresholding was used to segment the lung tissue (inducing lymphatic and blood vessel walls) of each subvolume using the Fiji thresholding tool. The threshold level was chosen by

eye to encompass as much of the tissue, and as little of the background (wax) as possible. This was a simple task due to the excellent contrast of tissue to wax in all µCT volumes. To confirm this segmentation method is accurate, the volume fraction of this subvolume was calculated. The total lung volume was segmented in the same method as the tissue, except the alveolar space were filled with the "Fill holes" algorithm in Fiji. The resulting volume fraction for this subvolume was 0.18. The average volume fraction (tissue volume/total lung volume) of an adult human is 0.2 (Coxson *et al.*, 1999).

2.3.6 Assessing the Need for Immunohistochemistry for Segmentation of Features Within the µCT Volume

The IHC protocol (section 2.2.2) was repeated using CD31 and D240 on the same subvolume series, so CD31+ and D240+ sections were available every 25 µm (every 5th section) through the subvolume of the tissue sample. Segmentation was then repeated from scratch on the same µCT subvolume using the larger amount of IHC data.

Using a voxel counting algorithm in Fiji, a volume calculation was made to see if the segmented volume of the lymphatic and blood vessel features changed when segmented with a larger amount of IHC data avaliable. There was less than a 5% difference between both the segmented lymphatic and blood vessel volumes when using a staining frequency of 1 in every 5 tissue sections (every 25 µm) rather than 1 in every 10 tissue sections (every 50 µm). However increasing the frequency of IHC staining of CD31 and D240 simplified manual segmentation and enabled segmentation interpolation at a faster rate. CD31 was therefore used at a staining frequency of 1 in every 5 tissue sections for staining of the subvolumes of all the other lung samples. Although D240 showed no T1 cell staining on the sample used for this investigative test, it was considered that LP21 would be the most suitable for the IHC high-frequency staining due to the prevelance of T1 cell cross reactivity in the other samples. Therefore LP21 was used for IHC staining on 1 in every 5 sections in all other lung sample subvolumes. Due to the observation that D240 is needed to visualise some larger lymphatic vessel structures, D240 was used three times, at the beginning, the middle and the end of each subvolume tissue series.

All airway structures and large blood vessels (luminal diameter >25 µm) could be identified using the µCT scan alone owing to the ability to trace anatomical structures through the data set in three different planes. Despite this, one section at the top bottom and middle of every tissue series subvolume was stained with the PCK and αSMA antibodies to confirm their identification within the µCT dataset.

The staining sequence outlined above (full details given in Appendix B) was used to perform the IHC protocol (section 2.2.2) on all the remaining lung samples' subvolumes. Subsequent IHC -µCT alignment and feature segmentation was also performed (sections 2.3.4 and 2.3.5). Segmented data of the lymphatic vessels network, the blood vessel network, the airways and the lung parenchymal tissue were exported as a 3D 8-bit file in a "raw" format for subsequent multi-software use.

2.3.7 Data Archiving

µCT scan data, digitalised IHC sections, re-aligned µCT scans, and segmentation data collected from all human lung samples used in the 3D study amounts to 2.4 terabytes of data. This is stored at the Biomedical Imaging Unit data storage facility indefinitely, and in the µ-VIS Imaging Centre data archive. Both centres are core facilities at the University of Southampton.

2.4 Morphometery of Human Pulmonary Lymphatics

2.4.1 3D Sampling Strategy for Morphometry

Once the lymphatic volumes had been segmented, the strategy of how they could be characterised was investigated. The value of qualitative observation is high and often overlooked. However, an automated numerical method is also desired for an unbiased comparison of lymphatic morphology between sample groups.

When observing the complete network of lymphatic structures in 2D by histology, and in 3D by µCT it was evident that lymphatic structural heterogeneity exists in the subvolumes of the lung tissue samples (see Figure 2.6d and 2.7c). A single global numerical assessment of the structures within a subvolume of tissue was therefore not informative. Sampling these networks into smaller volumes of interest (VOIs) was decided to be the most suitable strategy (see Figure 2.6e as an example).

Also, when observing the lung structure of samples, it was evident that samples were at different levels of inflation before fixation. Although unfortunate, this finding was not surprising as this process is not always standardised for diagnostic samples. As such, if a healthy sample with an idealised lymphatic pattern were inflated to different pressures, using a set VOI sampling size would result in different morphometric measurements of the same sample (see Figure 2.8). The VOI sample size would therefore have to be adjusted for each sample.

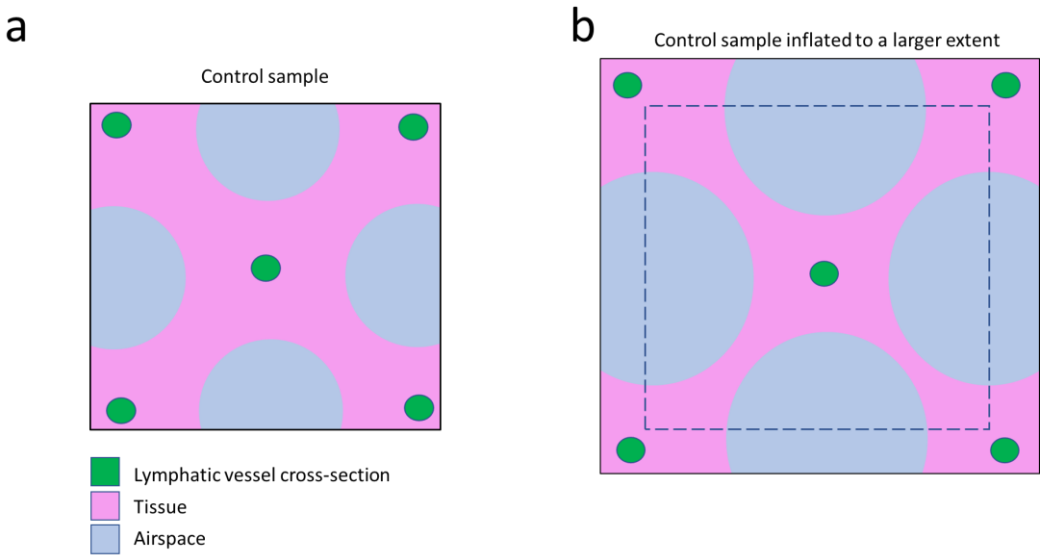

Figure 2.8 Justification for Using Different Sampling Sizes for Diagnostic Samples. a An idealised 2D geometry of a control lung sample (blood vasculature omitted). **b** An idealised 2D geometry of the same control lung sample when inflated to a larger extent than in panel **a**. The dotted line depicts the same sampling size as in panel **a** demonstrating how the lymphatic patterning is now missed.

To decide on the suitable sampling size to capture lymphatic patterning within each sample, two VOI size refinement studies were undertaken. The first was to gauge a rough idea of the lymphatic patterning size at a set location, the second was used to readjust this size to best capture as much of the inter-subvolume variation as possible.

For the first study (see Figure 2.9a), a random number generator was used to define the coordinates of a single region of interest (ROI) of 33x33 pixel dimension (435x435 µm) on the central X-Y plane of the "test" lung subvolume. This ROI was increased in the X and Y dimension by 5 pixels, keeping the coordinates of the ROI origin the same. This new ROI was then saved as a separate ROI to the first by the ROI manager plugin in Fiji. This was repeated until 14 ROI existed with their X and Y dimensions ranging from 33-98 pixels (450-1293 µm) in size.

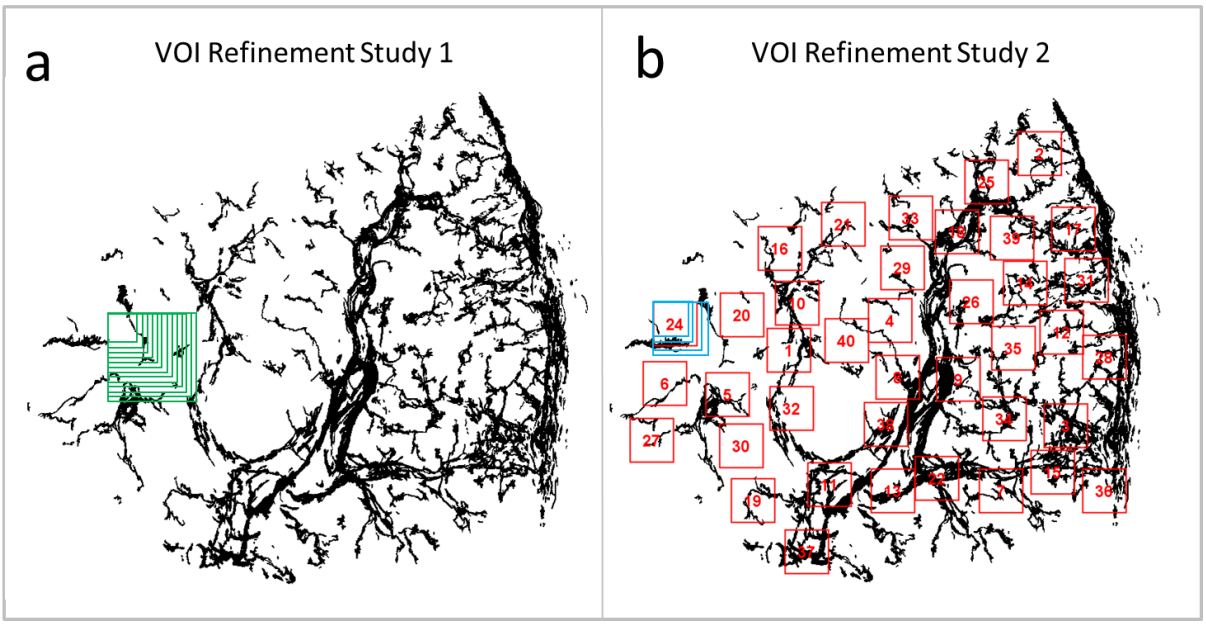

Figure 2.9 Visual Description of VOI Size Refinement Studies. a. 14 ROIs of different sizes (green squares) were created at a single randomly chosen X-Y coordinate on the central X-Y plane of a subvolume of a control human lung sample's lymphatic network (black). These were made into VOIs. The lymphatic volume and surface area were then measured in each VOI normalised to the VOI size. **b.** 2 VOIs larger, and 2 VOIs smaller (blue squares) and the optimal VOI defined from (**a**) were used to create a VOI set in the subvolume (the red squares show this for the optimal VOI size from (**a**)). The lymphatic volume and surface area were then measured (normalised to the VOI size) for every VOI in each size-set.

The 14 ROIs were extended in the Z-axis away from the central X-Y-plane by 250 µm in each direction to make 3D VOIs.

The volume of the lymphatic network in each VOI was measured by a voxel counting algorithm in Fiji. The lymphatic volume fraction (lymphatic volume/ VOI volume) for each VOI was plotted against the length of the X and Y VOI axis. The point at which the measurement did not change more than 5% signified the minimum VOI size for sampling the lymphatic shape at a single point within the lung tissue. To confirm this was not only valid for the volume metric, the lymphatic surface area to lung volume ratio was also calculated (surface area/ VOI volume). The lymphatic surface area was calculated by a surface pixel counting algorithm.

The results of the first VOI refinement study indicated the approximate X and Y VOI dimension required to describe the lymphatic patterning in a randomised position in a control human lung sample subvolume is between 810-860 µm (see Figure 2.10**Error! Reference source not found.**a and b).

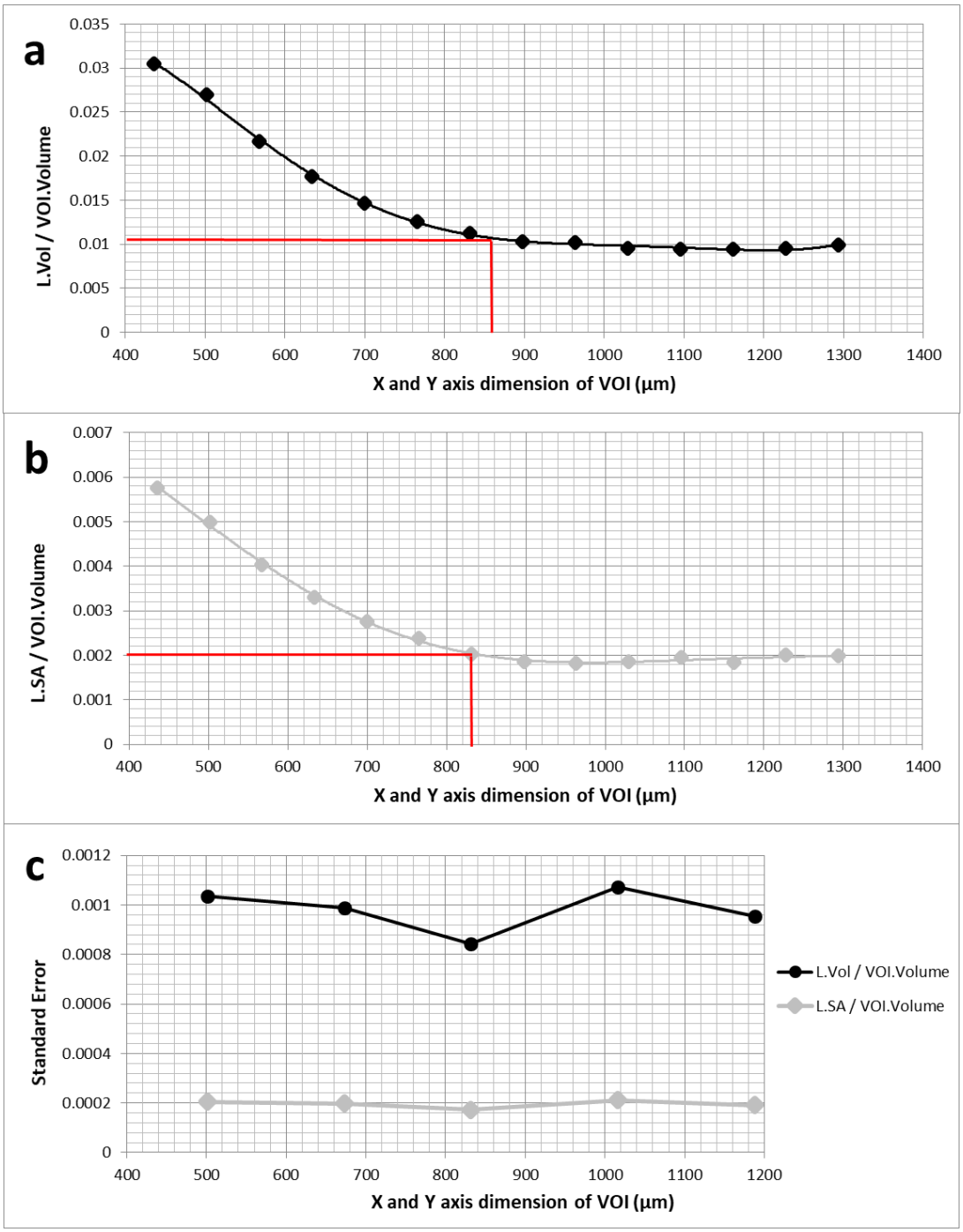

Figure 2.10 Results of the VOI Size Refinement Studies. **a** How the lymphatic volume fraction (L..Vol)/VOI Volume), taken at a single location within a control samples subvolume, changes with increased VOI sampling size. **b** A graph showing the lymphatic surface area (L.SA)/VOI volume ratio taken at a single location within the same subvolume changes with increased VOI sampling size. The red line in each graph **a** and **b** indicates when the derived morphological measure change is <5%. **c** A graph showing the standard error for the volume fraction and lymphatic surface area/ VOI volume ratio for each and the of the 5 VOI sampling size sets (VOI size-refinement study 2).

For the second VOI size refinement study (see Figure 2.9), a macro-language script (see Appendix C) was written in Fiji to define sampling ROIs automatically within the central X-Y plane of the lung samples' subvolumes. On the central X-Y plane of the subvolume, this script randomly identified coordinates within the full 2D extent of the lung tissue by use of a random number generator.

These coordinates were used as an origin to make into ROIs of predefined dimensions. The X-Y size of the ROI for each tissue sample were chosen to be 832 µm taken as an average of the first VOI size refinement study result. Any ROIs that overlapped were excluded, and the script automatically reiterated until the maximum (or desired) number of ROI was achieved.

As in the first study, the ROIs were extended in the Z-axis away from the central X-Y-plane by 250 µm in each direction to make 3D VOIs.

Four more VOI sets were made with two 25 and 12 pixels smaller in the X and Y dimension than the optimal size and two 25 and 12 pixels larger in the X and Y dimension. The number of VOIs created by the random ROI generator script (iteration value of 1000) for the VOI sets of X and Y dimensions: 502 µm; 673 µm; 832 µm; 1016 µm; 1188 µm; were: 40; 40; 26; 19; 16 respectively.

The lymphatic volume and surface area measurements were then assessed within each of the VOI across all VOI size sets, and the standard error calculated for each set. The VOI size that had the lowest standard error across the two measurements suggested the best-suited sampling size to describe the lymphatic patterning throughout the lung tissue sample.

The second VOI size-refinement study showed the VOI set with X and Y dimensions of 832 µm had the smallest standard error across all VOIs in both morphometric measurements for this “test” sample (see Figure 2.10c). It should be noted the result was more significant with the volume measure than the surface area measure.

Visual observation of the lymphatic networks between subvolumes of the same sample suggested the lymphatic patterning (including the anatomical heterogeneity) was similar. Therefore it was not necessary to repeat the VOI refinement studies for both subvolumes within a sample. In contrast, as mentioned above, the patterning between samples appeared variable. Therefore, to be confident lymphatic patterning in each sample is captured, the VOI refinement studies were repeated for each patient sample used.

In Table 2.2 the calculated VOI size, determined for pulmonary lymphatic sampling of each lung sample used in the full 3D analysis, is shown. The number of VOI obtained for each sample’s subvolumes are detailed in Appendix B.

Table 2.2 Optimum VOI Sampling Size for Pulmonary Lymphatics for Each Sample Studied

Category of Sample	Sample ID CODE	VOI sampling size (μm^3)
Control	EV090	832
	HL088	800
	HL079	820
	HL106	800
Active Disease	EV020	820
	EV024	840
	EV014	780
	EV104	800
COPD	HL150	841
	HL108	840

2.4.2 Subvolume VOI Classification

Each VOI within each subsample was labelled based on their anatomical location within the peripheral lung. All VOIs were assessed by their distance away from anatomical structures in the lung using a 3D 32-bit pixel distance map. The median pixel average within each of the VOIs (multiplied by the voxel size of the image) was recorded as the distance each VOI was away from the reference structures.

A VOI with any voxel lying within a third of a VOI width (X or Y dimension) from the centre of the interlobular septa, bronchovascular bundle or the visceral pleura would be labelled as such. The remaining VOIs will be assigned as intralobular. The labels were therefore designated in the following order based on the size of the anatomical feature. No VOI had more than one label. The abbreviations in brackets will henceforth be used in most data presentation.

- Interlobular Septa (IS)
- Bronchovascular-bundle (BVB)
- Subpleural (SP)
- Intralobular (IL)

An example of this is shown in one subvolume of an active disease sample in Figure 2.11.

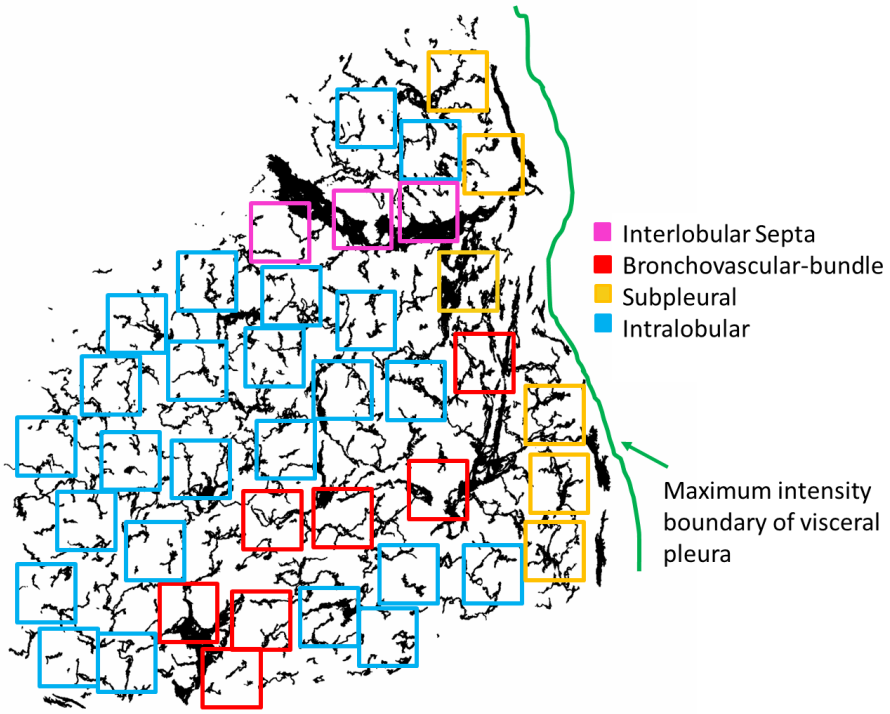

Figure 2.11 Anatomical Classification and Labelling of VOIs in Human Lung. A maximum intensity Z-stack of the lymphatic network (black) in a subvolume of an active disease human lung sample. Overlaid are the randomly generated (with overlap restriction) VOIs within this subvolume. All VOI are labelled based on their vicinity to notable anatomical locations. The tissue limits of the pleural surface are shown by a green line. This is a maximum intensity image. Therefore, part of the pleural surface may be closer to the lymphatic network than appears in this diagram.

The decision to link the VOI to an anatomical area in the lung was taken for two reasons. Firstly, the high standard error values seen in the second VOI size-refinement study suggested inter-subvolume variation of lymphatic morphology was present. Secondly, from qualitative observations, it was clear that around certain anatomical features, there was a notable difference in lymphatic vessel structure. When labelling the VOIs, the aforementioned rules were essential to prevent any biasing of classification.

2.4.3 Metrics for Describing Pulmonary Lymphatic Morphometry

Morphometry metrics were selected by rigorously assessing their benefit in describing the lymphatic structures, and how the metric may relate to function. As there are no previous studies on the assessment of 3D pulmonary lymphatic morphology, the choice of metrics used in this study have been selected based on knowledge of blood vasculature studies.

The basic volume metric (see Figure 2.12a) gives a simple quantitative assessment of the space the lymphatic system occupies in the sample. The surface area measurement (see Figure 2.12b) starts to relate to the lymphatic function as a greater surface area results in a higher opportunity

for fluid to move into the lymphatic vessel. Two samples with the same volume of lymphatics would be expected to absorb fluid differently and have different intra-luminal flow patterns if they have a different surface area (see Figure 2.12 a and b). The different flow pattern would exist because it is assumed that more branches are present with narrower lumens in the lymphatics with a higher surface area. Resistive pressures from the wall of the lymphatic vessels could therefore affect the flow rate and pressures within the vessel.

Similarly, determining the number of branches and junctions that make up the lymphatic patterning is a useful metric as it indicates the extent of lymphatic remodelling that may have occurred within different samples. Flow patterns inside structures with high junction and branch numbers would be different from that of straight vessels as there are more points where the fluid can exert shear stress on the endothelium (see Figure 2.12 c). In blood vessels, it has been shown that increased fluid-induced shear stress on the endothelium can activate vascular endothelial growth factor receptor 2 (VEGFR-2) in a ligand-independent manner to regulate endothelial nitric oxide synthase (eNOS) (Jin *et al.*, 2003). eNOS produces nitric oxide in the endothelium, which is a potent neovascularisation inducing agent in the lung (Bhandari *et al.*, 2006). Therefore, evaluating the ratio between the number of lymphatic branches to junctions would be of interest. If there is a high branch number with only a few junctions, historical or present system stresses may be indicated.

Blood vessel tortuosity is a well-used metric in the assessment of vasculopathies in metabolic disorders, hypertensive disease and oncology (Han, 2012; Diedrich *et al.*, 2011; Sodi *et al.*, 2013; Bullitt *et al.*, 2005). It defines how much a branch length deviates from being a straight line. Although this measure can have numerous mathematical descriptions, the most commonly used is a ratio between the actual length of a vessel branch divided the direct distance (also termed the Euclidian distance) between its endpoints (Smedby *et al.*, 1993) (see Figure 2.12d). Although more commonly used as a metric for 2D images, it has been used as a metric for 3D image assessment (Folarina et al., 2010; Helmberger et al., 2014).

The complexity of an object can be measured over different dimensions by measuring its fractal dimension (FD) which is a measure of space-filling by a uniform object over different scales (Huo & Kassab, 2012; Mandelbrot, 1967). A measure of FD is distinct from the tortuosity measure as FD takes into account an objects spatial dimension (see Figure 2.12e). Two studies have found 2D FD of the pulmonary vascular system to be an indicative measure for assessing patients with pulmonary hypertension (Haitao et al. 2011; Moledina et al., 2011). A 3D study showed that tortuosity was a useful indicator of pulmonary hypertension, but the FD measure was not (Helmberger *et al.*, 2014).

In addition to lymphatic volume, lymphatic surface area, and lymphatic branch and junction number there is therefore a clear reason to investigate both the tortuosity and FD measure of pulmonary lymphatics.

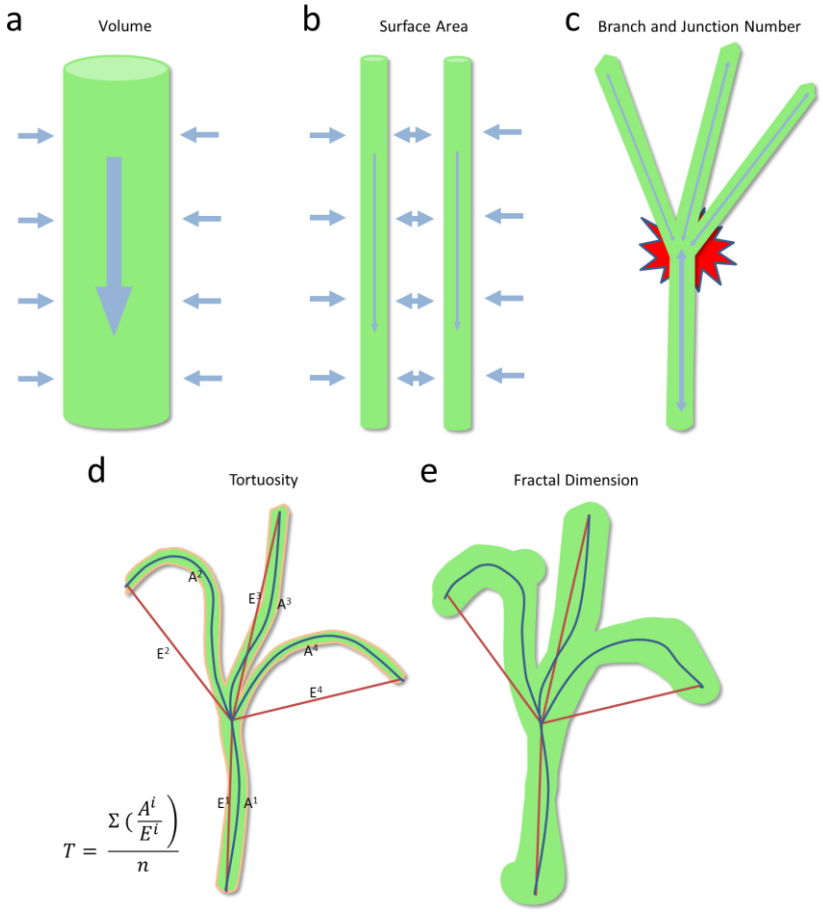

Figure 2.12 Idealised Representation of Morphometric Analysis. a A lymphatic vessel with a set volume. **b** A lymphatic vessel with the same volume as panel **a** but with a different surface area. **c** Same lymphatic vessel volume and surface area as panel **b** but with four branches and one junction. Pressure points may be present in this geometry. **d** The branch morphology as panel **c** but with higher tortuosity value, suggesting pathology may be present. The equation given is for how tortuosity (T) is calculated within each VOI. A= actual branch length, E=Euclidian length, i= individual branch identity, n= number of branches present in the VOI. **e** A vessel with the same tortuosity as panel **d** but with a greater FD.

In all VOIs, the volume and surface area metrics were measured as a summation of voxels and pixels respectively for all segmented lymphatic features within a VOI. These metrics were calculated by using the "3D geometrical shape" analysis tool of the 3D Suite Fiji plugin version 3.9 (Boudier *et al.*, 2013). The voxel volume of each structure was converted to unit measurements by multiplying the voxel count by the pixel size of the image cubed. The pixel surface area of each structure was converted to unit measurements by multiplying the pixel count by the pixel size of the image squared.

The lymphatic vessel fractal dimension (complexity) of the vessel structures for each VOI was calculated using the BoneJ Fiji plugin version 1.4.2 (Doube *et al.*, 2010).

To obtain the lymphatic vessel branch number, junction number and tortuosity, each 8bit lymphatic vessel volume was first skeletonised using the "skeletonize 2D/3D" plugin. The "analyse skeleton 2D/3D" plugin was then used to obtain the total branch number and total junction number (points where a branch splits) for each VOI. Each of the branches of the skeleton was also measured by their actual length and Euclidian length. The ratio between the actual branch length and the Euclidean branch length gave the lymphatic vessel tortuosity for each branch. A mean average was taken of each branch's tortuosity to give the tortuosity of the lymphatic vessels within each VOI.

The above raw data collection and processing was automated through a script (macro language) written in Fiji. A copy of this script can be found in Appendix D.

2.4.4 Normalisation Strategy

Apart from the tortuosity and fractal dimension metrics, It was necessary to normalise the other four metrics because each sample had different optimal VOI sizes. It was further decided to normalise these metrics to a specific tissue parameter rather than lung volume (VOI volume). Normalising by the tissue volume considers tissue fibrosis and emphysema which may be present in the samples collected. Assuming that there is no difference in lymphatic patterning between samples, Figure 2.13 depicts why information may be lost if the lymphatic morphometry was normalised by the VOI volume. In the idealised fibrotic sample, each lymphatic vessel serves a larger tissue space, thus flow towards and into these vessels may be greater than seen in the control or emphysematous samples. Also, as the lymphatics drain fluid from the tissue and not the airspace, the function of the lymphatics in the emphysematous sample may, therefore, be different from the control.

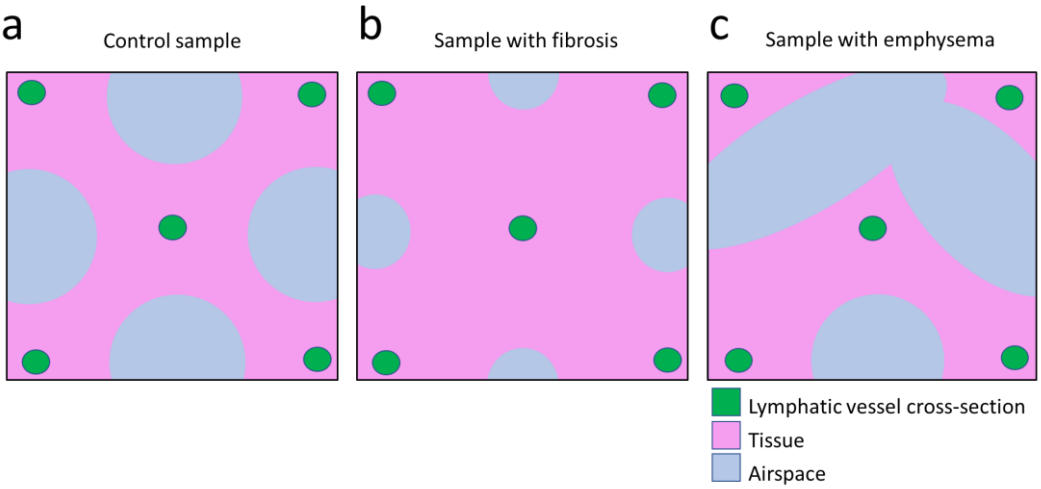

Figure 2.13 Normalising Lymphatic Morphology by Tissue Volume Infers Lymphatic Functionality. **a** An idealised geometry of a control lung sample (blood vasculature omitted). **b** An idealised geometry of a lung sample with the same lymphatic patterning as in panel **a** but with tissue fibrosis. **c** An idealised geometry of an emphysematous lung sample with the same lymphatic patterning as in panel **a**. IT would be expected the lymphatics would be functionally different in these samples regardless of the lymphatic pattering being identical as the tissue volume they serve is variable

The data calculated for each VOI across all subvolumes were ultimately used to describe the lymphatic structures in the following way:

- Lymphatic vessel volume/ lung tissue volume.
- Lymphatic vessel surface area/ lung tissue volume.
- Lymphatic branch number/ lung tissue volume.
- Lymphatic junction number/ lung tissue volume.
- The average tortuosity of the lymphatic vessels.
- The fractal dimension of lymphatic network.

The tissue volume for normalisation purposes was calculated in the same manner as the lymphatic volume. When not detailing statistical comparison analysis, morphometry data will be graphically presented with the dataset's median value and its interquartile range.

2.4.5 Statistical Analysis of Lymphatic Morphometry

These methods are detailed specifically for data in the relevant chapters.

2.5 General Discussion of Imaging Methods

The methodology presented in this chapter enables, for the first time, human pulmonary lymphatics to be imaged and analysed in 3D.

Developing this methodology for paraffin-embedded samples provides the opportunity to use archived collections of clinical human tissue samples. This access to an almost unlimited sample source is advantageous as it prevents the need for prospective tissue collection which can be a lengthy process, particularly for human tissue.

Using IHC alone to attempt 3D tissue morphometrics on these samples is time consuming and has many limitations. Serial sections are rarely complete or of consistent thickness (Mega *et al.*, 1997). In addition, particularly for the open structure of the lung, sections can be significantly deformed due to microtome artefacts such as blade compression or stretching due to water bath heating (Scott *et al.*, 2015). Finally, as shown with CD31 staining, the IHC protocol itself can induce artefacts. Therefore, obtaining an isotropic µCT scan of the lung sample before IHC cutting provides a robust 3D reference structure that can be used to compensate for histological artefacts.

Using an optimised high-resolution µCT machine and scanning protocol, alongside a wax contrasted and stabilised sample, has enabled some pulmonary structures to be imaged and identified in 3D with only the need for confirmatory IHC. In time and with experience, it is anticipated for some large structures, confirmatory IHC may not be necessary. However, full sample depth IHC will still be required to discern and segment cellular level structures and biomarkers in 3D. The success of this arm of the methodology, therefore, relies heavily on the quality of the antibody used.

One of the most exciting finds in the whole body of work is the discovery of LP21 as a pulmonary lymphatic imaging tool. Although to date not commercial, it is anticipated in the future this will become the antibody of choice for lymphatic imaging in the human lung. As a direct comparison to D240, LP21 is a superior antibody for unambiguous imaging of lymphatics in human peripheral lung as no T1 cell staining was evident across all lung samples studied, supporting the findings of the paper that initially characterised LP21 (Kaneko *et al.*, 2017). This higher specificity is essential in diagnostic human lung studies as the majority of samples will have some injury or damage which is known to upregulate podoplanin expression in T1 cells (Schacht *et al.*, 2005).

In large scale studies, a time-efficient workflow is essential. In this methodology, a balance was struck between obtaining as much information as was necessary to image 3D structural networks confidently, while being as time efficient as possible. Obtaining the highest resolution µCT scan for each sample significantly reduced the time taken for manual segmentation due to an improved signal to noise ratio. This saved more time than the additional image processing complexity cost. Also, although increasing the IHC staining frequency showed no increase in

segmentation accuracy, manual segmentation rates were much faster with the larger 2D IHC dataset, which, overall, saved more time than it cost producing the extra IHC stained slides.

Manual segmentation is the rate-limiting step of the imaging section of the workflow. However, due to the high 3D complexity of both the lymphatic and blood vessel structures, manual segmentation was essential for maintaining 3D lymphatic structure fidelity, particularly in areas of vessel collapse or IHC data distortion. At present, automatic alignment, registration, and segmentation software require both images to be at the same resolution and of identical dimensions. Even then, if the 2D inputs are not complete, 2D-3D interpolation would still require manual input. IHC resolution required to visualise the stained feature would be lost if down sampled to the µCT resolution, and, at present, the computational memory requirements to increase the µCT resolution to match that of the histology would be impractical for a large study. Due to the demand for automating 2D-3D image registration and segmentation however, advancement of computer software systems in this field is rapidly accelerating. It is expected, therefore, that automated or semi-automated soft tissue segmentation will be possible in the near future.

Chapter 3 Development of Methods for Image-Based Mathematical Modelling of Pulmonary Fluid Flow

This chapter details the chronological development of the mathematical model used to simulate fluid flow within real 3D human lung geometries as obtained in Chapter 2. First, the mathematical model design is described, then the methods for implementing this model to simulate fluid flow within a simplified 2D geometry of human lung will be given. Following this, methods for 3D image processing and finite element meshing, both required to enable successful simulation of fluid flow in real 3D geometries will be given. Finally, the model design will be simulated in an example volume of interest (VOI) of real human lung tissue and the model design will be finalised based on the simulation results.

3.1 Model Design and 2D Simulation

3.1.1 2D Geometry and Mesh Obtainment

To permit rapid feedback of the model design as it was being developed, a simplified 2D lung geometry was created in COMSOL Multiphysics version 5.3.0, (COMSOL Ltd, Cambridge, UK) representing a lymphatic vessel and a blood vessel situated within the pulmonary interstitium. These regions in the geometry will be henceforth referred to as simulation domains. The simulation area for the 2D geometry was 500 μm^2 as the VOI size refinement study had not been undertaken at this stage. A finite-element mesh was created for this geometry within the same COMSOL software. A schematic illustration of this geometry is given in Figure 3.1.

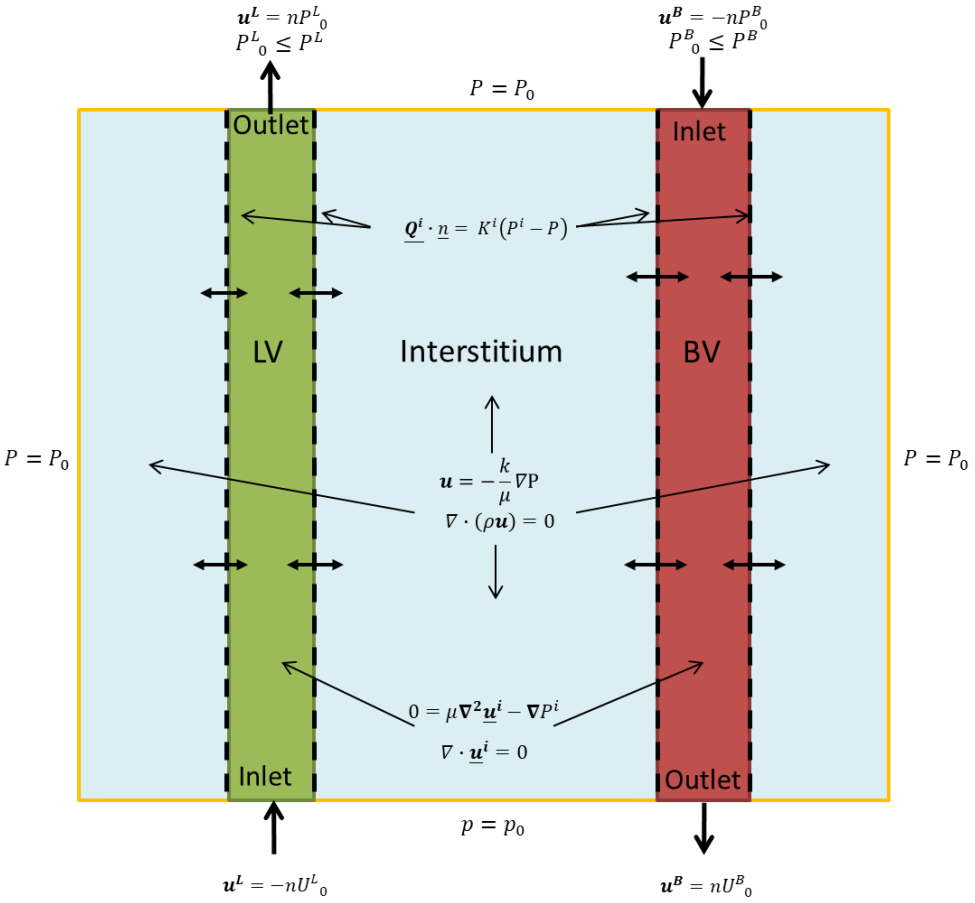

Figure 3.1 Illustrative Schematic of Model Design for Pulmonary Fluid Flow. The blood vessel is shown in red (BV), the lymphatic vessel in green (LV) and the interstitial tissue in blue. This geometry was used for all 2D simulations of the model. Flow through the interstitium is described by Darcy's Law (equations 3.1) and flow in the vessels are described by Stokes' flow (equations 3.2) with defined inlet and outlet conditions (equations 3.5-3.8). The dotted lines represent a flux boundary condition described by the Starling's Equation (3.3). The model constraints are shown by orange boundaries where an interstitial pressure condition (equation 3.4) was applied. All symbol definitions and equations are given in the text.

3.1.2 Governing Equations of Pulmonary Fluid Flow Model Design

The equations describing the pulmonary fluid flow regimes and boundary conditions in the 2D geometry are shown in Figure 3.1.

The fluid conservation in the interstitial domain was modelled using Darcy's law that links the fluid velocity ***u*** to interstitial pressure gradient *P*:

$$\nabla \cdot (\rho \boldsymbol{u}) = 0, \tag{3.1a}$$

$$\boldsymbol{u} = -\frac{k}{\mu}\nabla P, \tag{3.1b}$$

where ***u*** is the interstitial lymph fluid velocity, *k* is the interstitial permeability, *P* is the interstitial fluid pressure, and μ and ρ are the dynamic viscosity and mass density of the fluid respectively.

The fluid within the lymphatic and the blood vessel domains was described as a Newtonian fluid by the Navier-Stokes Equations with the inertial term neglected resulting in the so-called Stokes flow equations. This assumption is valid as the Reynolds number for flows in the microvasculature is very low (Krouskop, Newell & Reddy, 1975).The Reynolds number is a dimensionless quantity which characterises the magnitude of inertial effects compared to the magnitude of viscous effects. A low Reynolds number indicates that viscous forces are very strong compared to inertial forces. Thus, Stokes' equations were used *i.e.,*

$$\nabla \cdot \underline{\boldsymbol{u}^{\boldsymbol{i}}} = 0, \tag{3.2a}$$

$$0 = \mu \boldsymbol{\nabla^2} \underline{\boldsymbol{u}^{\boldsymbol{i}}} - \boldsymbol{\nabla} P^i, \tag{3.2b}$$

where *i=L* and *i=B* are lymphatic vessel and blood vessel quantities respectively, and $\underline{\boldsymbol{u}}$ is the fluid flow velocity in a vector form. A no-slip boundary condition was applied to the vessel walls.

3.1.3 Boundary Conditions of Pulmonary Fluid Flow Model Design

A flux boundary condition that considers both osmotic and hydrostatic pressure gradients was applied to each boundary at the vessel wall-interstitium interface. This condition is commonly known as Starling's Equation (Starling, 1896) which is given by:

$$\underline{\boldsymbol{Q}^{\boldsymbol{i}}} \cdot \underline{n} = K^i \left(\left(P^i - P \right) - \sigma^i \left(\pi^i - \pi \right) \right) \tag{3.3}$$

where *i=L* and *i=B* are lymphatic vessel and blood vessel quantities respectively, $\boldsymbol{Q}^i \cdot \underline{n}$ is the volumetric flux normal to the vessel wall surface, *K* is the hydraulic conductivity specific to each vessel's wall, σ is the osmotic reflection coefficient specific to each vessel wall, π is the osmotic pressure of the interstitium and π^i is the plasma osmotic pressures specific to each vessel.

The external boundaries of the interstitial domain had the following pressure boundary constraint applied:

$$P = P_0, \tag{3.4}$$

where P_0 is the interstitial pressure parameter defined by the literature (Kurbel *et al.*, 2001).

As the lymphatic vessels modelled in this geometry were not "blind ended", the boundary condition at the inlet of the lymphatic vessel used the literature defined lymphatic flow velocity:

$$\boldsymbol{u^L} = -\boldsymbol{n} {U^L}_0, \tag{3.5}$$

Where $\boldsymbol{u^L}$ is the lymphatic vessel flow velocity, *n* is the normal boundary vector pointing out of the lymphatic vessel domain and $U^L{}_0$ is the magnitude of lymphatic inflow velocity.

The lymphatic system drains fluid from the interstitium principally by a pressure gradient (Ohtani, 2008). Thus, a negative pressure downstream of the lymphatic simulation domain needs to be maintained to enable the fluid to flow out of the lymphatic vessel. Backflow of fluid flow at this outlet was supressed. The following pressure condition was therefore applied as the lymphatic vessel outlet boundary condition:

$$\boldsymbol{u^L} = \boldsymbol{n}P^L{}_0, \quad \textbf{(3.6a)}$$

$$P^L{}_0 \leq P^L \quad \textbf{(3.6b)}$$

where $P^L{}_0$ is the literature defined lymphatic pressure.

The literature quoted value for the blood domain pressure is an estimate of the capillary vessel pressure before any fluid filtration has occurred (Kurbel *et al.*, 2001). The pressure would reduce when filtration occurs, thus no backflow would occur. Due to these facts, a pressure boundary condition was placed on the inlet of the blood domain:

$$\boldsymbol{u^B} = -\boldsymbol{n}P^B{}_0, \quad \textbf{(3.7a)}$$

$$P^B{}_0 \leq P^B \quad \textbf{(3.7b)}$$

where $\boldsymbol{u^B}$ is the blood vessel flow velocity, *n* is the normal boundary vector pointing out of the blood vessel domain, and $P^B{}_0$ is the literature defined blood pressure.

The volumetric flux ($\boldsymbol{Q^B}$) out of the blood vessel wall would dictate the pressure and therefore flow velocity within and out of the blood vessel domain. Laminar blood flow velocity, $U^B{}_0$, was therefore used as boundary condition at the outlet of the blood vessel domain:

$$\boldsymbol{u^B} = \boldsymbol{n}U^B{}_0 \quad \textbf{(3.8)}$$

3.1.4 Input Parameters of Mathematical Model

The human lung input parameters for all model designs unless stated otherwise are shown in Table 3.1. All values of these input parameters have been taken from the literature and experimentally verified where possible or estimated using validated modelling methods. Please note, all pressures in this thesis are given as gauge pressures.

Table 3.1 Model Input Parameters for Healthy Lung Tissue

Domain Type	Parameter	Value	Units	Description	Literature Source
Fluid	μ	$1.2\text{x}10^{-3}$	Pas	Dynamic Viscosity	(Sugihara-Sekim & Fu, 2005)
	ρ	1030	Kg.m^{-3}	Mass Density	(Swabb, Wei & Gullino, 1974)

Interstitium	κ	$4.4x10^{-18}$	m^2	Permeability	(Swabb, Wei & Gullino, 1974)
	φ	0.13	n/a	Porosity	(Baxter & Jain, 1989)
	P	-1064	Pa	Pressure (interstitial)	(Kurbel *et al.*, 2001)
	π	1862	Pa	Osmotic pressure	(Kurbel *et al.*, 2001)
Lymphatics	$\boldsymbol{u^L}$	$5x10^{-4}$	$m.s^{-1}$	Flow velocity (normal to surface boundary)	(Fujiwara *et al.*, 2014)
	P^L	-1200	Pa	Pressure	(Erbertseder *et al.*, 2012)
	K^L	$1.9x10^{-12}$	$m.s^{-1}$	Hydraulic conductivity of vessel wall	(Erbertseder *et al.*, 2012)
	π^L	1862	Pa	Osmotic pressure	(assumption see section 3.1.7)
	σ	0.8	n/a	Osmotic reflection coefficient	(assumption see section 3.1.7)
Blood Vessels	$\boldsymbol{u^B}$	$3.5x10^{-2}$	$m.s^{-1}$	Flow velocity (normal to surface boundary)	(Guyton & Hall, 2010)
	$P^{B(O)}$	+2000	Pa	Pressure (sphincters open)	(Kurbel *et al.*, 2001)
	$P^{B(c)}$	+800	Pa	Pressure (sphincters closed)	(Kurbel *et al.*, 2001)
	K^B	$2.7x10^{-12}$	$m.s^{-1}$	Hydraulic conductivity of vessel wall	(Erbertseder *et al.*, 2012)
	π^C	3724	Pa	Osmotic pressure	(Kurbel *et al.*, 2001)
	σ	0.8	n/a	Osmotic reflection coefficient	(Negrini & Passi, 2007)

3.1.5 Solver Settings and Dependent Variables

As the model given by equations (3.1)-(3.8) is time-independent, a MUMPS direct linear solver using a segregated algorithm was used to resolve the equations (3.1)-(3.8) for five dependent variables: interstitial pressure, P (Pa), blood vessel pressure P^B (Pa), lymphatic vessel Pressure P^L (Pa), lymphatic fluid velocity field, $\boldsymbol{u}^L$($m.s^{-1}$) and blood vessel fluid velocity field, $\boldsymbol{u}^B$($m.s^{-1}$).The maximum iteration number to reach solution convergence was set to 150.

3.1.6 Numerical Output of Model for 2D Geometry

The numerical outputs of the model simulation on the 2D geometry were the following:

- Mean interstitial, lymphatic and blood vessel domain pressure change from baseline (input pressures (see Table 3.1)), P, P^L and P^B (Pa).
- Mean lymphatic and blood domain fluid flow velocity, $\boldsymbol{u}^L$ and $\boldsymbol{u}^B$ ($mm.s^{-1}$).
- Fluid flux into the interstitium, lymphatic and blood vessel domain integrated along the boundary each vessel wall then normalised by the surface of the boundary $\boldsymbol{Q_{norm}}$, $\boldsymbol{Q^L_{norm}}$ and $\boldsymbol{Q^B_{norm}}$($\mu l.m^{-1}.min^{-1}$)**.**

- Inlet mass flow (blood vessel inlet) integrated across boundary surface, M^{In} (kg.m.s^{-1}).
- Outlet mass flow (lymphatic outlet and ROI boundary) integrated across boundary surfaces, M^{out} (kg.m.s^{-1}).

3.1.7 Model Simulation on 2D Geometry

The model design, input parameters and solver settings outlined in sections 3.1.2- 3.1.5 were used to simulate fluid flow in the 2D geometry (see section 3.1.1) to see if the model design could be simulated using COMSOL, and to test the accuracy of the model. The simulation was repeated on a range of interstitial osmotic pressures, π, (0-3500 Pa) to see if the simulation results reflected Starling's hypothesis which predicts an increase of osmotic pressure in the lung interstitium would increase fluid moving into the domain (Starling, 1896).

The following assumptions were made for this simulation:

- All independent parameters were constant across each domain with that quoted from the current literature (see Table 3.1).
- Initial flow velocities in the lymphatic and blood vessels domains were quoted from the current literature (see Table 3.1).
- The lymphatic vessel osmotic pressure was the same as the interstitial osmotic pressure.
- The osmotic reflection coefficient is the same for each vessel and constant across their domains.
- Pressure downstream of the lymphatic vessels is maintained at -1200 Pa.
- The pressure at the boundary of the interstitium domain remained constant.

Model simulation times, error values, and computer memory usage for all simulations in this study is given in Appendix E. The mass balance (M^{in}- M^{out}) of the inlet and outlet boundaries was smaller than the simulation error in all simulations presented in this Chapter.

An illustration of the simulation results was created in COMSOL and it is shown in Figure 3.2a. The numerical simulation result for the normalised fluid flux across the interstitium, lymphatic and blood vessel domains $\boldsymbol{Q}_{norm}$, $\boldsymbol{Q}^{L}_{norm}$ and $\boldsymbol{Q}^{B}_{norm}$(µl.m^{-1}.min^{-1}) with changing interstitial osmotic pressure is shown in Figure 3.2b and at physiological interstitial osmotic pressure in Figure 3.2c . The change in mean interstitial, lymphatic and blood vessel domain pressure (from baseline), P, P^L and P^B (Pa), and mean lymphatic and blood domain fluid flow velocity, $\boldsymbol{u}^L$ and $\boldsymbol{u}^B$ (mm.s^{-1}) is shown in Figure 3.2d and Figure 3.2e respectivly.

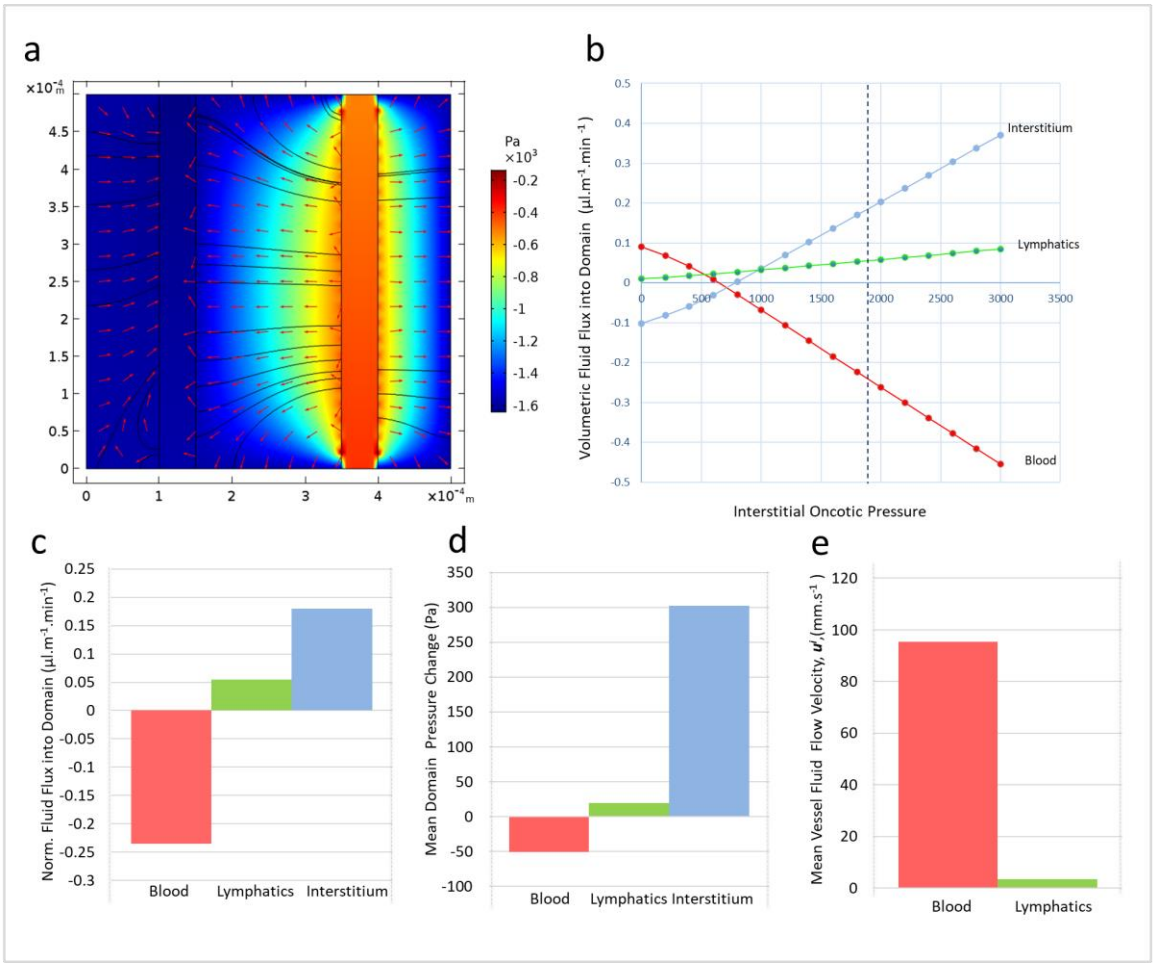

Figure 3.2 Model Simulation Results Using a 2D Geometry. **a** An image of the simulation result for pressure (Pa) of the model design with streamlines shown in black, and red arrows showing the direction of fluid flow. The geometry is identical to that shown in Figure 3.1. **b** The change in fluid flux into each domain with increasing interstitial oncotic pressure. Black dotted line represents the literature quote value for interstitial osmotic pressure (1862 Pa) in the human lung. **c** The normalised fluid flux into each domain. **d** The change in domain pressure from baseline. **e** Mean vessel flow velocity in domain. **c, d** and **e** are results given when the interstitial osmotic pressure = 1862 Pa.

The model simulation result of the 2D idealised lung geometry confirmed convergence was achieved thus the model design was well-conditioned. The illustration of the simulation showed the direction of fluid flow through the walls of the blood vessel, through the interstitial space and into the lymphatic vessel (see Figure 3.2a). This direction of flow through the geometry was confirmed in the numerical results with both the domain fluid flux and pressure change (see Figure 3.2 c and d). Fluid flow velocity values within the vessels confirmed flow was maintained, but the average blood flow velocity was 2x, and lymph flow velocity approximately 6x, that which was expected from the literature (Fujiwara *et al.*, 2014; Guyton & Hall, 2010). At this stage of the model development this discrepancy was not a concern as a non-realistic and idealised 2D geometry was used.

Increasing the interstitial osmotic pressure from the literature quoted value showed more fluid leaving the blood vessel and entering the lymphatic vessels at equilibrium (see Figure 3.2b). This pattern was reversed when the interstitial osmotic pressure was reduced, consistent with what would be expected from Starling's hypothesis (Starling, 1896). This result confirmed the success of the model design for the 2D lung geometry.

3.2 3D Modelling of Lymph Flow in Peripheral Human Lung Tissue

3.2.1 Image Processing for 3D Lung Geometries

The main modelling study in this thesis (Chapter 6) considers how changes in the 3D lung geometry impacts the results of the mathematical model simulation. The volumes of interest (VOIs) of the human lung samples, as created in Chapter 2, section 2.4.1, were therefore used as input geometries for 3D model simulation. The VOI sample size, and selection methods are given in Chapter 6.

Within each VOI chosen for simulation, separate binary images were created for each of the individually segmented features: lymphatics; blood vessels and interstitial tissue. The VOIs of the three features were scaled up in size by a factor of 3 in each orientation so that one voxel was then represented by nine voxels. This scaling step did not alter the geometry of the VOI but enabled finer subsequent filtering steps. A 1 voxel 3D median filter was then applied to each image. This filter assigns each voxel's value by the median average of its surrounding 8 voxels' values to preserve edge information while removing noise. Any lymphatic vessel or blood vessel that did not exit the VOI on the surface of at least two external VOI boundaries were removed. To avoid voxel-overlap of segmented features when the images were later combined in the meshing process, the lymphatic vessel image was subtracted from the blood vessel image using the image calculator tool in Fiji. The resulting blood vessel image and the lymphatic vessel image were then subtracted from the interstitial tissue image (see

Figure 3.3). All processed images were then exported as 3D images in a raw format for finite element meshing.

An example of the above image processing steps is shown in

Figure 3.3.

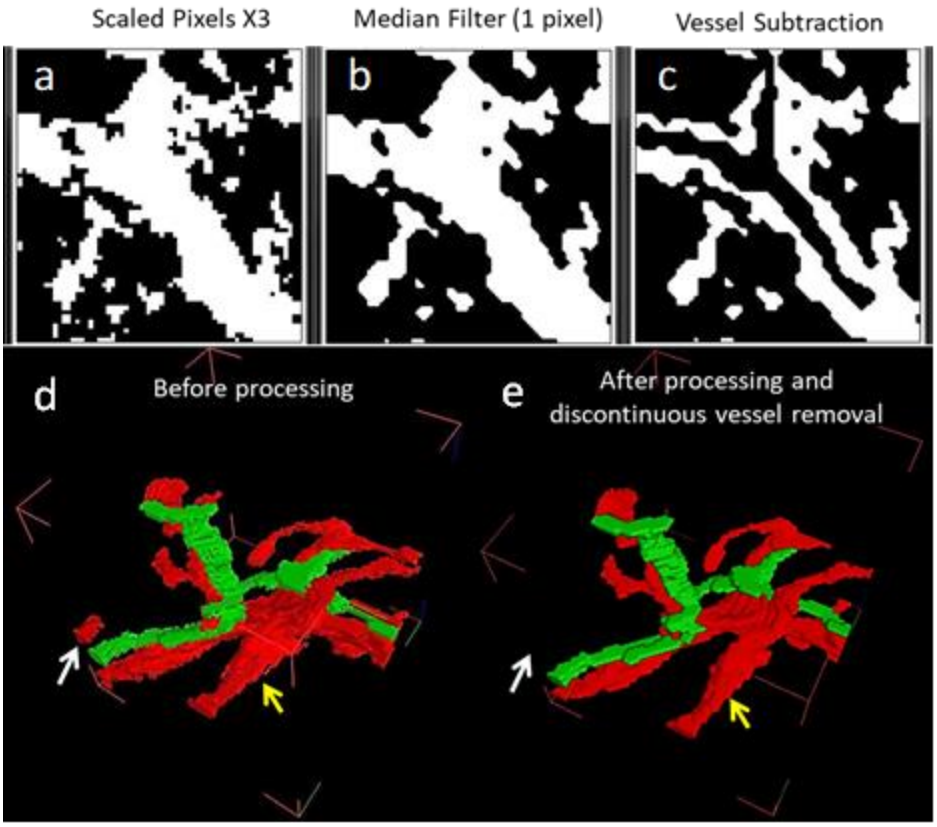

Figure 3.3 Image Processing of VOI Geometries for Modelling. **a** An X-Y section of a VOI tissue geometry in Fiji after it has been scaled by a factor of three. **b** An X-Y section of the same tissue geometry as shown in panel **a** after a median filter was applied. **c** An X-Y section of the same tissue geometry as shown in panel **b** after subtraction of the vessel geometries of the same VOI. **d** Volume rendering of the vessels in the VOI before any processing. **e**. Volume rendering of the vessels in the VOI after all processing (yellow arrow shows example) including removal of discontinuous vessel structures (white arrow shows example).

Image editing, processing and smoothing were necessary steps for the successful generation of a FE mesh. These processes also mitigate small errors that may have occurred through image segmentation, yet it should be noted that it does not eliminate them. Scaling up the number of voxels in each image before applying the median filtering step allowed filtering to be three times finer than it would be if applied to the original image thus minimising alterations to the original data. The volume of discontinuous vessel data removed was minimal and unlikely to be significant.

3.2.2 Alteration of Boundary Condition Placement for the 3D Geometries

In the 3D VOI geometries, there were often more than two boundaries at the VOI surfaces for both the blood and lymphatic the vessel domains. As lymph drainage and blood flow are thought to occur predominantly in the direction of the pleural surface (Negrini & Passi, 2007; Leak & Jamuar, 1983; Fleischner, 1967; Erdmann *et al.*, 1975), the vessel boundaries positioned on the 3 VOIs faces furthest away from the pleural surface were selected as inlet boundaries. The inlet

boundaries for the lymphatic and blood vessel domains were modelled as stated in equations 3.5 and 3.7 respectively. The output conditions for the blood and lymphatic vessels were applied to the remaining external boundaries on the 3 VOI faces closest to the pleural surface and modelled as stated in equations 3.6 and 3.8 respectively.

There was no accounting for the alveolar walls in the 2D model which are present in the 3D geometry. The interstitial pressure boundary condition (equation 3.4) as applied to the external VOI boundaries was therefore extended to these boundaries.

The 3D model simulations were performed in the same COMSOL software package as the 2D simulations but on two high powered Linux operating systems. The first, an AMD Opteron™ Processor 6344 (2x 12core CPU and 500 GB of RAM) and the second, an AMD Opteron™ Processor 6380 (4x 16core CPU and 1 TB of RAM).

3.2.3 Numerical Output of Model for 3D Geometries

All geometry VOI variations such as tissue volume and lymphatic surface are taken into account when simulating the model within the VOI. Therefore, as long as the VOI size-refinement studies are performed initially (see section 2.4.1), the lymphatic patterning is captured within the sample, there is no need to normalise the results for the comparison of the VOI geometries. Despite this, when comparing VOI of different sizes, it is sometimes easier to normalise results for ease of interpretation.

Therefore, the numerical outputs of the model simulation on the 3D VOI geometries were the following:

- Mean interstitial, lymphatic and blood vessel domain pressure change from baseline (input pressures (see Table 3.1)), P, P^L and P^B (Pa).
- Mean lymphatic and blood domain fluid flow velocity, $\boldsymbol{u}^L$ and $\boldsymbol{u}^B$ (mm.s^{-1}).
- Total fluid flux into the interstitium, lymphatic and blood vessel domain $\boldsymbol{Q}_{\text{Total}}$, $\boldsymbol{Q}^{\boldsymbol{L}}_{\text{Total}}$ and $\boldsymbol{Q}^{\boldsymbol{B}}_{\text{Total}}$ (µl.min^{-1}). This is calculated by integrating along the lymphatic wall or blood vessel wall or, for the interstitium, by integrating along surface area of both vessel walls.
- Fluid flux into the lymphatic and blood vessel domain integrated along the boundary each vessel wall then normalised by the surface area of the boundary $\boldsymbol{Q}^{\boldsymbol{L}}_{\boldsymbol{norm}}$ and $\boldsymbol{Q}^{\boldsymbol{B}}_{\boldsymbol{norm}}$ (µl.m^2.min^{-1})**.**
- Total lymphatic and blood volumetric fluid flow integrated within the volume of each domain, V^{L}_{Total} and V^{B}_{Total} (ml.min^{-1}).
- Lymphatic and blood volumetric fluid flow integrated within each domain then normalised by the volume of the domain, V^{L}_{norm} and V^{B}_{norm} (ml.mm^{-3}.min^{-1}).

- Inlet mass flow (blood vessel inlet) integrated across the boundary surface area, M^{In} ($kg.m^2.s^{-1}$).
- Outlet mass flow (lymphatic outlet, VOI external boundaries and alveolar walls) integrated across the boundaries' surface area, M^{out} ($kg.m^2.s^{-1}$).

3.2.4 3D Mesh Creation and Mesh Refinement Study

Scan IP (Simpleware, Exeter, UK) was used to make a mask of the edited lymphatic, blood vessel and interstitial tissue images of the 3D VOIs. Using the "+FE-Free "algorithm, a high-quality 3D mesh volume of all three masks assembled together was created and exported in a COMSOL file format.

Although expensive as a commercial software, using ScanIP as meshing software is recommended for high throughput image-based mathematical modelling. The "FE-Free" meshing algorithm can significantly reduce mesh size while still preserving complexity around small features, a unique feature of this software. Mesh size reduction was essential in reducing the memory required, and the time needed to create and simulate the models.

A mesh refinement study was undertaken to identify the ScanIP mesh-size setting to be used on the VOIs image data. This study identified the optimal mesh size required to simulate repeatable model results in a realistic time frame. If the mesh was too coarse, the simulation results would not have been accurate and, in some cases, resulted in simulation failure. If the mesh was too fine, the time taken, and the computing power needed to reach a solution of model would have been greater than necessary. This increase computational load could have also been terminal for the model simulation.

An intralobular VOI taken from a subvolume of a control lung sample was used for the mesh refinement study. The µCT voxel resolution of this subvolume was the poorest acquired in the study (13.2 µm). Therefore, as the mesh settings in ScanIP are based on the input voxel resolution, the setting that produced the most suitable mesh size for this VOI would suffice for the other VOIs in the study. It was assumed the time taken to repeat the mesh refinement study for each VOI used for modelling would have been greater than the time saved in model simulation time.

The VOI underwent image editing and processing (section 3.2.2) and was loaded into Scan IP and meshed using 6 different setting for mesh coarseness: -50(most coarse), -26, -12, 0, +12, +26(most fine). In this (13.2 µm voxel resolution) VOI geometry, the tetrahedral element number for the-50 setting = $0.9x10^6$ and for +26 setting = $15.2x10^6$.

The meshed volume files were used as the input geometry to resolve the model as described in sections 3.1.2-3.1.6 in COMSOL with the boundary placement variants implemented for the 3D geometry as described in section 3.2.2. The general assumptions for simulating this model were identical to those detailed for the 2D simulation as described in section 3.1.7.

The normalised fluid flux across lymphatic and blood vessel wall, $\boldsymbol{Q}^{L}_{Norm}$ and $\boldsymbol{Q}^{B}_{Norm}$ ($\mu l.m^{2}.min^{-1}$) and the interstitial pressure, P (Pa) were used to determine the minimum mesh size, thus coarseness setting, to be used for the ScanIP meshing process. A change of less than 5% in the model simulation result suggested the mesh coarseness setting of the previous geometry would be sufficient to produce reliable results. This is a reasonable assumption as the model is predicting physiological measurements.

When resolving for interstitial pressure, a ScanIP coarseness setting of -50 (~1 million elements) was sufficient for the VOI geometry as there was no added benefit from having a finer mesh (result change from -50 to -26 = 1.3%).To resolve the integrated fluid flux across lymphatic and blood vessel wall, $\boldsymbol{Q}^{L}_{Total}$ and $\boldsymbol{Q}^{B}_{Total}$ ($\mu l.min^{-1}$), a ScanIP coarseness setting of 0 (~5.5 million elements) would be sufficient (results change from 0 to +12=3.2% and 1.9% respectively). See Figure 3.4 for full results. The +26 coarseness geometry was not simulated as the change in results was already below threshold.

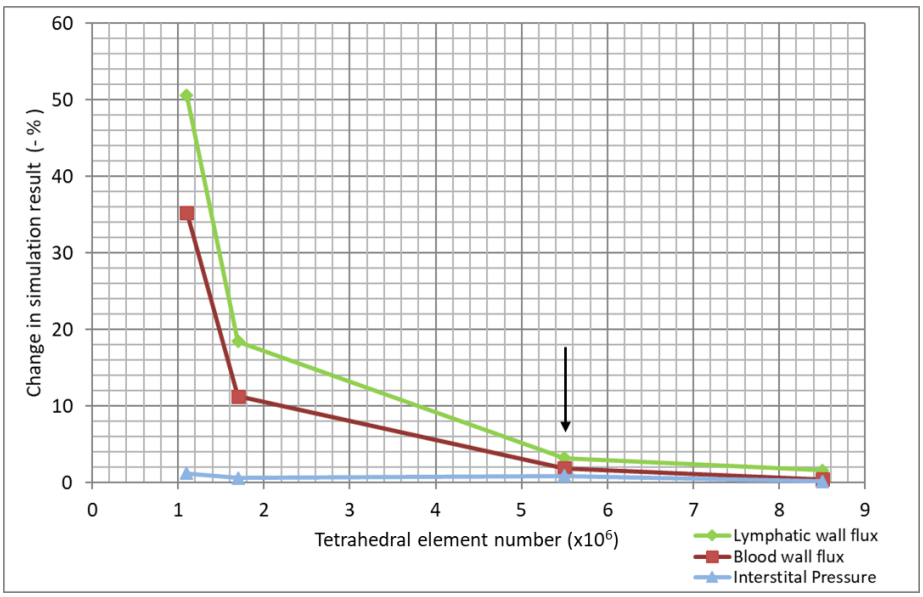

Figure 3.4 Results of the Mesh Refinement Study. The change (given as a percentage) in the result of the fluid flux across the lymphatic vessel wall (green), the fluid flux across the blood vessel wall (red), and the average pressure in the pulmonary interstitium (blue) with increasing tetrahedral element number (reduction in mesh coarseness). The black arrow points to the first ScanIP mesh coarseness setting used (0) where the change in all the results were <5%.

3.2.5 Model Simulation Result on a Real 3D Lung Geometry

An illustration of the simulation result of the mathematical model simulated on the optimally meshed intralobular VOI geometry is shown in Figure 3.5. Figure 3.6a. shows a comparison of the numerical simulation result between the 2D (i) and 3D (ii) geometry for the normalised fluid flux across the interstitium, lymphatic and blood vessel domains $\boldsymbol{Q}_{norm}$, $\boldsymbol{Q}^{L}_{norm}$ and $\boldsymbol{Q}^{B}_{norm}$($\mu l.m^{-1or-2}.min^{-1}$) at physiological interstitial osmotic pressure. Figure 3.6b and Figure 3.6c shows a comparison of the numerical simulation result between the 2D(i) and 3D (ii) geometry for the change in the mean interstitial, lymphatic and blood vessel domain pressure (from baseline), P, P^{L} and P^{B} (Pa), and mean lymphatic and blood domain fluid flow velocity, $\boldsymbol{u}^{L}$ and $\boldsymbol{u}^{B}$ ($mm.s^{-1}$) respectivly.

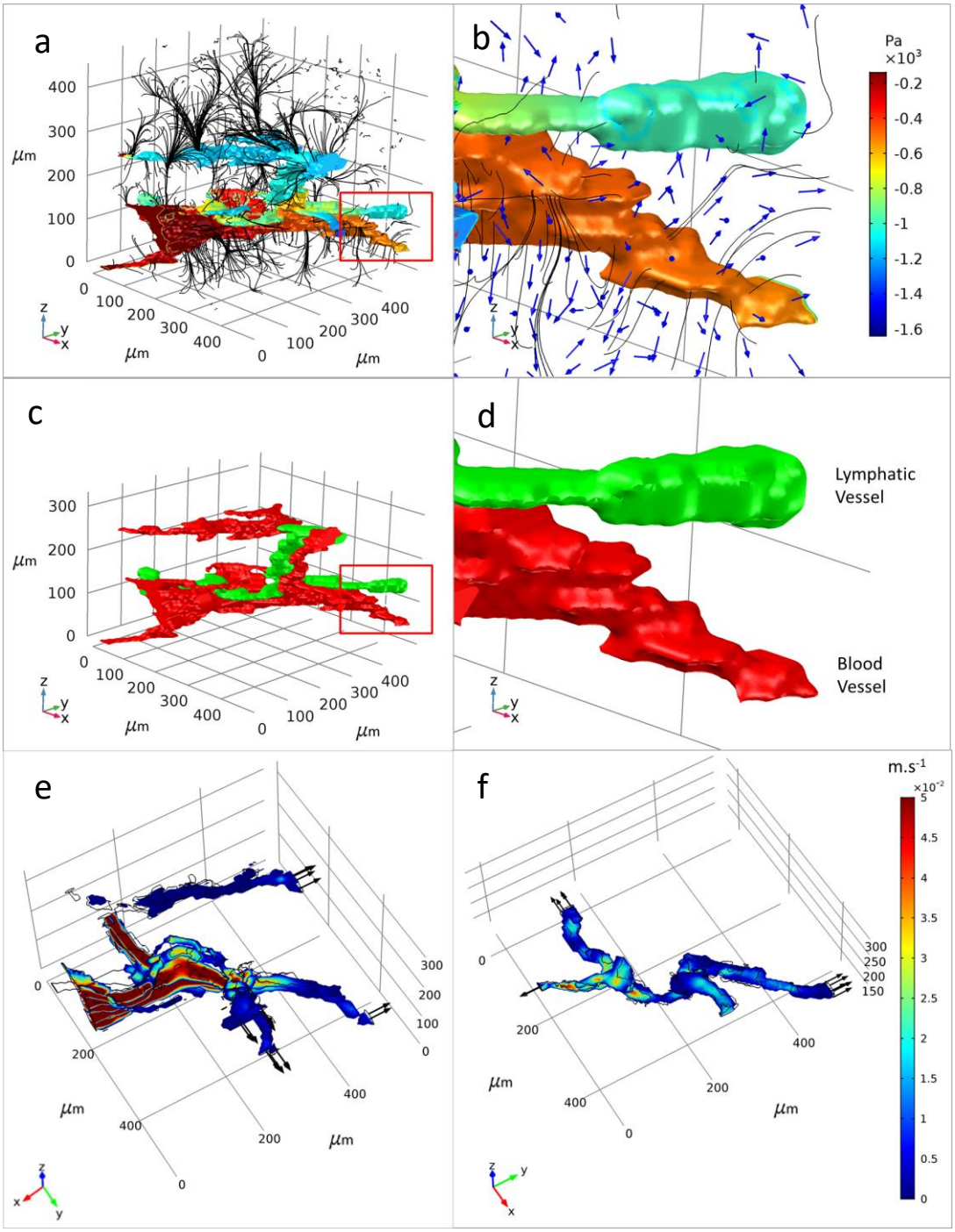

Figure 3.5 **Visual Simulation Result of Model in a Real 3D Lung Geometry. a** The pressure (Pa) result of model simulation in a whole 3D lung geometry. Darcy's flow streamlines are shown in black and normalised directional arrows in blue. Interstitial pressure result omitted for visualisation purposes. **b** A zoomed in area of the image in panel **a**. Pressure legend identical in panel **a** and **b**. **c** The geometry of panel **a**. **d** The geometry of panel **b**. Blood vessel = red, lymphatic vessel = green. **e** Velocity result of model simulation in the blood vessel. Ten cross-sectional slices are shown. Normalized directional arrows are shown in black. **f** same presentation as in panel **e** but the results are shown for the lymphatic vessel. Velocity legend identical in **e** and **f.**

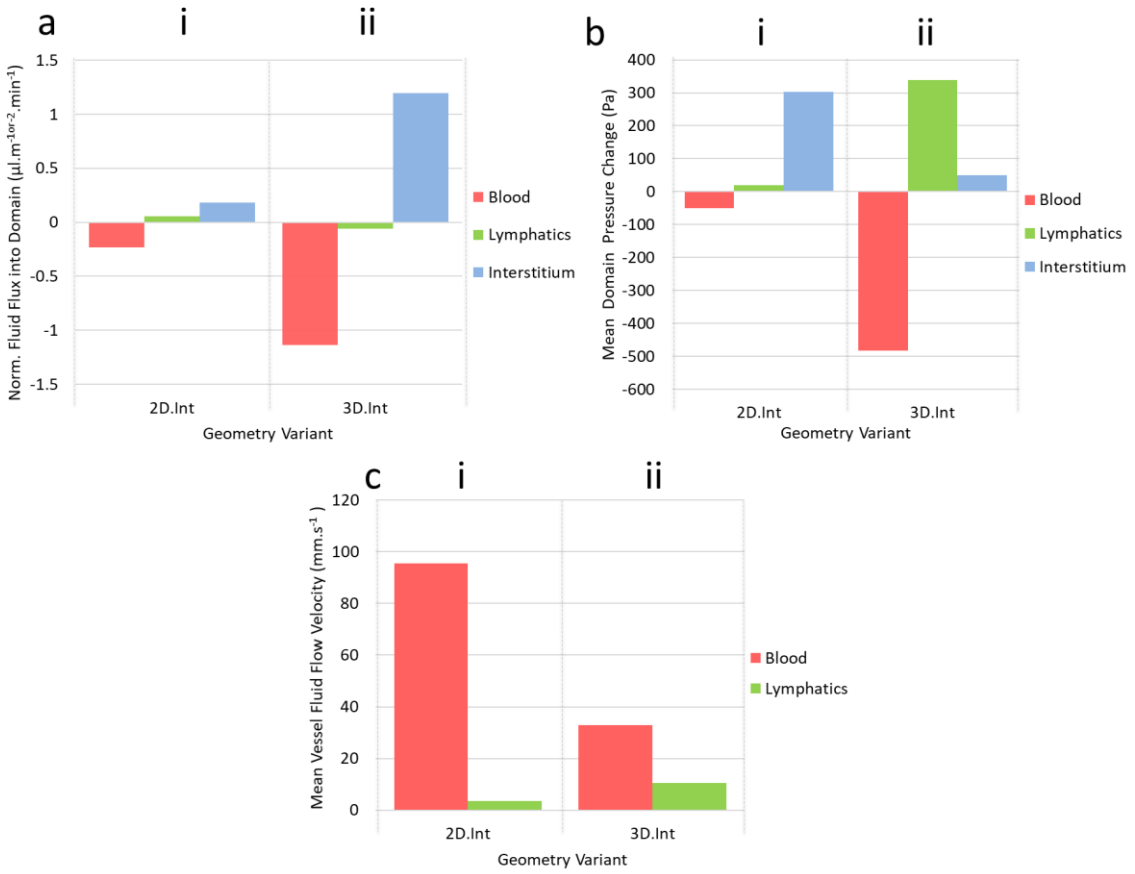

Figure 3.6 Comparison of Model Simulation Results when Using an Idealised 2D and a Real 3D Lung Geometry. Comparison of the numerical simulation result between the 2D (**i**) and 3D (**ii**) geometry for: **a** the normalised fluid flux into the interstitium, lymphatic and blood vessel domains; **b** the change in the mean interstitial, lymphatic and blood vessel domain pressure (from baseline); **c** mean lymphatic and blood domain fluid flow velocity.

As with the 2D geometry, model simulation on the 3D real lung geometry showed fluid generally moved out of the higher pressured blood vessel walls, travelled through the interstitial tissue and entered the lymphatic vessel (see Figure 3.5a and b). Full patent flow was apparent through the vessel domains with fluid exiting from the VOI in all output surface boundaries (see Figure 3.5 e and f).

Compared to the 2D simulation result, there was great variation in pressure and therefore fluid flux down the blood and lymphatic vessel length. Within the complex 3D geometry, interpreting the visual simulation result was therefore difficult. Indeed, the numerical results of the 3D model actually showed the lymphatic pressure increases substantially in the 3D geometry, resulting in an outward rather than inward movement of fluid across the lymphatic vessel wall (See Figure 3.6a and b). Also, the numerical results showed the average blood vessel pressure drop, and outward fluid flux was greater in the 3D geometry compared to the result from the 2D geometry (see Figure 3.6 a and b). These observations were a result of the higher dimension and complexity of the 3D geometry.

The interstitial domain was proportionally larger than both vessels in the 3D geometry compared to the 2D geometry, thus the pressure changes in interstitial domain was not as heavily influenced by the vessel wall flux. The pressure gradient between the blood vessel and interstitium was therefore larger in the 3D geometry compared to the 2D geometry, thus there was a greater outward fluid flux from the blood vessel resulting in a fall in average domain pressure. The reduction in pressure within the blood vessel resulted in the blood flow velocity dropping nearer to the literature estimations (35 $mm.s^{-1}$, (Guyton & Hall, 2010)).

In the 3D geometry, the lymphatic vessel was smaller and positioned closer to the blood vessel compared to the 2D geometry. The fluid entered the lymphatic vessel from the blood-vessel side and as the lymphatic vessel is small, pressure increased quickly compared to the 2D geometry. This high pressure caused an increase in vessel flow velocity compared to the 2D geometry result (20x literature quote levels). As the interstitial pressure remained low as explained above, the pressure gradient that drove fluid flux between the lymphatic vessel and the interstitium reversed. In reality, this observation would not be expected to occur as the primary valve system (as discussed in Chapter 2, section 1.1.4) is generally accepted to function to prevent this event.

3.2.6 Alterations to the Mathematical Model (Model 2)

To prevent retrograde flow of lymph from the lymphatic vessels into the tissue (as described in section 3.2.5), on the lymphatic wall-tissue boundary, a uni-directional condition was applied to equation 3.3 so that if the righthand side of the equation is negative, $K^L=0$. This local condition numerically models the primary valve system as discussed in Chapter 1, section 1.1.4.

Also, the interstitial pressure constraint on the VOI boundaries (equation 3.4) artificially forced a lower pressure at these boundaries than may be the case. To have less of an impact on localised and averaged domain pressure results, and consequently fluid flow, the pressure boundary condition (equation 3.4) at the external VOI boundaries was therefore changed to the following "no flux" condition:

$$-\boldsymbol{n} \cdot \rho \boldsymbol{u} = 0 \qquad \textbf{(3.9)}$$

where, *n* is the normal boundary vector pointing out of the interstitium domain, ***u*** is the interstitial lymph fluid velocity, and ρ is the mass density of the fluid.

Please note, the pressure condition (equation 3.4) was still maintained on the alveolar wall surface boundaries. Mass flux at the alveolar surface boundary was therefore still included as a mass outlet, M^{out} ($kg.m^2.s^{-1}$), thus also used to confirm the mass balance of the model. This is an important feature to retain in the model as, although not directly calculated, it enables the

inference of alveolar fluid accumulation, an important indicator of lung pathology. At steady state, any net fluid flux into the interstitium is also lost through the alveolar walls. Therefore, the total fluid flux into the interstitium, $\boldsymbol{Q}_{\text{Total}}$ (µl.min^{-1}) (described in section 3.2.3) will be the model's output to infer this pathology.

To be able to compare the inferred rate of alveolar accumulation between different VOIs the volume of lung tissue in each VOI must be considered. Therefore the following model output will be used when comparing different VOIs in Chapter 6:

- Fluid flux across the alveolar wall normalised by the volume of interstitial domain $\boldsymbol{Q}^{\boldsymbol{A}}_{\boldsymbol{norm}}$,(µl.m^{-3}.min^{-1}).

A summary of the changes from the original model to model 2 design using a 2D illustration of the 3D geometry is given in Figure 3.7.

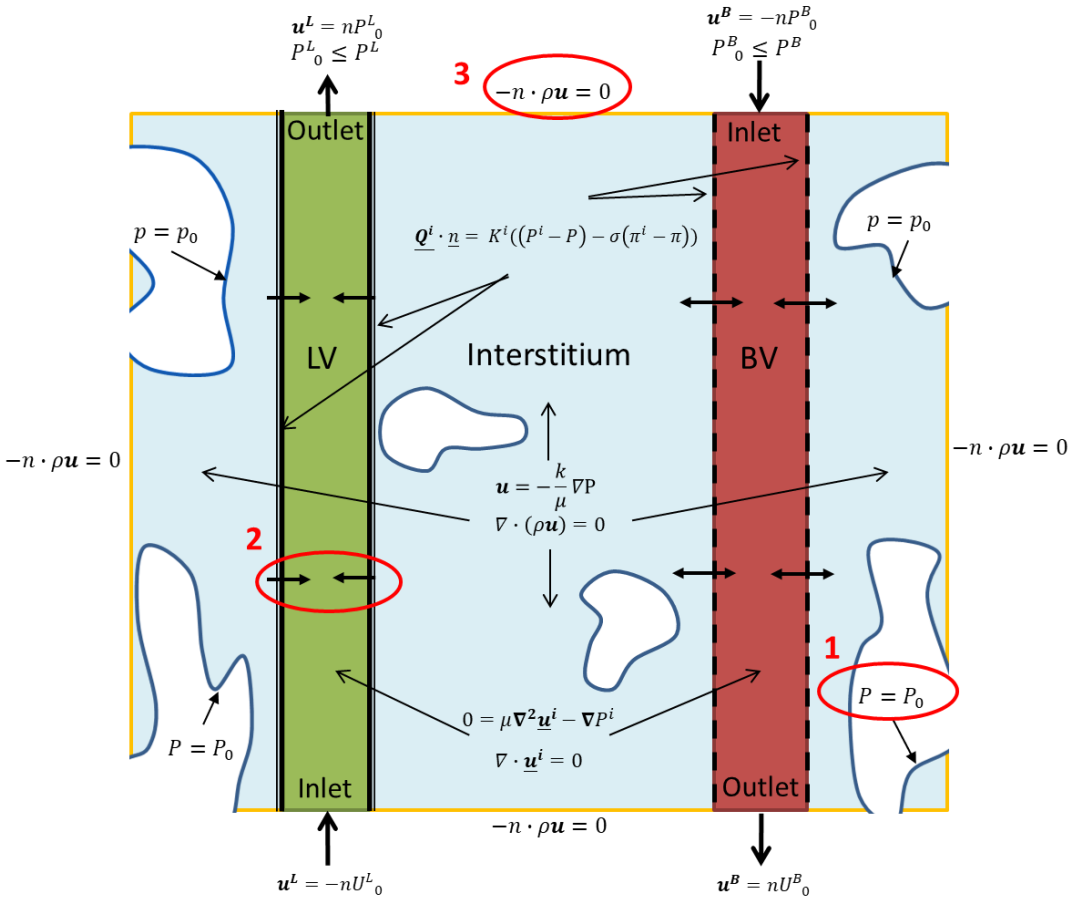

Figure 3.7 Illustrative Schematic of Model 2 for Pulmonary Fluid Flow. The blood vessel is shown in red (BV), the lymphatic vessel in green (LV) and the interstitial tissue in blue. This geometry is a 2D representation of the 3D geometry. Flow through the interstitium is described by Darcy's Law (equations 3.1) and flow in the vessels are described by Stokes' flow (equations 3.2) with defined inlet and outlet conditions (equations 3.5-3.8). The dotted lines represent a flux boundary condition described by the Starling's Equation (3.3) with an added unidirectional constraint (solid line) on the lymphatic vessel wall only. The interstitial pressure boundary condition (equation 3.4) was applied to the alveolar walls (blue boundaries) The model simulation

constraints are shown by orange boundaries where the new no flux boundary condition (equation 3.9) was applied. All symbol definitions and equations are given in the text. The red circles highlight the main differences from Model 1 to Model 2.

3.2.7 Simulation of Model 2 on a Real 3D Geometry

Model 2 was then simulated within the same 3D intralobular VOI geometry mesh, as used in section 3.2.5. The same assumptions were made for this simulation as detailed in section 3.1.7, with the exception that no fluid leaves the lymphatic vessel domain except and the outlet boundaries and the pressure at the external boundary of the VOI no longer remained constant.

Figure 3.8 Simulation Results of the Two Models Simulated in Different Dimensions. shows the numerical simulation result of model 2 of the 3D (iii) geometry directly compared to the orginal model design simulations of the 2D (i) and 3D (ii) geometry (as shown in Figure 3.6). Figure 3.8 Simulation Results of the Two Models Simulated in Different Dimensions. a shows the normalised fluid flux across the interstitium, lymphatic and blood vessel domains $\boldsymbol{Q}_{norm}$, $\boldsymbol{Q}^{L}_{norm}$ and $\boldsymbol{Q}^{B}_{norm}$($\mu l.m^{-1or-2}.min^{-1}$) at physiological interstitial osmotic pressure. Figure 3.8 Simulation Results of the Two Models Simulated in Different Dimensions.b and Figure 3.8 Simulation Results of the Two Models Simulated in Different Dimensions.c shows the change in mean interstitial, lymphatic and blood vessel domain pressure (from baseline), P, P^{L} and P^{B} (Pa), and mean lymphatic and blood domain fluid flow velocity, $\boldsymbol{u}^{L}$ and $\boldsymbol{u}^{B}$ ($mm.s^{-1}$) results respectively.

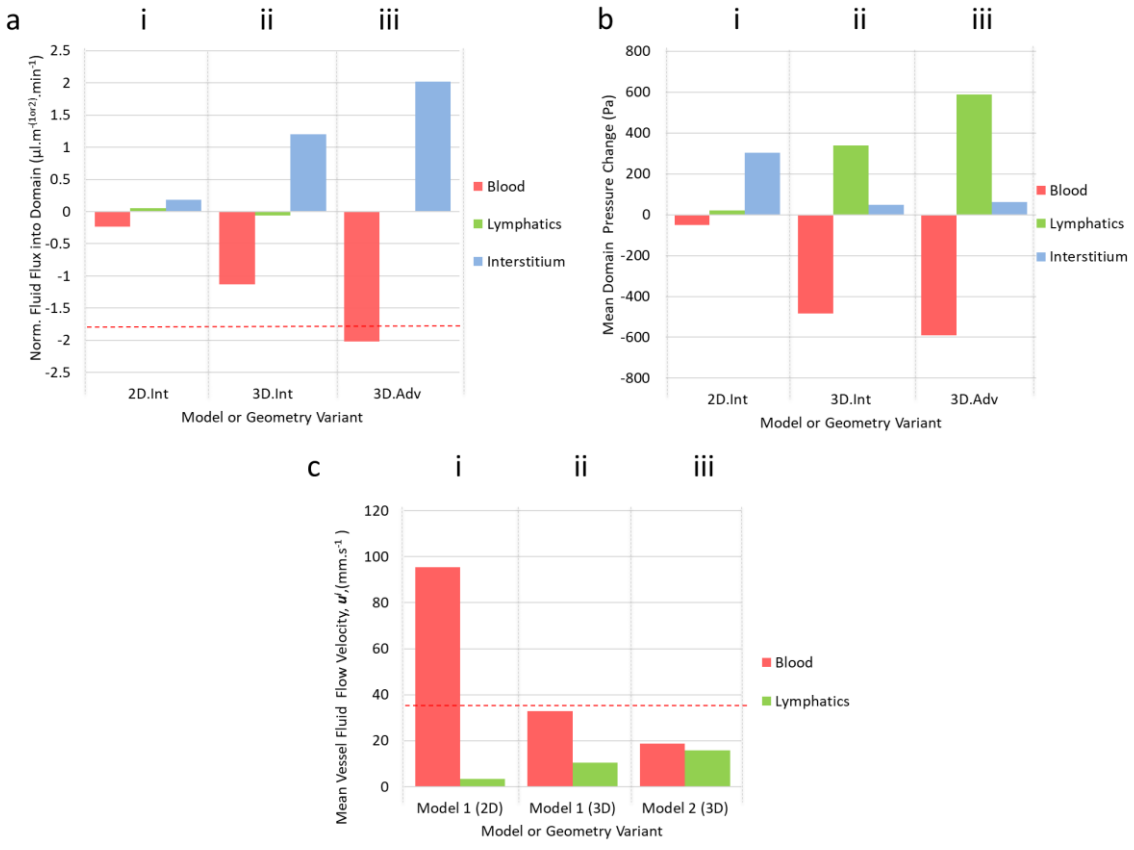

Figure 3.8 Simulation Results of the Two Models Simulated in Different Dimensions. Comparison of the numerical simulation result of model 1 used on the 2D (**i**) and 3D (**ii**) geometry, and model 2 on the 3D geometry (**iii**) for: **a** the normalised fluid flux into the interstitium, lymphatic and blood vessel domains; **b** the change in the mean interstitial, lymphatic and blood vessel domain pressure (from baseline); **c** mean lymphatic and blood domain fluid flow velocity. The dotted red lines show the expected values for the blood vessel measurements based on current literature.

The inclusion of the primary lymphatic valve (model 2) changed the simulation results as expected. There was no outward fluid flux across the vessel wall at equilibrium (see Figure 3.8iii). This resulted in an increase in lymphatic vessel domain pressure from the baseline and an increased lymph flow velocity compared to the 3D simulation results of model 1(see Figure 3.8 b and c).

As fluid could not leave the lymphatic vessel; the interstitial pressure surrounding the lymphatics was only being influenced by the outward blood vessel flux. The blood flux was therefore greater than that seen in the 3D result of model 1 (see Figure 3.8 b and c) now consistent with literature estimated capillary filtration rate of approximately 10 $ml.min^{-1}$ which equates to 1.65 $\mu l.m^{2}.min^{-1}$ in the lung (Brandis, 2020; Jones, 1968). As a result of a drop in pressure in the blood domain, the flow blood velocity in the 3D advance model was slower than seen in model 1, dropping to just over half that of the literature estimate of 35 $mm.s^{-1}$, (Guyton & Hall, 2010) (see Figure 3.8 c).

Figure 3.9 shows a 2D slice of the pressure result in the 3D real lung geometry simulated using both model 1 and model 2. The slice was randomly selected from those slices containing both a blood vessel and a lymphatic vessel. This illustration highlights the discontinuous pressure gradient between the lymphatic vessel lumen and surrounding interstitial tissue depicting the resultant primary valve effect in model 2. Figure 3.9 also demonstrates that the pressure constraint (equation 3.6) put on the VOI external boundaries may well have had an influence on the 3D result of model 1 and shows that once this condition was changed to a no flux condition (equation 3.9) (model 2) this effect is resolved.

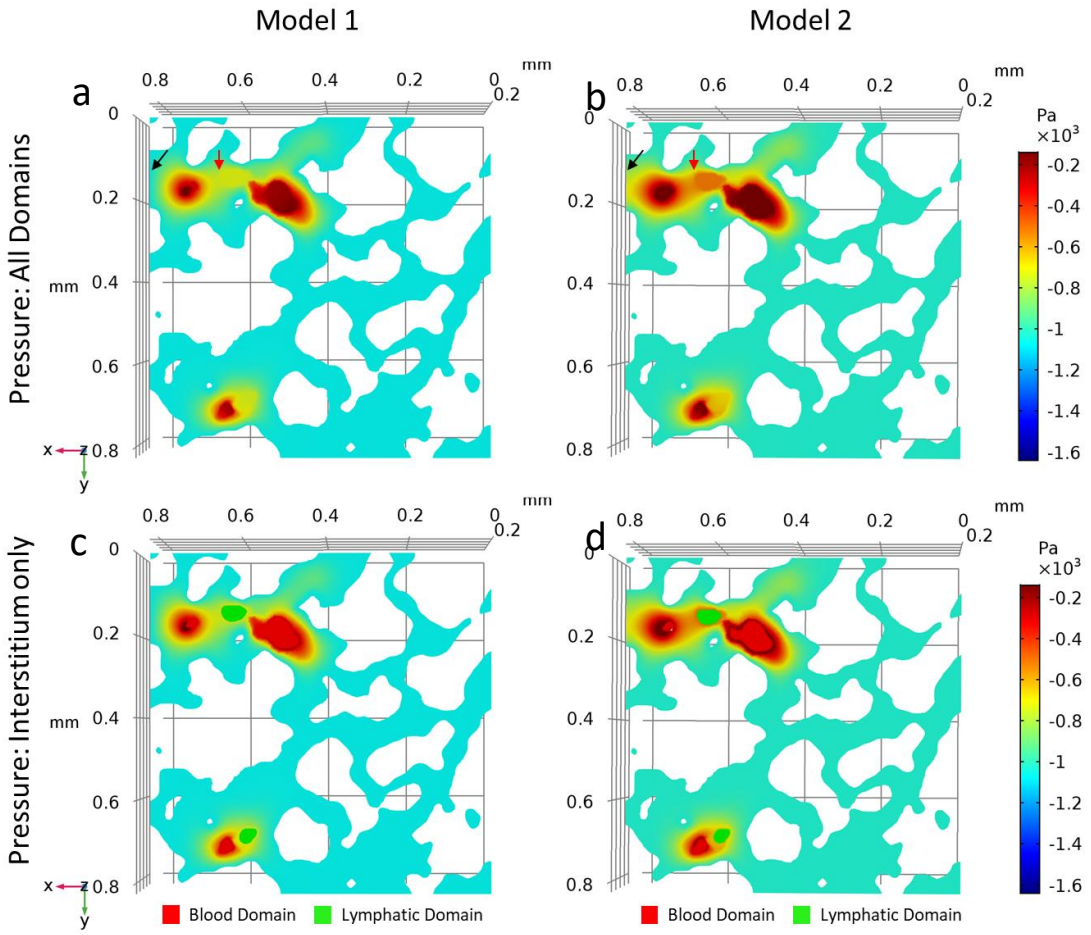

Figure 3.9 Difference in Visual 3D Simulation Result using Model 1 and Model 2. **a** An X-Y plane of the 3D pressure (Pa) simulation result of model 1 and **b** model 2. The black arrow indicates how the pressure boundary condition (equation 3.4) in model 1 creates artificially low pressure in areas of the interstitium where fluid movement and pressure changes should have no constraints. This effect is lost in model 2 simulation using the no flux boundary condition (equation 3.9). Red arrow shows how the luminal lymphatic pressure is equal to that of the surrounding interstitial tissue without a valve condition in place (model 1), where a higher pressure can be seen inside the lymphatic vessel when the primary valve is modelled (model 2). Panels **c** and **d** show the same as panels **a** and **b** respectively but have replaced the vessel result with a solid red(blood) and solid green (lymphatics) label.

3.3 Discussion

3.3.1 Results from 3D Simulation of Model Design in a Real Lung Geometry

In this example 3D geometry, the model prediction that the lymphatic vessels would leak without the valve system in place, suggested the rate of flow away from the vessel is not sufficient to keep the pressure below that of the interstitium. The modelled downstream negative pressure could have been inaccurate and if it was lower than the currently accepted value (-1200 Pa) lymphatic vessel leakage may not have occurred. However, as primary valves have been shown to exist in other organs, it is more likely they are required in the lung to prevent this backflow, and thus will

be kept in the model design. How downstream pressure gradients across the organ maybe be accounted for in the future is discussed in Chapter 6.

As only one VOI was used to develop the model, exact matches of simulation results to the literature were not expected, thus there were some discrepancies of the simulated results compared to literature values.

Firstly, the model 2 estimate for 3D blood vessel flow velocity was about half that which would be expected in the capillaries based on literature values (Guyton & Hall, 2010). This discrepancy is thought to be as a result of the blood vessel's geometry. The inputs of this geometry are of capillary values, and the blood vessel domain is known not to be representative of the smallest capillary beds as these were not possible to segment from the histology (see Chapter 2. Section 2.3.5). In two systems which have the same pressure and volumetric flow, a decrease in flow velocity would estimate the diameter of the vessel to be larger by the square root of the change. In this case, as the velocity is half that expected for a capillary size of ~8 μm, the diameter of the vessel geometry simulated can be estimated as being 11.3 μm. Indeed, an actual calculation of the blood vessel domain by Fiji confirmed the average segmented blood vessel diameter for this VOI is 11.6 μm.

As a result of this observation, using the literature defined capillary filtration coefficient and flow velocity values as model inputs may, therefore, be ill-advised. Although not preferred, it should be remembered that this model was designed to be used for assessing the geometry changes in the lung. It would not, therefore, be scientifically valid to change input parameters based on the geometry of each VOI. Although it was known that no capillaries were segmented in any VOI, capillary values were the only measured data available in the current literature. Although, as above, small arteriole/ venule input parameters could be estimated, for the comparison lung geometry in this body of work, the scientifically measured capillary values were used while being aware of this limitation. As image-based mathematical modelling is frequently used to estimate unmeasurable parameters, certain blood and lymphatic input parameters including pulmonary blood flow velocity were challenged to see how the pulmonary flow simulation results may be influenced. Chapter 7 details these experiments.

Secondly, using model 2 on the 3D geometry, there is a net positive change in interstitial pressure, inconsistent with the lungs being a "dry" organ based on a net negative pressured system (Schraufnagel, 2010). This model assumes that the blood vessel starting pressure is set at 2000 Pa as a result of pre-capillary sphincters being relaxed. Pre-capillary sphincters are cylindrical, smooth muscles located at the beginning of a capillary bed that are responsive to environmental stimuli. They can enter a tonic contractive state at low oxygen concentrations and restrict blood

flow to the capillary bed. These muscles are, therefore, are not always relaxed in the lung. The effect of closing these sphincters on the model simulation results and this apparent error in the simulation results is also addressed in this thesis, with the results given in Chapter 7.

Finally, the model 2 estimate for the 3D lymph flow velocity was 30x greater than that of the cutaneous lymphatic flow rate of 0.5 mm/s experimentally measured in the human skin (Fujiwara *et al.*, 2014). As no experimental data exists measuring the lymphatic flow velocities at the microlymphatic level in the lung, it is difficult to comment on the accuracy of this result. In higher vessels, such as the lymphatic ducts, the flow has been measured as increasing by 90x baseline levels in extreme circumstances (Taylor, 1981). As the VOI being modelled is in a region of the lung where pressures would be expected to be at the most extreme due to alveolar space filling, and the pre-capillary sphincters modelled as being open, it is not beyond reason for this flow velocity to be accurate.

3.3.2 Model Limitations and Future Developments

Despite the design of model 2 simulating pulmonary fluid flow as expected, with the explained exceptions mentioned above, the model still has several limitations.

The lung capillary bed was modelled as a porous media domain within the interstitial tissue by Darcy's law. This assumption has been seen in non-imaged based models of the lung and although not perfect; it is argued that the model is still representative as long as values for interstitial tissue porosity are altered to take this into account (Erbertseder *et al.*, 2012). As the capillary beds are known to be extremely dense in the lung, this simplification is not anticipated to impact significantly on the model's accuracy; however, further analysis in the future is needed to confirm this.

Gravitational forces have been ignored in this system as, even with the knowledge of the pleural surface location, it was not possible to determine the direction of its influence on the geometry. It is anticipated that the gravitational influence on fluid flow across the whole lung would be great (Grotberg, 2011). If strategical sampling of the lung was possible at different heights, gravitational effects should be included in the model design. However, over the distance between the geometries of the VOIs being compared in this study, it is questionable whether these effects would be influential. The interstitial porosity was assumed constant throughout the geometry. In reality, the interstitial tissue is made up of large numbers of extracellular matrix proteins and glycoproteins. All of these are of varying density, arranged differently and retard fluid at differing rates. It is not clear what impact these tissue constituents have on fluid flux, but it may be important. Building upon this methodology, it will be possible to use the methods similar to

previous work carried out where a model for fluid flow within a mouse lymph node was created that considered the hydraulic conductivity to be dependent on the pixel brightness in the image of the interstitium (Cooper *et al.*, 2016).

It could only be assumed that the permeability of the blood and lymphatic vessel walls throughout each VOI is constant as no variation in wall thickness was apparent in the 3D images of the vasculature. Also, in this VOI, and all those in the intralobular VOI category (see Chapter 2, section 2.4.2, the blood vessels were not αSMA+, therefore, the permeability of smooth muscle was not considered. As above, to enable geometrical comparison, the model design must remain constant, therefore it must be assumed blood vessels in all VOI geometries compared do not contain smooth muscle.

No cellular components were taken into account when modelling flow in the blood and lymphatic vessel; however, this enables Stokes' flow to be suitable for use in this model. Using Stokes flow considerably reduces mathematical complexity within the vessel lumen. To encompass cellular components in an image-based mathematical model with realistic computational and time constraints, it is expected that only one vessel at a time could be simulated. The dynamic influence of cyclic strain on fluid flow has not been included in this model. The importance of stresses and strains on fluid movement a biological system should not be underestimated, especially in such an active system such as the lung. Variable compliance of the pulmonary interstitium and the lymphatic vessel wall has been well documented (Miserocchi *et al.*, 2001; Jakus *et al.*, 2014; Burrowes *et al.*, 2008) and would be a good direction for improvement of the current model in the future

Finally, in reality, fluid flow through the simulating domain (each lung VOI) should be continuous with the surrounding geometry. Although changing the VOI external boundary condition from a pressure constraint to a no-flux condition reduces artificial flow conditions near the VOI boundary, the model is still a closed and discrete system. This limitation still has knock on consequences when scaling up the model system to be representative of the organ as a whole.

To overcome this problem, some modellers aim to model the smallest repeating unit in a system, often denoted "a cell". Periodic boundary conditions can then be applied to these "cells" so that when they are assembled or "tiled" together, approximations of the function of the large system can be made. The smallest repeating unit in the lung is often accepted to be the secondary lobule. It would not be appropriate therefore to model each VOI as a repeating unit. However, methods for approximating the fluid flows through the secondary lobule to then enable periodic scaling techniques are discussed in Chapter 6.

Chapter 4 Characterising Lymphatic Populations in Peripheral Human Lung

4.1 Introduction

The lymphatic system is known to have different hierarchal populations of lymphatic vessels characterised by their size, but also by other structural features. For example, microlymphatics frequently have blind-ended endothelial structures, have variable diameters and are often closely associated with blood vessels while collecting lymphatics have lymphangion structures and secondary valves (Swartz, 2001; Pan *et al.*, 2010).

As reasoned in Chapter 2, section 2.4.4, four out of the six metrics used for quantitative assessment of the obtained lymphatic network were normalised by the lung tissue morphometry. This choice was made to enable direct statistical comparison between specific networks and to infer functionality. However, this assessment fails to portray certain structural characteristics of the lymphatic network, which are independent of their surrounding tissue.

This chapter, therefore, will present examples of the images obtained over the course of this study showing a complete lymphatic network in a subvolume, and also within the anatomically-located volumes of interest (VOIs), of the peripheral human lung. Observable features that link the networks to separate lymphatic populations will be qualitatively discussed.

Subsequently, a quantitive, statistical comparison of lymphatic structural morphology within all VOIs across all human lung samples will be made as detailed in chapter 2, section 2.4. The VOIs will only be grouped by their anatomical location in the secondary lobule. This assessment will ignore any intra-sample, inter-sample and clinically-linked variation, to give a global assessment of the abundance and morphometry of lymphatic networks across all ten lung samples. This analysis will demonstrate if the chosen strategy for quantitive lymphatic morphometry can identify lymphatic populations in the human lung.

Finally, individual lymphatic vessels will be studied to further aid categorisation of pulmonary lymphatic populations.

4.2 Specific and Additional Materials and Methods

4.2.1 Qualitative Assessment of Lymphatic Networks in Human Lung

The lymphatic vessel network, blood vessel network and airway network of the subvolumes of human lung were obtained as described in Chapter 2, sections 2.3.1-2.3.5. These structures were rendered in 3D using Amira 6.0 to visually assess the pulmonary lymphatic network and its associated pulmonary structures. The blood vessel and airway networks were removed for image presentation as they obscured a lot of the lymphatic network. The network instead was set within a semi-transparent µCT density map for structural context.

Henceforth, in the current and future chapters, any figure depicting volumetric data of a samples will be labelled with their sample ID number and categorised group in the bottom left hand corner of each sample.

Example VOIs located in the interlobular septa region (IS), the bronchovascular-bundle region (BVB), the sub-pleural region (SP) and the intralobular region (IL) were also rendered in Amira. In addition to the lymphatic network, the blood vessel and airway segmentation were included in these volume renderings. To enable these structures to be seen in context, the VOIs used were larger than the size-optimised VOIs used for morphometry assessment (see Chapter 2, section 2.4.1). In the IS VOI, observable projections from lymphatic vessel wall into its lumen in the µCT dataset were also segmented. Again, to make these structures visible, only the surface of the main vessel wall was segmented for visualisation purposes.

4.2.2 Quantitative Comparison of Anatomically Located Lymphatic Networks in Human Lung

Across all ten lung samples (20 subvolumes), 717 VOIs, size-optimised for each sample, were grouped only by their anatomical location (as described in Chapter 2, section 2.4.1 and 2.4.2 respectively). The proportions of the total VOI number that were categorised into each anatomical region were calculated. Also, the morphology of all the lymphatic networks sampled at each anatomical location were statistically compared against each other, using the methods laid out in Chapter 2, sections 2.4.3-2.4.5.

4.2.3 Statistical Analysis

All raw data processing and statistical analysis were performed in Graph Pad Prism (version 8.0).

All morphometric data used for grouped statistical analysis was of lognormal distribution permitting parametric statistical tests to be performed. The Shapiro-Wilk test confirmed this for every log transformed dataset.

When comparing the variance between lymphatic populations associated with different anatomical locations an ordinary one-way analysis of variance (ANOVA) was performed followed by a Tukey test which corrects for multiple comparisons.

On all graphs representing data upon which statistical analysis was performed, the error bars displayed are the mean value and 95% confidence interval of the mean. In addition, the P values are denoted as follows: P values> 0.05 are not given. Any comparison without a significance notation assume as not significant. P values ≤ 0.05 are represented as "*"; P values ≤ 0.01 are represented as "**"; P values ≤ 0.001 are represented as "***"; P values ≤ 0.0001 are represented as "****".

4.2.4 Characterising Individual Lymphatic Vessels as a Continuum

The 3D shape of individual lymphatic vessels within the example subvolume was analysed using the BoneJ thickness plugin. This plugin is a specialised implementation of Bob Dougherty's Local Thickness plugin, which defines the thickness at a coordinate within a structure as the diameter of the greatest sphere that fits within the structure at that coordinate (Dougherty & Kunzelmann, 2007). Using the segmented lymphatic data set from an example subvolume, acquired as detailed in Chapter 2 (section 2.3.1-2.3.5) the plugin calculated an 8-bit 3D thickness map of the individual lymphatic vessel structures in the whole subvolume.

This 3D lymphatic thickness map was eroded down to a single voxel trace of the lymphatic network using the BoneJ plugin: Skeletonise 3D (Ta-Chih & Kashyap, 1994). The voxels of this skeleton are furthest away from the background of the thickness map, therefore the value of the voxel is equivalent to the minimum diameter of the respective vessel. These values, taken from four of highest calibre vessels and four from the smallest calibre vessels, were plotted against distance along each vessels' length to assess the cylindricity the lymphatic vessels.

The direction of sampling was assessed by using the direction in which fluid is expected to flow along their length. Some vessels had valves which enabled the direction of fluid flow to be assumed, and those with no valves present, the direction of fluid flow was assumed to be towards the larger calibre vessels.

This assessment of individual lymphatic shape was performed on only one subvolume due to time constraints. Therefore, the results predominately assessed the usefulness of this quantitative

assessment method for future use. To gather as much information possible, the selection of the subvolume used was not, therefore, a randomised choice. The subvolume was taken from the lung sample that showed the greatest variability in its lymphatic network structure to understand individual lymphatic vessel structure in the most extreme example available in a quantitative form.

4.3 Results

4.3.1 Structural Heterogeneity of Pulmonary Lymphatics Networks

An example of a complete lymphatic network in a subvolume of human lung is shown in Figure 4.1. A subvolume taken from each lung sample is shown in Appendix F. Once visualised in 3D volumes, clear interconnected lymphatic networks were seen in each subvolume in all human lung tissue samples. There were a small number of isolated, or discontinuous vessel structures. Also, when observing the human pulmonary lymphatic network, great variability in the lymphatic vessels size and shape was apparent which appeared to be linked to an anatomical location in the secondary lobule (see Figure 4.1).

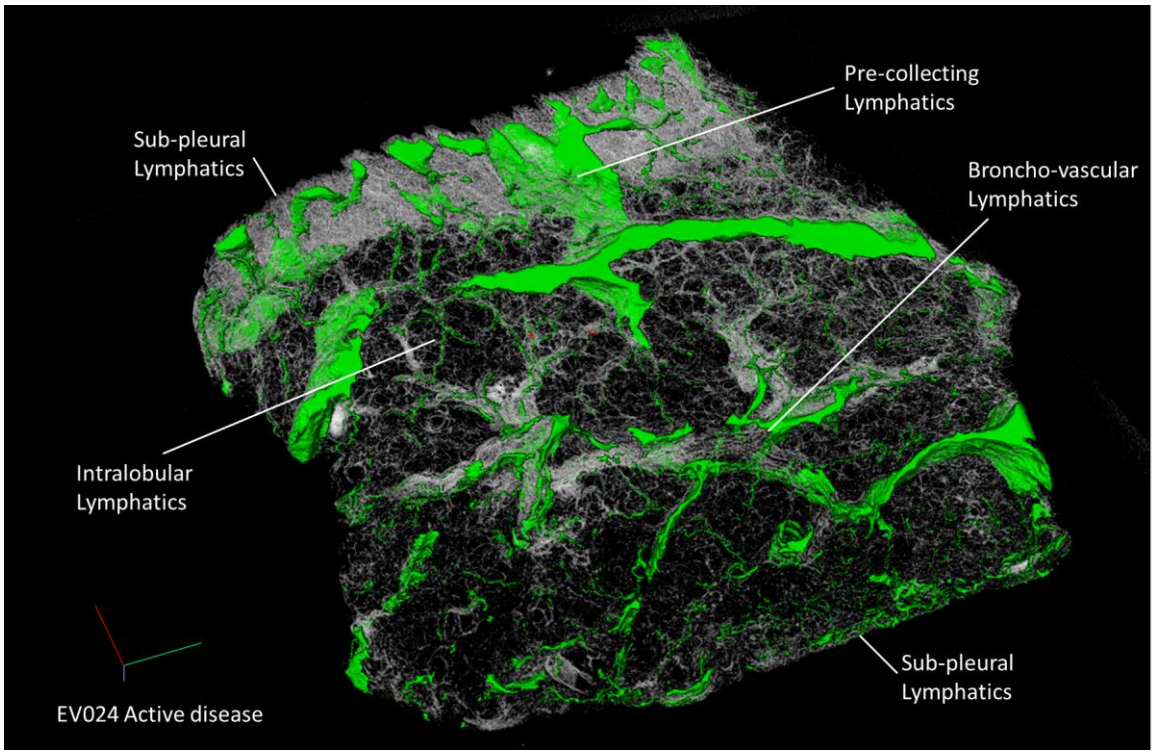

Figure 4.1 3D Volume Rendering of the Pulmonary Lymphatic Network in a Subvolume of Human Lung. The lymphatic vessel network is shown in green, µCT density map of the lung tissue is shown in grey. The areas which the VOIs are categorised by are labelled for this subvolume. The dimensions of the extent of this subsample are 9.7 mm; 7.5 mm; 0.5 mm in the green red and blue axes respectively.

4.3.2 The Intralobular Lymphatic Network

Across most of the lung samples, the intralobular (IL) lymphatic networks were nearly always cylindrical and almost exclusively linked with blood vessels, as shown in an example VOI in Figure 4.2. A few independent vessels travelled through the intra alveolar septa, but shortly returned to the network that runs alongside a blood vessel. These blood vessels had moderate to strong staining of αSMA and were, therefore, most likely to be arterioles. IL lymphatics were mostly interconnecting no larger than 15 µm in diameter but showed more "blind-ended" vessels than any other VOI category. Ultra-microscopy would be needed to observe if these vessels have pre-lymphatics adjoining them or have primary valves.

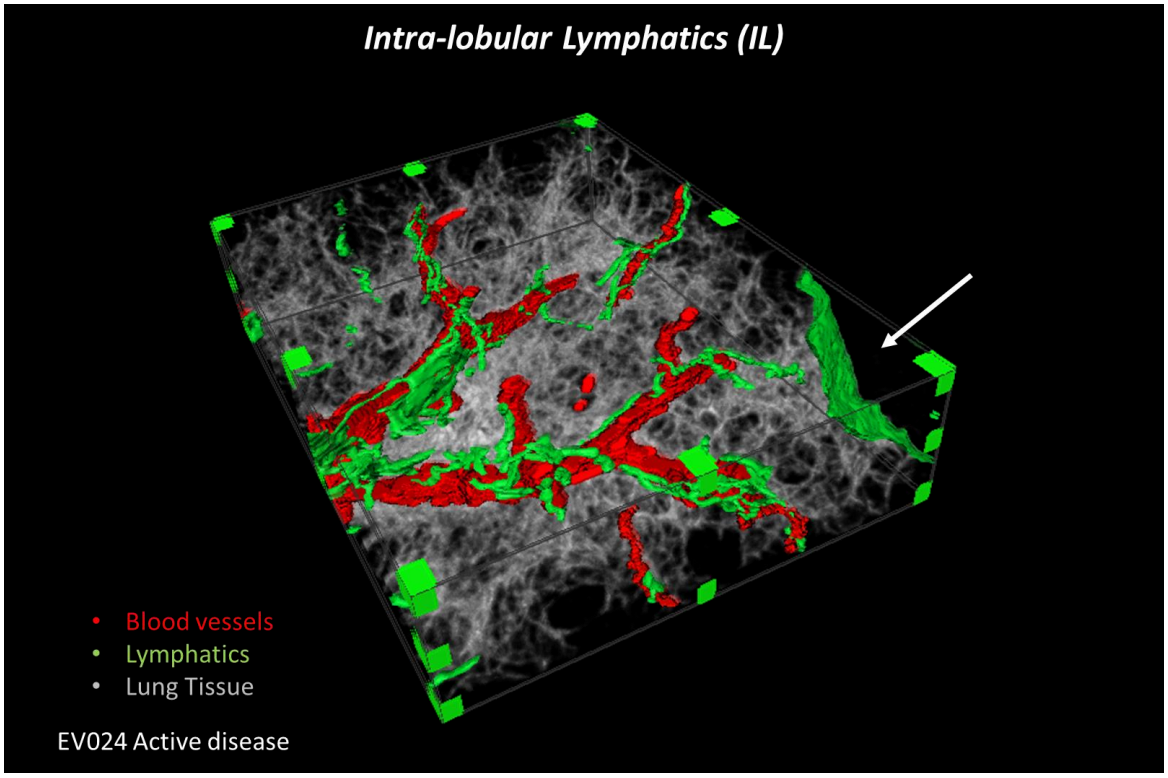

Figure 4.2 The Intralobular Lymphatic Network. The lymphatic vessel network is shown in green, µCT density map of the lung tissue is shown in grey and the blood vessel network shown in red. This VOI has a partial section of the IS associated lymphatic vessel wall included (white arrow). VOI dimensions= 1.9 mm x 3.8 mm x 0.5 mm

4.3.3 Subplural Lymphatic Network

The lymphatic network at the pleural surface (SP) had the most intra-VOI heterogeneity of all four anatomical locations both in the larger VOI (see Figure 4.3), and the size-optimised VOIs. The lymphatic vessels furthest from the visceral pleura often resembled the IL lymphatics of that particular sample, suggesting the subpleural VOIs were sampling some of the IL lymphatic networks. In eight out of the ten samples, luminal expansion of the lymphatic vessel was apparent towards visceral pleura. These dilated vessels often maintain a cylindrical shape, but at the pleural

surface, the vessel changed into a more flattened shape (as seen in the example SP VOI in Figure 4.3). There was no evidence of valves in any SP lymphatic networks. Compared to IL networks, SP networks had more vessels that were independent of any blood vessel structure (all of which had moderate αSMA staining of the walls). Also, in 3 samples, the density of lymphatic vessels appeared greater. In two samples, the opposite effect was seen with the SP network getting smaller in calibre and less dense compared to the IL network.

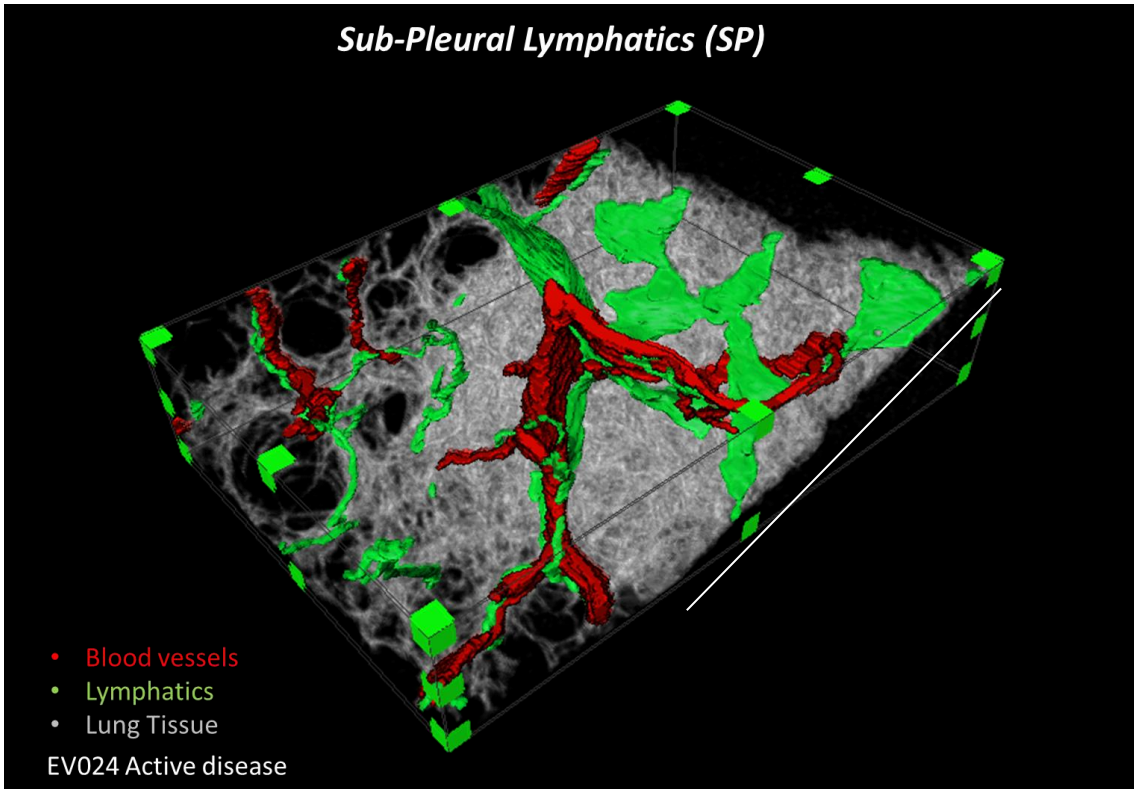

Figure 4.3 The Subpleural Lymphatic Network. The lymphatic vessel network is shown in green, µCT density map of the lung tissue is shown in grey and the blood vessel network shown in red. The white line denotes the orientation of the face of the pleural surface. VOI dimensions= 1.9 mm x 3.8 mm x 0.5 mm

4.3.4 The Bronchovascular-Bundle Lymphatic Network

Across all samples, the bronchovascular-bundle (BVB) lymphatic networks were different from those mentioned above. These lymphatic structures are conduits that mostly enwrap the blood vessels and bronchioles with a tight plexus of cylindrical vessels that on occasions deform from cylindricity to be sheet-like with holes (see example VOI in Figure 4.4). Most lymphatic vessels had obvious lumens of approximately ~50 µm in diameter and no valves were seen. The lumens had walls that were continuous with podoplanin+ positive cells. In places, on independent large blood vessels (>100 µm in diameter) these BVB lymphatic networks fully encircle the blood vessel and take on a sheath-like appearance while still maintaining a lumen. The segmentation data of the

different blood vessel populations showed that the BVB lymphatics had proximity to blood vessels that had strong staining for αSMA, suggesting these to be arteries or arterioles.

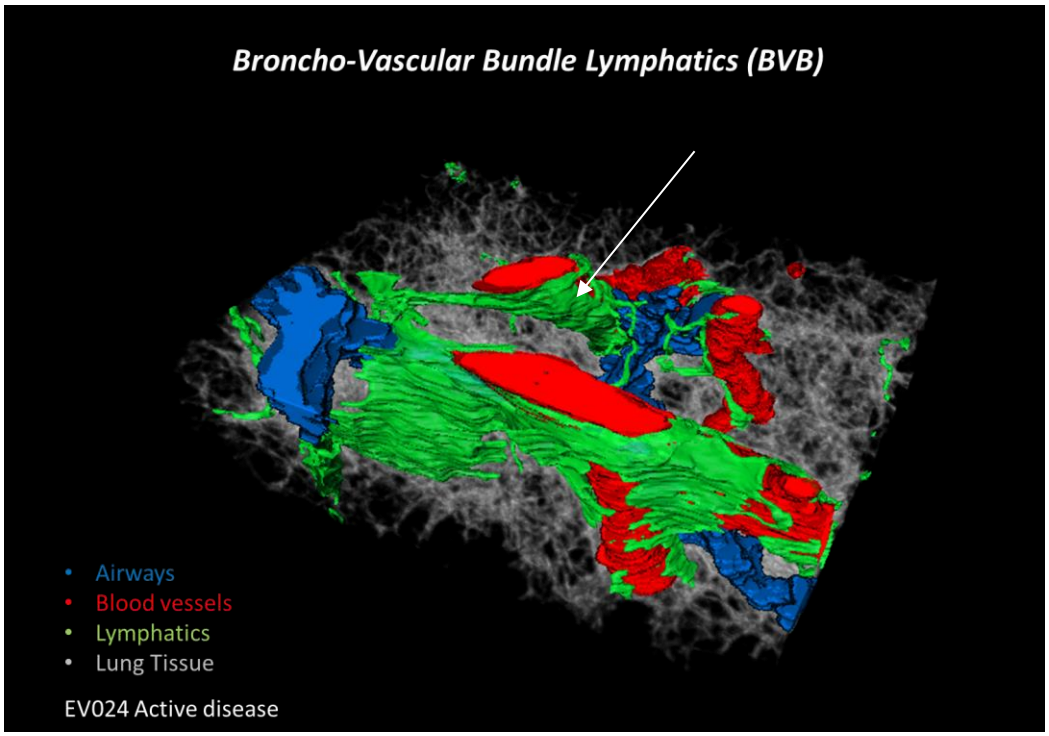

Figure 4.4 The Bronchovascular-Bundle Lymphatic Network. The lymphatic vessel network is shown in green, µCT density map of the lung tissue is shown in grey, the blood vessel network shown in red and the airways shown in blue. The white arrow shows the "sheath-like" structure around a blood vessel. VOI dimensions= 2.9 mm x 3.8 mm x 0.5 mm

4.3.5 The Interlobular Septa Lymphatic Network

In the whole subvolume lymphatic network shown in Figure 4.1, three vessels were seen inside or very close to the interlobular septa (IS) and formed a large sheet-like conduit that ran through the whole subvolume. The minimum diameter of these vessels was approximately ~ 250 µm. Two of these vessels merged outside of this subvolume shown in Figure 4.1 and continue in a sheet-like fashion through the whole sample depth (800 mm), terminated and split at the pleural surface (as seen in part of the vessel in Figure 4.1).

Figure 4.5 shows the luminal cavity of one of these vessels in an IS VOI. Luminal projections can be seen in these vessels segmented in white which are seen in the µCT scan dataset but are unrecognisable as valves in the IHC data (Figure 4.5b and c). As these projections are present at lymphangion-like constrictions of the vessel wall, they are assumed as being valves. Some valves appear monocuspid, some bicuspid, but all leaflets appear incomplete or damaged. The blood vessels located around the IS lymphatic networks in all samples had very weak staining for αSMA, suggesting them to be venules or veins. It was also observed that the IS lymphatics were negative for αSMA staining throughout all samples. In every sample that had IS associated lymphatics

present (5/10 samples), all had weaker and sometimes faint staining for LP21 compared to D240 as mentioned in Chapter 2, section 2.2.5.

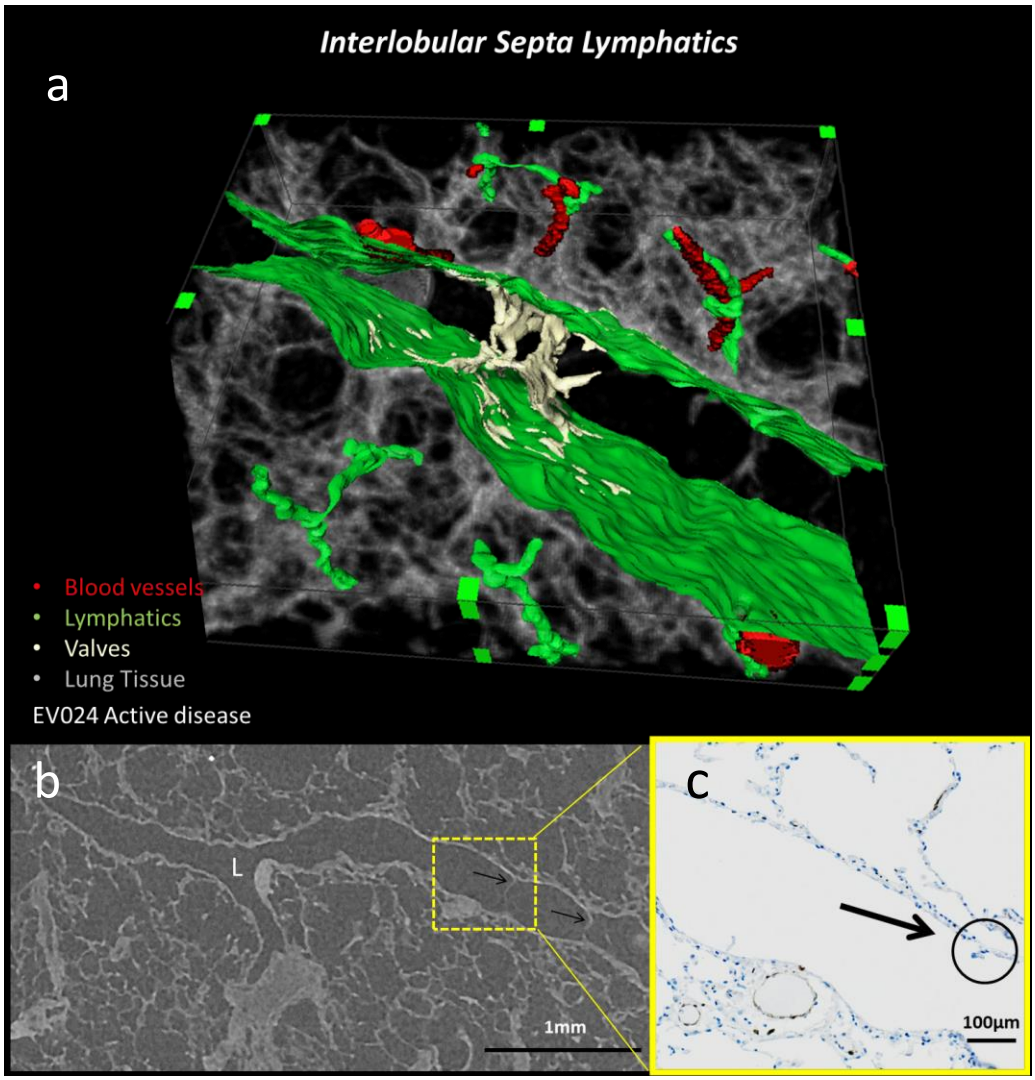

Figure 4.5 **Example an Interlobular Lymphatic Vessel. a** 3D rendered image of segmented data. The walls of a lymphatic vessel are shown in green, luminal projections (valves) shown in white, µCT density map of the lung tissue is shown in grey and the blood vessel network shown in red. VOI dimensions =2.9 mm x 3.2 mm x 0.5 mm **b** µCT orthoslice of a larger ROI showing a cross-section of the vessel shown in panel **a** with the luminal projections (valves) marked with black arrows. **c** a corresponding IHC section (stained with αSMA) of the marked yellow ROI of panel **b**. The black arrow and circle show one of the luminal projections shown in **b** but shortened by IHC damage.

4.3.6 The Morphology of Anatomically-Located Pulmonary Lymphatic Networks

Across all 717 human lung sample VOIs, 52% were categorised as IL, 20% as SP, 18% as BVB and 10% as IS (see Figure 4.6). The median value of each morphometric measurement (see Chapter 2.4.3) for each anatomically-associated lymphatic network is summarised in Table 4.1, with all data shown in Figure 4.7a-f. Statistical comparisons between the lymphatic networks is shown in Figure 4.7g-l.

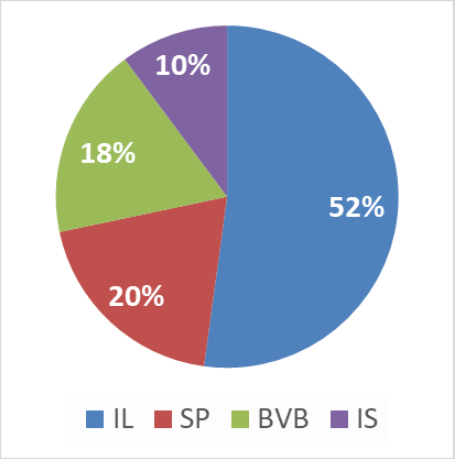

Figure 4.6 Proportion of All Anatomically-Located VOIs Across All Human Lung Samples. Data given as a percentage of the total number of VOIs (717) across ten human lung samples.

Table 4.1 Median Values of Lymphatic Network Morphometry for Each VOI Category

Morphometric Measurement	Categorised Lymphatic Networks (all data)			
	SP	IL	BVB	IS
Lymphatic Volume/Tissue Volume	0.016	0.014	0.031	0.134
Lymphatic Surface Area /Tissue Volume	0.0050	0.0046	0.0077	0.0176
Lymphatic Branch #/mm^3 Tissue Volume	840.10	1030	1786	1877
Lymphatic Junction #/mm^3 Tissue Volume	366.6	398.8	687.6	866.2
Tortuosity	1.30	1.31	1.29	1.28
Fractal Dimension	2.47	2.40	2.63	2.97

The lymphatic volume and lymphatic surface area (normalised to tissue volume) of the lymphatic networks were all significantly different from each other except for the SP and IL lymphatics (see Figure 4.7h and i). Significant differences were seen in the lymphatic branch and junction number data between all VOI categories except between the SP and IL networks and between the BVB and IS networks (see Figure 4.7j and K). The IS lymphatics were the only network where the tortuosity measure was significantly different from other VOI categories.

In the fractal dimension analysis, the log-log plots of box number Ns against box side length s produced a straight line in all of the patients (mean correlation coefficient r= 0.994; SD =0.001) confirming a fractal pattern was present. All anatomically located lymphatic networks showed significant differences in their fractal dimension from each other (see Figure 4.7l).

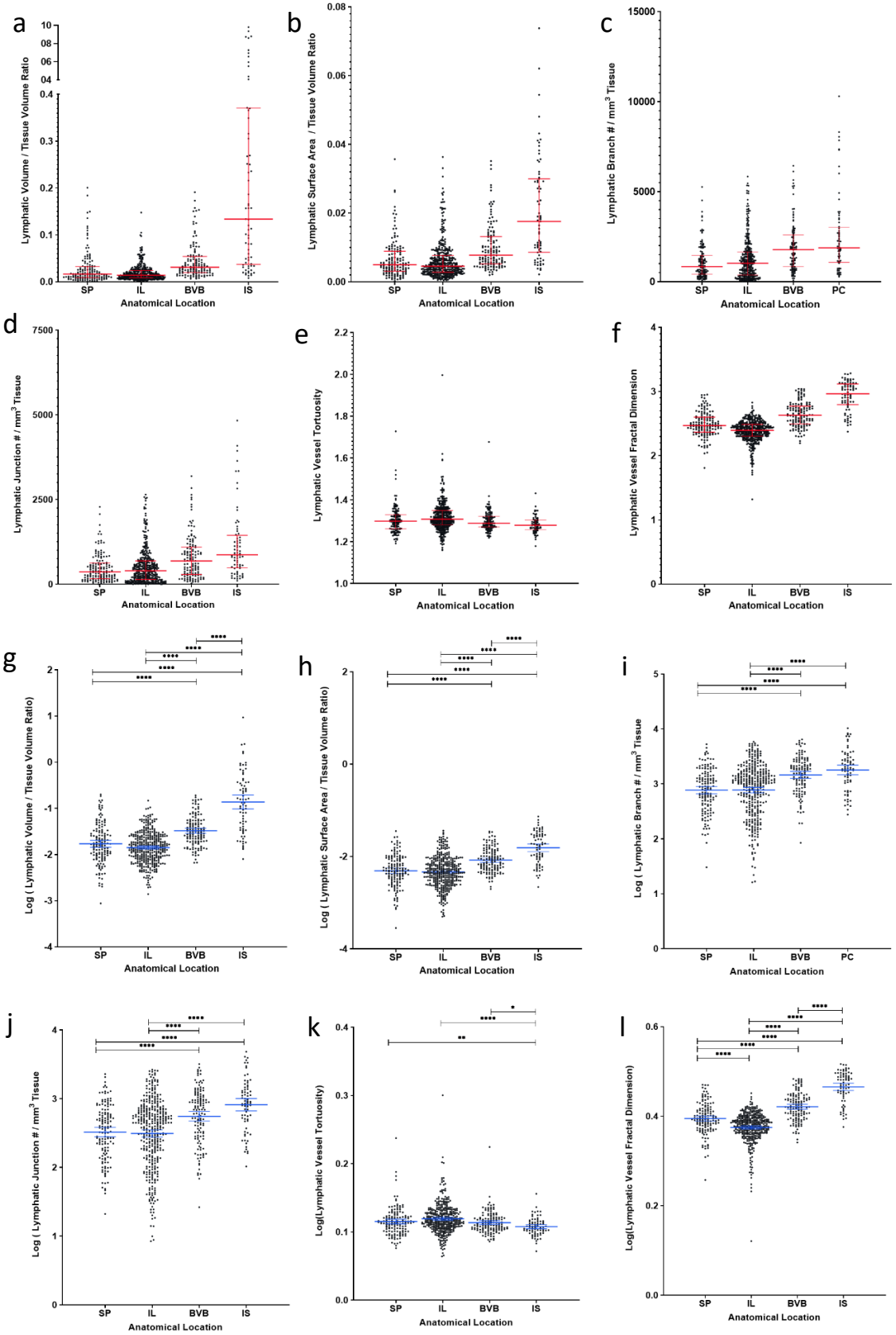

Figure 4.7 Morphology of Anatomically Associated Lymphatic Networks in Human Lung. The morphology and statistical comparison of the sub-pleural (SP), intralobular (IL), bronchovascular-bundle (BVB) and interlobular septa (IS) pulmonary lymphatic networks. **a** The lymphatic network volume/tissue volume ratio **b** The lymphatic network surface area/ tissue volume ratio **c** The lymphatic network branch number/unit tissue volume **d** The lymphatic network junction number/ unit tissue volume **e** The average vessel tortuosity of the lymphatic

network **f** The fractal dimension of the lymphatic network. (**a-f**) red bars are showing the median value and the interquartile range. (**g-l**) showing the log transform of (**a-f**) Blue bars are showing the mean value and the 95% confidence interval. Statistical significance denoted as described section 4.2.3

4.3.7 Morphometry of Individual Lymphatic Vessels

A maximum intensity Z-projection of the 3D skeletonization and thickness map of the segmented lymphatic data of the example subvolume is shown in Figure 4.8a and b respectively. The selected vessels' location and their sampling length are shown in yellow in Figure 4.8b (V1-V4 = the largest capacity vessels, V5-8= the smallest capacity vessels).

The minimum diameter varied along the length of the larger capacity lymphatic vessels, V1, V2 and V3 (see Figure 4.8c). There were periodic peaks (at an average minimum diameter of ~250-300 µm) and troughs (at an average minimum diameter of ~150-200 µm) along their length. The peaks in minimum vessel diameter were maintained for ~400 µm along the vessels length whereas, in a trough, the vessel minimum diameter was maintained for ~100-200 µm. V4 had some peaks and troughs in its vessel diameter along its length, but these were not as consistent in size or length compared to V1, V2 or V3. Unlike V1, V2 and V3, no valves were discernible in V4 in the µCT dataset. The maximum diameter for V1, V2, V3 and V4 were not measurable as they formed large sheet structures (as discussed in section 4.3.5) which extended outside the subvolume extents.

The smaller capacity vessels (V5, V6, V7 and V8) had no distinct periodicity in their minimum vessel diameter which ranged from 8 µm to 50 µm.

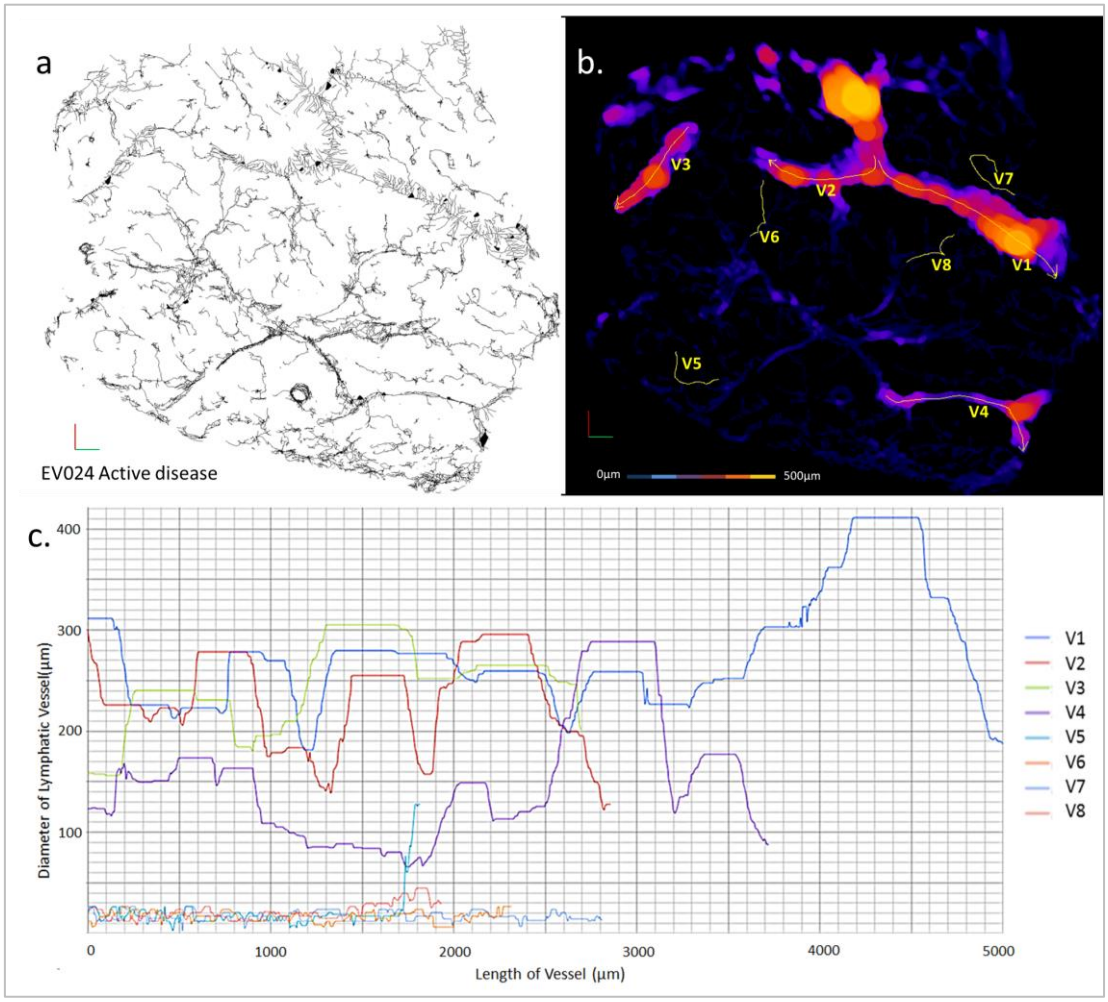

Figure 4.8 Quantitive Assessment of Individual Lymphatic Vessel Morphology. a Maximum intensity image of the skeletonised lymphatic network shown in Figure 4.1. **b** A thickness map of the lymphatic network shown in Figure 4.1. The eight vessels used for analysis are traced in yellow. **c** The minimum diameter of the lymphatic vessels shown in panel **b** measured along their length.

4.4 Discussion

4.4.1 Method Assessment Based on 3D Observations of Lymphatic Networks

Obtaining a complete and distinct pulmonary lymphatic vessel network within its 3D lung volume, confirms the success of manual segmentation and the specificity of the antibody used for lymphatic endothelial cell identification (LP21 and D240).

A small number of vessels appeared floating or not connected to anything in the 3D rendered images. This anomaly is the result of two factors. Firstly, as the presented images are a 2D image of a cropped 3D volume, some of these vessels travel between the extents of the VOI boundary and thus appear not connected to any other vessel but may well connect to a network outside the viewing area. Secondly, there is a chance these vessels were connected to a collapsed structure

that was missed in segmentation. However, as segmentation was performed manually, great effort was made to segment all structures with LP21 or D240 staining, including what appeared to be collapsed structures. It is anticipated the risk of these features being lost would be significantly higher if automated segmentation algorithms were employed in the future.

4.4.2 Defining Pulmonary Lymphatic Populations

On summation of the result of this chapter, two hierarchical populations of lymphatics exist within peripheral human lung samples:

- Vessel conduits of a cylindrical shape with an average diameter less than 50 µm, that contain no valves and which are closely associated with blood vessels.
- Vessel conduits that have a sheet-like appearance in 3D, with a minimum diameter of 150 µm and a maximum diameter often greater than 500 µm. These vessels also have a lymphangion-like profile to their vessel walls, contain valves and are not closely associated with blood vessels.

The first population of lymphatic vessels can be named as microlymphatics primarily due to their average diameter. These vessels fit the 2D description of microlymphatic vessels previously described in the intralobular and interalveolar interstitium in 2D (Kambouchner & Bernaudin, 2009; Sozio *et al.*, 2012; Mori *et al.*, 2013). Of the anatomically-associated lymphatic networks, both the SP and IL lymphatic networks fit into this population, albeit the SP network does not have such a tight association to the blood vessel as the IL network. Assessing the morphometry of the SP and IL lymphatic networks suggests structural variability is still apparent in this pulmonary microlymphatic population which is lessened when normalised with tissue morphometry.

The characteristics of the second population of vessels suggest they are collecting or pre-collecting lymphatic vessels. These vessels have previously been described in one 2D study of human pulmonary lymphatic morphology, but the authors suggested the 2D sectioning of these vessels (as shown in a 2D µCT orthoslice Figure 4.5b) were of its longitudinal axis, not a transverse axis (Sozio *et al.*, 2012). These vessels presented in a whole subvolume in Figure 4.1, were the largest vessels that displayed this sheet-like structure in all of the lung samples in this study. However, sheet-like structures of similar dimensions were seen in separate lung samples, all of which had strong, continuous D240+ staining on their luminal walls. These observations reduce the possibility of these structures being sample collection or fixation induced artefact.

This second population of pulmonary lymphatic vessels do not have αSMA positive cells in their vessel walls. This which was not investigated in previous 2D work (Sozio *et al.*, 2012), thus, is a

novel finding in the human. This observation, however, has been corroborated in the mouse lung by oral communication with the McDonald group in California, whereas in mouse skin, lymphatics vessels of this size and shape were αSMA + (Sweet *et al.*, 2015). The finding that pulmonary lymphatic vessels that have secondary valves, but lack smooth muscles in their walls, suggests intrinsic contractile mechanisms do not actively influence the flow in these structures. The cyclic action of respiration in healthy lung may, therefore, be sufficient to maintain fluid drainage in the human lung.

Despite the presence of lymphangion beading and valves in these vessels, the lack of any αSMA in or surrounding their walls and their location being peripheral within the lung, would be reasons for these vessels to be described as pre-collecting lymphatics and not conducting lymphatics as suggested when observed in 2D (Sozio *et al.*, 2012). In the present study, all identified vessels across the ten lung samples that fitted into the pre-collecting lymphatic population were associated with the interlobular septa. It would, therefore, suggest the VOIs that sampled the interlobular septa network were all sampling pre-collecting lymphatic structures.

The tight plexus of lymphatics associated with the bronchovascular-bundle, and the “sheath-like” lymphatic structures that surround the vasculature seem distinct from the pre-collecting and microlymphatic populations. Like the pre-collecting lymphatics, the observed sheaths around pulmonary blood vessels and airways had a continuous inner and outer wall of D240+ and Lp21+ LECs, reducing the likelihood these observations being artefact.

Fluid-filled structures that surround the bronchovascular regions in the lung have been commented on in the literature since their discovery in oedematous dogs over 30 years ago (Michel, Meterissian & Poulsen, 1986). To the present day, these fluid-filled spaces are generally termed “adventitial cuffs” due to their sleeve like appearance and are seen in all organs of the body (Effros & Parker, 2009; Benias *et al.*, 2018; Dahlgren & Molofsky, 2019). These cuffs are now not described as only being fluid-filled, but as heterogeneous lymphoid aggregates, containing multiple immune and stromal components, with plexuses of lymphatic vessels running within them. Specifically in the lung, these cuffs are sometimes termed inducible bronchus-associated lymphoid tissue (iBALT) or tertiary lymphoid organs and have been shown to be continuous with draining lymphatic structures (Randolph *et al.*, 2017; Dahlgren & Molofsky, 2019). Although iBALT has been shown to develop in several human diseases, including, COPD, IPF and even rheumatoid arthritis, only Mori *et al.*, 2013, has described the presence of lymphatic vessels within human iBALT but this was in COPD patients in 2D (Rangel-Moreno *et al.*, 2006; Carragher, Rangel-Moreno & Randall, 2008; Mori *et al.*, 2013). Interestingly, of the other 2D studies of human lung lymphatics which had access to a reliable LEC marker for identification purposes, only

bronchovascular associated lymphatics have been mentioned with no discussion of iBALT (El-Chemaly *et al.*, 2009; Yamashita *et al.*, 2009; Kambouchner & Bernaudin, 2009; Sozio *et al.*, 2012; Stump *et al.*, 2017).

These studies, with the present finding that human pulmonary BVB regions have both a plexus and sheath-like structures suggest the formation of iBALT may be an intermediate development while BVB lymphatic vasculature is expanding under high fluid loads and immune cell proliferation. One study using confocal microscopy has inferred 3D lymphatic network expansion in iBALT after induced inflammation, but in a mouse model (Baluk *et al.*, 2014).

In the mouse, iBALT-associated LECs have button-like junctions as thus are assumed to have primary valves in the control lung (Yao *et al.*, 2012). Therefore, the human BVB lymphatic network in both the tight plexus and sheath-like form will be classified and modelled in subsequent chapters as microlymphatics. The BVB lymphatic network branch diameter and a lack of secondary valves also suggest they are not pre-collecting lymphatics.

Finally, the differential lymphatic vessel proximity to the blood vessel network in each VOI category is an interesting observation considering the accepted importance of VEC mediators for lymphangiogenesis in the lung (Miller, Mcdole & Newberry, 2010; Schulte-Merker, Sabine & Petrova, 2011; Randolph *et al.*, 2017). If VEC mediators are the main driving force of lymphangiogenesis, there would be a reason to suggest the IL and SP populations are more dynamic, and are continually remodelling themselves. Another possibility is that local environmental pressures mould lymphatic vessels after or during sprouting. For example, the respiratory cyclic stresses and strains in the interalveolar septae may force the sprouting lymphatics to remain near the blood vessel network. Although there is evidence for mechanical remoulding of pulmonary blood vessels, this has not been described in for the lymphatic vessels (Effros & Parker, 2009). Finally, there is a possibility the LECs within these networks respond differently to angiogenic mediators, suggestive of intra-organ LEC phenotype variability. Genomic and proteomic studies would need to be carried out to confirm this. The discovery in this study that the IS lymphatics have differential expression patterns of podoplanin (see Chapter 2, section 2.2.5) may give support to a hypothesis of the existence of separate LEC populations.

4.4.3 Future Sampling Strategy

It is clear from the global VOI comparison of lymphatic network morphology, and general observation, that lobular distribution affects their morphology and patterning. The use of sampling VOIs, as fully justified in Chapter 2, section 2.4.1, enables function to be implied from morphometry assessment as the smaller lymphatic vessels in particular do not function without a

network and tissue to drain. The morphometry assessment by VOI sampling also enables direct comparison of morphological inference to functional predictions made by image-based mathematical modelling.

However, the presence of certain pulmonary lymphatic vessels (e.g. V4 in Figure 5.8) that have features of both hierarchical populations demonstrates there is no definite separation of lymphatic vessel hierarchy or anatomically-located networks. The observation that the SP network shows increased vessel expansion towards the pleural surface, and finding the whole lymphatic network in a subvolume of human lung is interconnected, also demonstrate this point.

Therefore, changing the sampling strategy to reflect structural heterogeneity throughout the secondary lobule of the lung should be considered in future work. This consideration should definitely be the case for the precollecting lymphatics located in the interlobular septa as they are simply too large to assess in a network form using these sampling volumes. These vessels, therefore, need to be assessed individually, similarly to the quantitive method shown here (section 4.2.3) and subsequently modelled as such. Care must also be taken with the BVB lymphatic network. Although these structures are small enough to be sampled by a cubic VOI, if the VOI size has to be increased to be representative, inevitably, some larger IL lymphatic vessels that feed into (or possibly out of) these larger networks will be encompassed. If data becomes evident in the future that these BVB lymphatic networks do not have microlymphatic draining function, and thus would not be directly compared with the IL and SP networks, they also should be considered for being assessed individually.

It should finally be noted that the 3D pulmonary lymphatic features discussed in this chapter have only been described using knowledge from ten tissue samples. Once more tissues have been analysed, different lymphatic structures may yet become evident, and some recognised as artefact. Despite this, the novel finding of sheath-like microlymphatic structures and the extensive sheet-like appearance of the pre-collecting lymphatics, neither previously described in the literature, emphasises the importance of 3D qualitative observations alongside the 3D quantitative assessment of pulmonary lymphatic morphometry.

4.5 Conclusion

Microlymphatic and pre-collecting lymphatics are present in the human lung. Across both populations, human pulmonary lymphatics show both qualitative and quantitive structural heterogeneity both as individual vessels and as a sampled network. The heterogeneity seen in sampled lymphatic networks is linked to their anatomical distribution in the secondary lobule. 3D structural features in some pulmonary lymphatic networks, such as the sheath-like appearance of

the BVB lymphatic network, have been found which have not previously been described in the literature.

The lack of smooth muscle in pre-collecting lymphatic networks and their 3D sheet-like appearance is also a novel discovery. Pre-collecting lymphatics without smooth muscle appears to be a specific feature of the lung. Unfortunately, these vessels are too large to be sampled and analysed as described in this body of work. In contrast, the microlymphatic networks and their surrounding tissue are well suited to be analysed by the presented methods of morphometry and modelling in Chapters 2 and 3.

Chapter 5 Assessing the Morphology of Pulmonary Lymphatic Networks Within and Between Clinical Groups

5.1 Introduction

The results shown in Chapter 4 demonstrated that two pulmonary lymphatic populations exist in the human lung periphery. In addition, within the microlymphatic population, structural heterogeneity was apparent, linked to the subpleural (SP), intralobular (IL) and bronchovascular-bundle (BVB) regions of the secondary lobule of the human lung.

This chapter presents work further investigating these lymphatic networks and identify the factors that are the highest contributors to the observed variation seen in their morphology. As sampling was only suitable for microlymphatics (discussed in Chapter 4, section 4.4.3), only these networks will be quantitively assessed.

The intra-sample variation will be considered to see if the anatomical microlymphatic networks between subvolumes of the same lung sample are morphologically similar. Intra-clinical group variation will also be looked at to see if the morphology of the anatomical microlymphatic networks in patient samples within the control, active disease, and COPD groups are similar (see Chapter 2, section 2.1 for categorisation methods). Here a comparison will be made to see if the microlymphatic networks at different anatomical locations in the secondary lobule are still distinct from each other once clinically grouped.

Finally, the morphology of the same microlymphatic network between the different clinical groups will be compared to see if disease is the largest contributing factor in the variation seen in the global assessment of anatomically-located pulmonary lymphatic networks.

As this study is an observational study used to gain preliminary data to drive hypothesis generation, it should be stressed the same data as seen in Chapter 4 will be re-used for these assessments. Although multiple comparisons within statistical tests will be accounted for, this is a limitation of all statistical tests performed in this chapter.

5.2 Specific and Additional Materials and Methods

5.2.1 Variation of Microlymphatic Morphology Between Sample Subvolumes

To test for intra-sample variation, the lymphatic volume/ tissue volume measure of the SP, IL and BVB microlymphatic networks were calculated and statistically compared against the same microlymphatic networks in the other subvolume of the sample. The statistical methods are detailed in below in section 5.2.6. As an assessment of lymphatic network variation was being sought, not network characterisation, only the lymphatic volume/ tissue volume measure (see Chapter 2, section 2.4.3) was used. A visual example of this comparison is given in Figure 5.1.

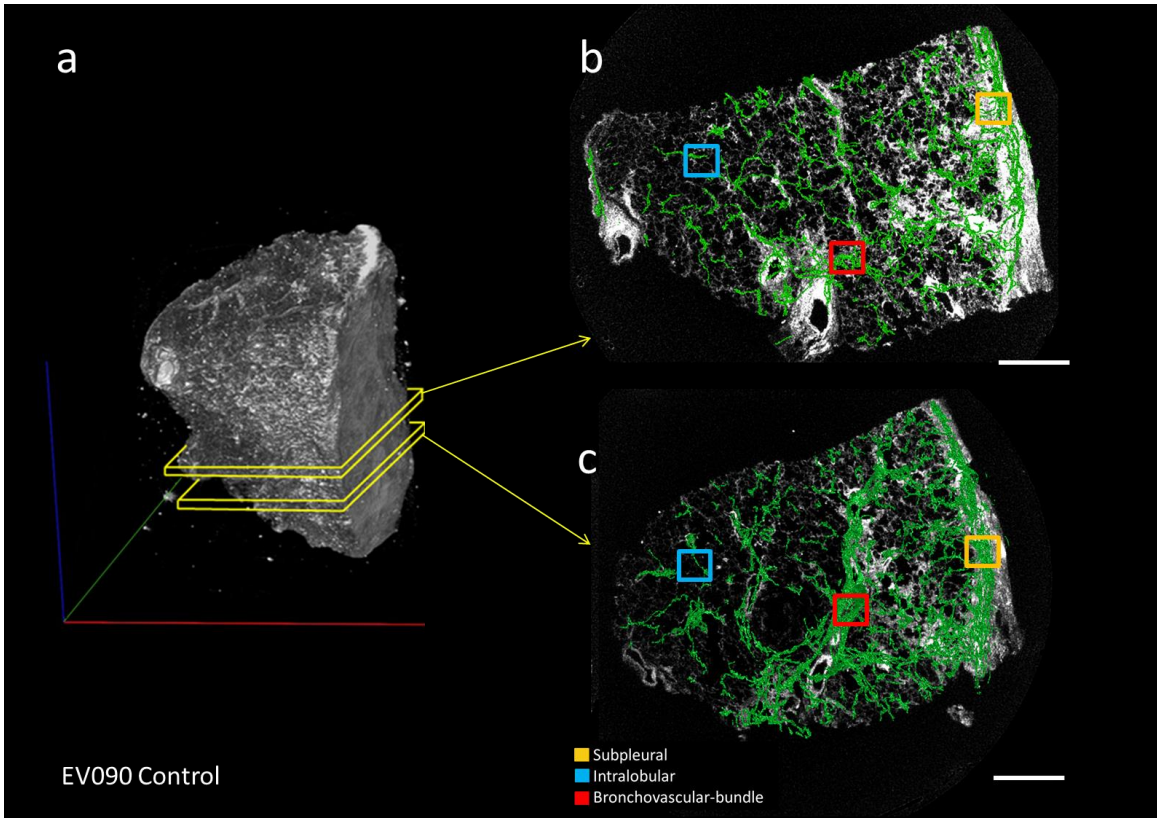

Figure 5.1 Calculating Intra-sample Microlymphatic Variation in Separate Anatomical Locations. a 3D volume rendering of a µCT data set of a human lung sample taken from the control group. Yellow lines denote the depth and location of the subvolumes taken from this lung sample. Scale bars are 18 mm (red); 12 mm (green); 12 mm(blue). **b** Maximum intensity projection of the lymphatic network (green) and µCT density map (white) of subsample 1 showing three sampling VOIs at different anatomical locations. **c** Showing the same presentation of panel **b** but for subsample 2. The lymphatic volume/ tissue volume measure of each anatomically located microlymphatic network in panel **b** is compared to the same networks in panel **c**. Scale bars for panels **b** and **c** = 2 mm.

5.2.2 Variation of Microlymphatic Morphology Within Clinical Groups

The sampling VOIs for each anatomical microlymphatic network in each subsample were collated together to represent one lung sample. The lymphatic volume/ tissue volume measure of the SP, IL and BVB microlymphatic networks in each sample were then statistically compared against the same microlymphatic network in other samples in the same clinical group. The morphometry and statistical methods are detailed below in section 5.2.6. Again, as an assessment of lymphatic network variation was being sought, not network characterisation, only the lymphatic volume/ tissue volume measure (see Chapter 2, section 2.4.3) was used. A visual example of this comparison is given in Figure 5.2 for the control group. A maximum intensity Z-projection image of the lymphatic network within the µCT data set from one subsample from every sample analysed is given in Appendix F.

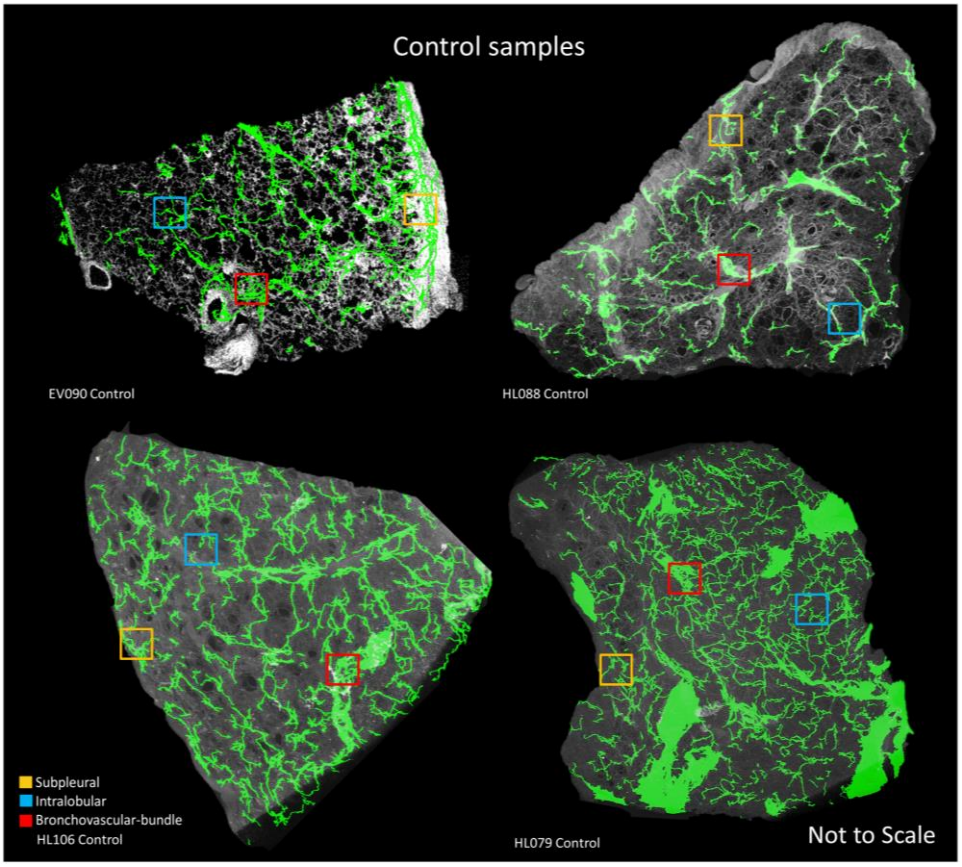

Figure 5.2 Structural Variation of Microlymphatic Networks Within the Control Group. Maximum intensity projections of the complete lymphatic network (green) within the µCT density map (grey) in one subvolume taken from all four human lung samples categorised into the control group. The coloured squares show the sampling VOIs at the three different anatomical locations. The lymphatic volume/ tissue volume measure of the microlymphatic network in these anatomical locations in each sample were compared to the same networks in the other samples. Images not to scale.

5.2.3 Abundance of Microlymphatic Networks within Clinical Groups

The sampling VOIs for each anatomical microlymphatic network were then collated into clinical groups. The proportion of the total number of VOIs within each clinical category (control= 284, active disease = 222, and COPD= 138) that were associated with an anatomical location was calculated. If the subvolumes within each lung sample were representative of the secondary lobule of the lung, the proportions of anatomical-located lymphatic networks should be similar between the clinical groups.

5.2.4 Comparison of Microlymphatic Morphology at Different Anatomical Locations Within Clinical Groups

The lymphatic morphology of the SP, IL and BVB microlymphatic networks within the same clinical group were calculated and statistically compared against each other (detailed below). As this assessment sought to characterise these anatomical microlymphatic networks within each clinical group, all six morphometric measures (see Chapter 2, section 2.4.3) were used. This statistical comparison was repeated within all three clinical groups. A visual example of this comparison is given in Figure 5.3a.

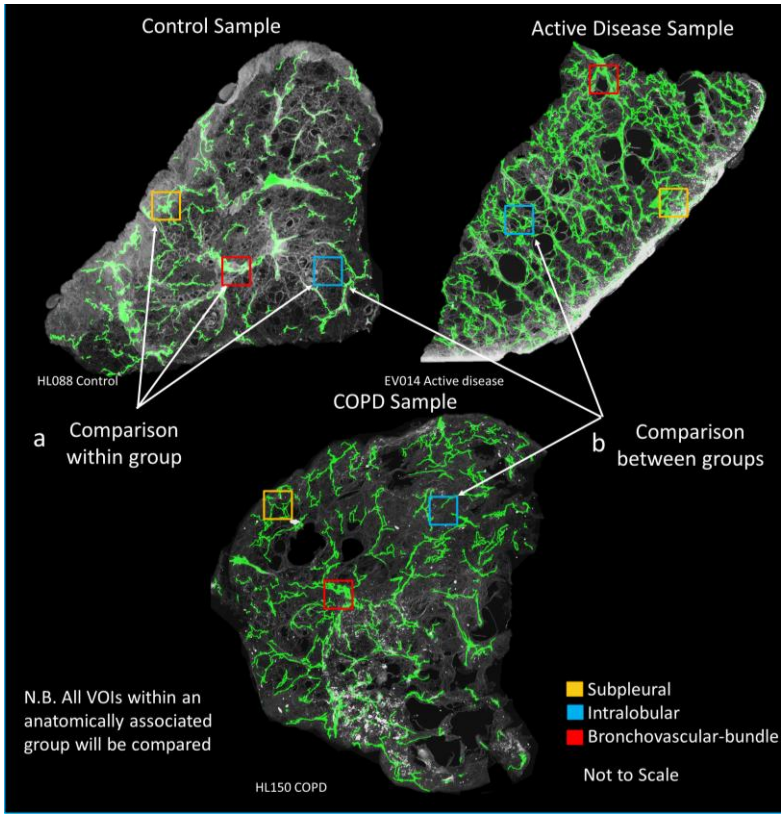

Figure 5.3 Structural Variation of Microlymphatic Networks Within and Between Clinical Groups. Maximum intensity projections of the complete lymphatic network (green) within the µCT density map (grey) in example lung sample subvolumes from each clinical group. The coloured squares show the sampling VOIs at the three different anatomical locations. The

morphology of the microlymphatic networks in these anatomical locations in each clinical group were: **a** compared against each other. **b** compared to the same networks in the other clinical groups. Images not to scale.

5.2.5 Comparison of Microlymphatic Morphology of the Same Anatomical Location Between Clinical Groups

Finally, the same morphometric assessment as section 5.2.5 was used, but the microlymphatic networks at a single anatomical region were statistically compared between the clinical groups. This statistical comparison was repeated for each of the three anatomical locations. A visual example of this comparison is given in Figure 5.3b.

5.2.6 Statistical Analysis

All raw data processing and statistical analysis were performed in Graph Pad Prism (version 8.0).

All morphometric data used for grouped statistical analysis was of lognormal distribution permitting parametric statistical tests to be performed. The Shapiro-Wilk test confirmed this for every log-transformed dataset.

When comparing specific lymphatic populations between the same sample's subvolume an unpaired two-tailed student T-test was performed.

When comparing the variance between lymphatic populations associated with different anatomical locations and when comparing population variance between health and disease, an ordinary one-way analysis of variance (ANOVA) was performed followed by a Tukey test which corrects for multiple comparisons.

A Brown-Forsythe and Welch ANOVA test was used for grouped comparisons where the SD differed significantly between each group, followed by a Dunnett T3 ($n<50$/group) or a Games-Howell ($n>50$/group) to correct for multiple comparisons.

On all graphs representing data upon which statistical analysis was performed, the error bars displayed are the mean value and 95% confidence interval of the mean. In addition, the P values are denoted as follows: P values> 0.05 are not given. Any comparison without a significance notation assume as not significant. P values ≤ 0.05 are represented as "*"; P values ≤ 0.01 are represented as "**"; P values ≤ 0.001 are represented as "***"; P values ≤ 0.0001 are represented as "****".

5.3 Results

5.3.1 Microlymphatic Network Morphology is the Same Between Subvolumes of the Same Lung Sample

No difference was seen in the lymphatic volume/tissue volume measure between microlymphatic networks between a sample's subvolumes when comparing networks from the same anatomical location. There was one exception to this where the SP network was different in one active disease sample. The normalised volume measure for an example sample from each clinical group is given in Figure 5.4. All 10 samples are shown in Appendix G.

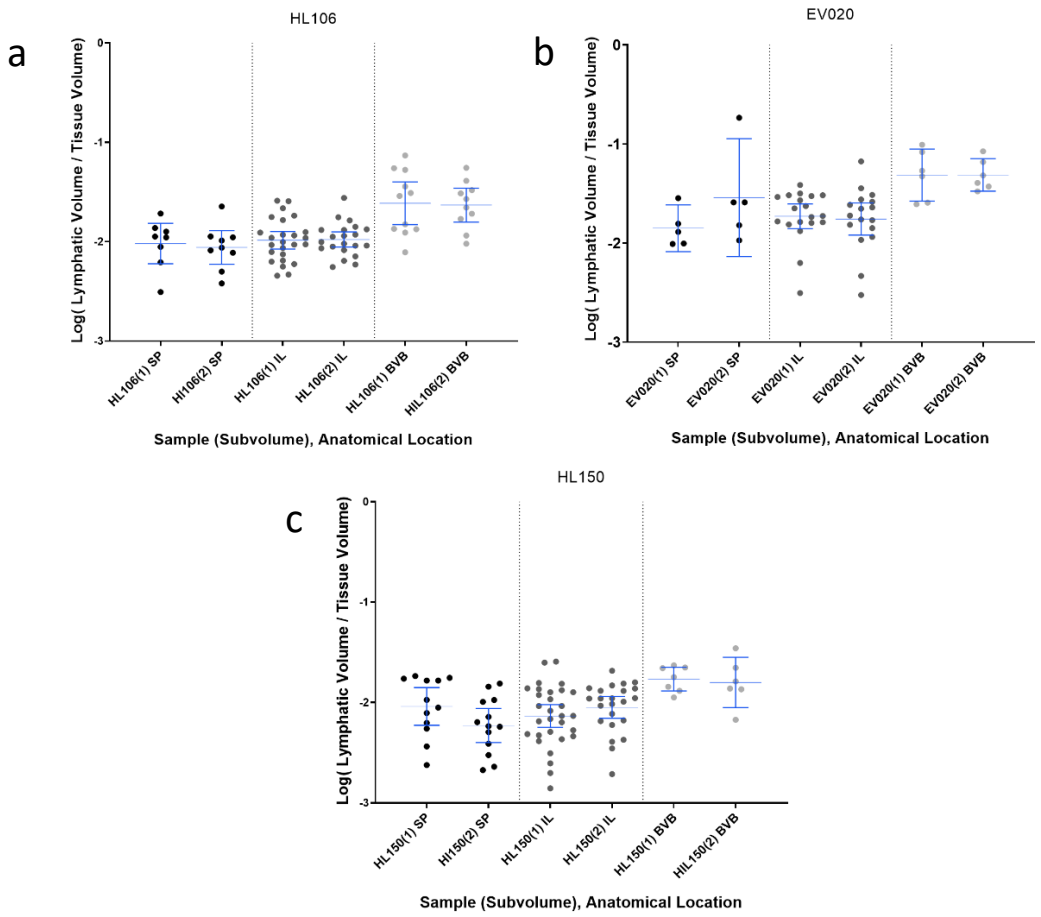

Figure 5.4 **Intra-sample Variation in Microlymphatic Networks.** The statistical comparison results of the transformed volume/ tissue volume dataset for the same anatomically associated microlymphatic networks between subvolumes taken from the same sample. An example is given from a sample taken from **a** the control group (HL106) **b** the active disease group (Ev020) **c** the COPD group (HL150). Blue bars are showing the mean value and the 95% confidence interval. There were no statistically significant differences ($p<0.05$) in the volume measures between the same network in separate subvolumes. Results for all other samples are given in Appendix G.

5.3.2 Microlymphatic Networks have Variable Morphology between Samples Within the same Clinical Group

There were significant differences seen in the lymphatic volume/tissue volume measure of the SP and IL microlymphatic networks between samples within a clinical group. No difference was seen in the lymphatic volume/tissue volume measure of the BVB microlymphatic network between samples within a clinical group (see Figure 5.5).

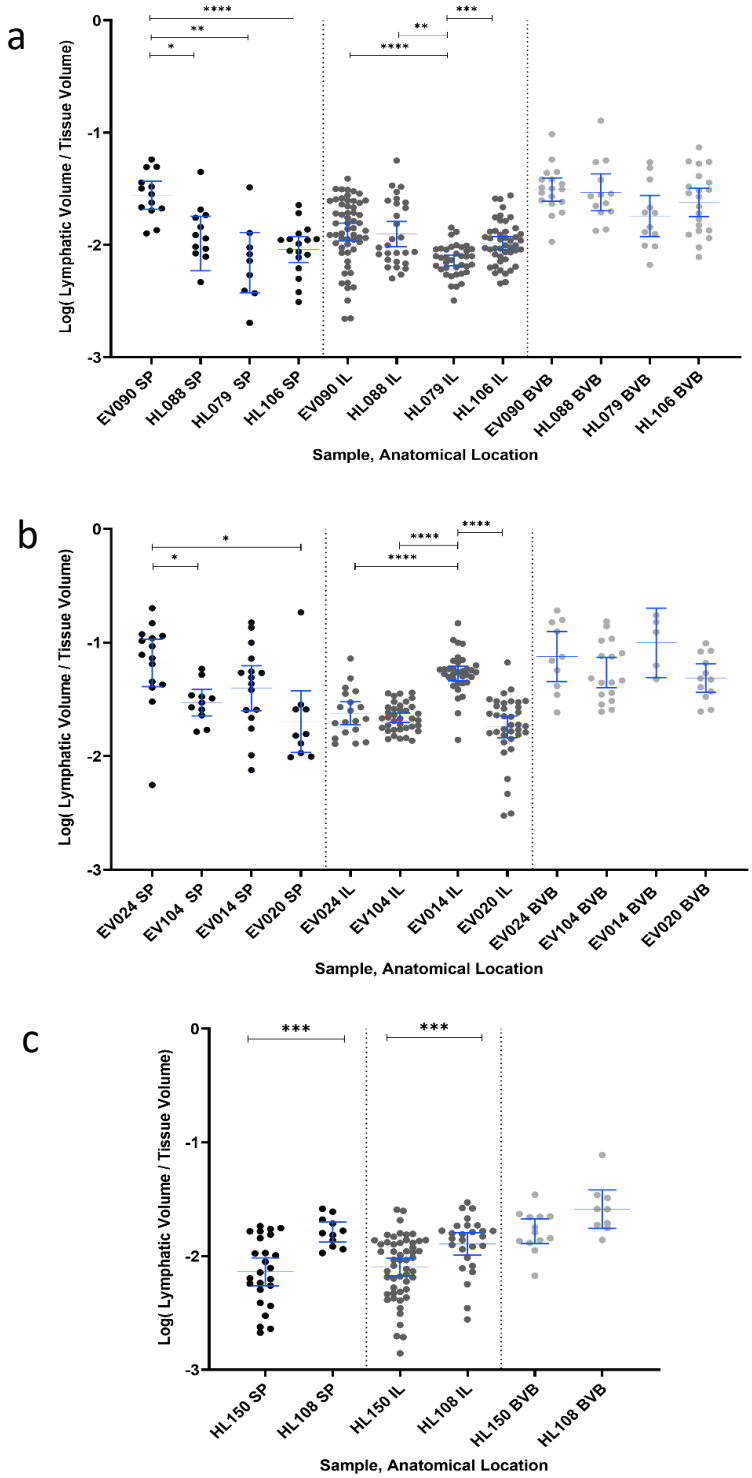

Figure 5.5 Inter-sample Variation of Microlymphatic Networks within Clinical Groups. The statistical comparison results of the transformed volume/ tissue volume dataset for the same

microlymphatic networks between samples of **a** the control group **b** the active disease group **c** the COPD group. Blue bars are showing the mean value and the 95% confidence interval. Statistical significance denoted as described section 5.2.6.

5.3.3 Network Representation within the Secondary Lobule is Similar in Each Clinical Group

The proportion of anatomically located microlymphatic networks in each clinical group, sampled as VOIs (as detailed in Chapter 2) are shown in Figure 5.6. This analysis suggests the representation of each anatomical location, and thus microlymphatic networks are similar between clinical groups, permitting fair comparisons of the morphology between these networks.

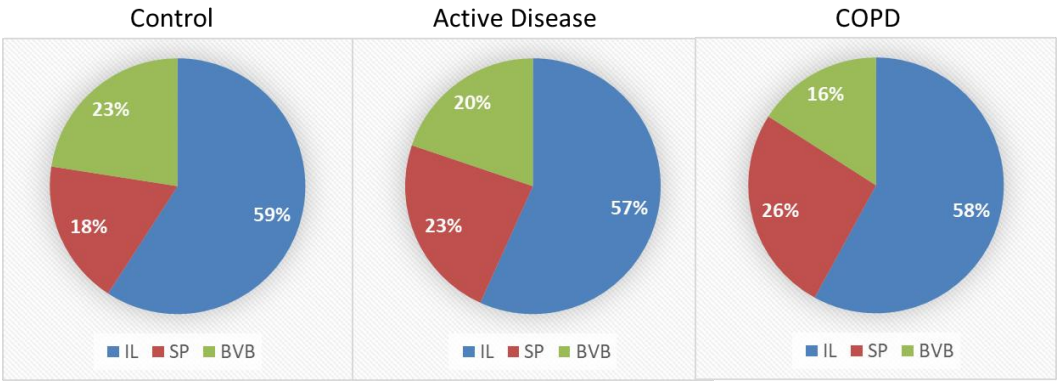

Figure 5.6 Proportion of Categorised Lymphatic Networks in Each Clinical Group. Data are given as a percentage of the total number of VOIs. The control group had 284 VOIs across 4 samples. The active disease group had 222 VOIs across 4 samples. The COPD group had 138 VOIs across 2 samples.

5.3.4 The Morphology and Statistical Comparison of Different Microlymphatic Networks Within Clinical Groups

The median value for all the morphometric data for each anatomically associated lymphatic network within each clinical group is summarised in Table 5.1. All data, including statistical comparisons, of the microlymphatic network morphology between each anatomical location is given for the control (Figure 5.7), active disease (Figure 5.8), and COPD (Figure 5.9) groups.

Within all three clinical groups, there was no difference seen in the morphometry between the IL and SP microlymphatic networks for the normalised volume, normalised surface area, normalised branch number and normalised junction number measures (detailed in full in Chapter 2, section 2.4.3). The exception to this was the active disease group where the volume of SP networks were statistically different from the IL networks (see Figure 5.8g). Differences were seen in all of these measures between the BVB network to both the SP and the IL networks in all three clinical groups.

The tortuosity measure was greater in the IL networks compared to the SP and BVB networks in the active disease samples which was not observed in the control and COPD groups (see Figure 5.8k).

Differences were seen in the fractal dimension measure of all three of the microlymphatic networks in each clinical group. The exception to this was in the COPD group where the fractal dimension of the SP microlymphatic networks were the same as the IL networks (see Figure 5.9l).

Table 5.1 Median Values of the Morphometry for Each Microlymphatic Network Within a Clinical group

Morphometric Measurement	Control			Active Disease			COPD		
	SP	IL	BVB	SP	IL	BVB	SP	IL	BVB
Lymphatic Volume/Tissue Volume	0.011	0.010	0.027	0.036	0.026	0.055	0.011	0.011	0.019
Surface Area /Tissue Volume	0.0039	0.0035	0.0058	0.0098	0.0093	0.0148	0.0038	0.0035	0.0060
Branch #/mm^3 Tissue Volume	580.8	557.4	907.5	1736	1857	2757	505.1	481.1	903.5
Junction #/mm^3 Tissue Volume	194.7	222.8	448	752.5	798.4	1256	227.5	218.4	411.5
Tortuosity	1.30	1.30	1.29	1.30	1.32	1.29	1.30	1.30	1.30
Fractal Dimension	2.45	2.38	2.63	2.57	2.46	2.73	2.40	2.34	2.51

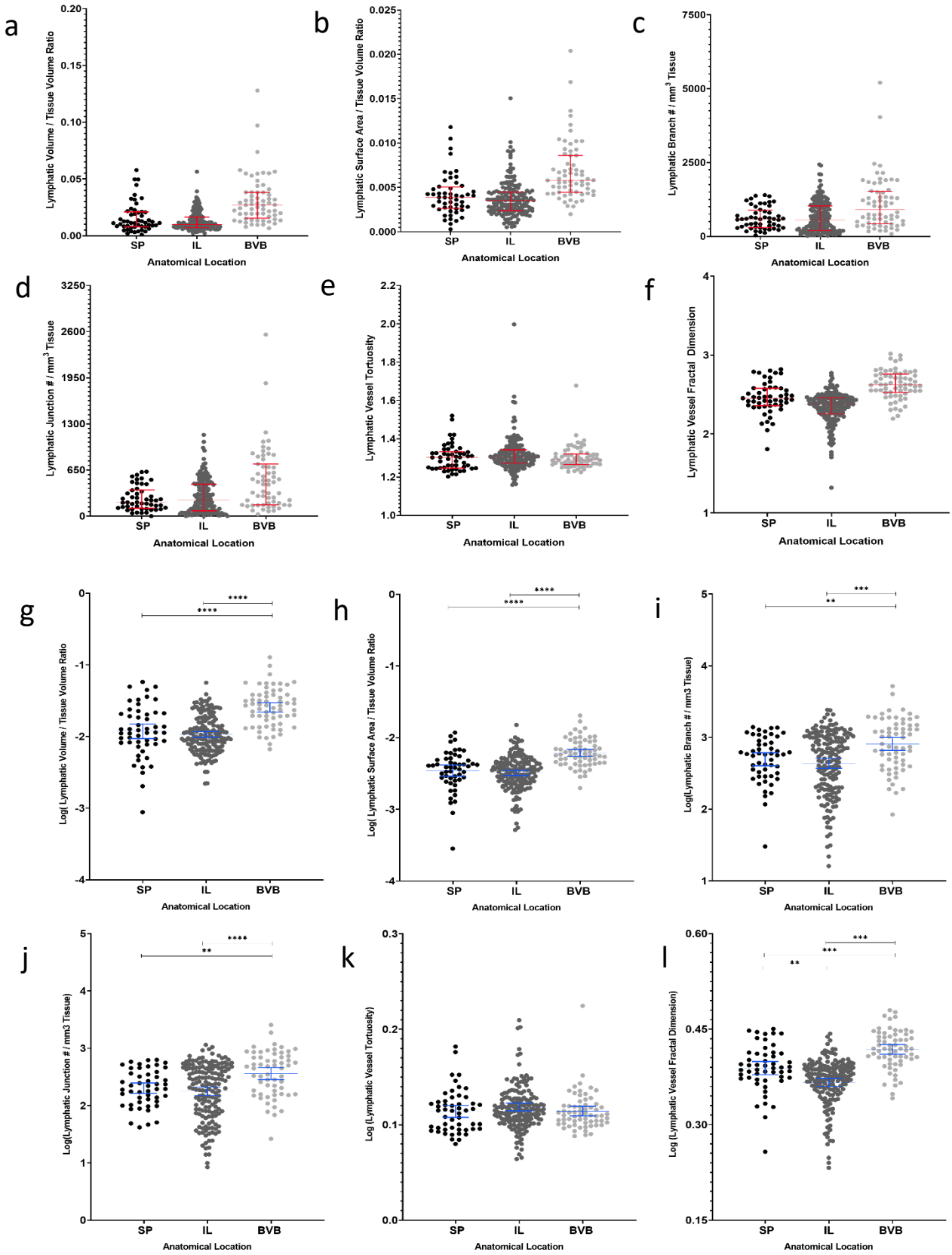

Figure 5.7 Human Pulmonary Microlymphatic Morphology in Control Lung Samples. a The volume/tissue volume ratio **b** surface area/ tissue volume ratio **c** branch number/tissue volume **d** junction number/ tissue volume **e** average vessel tortuosity **f** fractal dimension of the microlymphatic networks. (**a-f**) red bars are showing the median value and the interquartile range. (**g-l**) showing the log transform of (**a-f**) Blue bars are showing the mean value and the 95% confidence interval. Statistical significance denoted as described section 5.2.6.

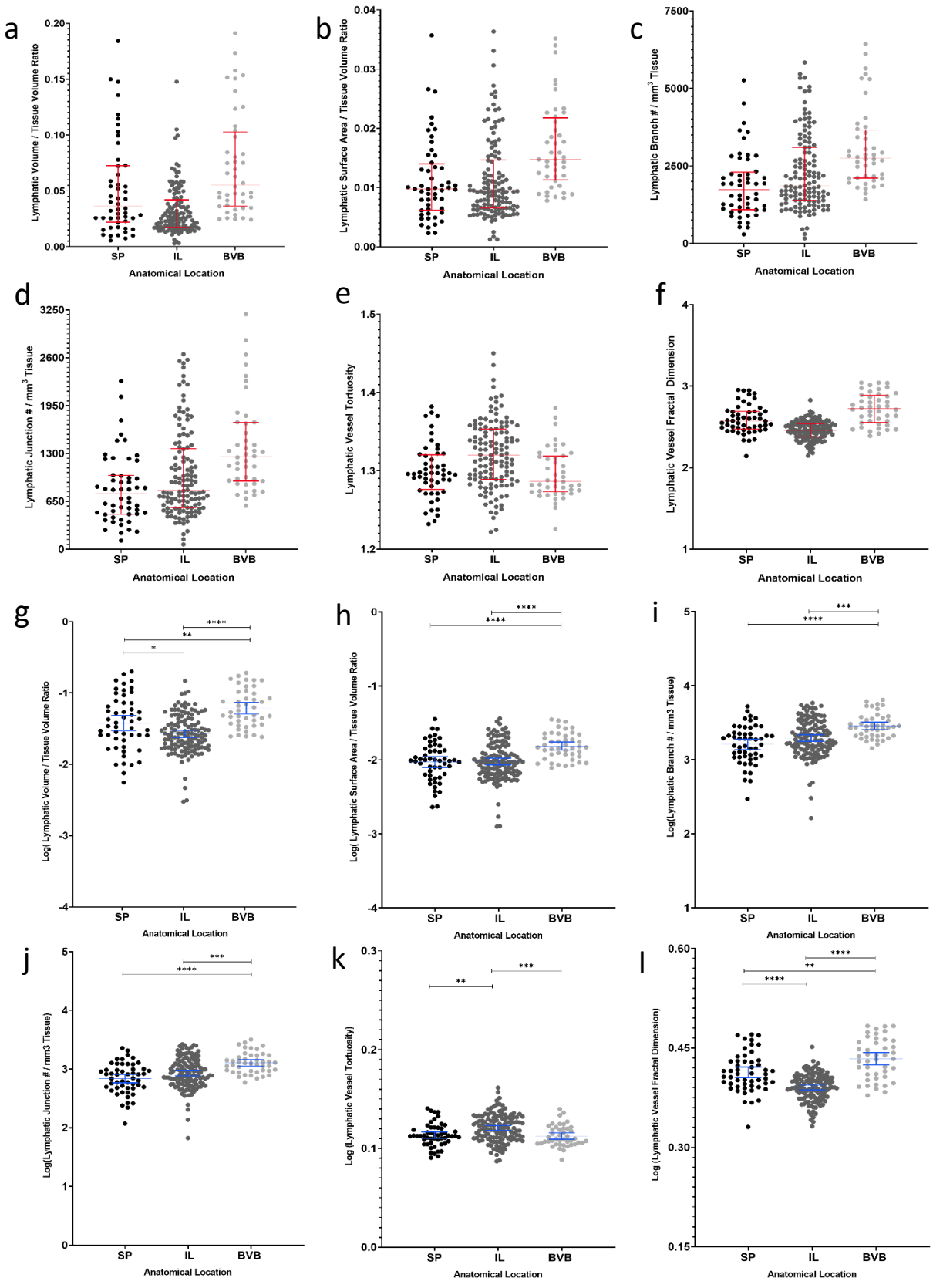

Figure 5.8 Human Pulmonary Microlymphatic Morphology in Active Disease Lung Samples. **a** The volume/tissue volume ratio **b** surface area/ tissue volume ratio **c** branch number/tissue volume **d** junction number/ tissue volume **e** average vessel tortuosity **f** fractal dimension of the microlymphatic networks. (**a-f**) red bars are showing the median value and the interquartile range. (**g-l**) showing the log transform of (**a-f**) Blue bars are showing the mean value and the 95% confidence interval. Statistical significance denoted as described section 5.2.6.

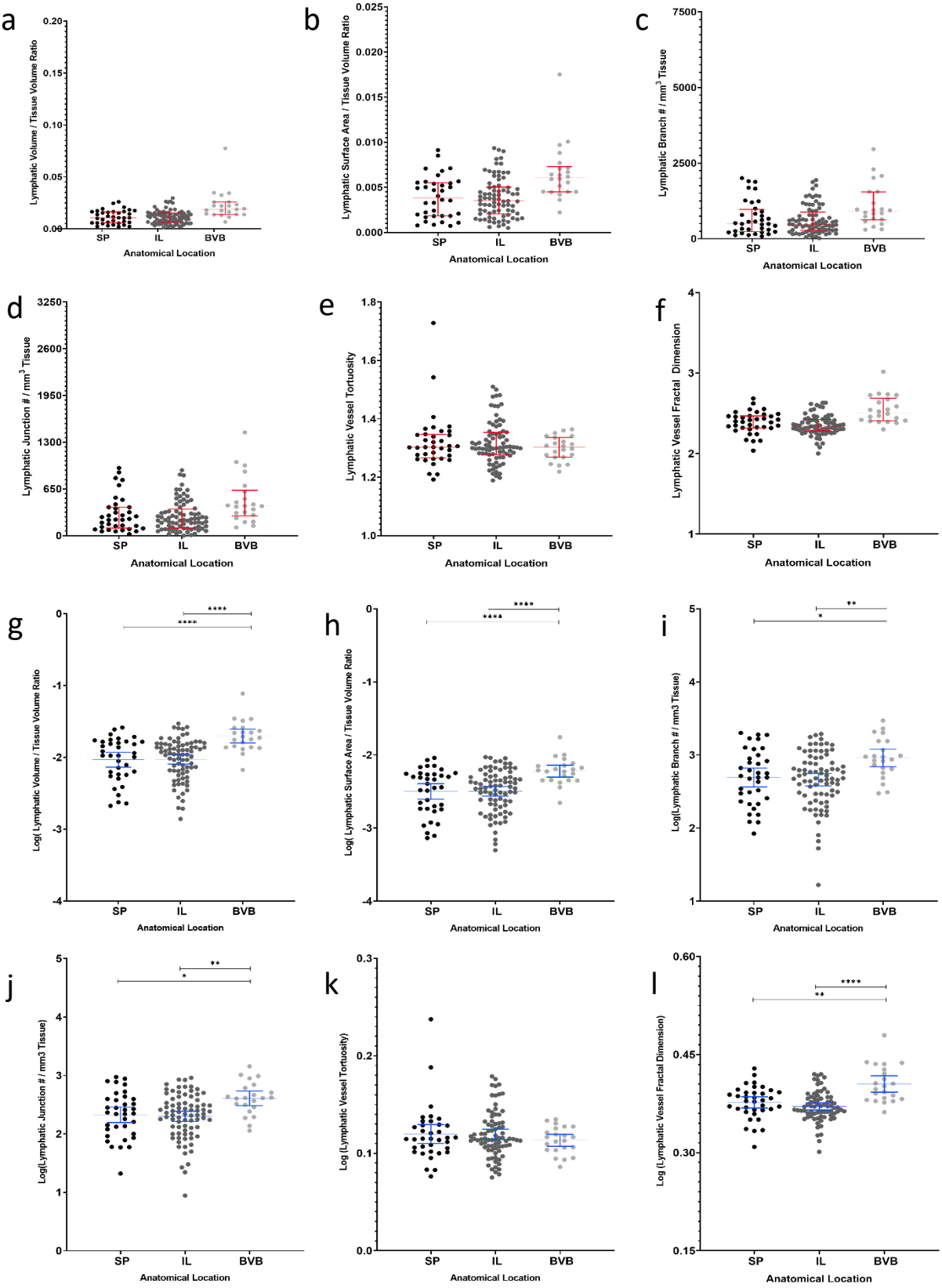

Figure 5.9 Human Pulmonary Microlymphatic Morphology in COPD Lung Samples. a The volume/tissue volume ratio **b** surface area/ tissue volume ratio **c** branch number/tissue volume **d** junction number/ tissue volume **e** average vessel tortuosity **f** fractal dimension of the microlymphatic networks. (**a-f**) red bars are showing the median value and the interquartile range. (**g-l**) showing the log transform of (**a-f**) Blue bars are showing the mean value and the 95% confidence interval. Statistical significance denoted as described section 5.2.6.

5.3.5 Patients with Active Pulmonary Disease Have Significantly Different Lymphatic Morphology to Other Clinical Groups

The median value for all the morphometric data for each anatomically associated lymphatic networks between a disease group is summarised in Table 5.2. This is the same data as shown in Table 5.1, but arranged differently to compare data between clinical groups. The statistical comparison of the log-transformed data, with the notation of the significance of the difference where applicable, is given in Figure 5.10.

There were no differences seen in any morphological measure of the SP, IL and BVB network between the control and COPD groups. The exception to this is in the fractal dimension measure of the SP network in the COPD group which was significantly different to that of the control group. The morphology of all three microlymphatic networks in the active disease group were significantly different to the same network in both the control and COPD group apart from the tortuosity measure where no differences were seen in all three networks (see Figure 5.10e).

Table 5.2 Median Values of the Morphometry for Each Microlymphatic Network Between Clinical Groups

Morphometric Measurement	SP			IL			BVB		
	Control	Active Disease	COPD	Control	Active Disease	COPD	Control	Active Disease	COPD
Lymphatic Volume /Tissue Volume	0.011	0.036	0.011	0.010	0.026	0.011	0.027	0.055	0.019
Surface Area /Tissue Volume	0.0039	0.0098	0.0038	0.0035	0.0093	0.0035	0.0058	0.0148	0.0061
Branch #/mm3 Tissue Volume	580.8	1736	505.1	557.4	1857	481.1	907.5	2757	903.5
Junction #/mm3 Tissue Volume	194.7	752.5	227.5	222.8	798.4	218.4	448	1256	411.5
Tortuosity	1.30	1.30	1.30	1.30	1.32	1.30	1.29	1.29	1.30
Fractal Dimension	2.45	2.57	2.40	2.38	2.46	2.34	2.63	2.73	2.51

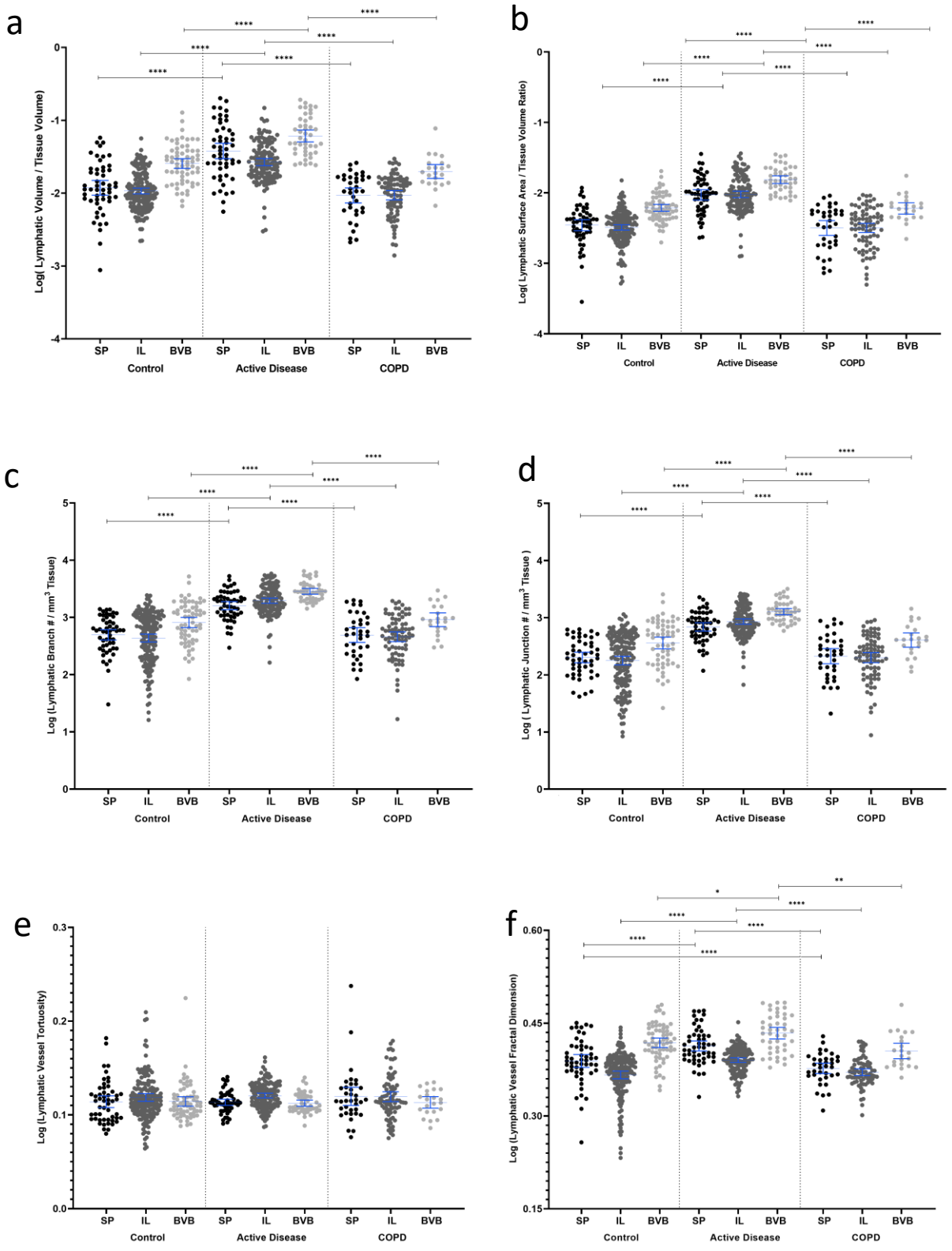

Figure 5.10 Statistical Comparison of the Morphology of Human Pulmonary Microlymphatic Networks Between Clinical Groups. a The log transform of the volume/tissue volume ratio **b** surface area/ tissue volume ratio **c** branch number/tissue volume **d** Junction number/ tissue volume **e** average vessel tortuosity **f** fractal dimension of the microlymphatic networks. Blue bars are showing the mean value and the 95% confidence interval. Statistical significance denoted as described in section 5.2.6 for the differences of the same anatomically associated microlymphatic network between clinical groups.

5.4 Discussion

5.4.1 Intra-sample and Inter-sample Variation of Microlymphatic Network Morphology

Intra-sample variation in the morphology of the microlymphatic networks is low. Data collected from individual subvolumes of the same lung can, therefore, be combined to describe the lymphatic morphometry of the whole tissue. This merging of data would only be valid if the anatomically associated networks and hierarchical populations of lymphatics are assessed separately.

In contrast, inter-sample variation in the morphology of the microlymphatic networks at the same anatomical locations was shown to be high. There could be several reasons for this observation. The sample size in each clinical group used in the study is small. Random anomalies due to natural human anatomical variation will, therefore, have a greater contribution to this variation than may be the case with a larger sample size. Also, there may have been insufficient reporting of clinical history at the time of sample collection. This could have led to an inaccurate classification of samples in this study. This shortcoming is a common occurrence in diagnostic samples as there is usually a single reason for sample harvesting, therefore getting a complete clinical history is not always achieved. As with the natural variation mentioned above, a larger sample size could help to dilute this limitation for future studies.

Greater variability was seen between the morphology of the IL and SP microlymphatic networks with none seen between the BVB lymphatic networks between samples. Putting the two methodological limitations detailed in the previous paragraph aside, this observation could suggest the IL and SP microlymphatic networks may be more sensitive to daily variation in fluid homeostasis as a result of breathing and gravitation influences compared to the BVB microlymphatic networks.

5.4.2 Structural Heterogeneity of Different Microlymphatic networks within Clinical Groups

The results of the comparative morphology between the different microlymphatic networks within clinical groups (section 5.3.4) showed interesting observations. The normalised volume of SP network was greater than the IL networks in the active disease group. This analysis was the only comparison where a change in normalised lymphatic volume was not equalled by a change in the normalised surface area measure. This result suggests a specific microlymphatic surface area/volume ratio is maintained in fluid homeostasis but changes when under high loads (this assumes patients with active disease have high fluid loads). The system either remodels itself to

increase the density of vessels if left under stress or regressess to original proportions if the fluid stress is lost.

Changes were also seen in the active disease group; for this group the tortuosity measure was significantly larger in the IL network compared to the SP and BVB networks. These changes were not seen between the control and COPD groups. This observation may be because in the IL region, high external pressures are exerted on the microlymphatic networks due to respiration. Less space is therefore available for the vessel volume to distend when under high fluid loads, and thus the walls buckle instead. An Increased inter luminal pressure with no ability to distend is hypothesised as the reason increased blood vessel tortuosity is seen in patients with hypertension (Helmberger *et al.*, 2014).

The lack of difference seen in the fractal dimension between the SP and IL microlymphatic network in the COPD group was another interesting observation. It should be remembered that the fractal dimension is not a normalised measure. This observation is a good example of where the morphometry data collected by the normalised data suggest the draining function of lymphatics in COPD patients is the same as the control group, but the absolute morphology may not be. This point is supported by the observation of the 3D morphology as shown in Figure 5.11, which clearly shows differences in the absolute structure of the SP and IL networks in the control group and not in the COPD group.

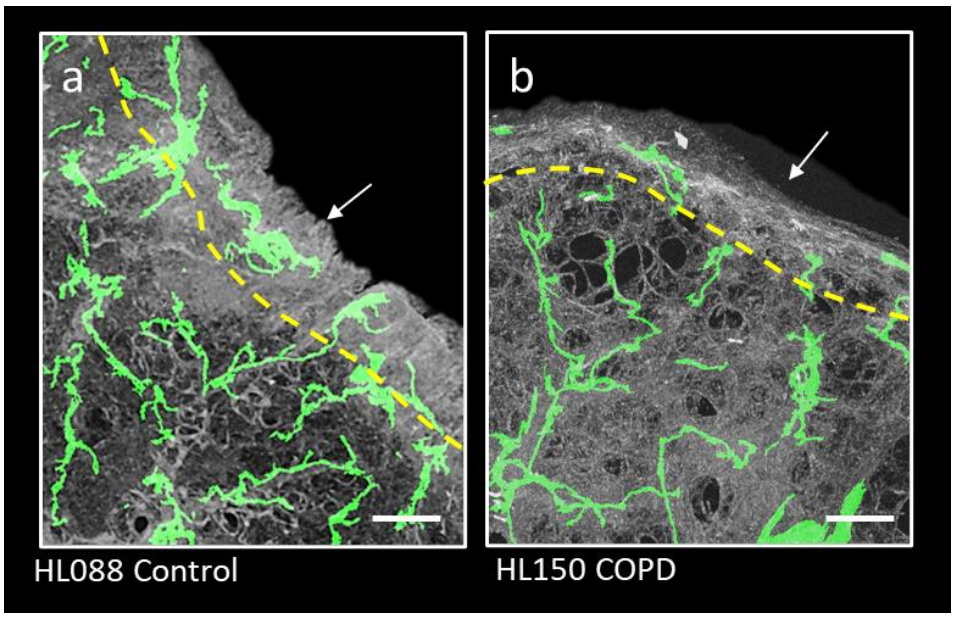

Figure 5.11 Images of the SP and IL Microlymphatic Networks in Control and COPD Groups. **a** Maximum intensity projection of the lymphatic segmentation data (green) and the µCT density map (grey) at the SP and IL regions in a control sample (HL088). The area between the dotted yellow line and pleural surface (white arrow) denotes the area within which VOIs are labelled as being SP. **b** Same presentation as in panel **a** but for a COPD sample (HL150). Scale bars =500 µm

5.4.3 Structural Heterogeneity of the Same Microlymphatic Networks Between Clinical Groups

With the exception of the vessel tortuosity measure, all other morphological measures of the microlymphatic networks at all three anatomical locations change significantly in the active disease group compared to the control group (see Figure 5.10). This change is expected as it is assumed the active disease system has been under a state of stress for a prolonged period, whether it be from sustained cardiovascular hypotension or osmotic changes that are seen in inflammatory responses to smoking. These stresses could increase vascular growth mediators and increase interstitial fluid accumulation, both known to induce lymphangiogenesis (Bhandari *et al.*, 2006; Boardman & Swartz, 2003; Favre *et al.*, 2003).

The level of significance between the active disease and control groups in the fractal dimension measure is less in the BVB networks compared to the SP and IL networks. The present finding counters the only study of acute pulmonary inflammation *(Mycoplasma pulmonis* infection) in the mouse model (Baluk *et al.*, 2014). The authors showed iBALT associated (equivilant to BVB associated in this text) lymphatic networks contributed most to the increase in lymphatic area density. It should be noted however, that IL and SP lymphatics are not as abundant in the mouse compared to the human (Baluk *et al.*, 2014).

Despite the COPD patient's respiratory system being diseased, the tissue at the time of biopsy may not have the same acute stresses on their pulmonary system compared to the active disease samples. Indeed, the fact they were healthy enough to have surgery at the time of sample collection would suggest they were comparatively fit considering their extreme disease. Due to the manifestation of COPD, at some time point, it is assumed that all these patients have had some level of active disease in the past. Results section 5.3.5 showed COPD patients have the same normalised microlymphatic morphology as the same networks in the control group (Figure 5.10). These results suggest the changes to the lymphatic network that probably would have occurred in the past during active disease may have been a temporary event, and permanent remodelling of the lymphatic network did not occur. Only temporal larger-scale studies would be able to support this hypothesis; therefore, animal studies will be necessary for the future to further this work.

In the induced pulmonary inflammation model in the mouse, the authors showed pulmonary lymphatic expansion is maintained after antibiotic treatment of the *Mycoplasma pulmonis* infection (Baluk *et al.*, 2014). However, the longest time point after antibiotic treatment the lungs were imaged was 2 weeks. Arguably imaging the lungs at a later timepoint after confirming the

infection was resolved by microbiology would be a more comparable dataset to the present study.

5.4.4 Limitations of Analysis

The largest limitation of the analysis presented is the sample size; this is evidenced in the results of the inter-sample variation study. Naturally, a total sample size of ten is not enough to make conclusions of high certainty. In addition, recycling the same data for multiple analyses is not ideal. However, as an observational study, multiple hypotheses have now been established from the collected data to permit a more informed study design. This design can be powered to collect more statistically conclusive results in the future.

The analysis in this chapter assumes the anatomical populations are discrete and not continuous as indicated in the previous chapter; this limitation is recognised and was discussed in detail in Chapter 4, section 4.4.3, but remains the most efficient method for lymphatic network comparison between samples.

Another limitation of this analysis is in the grouping of clinical samples. COPD patients have a well-established diagnostic procedure (GOLD standard), however, for the control and active disease groups, categorising each sample was a subjective process and extremely limited by the sample size. It was therefore justified that, despite the influence of multiple testing on the statistical results, the clinical groups were compared three ways, not just to the control group.

5.5 Conclusions

The observational results of this chapter suggest there is no difference in the morphology of the same microlymphatic network within human lung samples. However, the variation in morphology of the SP and IL networks between samples, even once grouped by clinical history, is high. Although this inter-sample variation could be natural variation, the fact no differences are seen between samples in the BVB network suggests the SP and IL microlymphatics could have a dynamic morphology that is sensitive to small changes in the physiological state of the lung at sample harvesting.

Microlymphatic morphology appears to be significantly altered in all normalised morphological measures across all microlymphatic networks during acute physiological lung stress. This observed change was above that seen in intra-group variability. Finally, despite some observational differences, the normalised morphology of the COPD group appears to be not significantly different from the control group.

In the future, to consolidate the findings of this chapter for the human lung, larger sample sizes will be needed. Preferably, in conjunction with this, temporal studies on animal models will be necessary to test hypothesis of pulmonary lymphangiogenesis that have been put forward from this chapter's results.

Chapter 6 3D Modelling of Fluid Drainage in the Peripheral Human Lung

6.1 Introduction

The two previous chapters have used 3D structural observation and quantitive morphology to describe lymphatic populations in peripheral human lung in differing states of disease. Based upon normalised morphology alone, these data suggest microlymphatic networks in different locations function differently. In addition, it is hypothesised that the same microlymphatic network functions differently in patients with acute but not chronic lung disease compared to the control.

This chapter investigates how differences in 3D lung geometry, as seen in the previous two chapters, may influence fluid movement through, and drainage from the pulmonary interstitium using image-based mathematical modelling. Image-based mathematical modelling permits a more sophisticated assessment of how the microlymphatic structure contributes to pulmonary function. Firstly, the mathematical model design, developed in full in Chapter 3, encompasses mechanical and biological complexities that cannot be predicted without computer simulation. Secondly, all structural domains in the pulmonary respiratory unit are used for the model simulation, thus, this assessment is not just limited to the relationship between microlymphatic and tissue morphology.

Unfortunately, the sophistication of these predictive methods comes with compromise. Image-based mathematical modelling within 3D geometries is time-intensive. Therefore, the 644 VOI geometries obtained and morphological assessed by the imaging methods (detailed Chapter 2), could not all be used for image-based modelling. Two small targeted studies will, therefore, be undertaken in this chapter.

Firstly, five VOI geometries from each of the subpleural (SP), intralobular (IL) and bronchovascular -bundle (BVB) microlymphatic networks will be used for simulation of mathematical model design. The results from these simulations will be compared to the conclusions made in Chapter 5 to see if, like the quantitative normalised morphology assessment, the model predicts the SP and IL networks to have a similar fluid drainage function.

Secondly, five VOI geometries of the IL microlymphatic network from each of the control, active disease and COPD groups will be used for simulation of the mathematical model design. These

simulation results will also be used to see if, like the quantitative normalised morphology assessment implies, flow patterns in the active disease VOIs are different compared to the control and COPD lung IL networks.

Here it is important to emphasise that the only change between each model simulation for both studies will be the input geometry. Input parameters will remain as healthy lung input parameters as detailed in Chapter 3, section 3.1.4. This will be a limitation of the active disease and possibly the COPD simulations as it would be expected the parameters of these patents when *in-vivo* would not be the same the healthy lung. Data on how these parameters actually vary in the disease lung compared to healthy lung is not available.

6.2 Specific and Additional Materials and Methods

6.2.1 Modelling Fluid Movement in Different Anatomical Locations of the Secondary Lobule

Using the image data from the four control lung samples, five VOIs were randomly selected from each of the SP, IL and BVB categories from a total pool of 168, 52 and 64 VOIs respectively. Chapter 2, section 2.1 detailed the criteria for control group classification, and sections 2.4.1 – 2.4.2 detailed VOI sampling methods. A diagrammatic representation of this selection is shown in Figure 6.1a within an example control lung subvolume.

Each VOI was made up of the segmented lymphatic, blood vessel, and interstitial image geometries. The BVB VOIs had segmented airway geometries too. Each VOI underwent VOI editing, processing and meshing as detailed in Chapter 3 sections 3.2.1 and 3.2.4. The average number of tetrahedral mesh elements for the SP, IL and BVB VOIs were 6.5×10^6, 4.9×10^6, and 11.2×10^6 respectively. Mathematical model design 2 as described in Chapter 3 section 3.2.6 was simulated within all fifteen VOIs using COMSOL.

The following assumptions were made to enable this simulation:

- All independent parameters were constant across each domain with that quoted from the current literature (see Chapter 3, Table 3.1).
- The pre-capillary sphincters were in a relaxed tone allowing full blood perfusion of the VOIs. Therefore, blood pressure = 2000 Pa.
- Initial flow velocities in the lymphatic and blood vessels domains were quoted from the current literature (see Chapter 3, Table 3.1).
- The lymphatic vessel osmotic pressure was the same as the interstitial osmotic pressure.

- The osmotic reflection coefficient is the same for each vessel and constant across their domains.
- Pressure downstream of the lymphatic vessels is maintained at -1200 Pa.
- All microlymphatic structures had primary valves of equal influence in all VOIs.
- The airway domain seen in the BVB VOIs were assumed as having no flux on their boundary like the VOI external boundaries (equation 3.9) and no flow within like alveolar airspaces.

The 3D simulation outputs (as described in Chapter 3, section 3.2.3) will be presented by the mean and the standard error of the five simulation results in each anatomical location. The standard error was calculated by dividing the standard deviation by the square root of the VOI number in each group (5). The non-normalised simulation results represent the functionality of the whole VOI which, due to the VOI size-refinement studies, encompasses a complete repeating unit of the microlymphatic network. The normalised simulation results can imply to what extent the shape of the domain geometries in the VOIs influences the simulation results.

An estimate of the fluid dynamics and pressure changes in the secondary lobule was also made. This estimate was calculated using the mean values of the model results from all three VOIs, weighted by their proportional representation of the control group within the secondary lobule (data taken from Chapter 5, Figure 5.6.). This estimate was only made using outputs that were averages or that were normalised by domain volume or surface area.

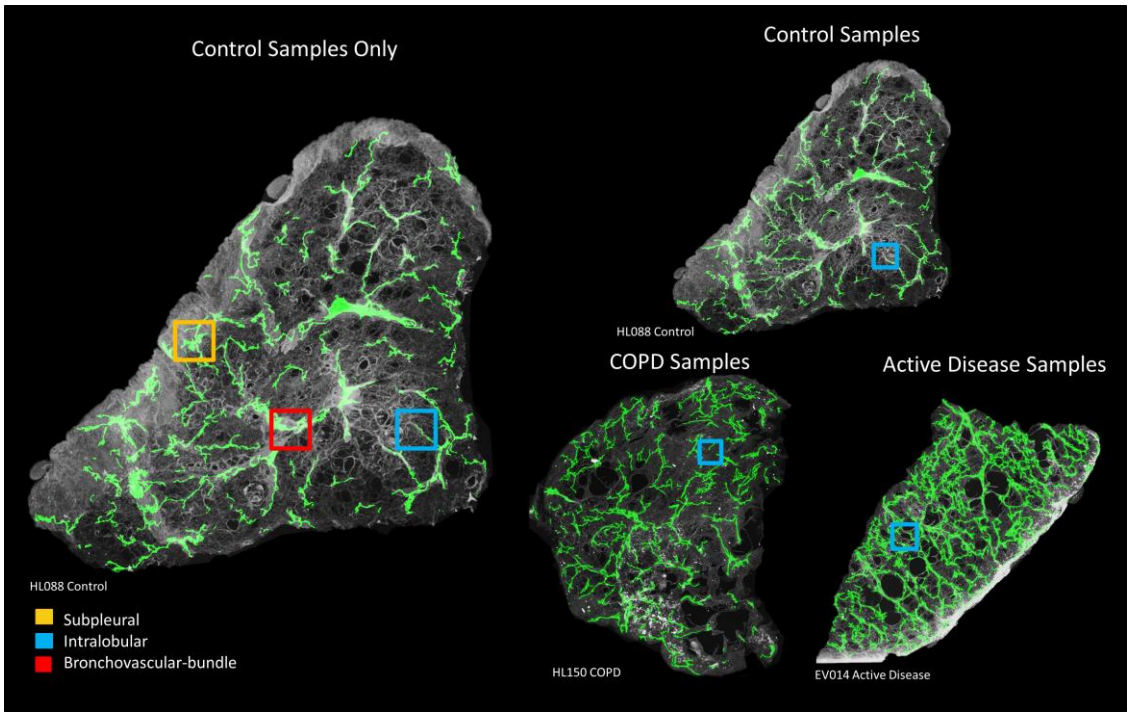

Figure 6.1 Visual Description of the Two Modelling Studies that Investigate the Influence 3D Geometry has on Fluid Dynamics in Peripheral Human Lung. a Illustrating the first study that compares how fluid moves and drains in different anatomical locations in the secondary lobule. VOIs were randomly selected from all 4 of the control samples. **b** Illustrating the second study

that compares how fluid moves and drains in IL VOIs in different clinical groups. IL VOIs were randomly selected from all samples in each clinical group. Yellow box=location of SP VOI, Blue box—location of IL VOI, Red box= location of BVB VOI. Images not to scale.

6.2.2 Modelling Fluid Movement in the Intralobular Region in Different Clinical Groups

Five VOIs of the IL microlymphatic network were randomly selected from each of the active disease group (pool of 126 VOIs) and COPD group (pool of 80 VOIs). Chapter 2, section 2.1 detailed the criteria for clinical group classification, and sections 2.4.1 – 2.4.2 detailed VOI sampling methods. A diagrammatic representation of this selection (including the control IL VOI section) is shown in Figure 6.1b within example subvolumes of lung taken from the clinical categories.

Each VOI was made up of the segmented lymphatic, blood vessel, and interstitial image geometries. Each VOI underwent VOI editing, processing and meshing as detailed in Chapter 3 sections 3.2.1 and 3.2.4. The mean number of tetrahedral mesh elements for the IL active disease VOIsand IL COPD VOIs were, $11.3x10^6$, and $3.8x10^{6,}$ respectively. Mathematical model design 2, as described in Chapter 3, section 3.2.6 was simulated within all ten VOIs using COMSOL.

The same assumptions were made as detailed in section 6.2.1 to enable this simulation except airway domains were not accounted for in these simulations as they were not present in the IL VOIs.

The 3D simulation outputs (as described in Chapter 3, section 3.2.3) will be presented by the mean average and the standard error of the five simulation results for the IL microlymphatic network in the three clinical groups. The same data as collected in section 6.2.1 was used for the control IL VOIs. As the model will only be simulated using the IL lung geometry, no estimation of secondary lobule fluid dynamics and pressure changes will be made.

6.3 Results

Model simulation times, error values, and computer memory usage for all simulations in this Chapter are given in Appendix E. The mass balance (M^{in}- M^{out}) of the inlet and outlet boundaries was smaller than the model simulation error for all 25 VOIs. Mass was, therefore, conserved in every simulation presented in this chapter.

6.3.1 Fluid Flow and Clearance in Anatomical Regions of the Human Lung

Figure 6.2a, c and e show schematic representations of geometry pressure (Pa) from the model simulation results in randomly chosen examples of the SP, IL, and BVB VOIs of control human lung

tissue respectively. The interstitial tissue pressure has been omitted to enable visualisation of the vessel domains. Darcy's velocity streamlines, which show the trajectory of fluid movement within the interstitium, are also shown as black lines. The labelled geometry of the example SP, IL and BVB VOIs is shown in Figure 6.2b, d and f, respectively. Here, the interstitium geometry was made transparent in the viewing line of the vessel geometries, so the vessel geometries were visible.

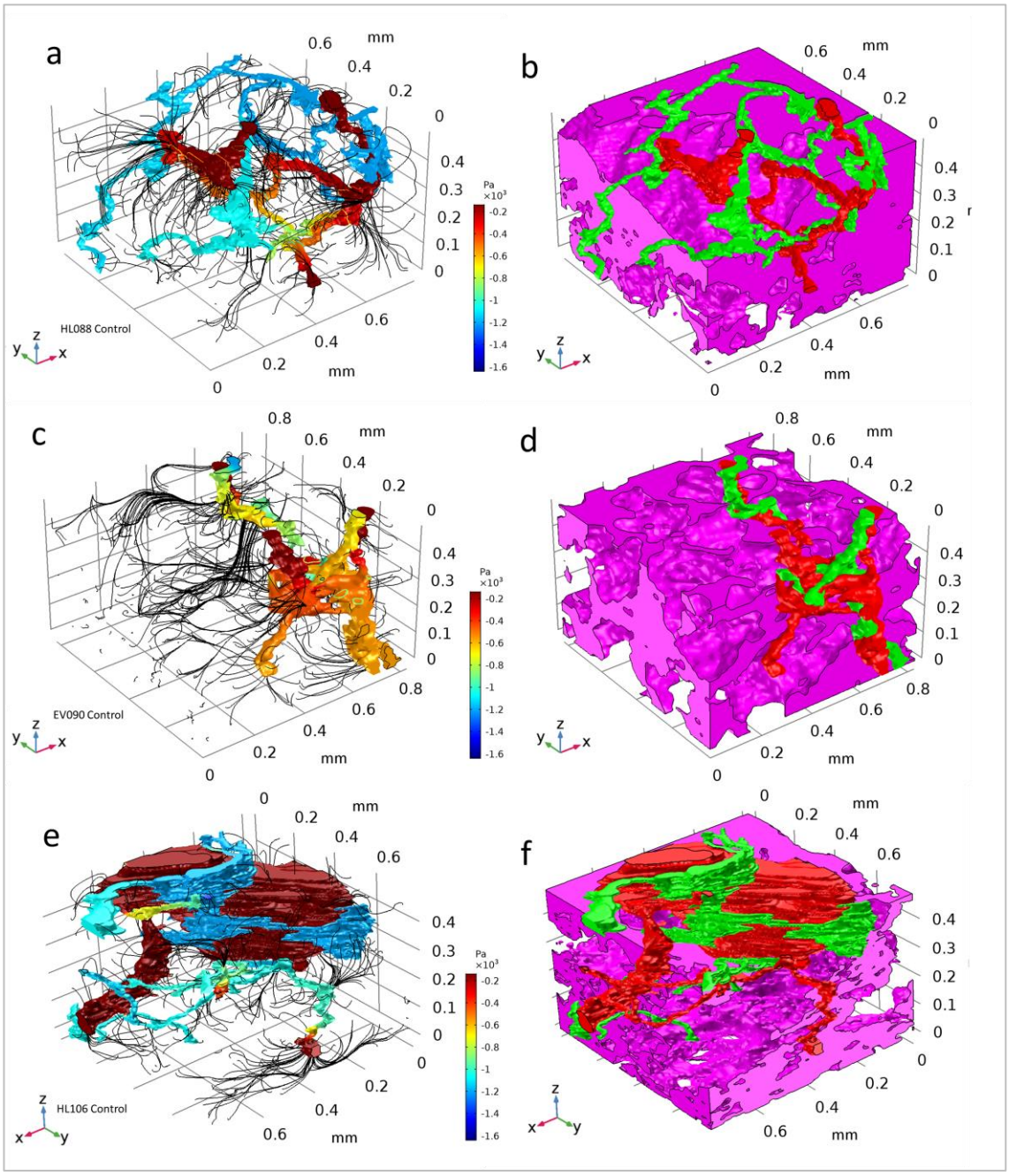

Figure 6.2 Examples of the Model Simulation Results in VOI Geometries from Different Anatomical Locations in the Secondary Lobule. a The vessel pressure results (Pa) and the Darcy's velocity streamlines (black) in one example of the SP VOI group. **b** The labelled geometry for the SP VOI in panel **a**. red = Blood vessel, Green = lymphatic vessel, pink= interstitial tissue. **c** and **d** shows the same information as panels **a** and **b,** but for the example IL VOI. **e** and **f** shows the same information as panels **a** and **b**, but for the example BVB VOI.

In all 15 VOI simulated in the control tissue, fluid was observed to be projected to, and drained from, all parts of the interstitial tissue geometry that were directly connected to a blood or lymphatic vessel domain (see Darcy's velocity streamlines in Figure 6.2 for examples in each anatomical location). On observation, the IL VOIs had higher pressured lymphatic vessels and longer Darcy's velocity streamlines compared to the SP and BVB VOIs.

Figure 6.3 shows the mean and the standard error of the numerical simulation results of the five VOI from each anatomical location along with the estimates for the secondary lobule where relevant (as detailed in section 6.2.1).

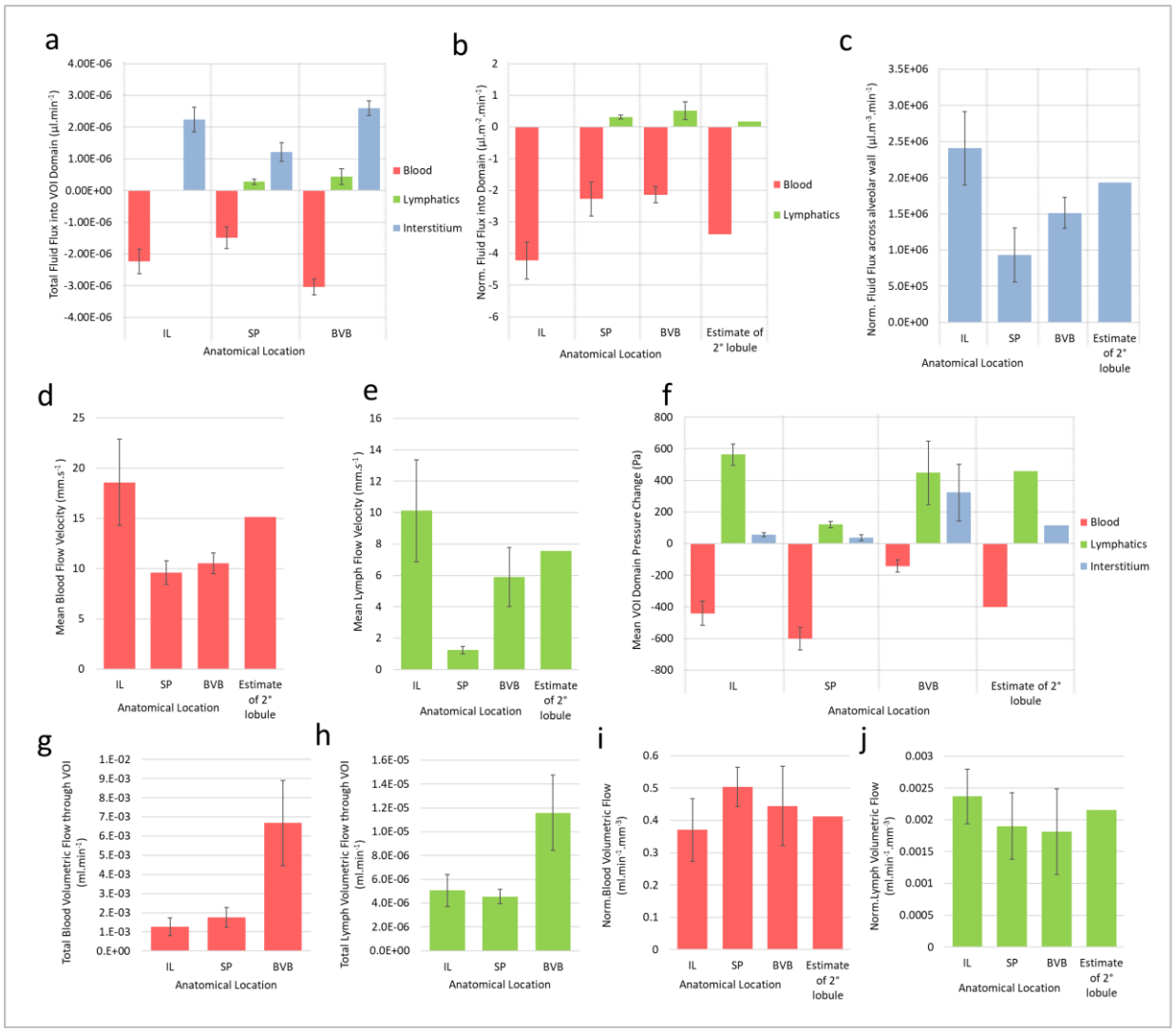

Figure 6.3 Numerical Simulation Results of the Model Simulated in Different Geometries within the Secondary Lobule. a Total fluid flux into the interstitium, lymphatic and blood vessel domains, Q_{Total}, Q^{L}_{Total} and Q^{B}_{Total}. **b** Q^{L}_{Total} and Q^{B}_{Total} normalised by the surface area of the boundary, Q^{L}_{norm} and Q^{B}_{norm}. An estimate of the secondary lobule is given (see text for details)**. c** Fluid flux across alveolar wall normalised by the volume of the interstitial domain, Q^{A}_{norm}. An estimate of the secondary lobule is given**. d** and **e** Mean blood domain and lymphatic domain fluid flow velocity, u^{L} and u^{B}, respectively. **f** The mean pressure change from baseline within the domains of the interstitial, lymphatic vessel, and blood vessel, P, P^{L} and P^{B} ,respectively. An estimate of the secondary lobule is given**. g** and **h** Total blood and lymphatic volumetric fluid flow

integrated within the volume of each domain**,** V^{B}_{Total} and $V^{L}_{Total,}$ respectively. **i and j** V^{B}_{Total} and V^{L}_{Total} normalised by the volume of the domain, V^{B}_{norm} and $V^{L}_{norm.}$ An estimate of the secondary lobule is given**.** Error bars= Standard error of the mean (n=5/group). IL= intralobular, SP=Subpleural, BVB=Bronchovascular bundle.

Although the model simulated flow within the blood vessel geometries, this work principally concerned the pulmonary interstitium drainage and the lymphatic fluid clearance. Therefore, the blood vessel results in Figure 6.3a.b,d,f,g and i, will only be mentioned where necessary in the discussion section. The blood vessel simulation results were still presented as they influence the pressures in the pulmonary interstitium and thus the lymphatic fluid clearance.

The anatomical VOIs with the highest total flux into the lymphatic vessel, $Q^{L}_{Total,}$ was the BVB VOI (see green bars Figure 6.3a). The SP VOI showed inward lymphatic fluid flux but at a slower rate to the BVB VOI. The IL VOI showed no inward fluid flux. This pattern of results was the same when the result was normalised to the lymphatic surface area of the VOI (see green bars Figure 6.3b). The model's estimate for the fluid flux into the lymphatic system in the secondary lobule was 0.18 $\mu l.m^{-2}.min^{-1}$.

The total flux into the interstitial domain $Q_{total,}$ calculated by the balance of fluid leaving the blood vessel, Q^{B}_{total} and fluid entering the lymphatic vessel $Q^{L}_{total,}$ infers the IL VOI and BVB VOIs had higher rates of alveolar fluid accumulation compared to the SP VOIs (see blue bars Figure 6.3a). It was predicted the IL VOI had the highest rate of alveolar fluid accumulation when normalised by interstitial volume, $Q^{A}_{Norm,}$(see blue bars Figure 6.3c). The model's estimate for alveolar fluid accumulation, normalised by interstitial volume in the secondary lobule was $1.94x10^{6}$ $\mu l.m^{-3}.min^{-1}$.

The mean microlymphatic fluid flow velocity, u^{L}**,** was highest in the IL VOIs, second highest in the BVB VOIs and lowest in the SP VOIs (see Figure 6.3e). The model's estimate for the average lymphatic flow velocity in the secondary lobule was 7.5 $mm.s^{-1}$.

The average increase in lymphatic domain pressure, P^{L}, from the baseline of -1200 Pa was highest in the IL VOIs, followed by the BVB VOIs, with the SP VOIs having the smallest average increase in lymphatic vessel pressure (see green bars Figure 6.3f). The model's estimate for the average change in lymphatic vessel pressure in the secondary lobule was +456 Pa.

The average increase in interstitial domain pressure, P, from the baseline of -1064 Pa was similar in the IL and SP VOIs (see blue bars Figure 6.3f). The average increase in interstitial domain pressure the BVB VOIs was much greater than the IL or SP VOIs. The model's estimate for the average change in interstitial pressure in the secondary lobule was +114 Pa.

Finally, the total lymphatic volumetric fluid flow integrated across the volume of each domain, $V^{L}_{Total,}$ was the same in the IL VOIs and the SP VOIs, but much higher in the BVB VOI (see Figure

6.3h). When this result was normalised by lymphatic vessel volume V^{L}_{Norm}, the IL VOI has the highest volumetric flow rate with the BVB VOIs having the lowest (see Figure 6.3j). The model's estimate for the lymphatic volumetric flow normalised by lymphatic vessel volume in the secondary lobule was 0.0026 $ml.mm^{-3}.min^{-1}$.

6.3.2 Changes in Intralobular Fluid Flow and Clearance in Disease States

In this section, the data displayed for the IL VOIs of the control group are the same as detailed in section 6.3.1.

A schematic representation of the the model simulation result in example IL VOIs taken from the control, active disease, and COPD clinical groups are shown in Figure 6.4a, c and e, respectively. Each VOI is displayed next to their labelled geometry (see Figure 6.4 b, d and f). The setup of these graphical representations are the same as detailed in section 6.3.1.

In the ten IL VOIs simulated in the active disease and COPD groups, fluid was observed to be projected to and drained from all parts of the interstitial tissue geometry that were directly connected to a blood or lymphatic vessel domain (see Darcy's velocity streamlines in the sample VOI in Figure 6.4c and e). However, compared to the control group and active disease groups, there were more regions of interstitial tissue where there was no observed fluid movement in the COPD group (see Figure 6.4 e). On observation, the control and COPD IL VOIs had higher pressured lymphatic vessels and longer Darcy's velocity streamlines compared to the active disease IL VOIs (again, for examples see Figure 6.4).

Figure 6.5 shows the mean and the standard error of the numerical simulation results of the five IL VOI from each clinical group.

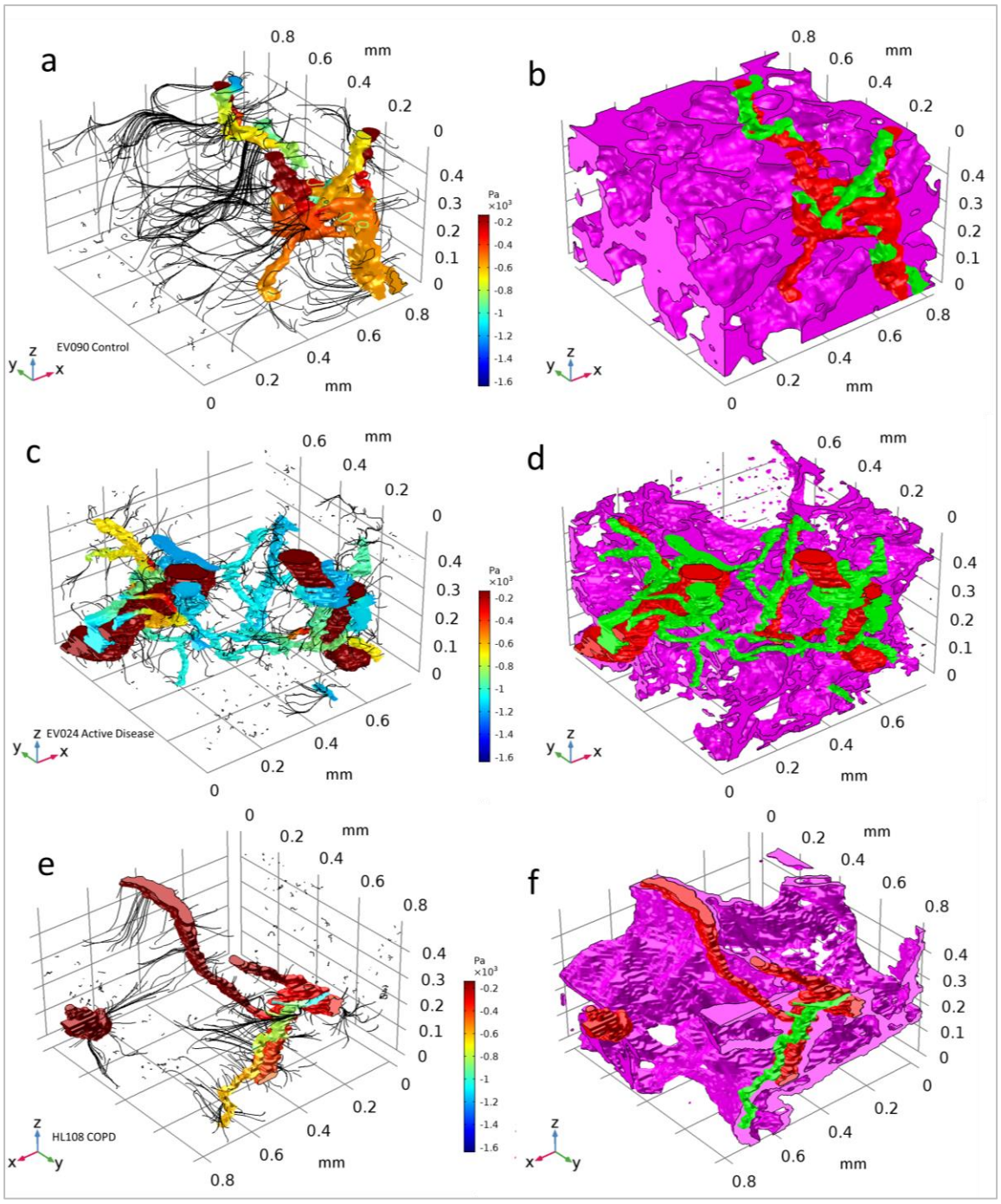

Figure 6.4 Examples of the Model Simulation Result in IL VOI Geometries from Different States of Human Lung Disease. a The vessel pressure results (Pa) and the Darcy's velocity streamlines (black) in one example of the control VOI group. **b** The labelled geometry for the control VOI in panel **a**. red = blood vessel, green = lymphatic vessel, pink= interstitial tissue. **c** and **d** shows the same information as panels **a** and **b,** but for one VOI in the active disease group. **e** and **f** shows the same information as panels **a** and **b**, but for one VOI in the COPD group.

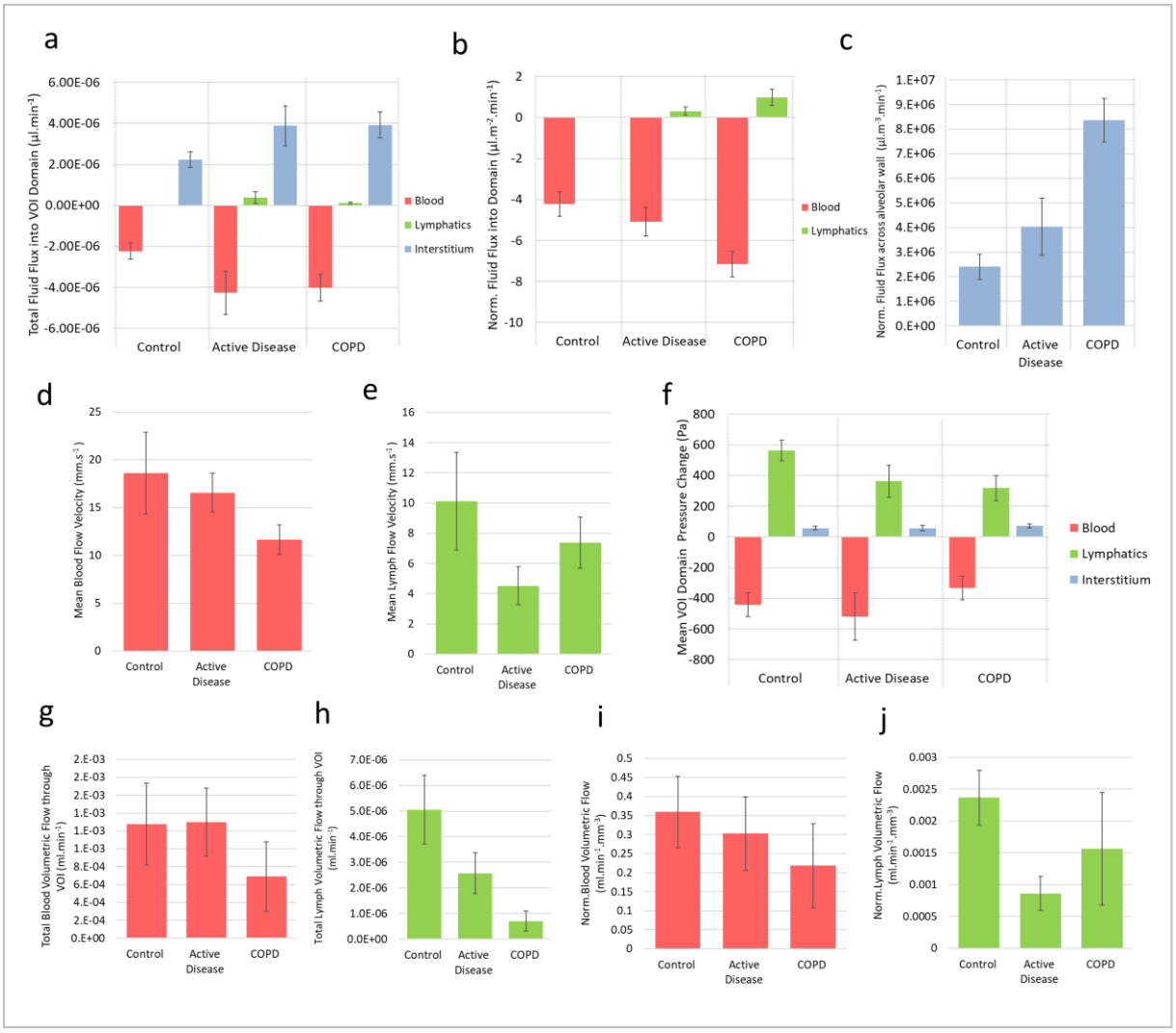

Figure 6.5 Numerical Simulation Results of the Model Simulated IL Geometries within Different Clinical Groups. **a** Total fluid flux into the interstitium, lymphatic and blood vessel domains, Q_{Total}, Q^{L}_{Total} and $Q^{B}_{Total.}$ **b** Q^{L}_{Total} and Q^{B}_{Total} normalised by the surface area of the boundary, Q^{L}_{norm} and Q^{B}_{norm}**. c** Fluid flux across alveolar wall normalised by the volume of the interstitial domain, $Q^{A}_{norm..}$**. d** and **e** Mean blood domain and lymphatic domain fluid flow velocity, u^{L} and u^{B} respectively. **f** The mean pressure change from baseline within the domains of the interstitial, lymphatic vessel, and blood vessel, P, P^{L} and P^{B} , respectively**. g** and **h** Total blood and lymphatic volumetric fluid flow integrated within the volume of each domain**,** V^{B}_{Total} and $V^{L}_{Total,}$ respectively. **i and j** V^{B}_{Total} and V^{L}_{Total} normalised by the volume of the domain, V^{B}_{norm} and $V^{L}_{norm.}$ Error bars= Standard error of the mean (n=5/group). Control data is the same as shown in Figure 6.3.

As in section 6.3.1 the blood vessel results of the IL VOIs in each clinical group, shown in Figure 6.5 a.b,d,f,g and i, will only be mentioned where necessary in the discussion section.

The IL VOIs of the active disease group showed the highest total flux into the lymphatic vessel, $Q^{L}_{Total,}$ (see green bars in Figure 6.5 a). The COPD IL VOIs showed inward lymphatic fluid flux, but at a slower rate to the active disease group. This pattern of results reversed when the result was normalised to the lymphatic surface area of the VOI (see green bars Figure 6.5 b).

The total flux into the interstitial domain Q_{total}, calculated by the balance of fluid leaving the blood vessel, Q^{B}_{total}, and fluid entering the lymphatic vessel, Q^{L}_{total}, inferred the active disease group and COPD groups would have higher rates of alveolar fluid accumulation compared to the control group (see blue bars Figure 6.5 a). It was predicted that the COPD IL VOIs has the highest rate of alveolar fluid accumulation, relative to tissue volume. The lowest rate of alveolar fluid accumulation was predicted in the control IL VOIs (see blue bars Figure 6.5 c).

The mean microlymphatic fluid flow velocity, u^{L}, was highest in the control IL VOIs, second highest in the COPD IL VOIs and lowest in the active disease IL VOIs (see Figure 6.5 e).

The average increase in lymphatic domain pressure, P^{L}, from the baseline of -1200 Pa was highest in the control IL VOIs, followed by the active disease IL VOIs, with the COPD IL VOIs having the smallest average increase in lymphatic vessel pressure (see green bars Figure 6.5 f).

The average increase in interstitial domain pressure, P, from the baseline of -1064 Pa was identical in the control and active disease IL VOIs (see blue bars Figure 6.5 f). The average increase in interstitial domain pressure in the COPD VOIs was greater (by 16 Pa) than the control and active disease IL VOIs.

Finally, the total lymphatic volumetric fluid flow integrated across the volume of each domain, V^{L}_{Total}, was highest in the control IL VOIs with the COPD IL VOIs having the lowest (see Figure 6.5 h). When this result was normalised by lymphatic vessel volume V^{L}_{Norm}, the IL VOI the control IL VOIs still had the highest volumetric flow rate, but the active disease IL VOIs showed the lowest normalised volumetric flow rate (see Figure 6.5 j).

6.4 Discussion

6.4.1 The Influence of Pulmonary Geometry on Fluid Flow and Clearance in The Human Lung

Under normal lung parameters, the model predicted the IL microlymphatic network reached a pressure relative to the surrounding interstitium that initiated the primary valve constraint, thus, at equilibrium, no fluid entered the vessels across the whole VOI domain (see Figure 6.2a, Figure 6.3a and b). The increase in intraluminal pressure, and the average flow velocity were higher in the IL VOIs than that seen in the SP and BVB networks (see Figure 6.3e and f). Assuming no elastic properties of the vessel, one can conclude from these results that when the capillary sphincters are relaxed (conditions of ventilation and full perfusion), the IL microlymphatic network had reached its full capacity.

Interestingly, the model predicted the SP and IL networks drain fluid in equal volumes (from their VOI (see Figure 6.3h). Although the intraluminal pressure, and thus flow velocity in the SP microlymphatic network is lower than the IL network, the absolute lymphatic vessel volume is greater, therefore, it is understandable that the total volumetric flow through the SP VOIs is similar to the IL VOIs. This finding supports the conclusion of Chapter 5 that, based on the normalised morphology of the control samples, the SP and IL lymphatics are functionally the same.

The modelling data, however, adds more to the conclusion of the morphometric study. Unlike the IL microlymphatic network, the SP network had not reached full capacity of lymph flow. As stated, the pressure in the vessel was not high enough to close the primary valves as there was inward fluid flux into the SP lymphatic network. This SP network, therefore, has the potential for intraluminal pressure to rise, along with flow velocity, and ultimately volumetric flow.

This observation suggests that how the lymphatic vessels are positioned in space within the tissue volume, and relative to the blood vessel network, has an impact on drainage capacity of the vessels. The IL microlymphatic network runs close to the blood vessel, leaving a large volume of interstitial tissue without immediate drainage passages compared to the SP network (see Figure 6.2a,b,c and d). Once the lymphatic vessel proximal to the blood vessel reaches capacity, overflow of fluid from the blood vessel enters this interstitial space, and ultimately in to the alveolar space. In the SP network this fluid is drained by other vessels distributed in the tissue which are not present in the IL VOI instead of leaving through the alveolar wall. As seen in Figure 6.3a and f, the average change in interstitial pressure and inferred alveolar fluid accumulation is, therefore, higher in the IL VOIs compared to the SP VOIs.

In the BVB VOIs, microlymphatic pressure and flow velocity were higher than the SP VOIs but not as high as seen in the IL VOIs. However, the total volumetric flow through the BVB VOI was predicted to be 3x higher than the IL and SP network. The larger volume of the BVB microlymphatic network compared to the IL or SP networks give a reason for this discrepancy (as shown in Figure 6.2). The reasoning is confirmed by Figure 6.3j, where BVB VOIs show less volumetric flow than the other two networks when normalised by microlymphatic volume.

There was less interstitial tissue surrounding the BVB microlymphatic network compared to the SP and IL networks (as was evident in Figure 6.2 and the normalised lymphatic volume/ tissue volume measure in Chapter 5, Figure 5.7g). Higher average interstitial pressure is therefore seen in the BVB VOI modelling results compared to the SP and IL results (as seen in Figure 6.3f). As a result of this higher interstitial pressure, a downward pressure gradient was maintained between the interstitium and the microlymphatic network. Thus, the primary valves do not close, and fluid

continues to enter these vessels at a higher rate than seen in the other two networks (see Figure 6.3a and b).

As the localised pulmonary geometry of the BVB regions is least likely to be affected by respiratory stresses such as ventilation compared to the IL and SP regions (Effros & Parker, 2009; Benias *et al.*, 2018), the higher capacity for fluid drainage may act as a buffer in the system and be influential in preventing oedema in times of exercise where the ventilation rate increases, or when the organ is attempting to resolve oedema in pathology.

6.4.2 Relating the Model's Predictions for Fluid Dynamics in The Control Lung Geometry to the Literature

Relating the models predictions of pulmonary fluid dynamics to recent scientific literature is difficult. As the pulmonary microlymphatic network is not near the surface of the body, methods that have enabled direct measurements in the dermal lymphatics, such as lymphoscintigraphy, are not possible (Keeley, 2006; Fujiwara *et al.*, 2014). Therefore, there are no studies that have directly measured lymph flow velocity in the human lung. The pulmonary lymphatic flow velocity predicted by the present model is 7.5 $mm.s^{-1}$, which is 15x greater than that measured by lymphoscintigraphy in the skin (Fujiwara *et al.*, 2014). As the pre-capillary sphincters modelled as being open, it is not beyond reason for this flow velocity to be a good estimate.

The lymph flow velocity is linked to volumetric flow rate. The first studies that measured volumetric lymph flow in the lung date back to between 1974- 1984(Parker, Ryan & Taylor, 1984; Parker *et al.*, 1981; Erdmann *et al.*, 1975; Meyer & Ottaviano, 1974; Vreim, Ohkuda & Staub, 1977). Here, the predominant method of measurement involved cannulation of a large pulmonary lymph vessel such as the pre-nodal lymphatic vessel of the left tracheobronchial node, or the right lymphatic duct. The movement of the fluid meniscus in volumetric micropipettes was then measured and normalised by either the hydrated or dried lung tissue weight. As the secondary lobule is the smallest repeating unit of the lung, calculating the weighted average of the present model outputs in the different regions of the secondary lobule hoped to give an estimation of fluid clearance values that would relate to these measured values obtained in the literature.

The last of the original papers of 1984 predicted the lymphatic volumetric fluid flow at 0.067 $ml.min^{-1}$ per 100g hydrated lung tissue(Parker, Ryan & Taylor, 1984). The model predicts lymphatic volumetric fluid flow integrated within the volume of each domain, V^{L}_{Total} ($ml.min^{-1}$). V^{L}_{Total} . This can be normalised by an estimate of the hydrated lung tissue weight in each VOI. Multiplying the interstitial tissue volume (m^3)by its density ($1030kg.m^{-3}$(Swabb, Wei & Gullino, 1974)) will give an estimate of the hydrated weight of each VOI used for simulation. This

calculation assumes the blood vessel and lymphatic walls have negligible mass. The calculation can then be made to show $\dot{V}^{L}_{Total}$ normalised by 100g hydrated lung tissue which gives a mean value of 4.6 $ml.min^{-1}.100g^{-1}$, 3.2 $ml.min^{-1}.100g^{-1}$ and 8.1 $ml.min^{-1}.100g^{-1}$ for the IL, SP and BVB VOIs respectively. The weighted estimate for the secondary lobule is therefore 5.1 $ml.min^{-1}.100g^{-1}$, which is ~100x greater than the experimentally measured value. Like discussed with the lymph flow velocity, in this model, the pre-capillary sphincters are modelled as being open. It is expected that this assumption may result in an overestimation of the volumetric flow rate. Chapter 7 will investigate this limitation further.

Since this study of 1984, all studies have measured pulmonary lymph drainage with a focus on pathology such as, hypoxia, hypertension, and sepsis with resultant oedema, and were therefore not comparable to this work (Hansen-Flaschen, Lanken & Pietra, 1986; Fukushima *et al.*, 1990; Pabst, 2004). In studies where other pulmonary fluid mechanics are explored such as vascular or tissue compliance or vascular permeability, either there was no mention of lymphatic drainage with focus being solely on transcapillary or alveolar fluid clearance, or the results obtained from the lymphatic clearance only detailed lymph constituents such as protein concentration, not the flow rate (Michel, Meterissian & Poulsen, 1986; Michel & Curry, 1999; Miserocchi, Negrini & Gonano, 1990; Miserocchi *et al.*, 2001; Dellacà *et al.*, 2008).

The present model's estimate for the absolute interstitial pressure is -950 Pa (baseline pressure (-1064 Pa (Swabb, Wei & Gullino, 1974)) added to the secondary lobule estimate for change in interstitial pressure from baseline (+114 Pa (see Figure 6.3f)). This result is in keeping with the most recent study that directly measured interstitial pressures in a control system (Miserocchi, Negrini & Gonano, 1990). This study used anaesthetized rabbits and, by specialised micropuncture techniques to prevent pneumothorax, showed pulmonary interstitial pressure to be -980 Pa. Again, since this time studies have moved onto interstitial measurements during physiological extremes, pathology, or during development thus more recent estimates have not been found (Palestini *et al.*, 2002; Botto *et al.*, 2006; Dellacà *et al.*, 2008; Allison *et al.*, 2010).

6.4.3 Intralobular Fluid Flow and Clearance in Pulmonary Disease States

Based on both the normalised and non-normalised morphology, the microlymphatics of the control and COPD group are functionally and structurally similar. However, the modelling results contradict this finding. The model predicts the COPD VOIs in the IL region of the secondary lobule drain less efficiently than the control VOIs of the same anatomical location (see Figure 6.5). The volume of blood vessels is greater in the COPD samples. Still, although this may give a reason for alveolar fluid accumulation to be higher, it does not give a reason for the COPD microlymphatic

flow velocity and volumetric flow to be lower than the control (see 6.5e and h). One would expect the lymphatic volumetric flow to be greater if there is more vasculature in the system. The only reasoning left for the observed difference in fluid clearance shown is how the vessels are arranged in space. Many microlymphatic vessels in the COPD group are distanced, or extend away from the blood vessels, which is not the case in the control group (Figure 6.4a and e). Also, there are some blood vessels with surrounding interstitial tissue that have no microlymphatic vessels present. This vessel distribution pattern is different from that described for the SP VOI in section 6.4.1. Although there was a greater distance between the blood and microlymphatic domain compared to the IL VOI, every section of interstitial tissue was supplied by both vessel types.

Concerning the active disease IL VOI geometries, great care must be taken when interpreting the model's predictions for fluid flow and clearance. As mentioned in the introduction, the input parameters for the model are taken from the normal lung and considered "healthy" as there was no other way to compare the geometries of the three groups directly. However, the assumption throughout this thesis is that the active disease geometries were taken from patients that were expected to have abnormal physiology such as blood pressure. Acknowledging this, the IL VOIs in the active disease group have greater inward flux than the other clinical groups, but the lowest average flow velocity and normalised volumetric flow rate (see Figure 6.5a,e and h).

However, the change in lymphatic pressure in the active disease IL VOIs is greater than predicted in the COPD group (see Figure 6.5f). This finding is probably because the pressure measurement is an average of the whole lymphatic domain within each VOI. There are a smaller number of vessels (branch number) in the COPD VOIs compared to the active disease VOIs, of which, some are further away from the blood vessels. Therefore, the microlymphatic vessel pressure is also highly variable within each COPD VOI (see Figure 6.4 e). This would affect the average value to a greater extent than would be the case with the active disease IL VOIs. The greater branch number in the active disease IL VOIs will also be the reason that the total volumetric flux through the active disease VOI is predicted to be greater than that seen in the COPD group.

Finally, the fluid flux into the interstitial domain of the active disease IL VOIs, normalised by the interstitial volume, is greater than seen in the control IL VOIs. It is unclear why this is the case as there are more lymphatics without a closed primary valve than seen in the control IL VOIs. It is possible that this finding is a result of the active disease VOIs having a larger volume of blood vessels and the microlymphatic network being more distanced from these blood vessels compared to that seen in the control VOIs. The active disease IL VOI also has a smaller interstitial volume than the control VOI, which will impact the normalisation value. The larger blood vessel size may be a consequence of long term hypertension, and the decreased interstitial volume is

assumed to be the consequence of the beginnings of emphysematous disease in this clinical group (Vogelmeier *et al.*, 2017).

6.4.4 General Discussion

This chapter aimed to investigate the potential of using image-based mathematical modelling to assess the importance of the 3D geometrical structure for fluid clearance in peripheral human lung. This method allowed a structural and mechanical assessment of the pulmonary unit, in contrast to morphometry which assesses only the structure of one or two features at a time.

Broadly the modelling results obtained in this chapter show that simulation of fluid flow within real human lung geometries is possible. Although the mathematical model has low complexity, with many biological simplifications (for model limitations see Chapter 3, section 3.3.2), its predictions are in keeping with literature values measured by experimental methods.

It has been shown that microlymphatic vessel proximity to the blood vessel network seems an essential characteristic for efficient fluid drainage in the lung. Also, the relationship of the lymphatic vessels, interstitial tissue and blood vessel geometries combined, not just the lymphatic and tissue morphology, is important in the assessment of lymphatic function.

As mentioned in Chapter 3, section 3.3.2, it is beneficial to obtain modelling results for the smallest repeating unit of the lung, the secondary lobule, to enable scaling methods for whole organ simulations. As there are different lymphatic populations across the secondary lobule it would be inappropriate to use the VOI simulation as a “unit cell” for this purpose. However, the method outlined in this chapter for estimating fluid drainage from the secondary lobule using the anatomical VOIs seems an appropriate one. The current limitation of the presented method is that it does not account for vessel pressure gradients across the secondary lobule. In the future imaging data, such as the distance each VOI is located away from the pleural surface, could be collected and used to address this limitation. As blood pressure is expected to reduce toward the lung periphery, a VOI distance map could inform blood pressure input value used for each VOI simulation. A similar technique could be used for choosing a downstream lymphatic pressure value too. Finally, the volumes or diameter of the vessels could also be used to infer the likely intra-luminal pressure for each VOI.

The results of this chapter highlight the benefit of using image-based mathematical modelling in biological studies. Ultimately physiology is complicated and is influenced by many interlinking factors that we, as humans, find difficult to calculate without the help of computers. However, any model is only as good, and as accurate, as its inputs. It is crucial, therefore, to continue a

synergistic relationship between biological experimentation and mathematical modelling techniques in future work.

6.5 Conclusion

Fluid flow and clearance is variable in different anatomical locations in the secondary lobule. BVB regions are distinct in their fluid clearance rate, whereas the IL and SP regions are similar, as was suggested by the morphometry assessment. However, modelling results predict that under normal physiological parameters, the IL regions have reached full capacity for fluid clearance, whereas SP regions have not.

Unlike the morphometry assessment, modelling results predict that fluid clearance is different between the IL regions of the control and COPD patients. Fluid clearance is less efficient in the IL pulmonary geometry of the COPD patients compared to the control. The modelling results of the active disease patients suggest the difference in IL pulmonary geometry observed is sufficient to increase the capacity of fluid clearance in the IL region. Yet, as a probable consequence of an increase in blood volume, a higher rate of alveolar fluid accumulation is seen compared to the control geometry.

Chapter 7 Modelling the Effect of Changing Input Parameters on 3D Human Pulmonary Fluid Mechanics

7.1 Introduction

The previous chapter detailed how changes in the geometry of the human lung might influence interstitial fluid flow and lymphatic drainage. In the control lung group, even when structural heterogeneity of the secondary lobule was considered, the model predicted alveolar fluid accumulation would occur. This finding is inconsistent with the knowledge that the lung is a "dry" organ and works to maintain interstitial fluid pressure at ~-1200 Pa (Kurbel *et al.*, 2001). As detailed in the previous chapter, to enable fair comparison of geometrical changes found in the secondary lobule, the inputs of the model such as blood pressure and blood flow velocity had to remain constant. In this chapter, rather than altering the input geometry, input parameters of the model will be changed. Pulmonary fluid flow and lymphatic drainage will be analysed after this change to assess the model's sensitivity to each parameter. Also, this analysis will attempt to identify a candidate parameter that may be the cause of the current fluid accumulation discrepancy found in the control group.

In the healthy lung, pulmonary blood pressure is highly variable due to gravitational influences, and concept known as hypoxic pulmonary vasoconstriction (Sarkar, Niranjan & Banyal, 2017). Hypoxic pulmonary vasoconstriction is a process where pre-capillary sphincter muscles constrict in response to low oxygen concentrations in areas of the lung which are not actively ventilated. Pre-capillary sphincter constriction results in the blood pressure in the capillary beds falling to 800Pa (Kurbel *et al.*, 2001). At rest, only ~8% of the lung is ventilated, predominantly in the hila regions of the lung (Lutfi, 2017; Guyton & Hall, 2010). Therefore, the pulmonary blood pressure has been predicted to fall to ~800Pa in ~92% of the lung volume (Kurbel *et al.*, 2001) (see Figure 7.1). In addition, in ventilated regions of the lung above the heart, high-pressured blood perfusion only occurs during systole (25% of the time) due to gravitational effects (Guyton & Hall, 2010; Lutfi, 2017). If it is estimated that a third of the ventilated lung volume is positioned above the heart, it can be calculated that at any one time 6.2% of the lung volume receives high-pressured blood flow (2000 Pa) and 94.8% receives low pressured flow (800 Pa) (Guyton & Hall, 2010; Kurbel *et al.*, 2001; Lutfi, 2017). Figure 7.1 summaries the theoretical estimations of pulmonary blood

pressure variance across the whole organ at any one time.

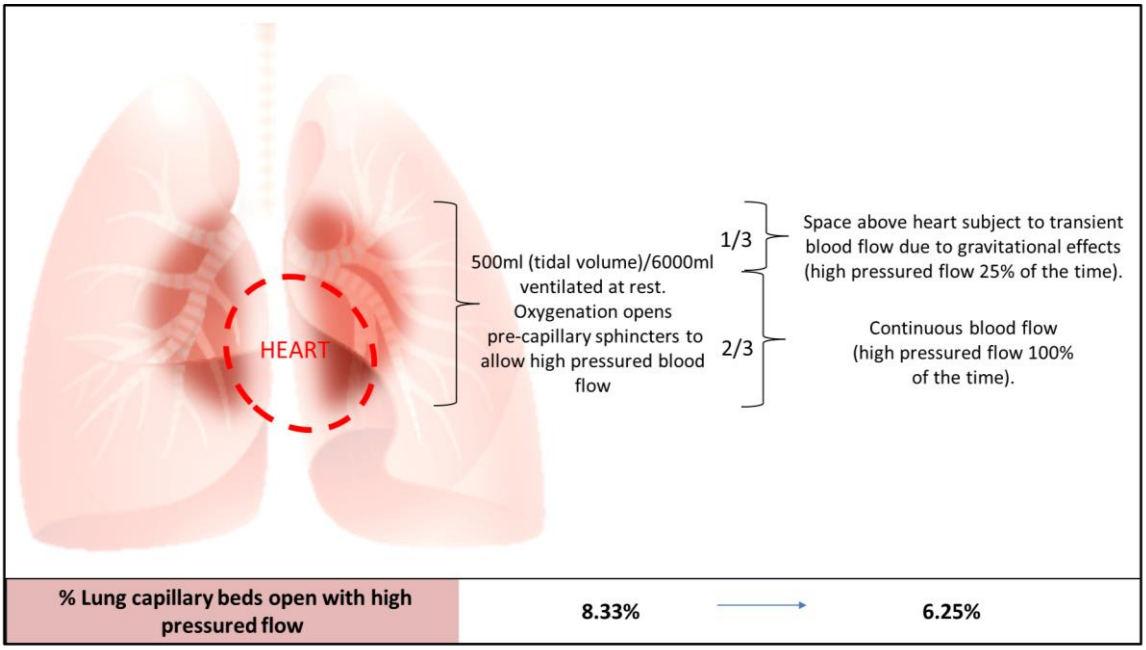

Figure 7.1 Theoretical Estimation of Pulmonary Blood Pressure Heterogeneity. A schematic diagram showing an estimation of the percentage of pulmonary blood capillary beds receiving high pressured flow. Estimations are based on current literature as detailed in text.

As such a large volume of the lung has a lower blood pressure than previously modelled, this chapter repeats the model simulations on the intralobular VOIs taken from the control lung group, but with the blood pressure parameter being set to 800 Pa rather than 2000 Pa. An estimation of the pulmonary fluid clearance across the whole organ can then be made by calculating a weighted average of the modelling results from the high and low- pressure regime. The weighting of the average will use the theoretical predictions of pulmonary blood pressure heterogeneity detailed in Figure 7.1.

The luminal fluid flow velocity and the hydraulic conductivity of the endothelium are two other input parameters that are hard to define in the lung for both the blood vessels and the lymphatic vessels.

Luminal blood flow velocity is inherently linked to luminal blood pressure (Rubenstein, Yin & Frame, 2015). As there is great variability in pulmonary blood pressure, as described above, one can assume blood flow velocity is also highly variable.

Blood vessel hydraulic conductivity is a measurement of the bulk flow of fluid through the vessel wall in response to applied pressure dependent on the permeability of the vessel's wall (Bressler & Bressler, 2012). This parameter can be estimated, but cannot be directly measured in a physiological state in the peripheral lung. The estimation used for the present model (see Chapter 3, Table 3.1) is indirectly calculated based on particulate filtration rate measurements through the

entire organ rather than localised studies at the micro-scale (Erbertseder *et al.*, 2012). It is, therefore, unclear if the literature quoted value has been influenced by other factors rather than just the permeability of the blood vessel wall and blood pressure.

With respect to the lymphatic vessel, the currently used lymphatic vessel flow velocity parameter is also questionable as this value was representative of the lymphatics in the human skin, not the lung, as peripheral pulmonary measurements of flow velocity could not be found in the literature (Fujiwara *et al.*, 2014). Also, the current estimates of the hydraulic conductivity of the lymphatic vessel wall are equally, if not more, uncertain as those of the blood vasculature as fewer particulate tracing studies have been performed (Erbertseder *et al.*, 2012).

Due to these uncertainties, the model will be re-run using a range of flow velocity values and hydraulic conductivity values for both the blood and lymphatic vessels. This range of values will span across the currently used values to extremes that are unlikely to be physiological values. It is hoped by using this strategy the true value of the parameter in question will be simulated. As this is a preliminary investigation, only a single intralobular lung geometry will be used.

All experiments presented in this chapter aim to inform future modelling work of the human pulmonary system. It will show the model sensitivity to the selected input parameters, and thus the relative importance of each parameter to the system function. This information will also guide the focus of future biological experimentation that hopes to improve the accuracy of experimentally measured input parameters.

7.2 Materials and Methods

7.2.1 Modelling the Heterogeneity of Pulmonary Blood Pressure

To obtain model outputs that encompass the variation in the human lung geometry, mathematical model design 2 as described in Chapter 3, section 3.2.6, was simulated on each of the five randomly selected, size-optimised intralobular volumes of interest (VOIs) taken from the control sample group. This intralobular VOI group was the same as used in Chapter 6, section 6.2.1. As time was limited, only one of the three anatomical locations could be used for this analysis. The IL VOI group was chosen as ventilation occurs in these regions of the secondary lobule, thus vasoconstriction is more likely to be dynamic at this location.

Two simulations were made using each of the five control IL VOI geometries. The first simulation used a blood pressure value that assumed the blood domain received high- pressured flow, $P^{B(o)}$ =

2000 Pa (see Table 3.1). The second simulation used a blood pressure value that assumed the blood domain received low-pressure flow, $P^{B(c)}$ = 800 Pa (see Table 3.1).

The following assumptions were also made to enable these simulations:

- All independent parameters except the blood domain pressure were constant across each simulation domain with that quoted from the current literature (see Chapter 3, Table 3.1).
- Initial flow velocities in the lymphatic and blood vessels domains were quoted from the current literature (see Chapter 3, Table 3.1).
- The lymphatic vessel osmotic pressure was the same as the interstitial osmotic pressure.
- The osmotic reflection coefficient is the same for each vessel and constant across their domains.
- Pressure downstream of the lymphatic vessels is maintained at -1200 Pa.
- All microlymphatic structures had primary valves of equal influence across all interstitial geometries used.

The non-normalised 3D simulation outputs (as described in Chapter 3, section 3.2.3) will be presented by the mean and the standard error of the five simulation results for when the blood domain is in a high -pressure state ($P^{B(o)}$ = 2000 Pa) and when the blood domain is in a low-pressure state ($P^{B(c)}$ = 800 Pa). The standard error will be calculated by dividing the standard deviation by the square root of the VOI number in each group (n=5). As the simulation results using the same geometries are being compared against each other, there will be no need to normalise the results as in Chapter 6, section 6.2.1 and 6.2.2. The non-normalised results represent the functionality of the whole VOI which, due to the VOI size-refinement studies, encompasses a complete repeating unit of the microlymphatic network.

An estimation of fluid drainage from the whole lung will be made, considering blood pressure heterogeneity across the whole organ. These estimates will be calculated by taking a weighted average of the high and low blood pressure regime simulation results. The weighting uses the estimation of how many capillary beds are expected to be receiving high or low blood pressure at any one time in the normal lung (open= 6.25%, closed= 93.75%) as shown in Figure 7.1.

As this study is preliminary, with a small sample size, it was decided that a statistical analysis of these results was not necessary.

7.2.2 Determining the Model Sensitivity to Blood and Lymphatic Flow Velocity

A single intralobular VOI was taken from the control group and used for the model sensitivity study. This was the same intralobular VOI as used for the model development (see Chapter 3).

To determine the model's sensitivity to blood flow velocity, the mathematical model design 2 (as described in Chapter 3, section 3.2.6) was simulated five times within the selected VOI. One simulation used the literature quoted value of $3.5x10^{-2}$ $m.s^{-1}$ as a control simulation (Guyton & Hall, 2010). Two simulations used a blood flow velocity value 10x and 100x larger than the literature quoted value and the final two simulations used a blood flow velocity value 10x and 100x smaller than the literature quoted value. In all simulations, all other parameters were kept as stated in Chapter 3, Table 3.1.

Using the literature quoted simulation result as a baseline, the change in the model result (measured by the percentage increase or decrease) was calculated for each simulation.

To determine the model's sensitivity to lymphatic flow velocity, the mathematical model design 2 (as described in Chapter 3, section 3.2.6) was simulated five times within the selected VOI. One simulation used the literature quoted value of $5x10^{-4}$ $m.s^{-1}$ as a control simulation (Fujiwara *et al.*, 2014). Two simulations used a lymphatic flow velocity value 10x and 100x larger than the literature quoted value and the final two simulations used a lymphatic flow velocity value 10x and 100x smaller than the literature quoted value.

The following assumptions were made to enable these simulations:

- All independent parameters other than the initial flow velocity of the relevant vessel were constant across each simulation domain with that quoted from the current literature (see Chapter 3, Table 3.1).
- The lymphatic vessel osmotic pressure was the same as the interstitial osmotic pressure.
- The osmotic reflection coefficient is the same for each vessel and constant across their domains.
- Pressure downstream of the lymphatic vessels is maintained at -1200 Pa.
- All microlymphatic structures in the interlobular geometry had primary valves of equal influence.

Using the literature quoted simulation result as a baseline, the change in the model results (measured by the percentage increase or decrease) was calculated for each simulation.

7.2.3 Determining the Model Sensitivity to the Hydraulic Conductivity of Blood and Lymphatic Endothelium

The same intralobular VOI and methodology, as described in section 7.2.3, was used to determine the model's sensitivity to the hydraulic conductivity of the blood and lymphatic vessel's endothelium. The only change in methodology was only a 100x increase and decrease from the

literature quoted values was simulated due to time limitations. The literature quoted value for the hydraulic conductivity of the blood vessel endothelium and lymphatic vessel endothelium is 1.9 $x10^{-12}$ $m.s^{-1}$ and $2.7x10^{-12}$ $m.s^{-1,}$ respectively (Erbertseder *et al.*, 2012).

The following assumptions were also made to enable these simulations:

- All independent parameters other than the hydraulic conductivity of the relevant vessel were constant across each simulation domain with that quoted from the current literature (see Chapter 3, Table 3.1).
- Initial flow velocities in the lymphatic and blood vessels domains were quoted from the current literature (see Chapter 3, Table 3.1).
- The lymphatic vessel osmotic pressure was the same as the interstitial osmotic pressure.
- The osmotic reflection coefficient is the same for each vessel and constant across their domains.
- Pressure downstream of the lymphatic vessels is maintained at -1200 Pa.
- All microlymphatic structures in the interlobular geometry had primary valves of equal influence.

7.3 Results

Model simulation times, error values, and computer memory usage for all simulations in this chapter are given in Appendix E. The mass balance (M^{in}- M^{out}) of the inlet and outlet boundaries was smaller than the model simulation error for all 26 VOI simulations. Mass was, therefore, considered to be conserved in every simulation presented in this chapter.

7.3.1 Changing the Control Intralobular Blood Domain Between a High- or Low-Pressure State

Figure 7.2 shows the comparison of the non-normalised 3D numerical simulation results when the blood domain is in a high -pressure state ($P^{B(o)}$ = 2000 Pa) and when the blood domain is in a low-pressure state ($P^{B(c)}$ = 800 Pa). The presented numerical values for each pressure state in Figure 7.2 a-f shows the mean of the simulation results from the intralobular geometry from the control group (n=5) with the error bars showing the standard error of the group. Figure 7.2 g and h is an illustration of the model's results in one control IL geometry. Figure 7.2 g and h show the change in the directional movement (blue arrows) of interstitial fluid when the blood domain is modelled in different states of pressure.

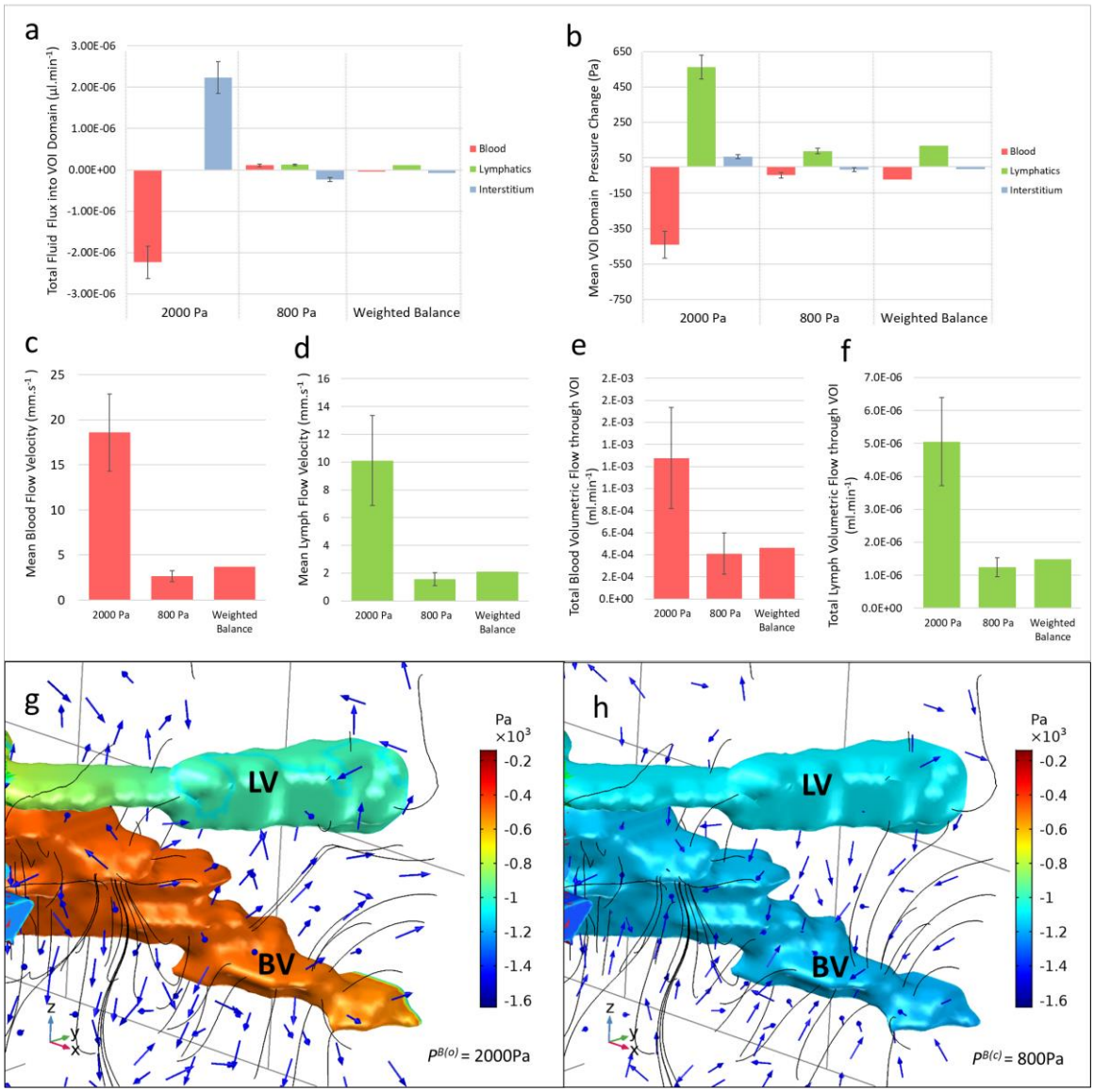

Figure 7.2 Simulation Results of the Model Simulated in Control Intralobular Geometries in a High- and Low-pressure State. **a** Total fluid flux into the interstitium domain (blue bars), lymphatic domain (green bars) and blood vessel domain (red bars), $\boldsymbol{Q}_{\text{Total}}$, $\boldsymbol{Q}^{L}_{\text{Total}}$ and $\boldsymbol{Q}^{B}_{\text{Total}}$ when the blood vessel domain is modelled in a high-pressured state ($\boldsymbol{P}^{B(o)}$ = 2000 Pa), in a low-pressure state, ($\boldsymbol{P}^{B(o)}$ = 800 Pa), and with the weighted average of the high- and low-pressure results, calculated based on blood pressure heterogeneity in the lung (see text for details). Error bars= Standard error of the mean (n=5/group). **b** The same information as **a** but showing the mean change in pressure of the interstitium, lymphatic and blood vessel domain, $\boldsymbol{P}$, $\boldsymbol{P}^{L}$ and $\boldsymbol{P}^{B}$. **c and d** The same information as **a** but showing the mean blood and lymphatic flow velocity, $\boldsymbol{u}^{L}$ and $\boldsymbol{u}^{B}$, respectively. **e and f** The same information as **a** but showing the total blood and lymphatic volumetric fluid flow integrated within the volume of each domain, $\boldsymbol{V}^{B}_{\text{Total}}$ and $\boldsymbol{V}^{L}_{\text{Total}}$, respectively. **g** A zoomed-in representation of the blood vessel **(BV)** and lymphatic vessel (**LV)** pressure results (Pa), the Darcy's velocity streamlines (black) and the normalised directional arrows of interstitial fluid flow (blue) in one example of the intralobular geometry group when $\boldsymbol{P}^{B(o)}$ = 2000 Pa. **h** The same information as **g** but when $\boldsymbol{P}^{B(c)}$ = 800 Pa.

When blood domain is modelled in the high-pressure state, the rate of total fluid flux across the blood vessel wall, $\boldsymbol{Q}^{B}_{Total}$ (µl.min^{-1}), is high and directed towards the interstitium creating a decrease in blood pressure, $\boldsymbol{P}^{B}$ (Pa), from the baseline high-pressured state (see the red bars in

Figure 7.2a and 7.2b respectively when $P^{B(o)}$ = 2000 Pa). In addition, as shown in Chapter 6, section 6.3.1, no fluid flux is seen across the lymphatic vessel wall Q^{L}_{Total} (µl.min^{-1}) due to the high lymphatic intraluminal pressure, P^{L} (Pa), initiating the primary valve element of the model (see the green bar in 7.2b when $P^{B(o)}$ = 2000 Pa). The net effect of these two results is a high fluid flux into the intralobular interstitium, Q_{Total} (µl.min^{-1}) and an increase in interstitial pressure in intralobular regions of the lung, P (Pa) (see the blue bars in Figure 7.2a and 7.2b respectively when $P^{B(o)}$ = 2000 Pa). This result infers high rates of alveolar fluid accumulation would occur.

When the blood domain is modelled in the low-pressured state, there is an inward movement of fluid flux, Q^{B}_{Total} *and* Q^{L}_{Total} (µl.min^{-1}), across both the blood and lymphatic vessel walls at a similar rate (see the red and green bars in Figure 7.2a respectively when $P^{B(o)}$ = 800 Pa). This inward fluid flux increases the intraluminal pressure in both the vessel domains, P^{B} and P^{L} (Pa), to increase from baseline values (see the red and green bars in Figure 7.2b respectively when $P^{B(o)}$ = 800 Pa). This uptake of fluid by the vascular domains results in a net reduction of fluid flux into the interstitium, in turn causing a reduction in interstitial pressure from baseline values (see blue bars in Figure 7.2a and 7.2b respectively when $P^{B(o)}$ = 800 Pa). This result infers this system would uptake alveolar fluid accumulation present outside the simulation domain.

When blood domain is modelled in the high-pressured state, the inferred rate of fluid accumulation in the alveoli would be much greater than the rate of fluid reduction seen in the low-pressured state. If 50% of pulmonary capillary beds receive a high-pressured flow, alveolar fluid would rapidly accumulate. If pulmonary blood pressure heterogeneity is considered as described in section 7.1 and shown in Figure 7.1, it can be estimated that there is a small net removal of fluid from the alveoli across the whole organ (see the "weighted balance" blue bars in Figure 7.2a). This net removal of fluid would maintain a small negative pressure in the lung (see the "weighted balance" blue bars in Figure 7.2b), which is consistent with theoretical and experimental literature of pulmonary physiology (Kurbel *et al.*, 2001; Guyton & Hall, 2010; Lutfi, 2017).

The mean blood fluid flow velocity, u^{B}, and thus the total volumetric fluid flow, V^{B}_{Total}, was predicted to be smaller when the blood domain was modelled in a low-pressure state compared to when it was modelled in a high-pressure state. This result can be explained by there being net uptake of fluid into the blood vessel from the interstitium compared to there being a net loss. When fluid is lost from the blood vessel lumen into the interstitium, there is a large reduction of pressure in the blood vessel lumen which creates a higher-pressure gradient between the blood vessel inlet boundaries and the blood vessel lumen which raises flow velocity and volumetric flow.

The mean lymphatic fluid flow velocity, u^L, and thus the total volumetric fluid flow, V^L_{Total}, was also predicted to be smaller when the blood domain was modelled in a low-pressure state compared to when it was modelled in a high-pressure state. The greater increase of luminal lymphatic pressure when the blood domain was modelled in a high-pressure state, resulted in a higher pressure gradient between the lumen of the lymphatic vessel and the lymphatic outlets which raised the flow velocity and volumetric flow compared to that seen when the blood domain modelled in a low pressured state.

7.3.2 The Model's Sensitivity to the Blood and Lymphatic Vessel Flow Velocity

The effect of increasing and decreasing the blood flow velocity and the lymphatic flow velocity, relative to the literature quoted value, is shown in Table 7.1 and 7.2, respectively. For each simulation, these tables show the percentage increase (+) or decrease (-) in the model's outputs from the models outputs of the control simulation (highlighted in blue in Table 7.1 and Table 7.2).

Table 7.1 Result of the Model's Sensitivity to the Blood Flow Velocity

	Change in Model Simulation Result from Model Result when Using Literature Quoted Parameter Values (Table 3.1) (%)						
	Fluid Entering Vessel		Domain Pressure			Average Velocity	
Blood flow velocity ($m.s^{-1}$)	Blood Vessel	Lymphatic Vessel	Blood Vessel	Lymphatic Vessel	Interstitium	Blood Vessel	Lymphatic Vessel
3.5	+228.06	-531.91	-30.73	-9.26	-2.55	+184.30	-108.82
3.5×10^{-1}	+20.79	-20.50	-2.83	-1.11	-0.24	+16.74	-7.77
3.5×10^{-2}	0.00	0.00	0.00	0.00	0.00	0.00	0.00
3.5×10^{-3}	-2.08	+1.80	+0.28	+0.11	+0.02	-1.61	+0.75
3.5×10^{-4}	-2.29	+1.97	+0.31	+0.12	+0.03	-1.77	+0.82

Table 7.2 Result of the Model's Sensitivity to the Lymph Flow Velocity

	Change in Model Simulation Result from Model Result when Using Literature Quoted Parameter Values (Table 3.1) (%)						
	Fluid Entering Vessel		Domain Pressure			Average Velocity	
Lymph flow velocity ($m.s^{-1}$)	Blood Vessel	Lymphatic Vessel	Blood Vessel	Lymphatic Vessel	Interstitium	Blood Vessel	Lymphatic Vessel
5×10^{-2}	0.00	+5.59	0.00	-0.04	0.00	-0.03	0.40
5×10^{-3}	0.00	+0.51	0.00	0.00	0.00	0.00	0.03
5×10^{-4}	0.00	0.00	0.00	0.00	0.00	0.00	0.00
5×10^{-5}	0.00	-0.05	0.00	0.00	0.00	0.00	0.00
5×10^{-6}	0.00	-0.06	0.00	0.00	0.00	0.00	0.00

Table 7.1 show that there is a notable change in the model's simulation results when the blood flow velocity is increased, with minor changes seen in the modelling results when the blood velocity is decreased. Table 7.2 shows there is only a minimal change in the simulation results when the lymphatic flow velocity is either increased or decreased. These results predict that fluid dynamics in the lung is more sensitive to blood flow velocity than lymph flow velocity.

7.3.3 The Model's Sensitivity to the Hydraulic Conductivity of the Blood and Lymphatic Vessel Wall

The effect of increasing and decreasing the hydraulic conductivity of the blood and the lymphatic vessel wall, relative to the literature quoted value, is shown in Table 7.3 and 7.4, respectively. For each simulation, these tables show the percentage increase (+) or decrease (-) in the model's outputs from the model's outputs of the control simulation (highlighted in blue in Table 7.3 and Table 7.4).

Table 7.3 Result of the Model's Sensitivity to the Hydraulic Conductivity of the Blood Endothelium

	Change in Model Simulation Result from Model Result when Using Literature Quoted Parameter Values (Table 2.2) (%)						
	Fluid Entering Vessel		**Domain Pressure**			**Average Velocity**	
Hydraulic conductivity of blood vessel wall ($m.s^{-1}$)	**Blood Vessel**	**Lymphatic Vessel**	**Blood Vessel**	**Lymphatic Vessel**	**Interstitium**	**Blood Vessel**	**Lymphatic Vessel**
$2.70x10^{-14}$	$+8.76\ x10^{-7}$	$-1.39\ x10^{-6}$	$+1.74x1^{-11}$	$-6.24x10^{-12}$	$-2.19\ x10^{-9}$	$-8.94\ x10^{-11}$	$-4.22\ x10^{-11}$
$2.70\ x10^{-12}$	0.00	0.00	0.00	0.00	0.00	0.00	0.00
$2.70\ x10^{-10}$	$-8.73\ x10^{-5}$	$+1.39\ x10^{-4}$	$-1.55x10^{-9}$	$+5.53x10^{-10}$	$+2.18\ x10^{-7}$	$+8.66\ x10^{-9}$	$+4.16\ x10^{-9}$

Table 7.4 Result of the Model's Sensitivity to the Hydraulic Conductivity of the Lymphatic Endothelium

	Change in Model Simulation Result from Model Result when Using Literature Quoted Parameter Values (Table 2.2) (%)						
	Fluid Entering Vessel		**Domain Pressure**			**Average Velocity**	
Hydraulic conductivity of lymphatic vessel wall ($m.s^{-1}$)	**Blood Vessel**	**Lymphatic Vessel**	**Blood Vessel**	**Lymphatic Vessel**	**Interstitium**	**Blood Vessel**	**Lymphatic Vessel**
1.9E-14	$1.94x10^{-8}$	$-1.00x10^{-5}$	$1.30x10^{-12}$	$-5.14x10^{-12}$	$2.68x10^{-10}$	$-7.30x10^{-12}$	$-9.47x10^{-13}$
1.9E-12	0.00	0.00	0.00	0.00	0.00	0.00	0.00
1.9E-10	$-1.94x10^{-6}$	$1.00x10^{-3}$	$-1.11x10^{-10}$	$4.90x10^{-10}$	$-2.68x10^{-8}$	$7.47x10^{-10}$	$9.97x10^{-11}$

Both Table 7.3 and Table 7.4 shows that there is no notable change in the model's simulation results when either the blood or lymphatic vessel wall's hydraulic conductivity value is increased

or decreased. In fact, changing the hydraulic conductivity of either vessel wall by 100 fold changed all model outputs by less than the simulation error. These results, along with those shown in section 7.3.1, predict that fluid flow across the vascular wall is much more sensitive to changes in luminal pressure than it is to the endothelium's inherent hydraulic conductivity value.

7.4 Discussion

7.4.1 Modelling Pulmonary Blood Pressure Heterogeneity

Hypoxic vasoconstriction is an essential physiological phenomenon in the lung. Although this process is frequently attributed to improving the efficiency of gas exchange in the lung, little discussion has been made in the literature about its relevance for pulmonary fluid accumulation and oedema. This is not true for the influence of gravitational forces on fluid accumulation and oedema, which has been detailed for many decades.

By selectively changing the pressure values for the blood domain in the presented model, this work shows fluid flow and clearance predictions can be made within real human lung geometries to reflect the known heterogeneity of pulmonary blood pressure. Here blood pressure heterogeneity is assumed to be as a result of two factors: 1) The tonality of pre-capillary sphincters as a result of environmental oxygen concentration; 2) the influence of gravitational forces.

When the pressure in the blood vessel domain is low due to upstream vasoconstriction or gravitational effects, the model predicts the blood vessel domain to become absorptive. This is because the hydrostatic pressure gradients are now reversed, and the osmotic pressure gradient becomes more influential. Interestingly, inward lymphatic vessel fluid flux is maintained in this state with a sustained volumetric flow rate and velocity. This finding demonstrates the pulmonary lymphatic system is essential in the reduction of interstitial fluid. This finding contradicts many theories that have developed from Starling's Hypothesis which assume that when the blood vessels are in an absorptive state, the lymphatic system becomes redundant (Negrini & Del Fabbro 1999, Negrini et al. 2004, Moriondo et al. 2005).

In addition, by weighting the average of the model simulations for when the blood pressure is high and low, an estimation of the fluid flow and clearance can be made for the whole lung. The model predicts that there would be no overall influx of interstitial fluid; thus, it infers alveolar fluid accumulation would not occur. In fact, overall, there is a small efflux of fluid out of the alveoli which serves to maintain the pulmonary interstitium at a negative pressure. This model's prediction estimations, therefore, has shown that in normal physiology the vascular beds that are

restricted to a low pressured state by hypoxic vasoconstriction play a critical role in the fluid balance of the whole organ, particularly the lymphatic vascular networks in these beds. Only when these "closed" vascular beds are taken into account does the model's prediction of lung fluid balance match that which has been experimentally measured in the literature (Kurbel *et al.*, 2001; Miserocchi, Negrini & Gonano, 1990).

Although these findings are now supportive of the accuracy of the mathematical model design, there are some limitations of this study. Firstly, using two defined pressure values is a crude assumption as pressure across the lung is realistically a continuum between the two values modelled. In addition, only the interlobular VOI were considered in this modelling study. Although, as stated in section 7.2.1, it is more likely that dynamic hypoxic vasoconstriction influences the intralobular regions, other regions of the lung will influence the whole organ fluid balance. Therefore, if the same modelling analysis should be undertaken in the future, the bronchovascular and subpleural lung geometries should be assessed. As shown in Chapter 6, section 6.2.1, the results could then be weighted accordingly by proportional representation.

7.4.2 Testing the Sensitivity of the Model to Different Input Parameters

The results presented in section 7.3.3 showed, of the four parameters investigated, only changing the initial blood flow velocity effects the output of the model simulation. Changing the initial lymphatic flow velocity, and the hydraulic conductivity of each vessel's endothelia had no notable effect on the simulation results. The average blood flow velocity at equilibrium was predicted to increase by 16 % when the input velocity is increased 10-fold. It should be noted, however, that even a 10-fold increase in blood flow velocity is a substantial change in the physiological system. In fact, this flow velocity rate is the same as that measured in the aorta; therefore, the level of parameter change modelled in this analysis can be considered theoretical (Guyton & Hall, 2010). This theoretical assessment, however, is useful for understanding the scope of the model's sensitivity and invaluable for informing study design for parameter assessment in the future.

The relatively small effects on the modelled system seen with these parameter sensitivity tests would be expected in an overall low pressured biological system such as the lung. Typically, considerable scope is needed for changes in physiological parameters in order to maintain homeostatic control. The main limitation of this assessment that should be noted is that only one representative lung geometry was used. As each simulation can take days even weeks to simulated depending on mesh size, a full sweep for each geometry potentially could take a month to complete. However, if run alongside other future work, the whole study could be repeated

across other geometries at different pulmonary locations to assess the parameter change's effect across the whole organ.

7.5 Conclusion

This chapter detailed preliminary studies to assess input parameter suitability for model simulation within real 3D human lung geometries. The results show physiologically accurate blood parameters, particularly blood pressure, to be essential to obtain realistic modelling predictions of pulmonary fluid dynamics. When blood pressure heterogeneity across the whole lung is considered, the modelling results predict an fluid balance which reflects measured values in the current literature. The low-pressured pulmonary capillary beds, sustained by hypoxic vasoconstriction and gravitational influences, and the pulmonary lymphatic system are both shown to be essential for maintaining this physiological fluid balance. Due to the preliminary nature of these studies, further study would be needed in the future to confirm the results presented in this chapter.

Chapter 8 Conclusions and Future Work

8.1 Introduction

This final chapter will firstly give an overview of the results from all chapters combined and discuss how they have forwarded the study and current understanding of lymphatic biology. As a detailed analysis of each specific chapter's results can be found in the respective discussion section, further expansion of these specific discussion points will not be made here.

Secondly, the largest portion of this chapter will focus on how the methods detailed in this thesis could be improved and used in the future. This section will be split into two parts. The first part will detail future work that could improve and extend the current application of methods detailed in this thesis. The second part will describe how the current methodology has potential for use in other avenues of pulmonary lymphatic research and suggest how the blueprint of the present methods could be easily adapted to investigate these questions in the future.

Finally, the success of this work in relation to the initial aims of the study will be reviewed and my final remarks on this thesis will be made.

8.2 Contribution to the Study and Current Understanding of Lymphatic Biology

8.2.1 Producing Methods for Imaging and Modelling Human Pulmonary Lymphatics

Lymphatic vessels in human lungs have not been imaged or characterized in 3D before, due in part to the lack of specific lymphatic endothelial cell biomarkers which are essential for most imaging methodologies.

Using a candidate therapeutic monoclonal antibody, LP21, this thesis provides a fully validated methodology to image the human pulmonary lymphatics in 3D. This work breaks through a large barrier that has been limiting the progress of pulmonary lymphatic research for many years. The fact that this methodology is designed for human tissue samples adds to its merit, as currently, only one other scientific research group images human lymphatics in 3D. This work concerns dermal lymphatics which appears not to present the same complexity of D240 cross-reactivity as seen in the lung.

Moreover, this thesis advances this methodology further by detailing how the acquired images can be processed for 3D image-based modelling, whilst providing a mathematical model that satisfactorily describes fluid flow in the peripheral architecture of the human lung. Although the basic principles of the mathematics in the model have been used to describe many aspects of biological fluid flow, the application of the model into a real 3D geometry of the human lung is novel.

8.2.2 Observations and Predictions of Human Pulmonary Lymphatics Structure and Function

By applying the methods developed, multi-facetted preliminary studies were undertaken to begin the characterisation of pulmonary lymphatics in human health and disease.

Preliminary results suggest the pulmonary lymphatic structure is highly variable, and that this variability is linked to their anatomical distribution in the lung. The modelling results also suggest that fluid movement and drainage in the same anatomical areas of the lung are distinct. Modelling indicated, however, that this anatomical distinction is not just due to lymphatic structural variation, but also the variation in interstitial tissue and blood vessel structures surrounding the lymphatics in 3D space.

Furthermore, pulmonary lymphatics in all areas of peripheral human lung seem to expand and change their morphology during active pulmonary disease. Modelling results also predict there to be differences in fluid movement and drainage in intralobular regions between these two clinical states. Based on qualitative and quantitative morphology of COPD patient samples, lymphatics in chronic disease regress into a “resting” or “normal” state and thus, any proliferative change is apparently unique to active pulmonary stress. However, modelling suggests the intralobular regions in COPD samples drain fluid less efficiently than the control group. This result is also thought to be influenced by structural variation in all three pulmonary geometries and their proximity to one another, rather than just lymphatic vessel morphology.

Overall, all the preliminary modelling results support the concept that a change in the 3D image geometry is equally as important as the model’s physiological input parameters, such as blood pressure, in its influence on fluid flow simulation within the lung. This concept is a key conclusion of this thesis, and it is hoped that more biological modelling studies will place higher importance on the geometry of modelled systems in the future.

This collection of observational work, although not giving conclusive results on the morphology or functionality of the lymphatics in the lung, generates multiple new hypotheses on the subject. It is

hoped that the findings of this work will save time and money by permitting a more targeted approach to study design in the future.

8.2.3 Compliance Hypothesis

Lymph flow appears to increase linearly with increased capillary filtration in most organs and reaches a plateau at high filtration rates. However, it has long been known that in organs such the intestine and lung with relatively large interstitial tissue volume, lymph flow decreases from this maximum (Granger, Mortillaro & Taylor, 1977; Parker *et al.*, 1979). These early studies showed that lymph flows increased immediately after elevations of capillary pressure, but lymph flow then fell to values roughly two-thirds of the maximal value after a few minutes. This effect was even more pronounced at high capillary pressures and in states of oedema. The authors interpreted these findings as indicating that lymph flow increases in response to the rate of change in tissue pressure, not in response to its absolute value. Lung interstitium was therefore described as behaving like a balloon. This effect can be described mathematically by the Laplace relationship between the radius and wall tension. A large change in pressure results from only small changes in tissue volume initially. The pressure then decreases as the volume increases (a negative compliance) until a critical volume is reached at which the pressure again rises. Since tissue compliance usually increases with hydration, more fluid must be filtered before a drop in tissue pressure is seen. This was the reason given for why lower lymph flows were seen in the oedematous state compared the non-oedematous state.

Although these authors could explain a potential mechanism for this observation physically, they could not explain why. To this day, this remains the case. Why do the lung lymphatics, compared to say the dermal lymphatics, fail to maintain their highest possible flow rates? Why don't the lung lymphatics provide the tissue with a better volume overflow mechanism when the tissues are in an oedematous state?

The two modelling studies performed in Chapter 6 suggests the relationship between the 3D pulmonary lymphatic network geometry to structures surrounding them may be influential. What appears to be due to their non-even distribution and extreme proximity to the blood vessels, the intralobular lymphatic network is at maximum flow rate under "normal" physiological parameters. Therefore, a small increase in capillary pressure in this system may result in the phenomena explained above where an oedematous state is initiated, tissue compliance increases, interstitial pressure drops and thus lymphatic fluid flow drops. In lung samples linked to active disease where the same geometries are arguably more likely to have been remodelled or in state of dynamic expansion, the network in the same anatomical location has not reached full capacity.

This suggests remodelling of the 3D geometry of the system compensates for increased tissue pressure if it is a persistent occurrence. It was not apparent in the original studies if any long-term investigations of a high capillary pressure states were investigated. This study may have shown lymphatic remodelling may result in the lymph flow returning back to a maximum flow rate.

The question then moves onto why the pulmonary drainage relies more heavily on dynamic lymphatic remodelling compared other organs? It could be due to the respiratory role of the pulmonary system. Compared to other organ systems, lung tissue endures continuous mechanical stresses. Ventilation may be a unique environmental stimulus that moulds the lymphatics, particularly the intralobular lymphatics, into their observed morphology. Also maintaining a lymphatic network in a proliferative state may have a negative impact on oxygen exchange. Therefore, the pulmonary LECs may be more predisposed to respond to environmental stimuli to regress the lymphatic system back to a necessary density. This hypothesis introduces the potential for the existence of a lung specific LEC phenotype with proteomic heterogeneity. Indeed, as this thesis demonstrates, lung LECs shows differential podoplanin expression to LECs in other organs.

In the future to address this question in full rather than just speculate, temporal studies would be required on animal models with inducible hypertension. Also, the model would need to be developed to include elastic mechanics and tissue compliances.

8.3 Future Work to Improve Upon Current Methods

Much care has been taken in the validation of the presented methods (see Chapter 2 and 3) to optimise efficiency without comprising the accuracy and reliability of the obtained data. Unfortunately, as time and resources are always limited in scientific research, a few outstanding limitations of the current methodology, including the mathematical model, remain. With more time and resources, there are ways in which these limitations can be improved upon in the future. Many of these have been documented in the discussion sections of the two methodology chapters (see sections 2.5 and 3.3.2). Here, three of limitations considered to be the most important to address are discussed with details of how they may be overcome.

8.3.1 Improve Speed of 2D to 3D Image Data Transfer

It was mentioned in section 2.5 that manual segmentation is the rate-limiting step of the imaging section of the workflow. One factor preventing the automated process of data transfer from the 2D IHC images to the µCT data set is the computer's ability to distinguish the positive DAB stain (brown) from the background haematoxylin stained parenchymal tissue (blue/white). Also, in a

particular IHC run, if the DAB stain is weak and haematoxylin counterstain is strong, manual segmentation becomes more difficult and the likelihood of human error increases.

In part, this limitation could be overcome by the use of the immunofluorescence technique rather than IHC. The only distinction between these 2D imaging methods lies in the way in which the antibody binding location is identified. With IHC, the location is marked by a large chromogen tag that forms from an irreversible enzymatic reaction within the tissue section. The immunofluorescence technique uses a smaller fluorescent tag which can be excited by a specific wavelength of light. Using immunofluorescence rather than IHC in the current methodology would enable the tagged antibody location, and the background tissue to imaged separately. This would enable the images to be contrasted separately to improve stain visibility, but also, if automatic alignment and registration of the two datasets become possible, rapid extraction and transfer of the staining data from the 2D image to the 3D dataset could be achieved. Preliminary work has shown that LP21 is compatible with immunofluorescence imaging (see Figure 8.1).

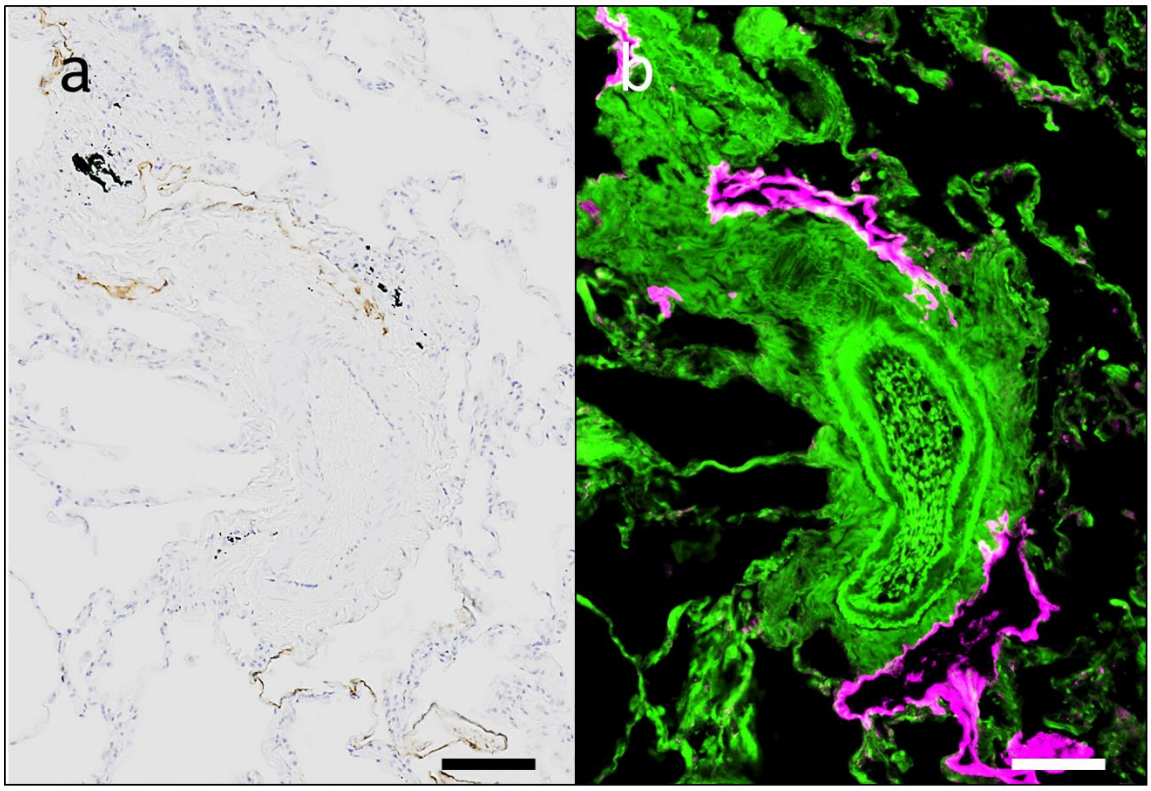

Figure 8.1 A comparison of Immunohistochemistry and Immunofluorescence staining using LP21. Images of imaging data from two serial human lung tissue sections. **a** DAB chromogen stain (brown) depicting LP21 localisation within the haematoxylin stained tissue (blue). **b** A fluorophore (Alexa Fluor 647) emission (pink) depicting the LP21 localisation overlaid onto a separately imaged tissue section that autofluoreses (green). Both scale bars= 100µm. Immunofluorescence imaging courtesy of Matthew Lawson, University of Southampton.

8.3.2 Address Tissue Shrinkage Artefacts in Archived Human Biopsies

Any model is only as good as its inputs and for image-based modelling, these inputs also include the input geometry. A limitation of sample preparation for histological investigation is that tissue shrinkage occurs due to dehydration steps in the protocol which can be as great as 50% of its original volume (Schneider & Ochs, 2014b). Most morphological studies, including the methods presented here, normalise the raw measurements to tissue volume. As all tissue types within the same sample shrink uniformly, shrinkage artefacts are therefore not too influential on morphological studies in isolation. However, it is expected that these shrinkage artefacts will have much more of an influence on the model simulation as length scales are essential for accurate predictions of fluid flow.

Preliminary work has shown that if archived biopsies are to be used in the model in the future, adjusting the image preparation methodology for modelling may be able to account for shrinkage artefacts. Specifically, the length scale of the geometry can be adjusted accordingly before simulation of the model takes place. Figure 8.2 a shows a schematic of the model simulation result (implemented as stated in Chapter 3 section 3.2.7) alongside the simulation result of the same geometry after being scaled by a factor of 2 in all three dimensions from the original volume (see figure 8.2b). Differences in vessel pressure and streamline density are clearly seen highlighting the importance of addressing the shrinkage artefacts of formalin fixation and paraffin embedding for modelling studies in the future.

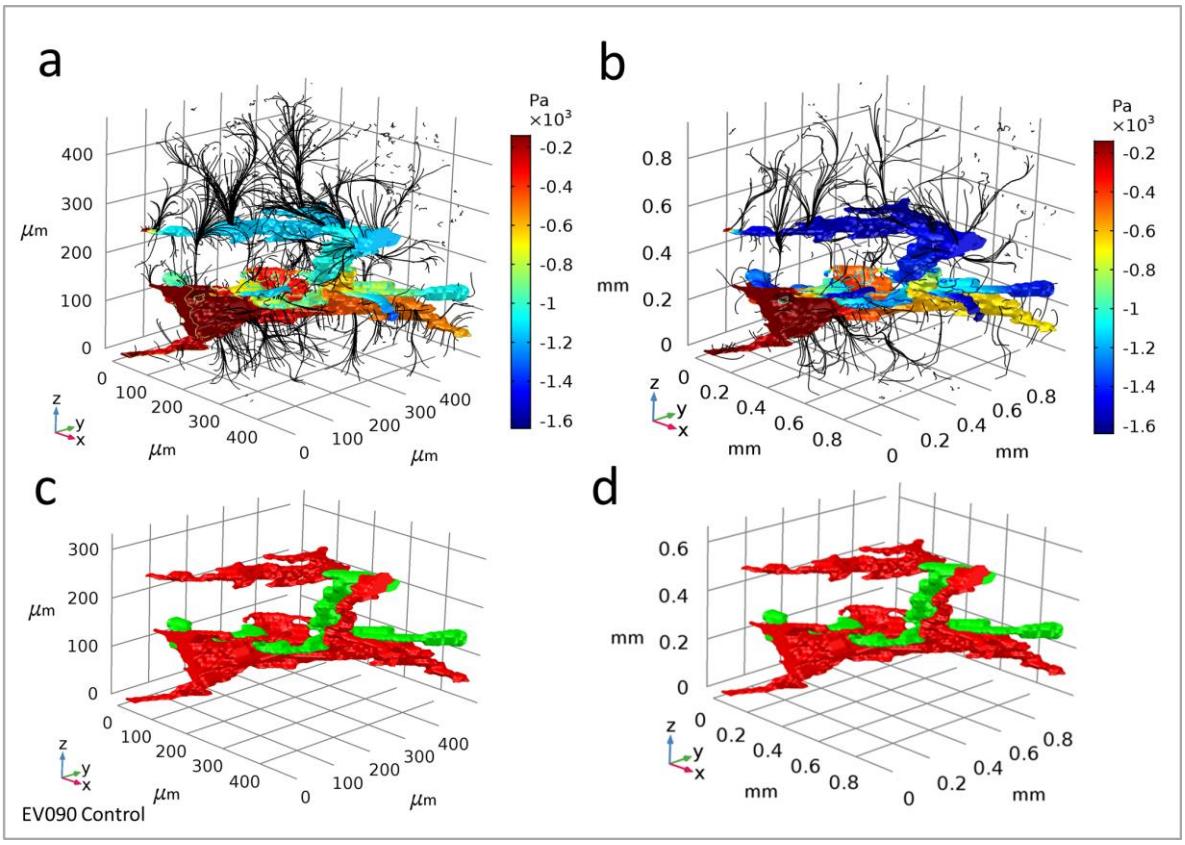

Figure 8.2 Visual Simulation Result of Model in a 3D Lung Geometry at Different Length Scales **a** The pressure (Pa) result of model simulation in a whole 3D lung geometry. Length scale determined by the original imaging methodology. Darcy's flow streamlines are shown in black and normalised directional arrows in blue. **b** The pressure (Pa) result of model simulation in the same 3D lung geometry as shown in panel **a** but with the dimensions of all constituent geometries scaled by a factor of 2 before simulation. Darcy's flow streamlines are shown in black and normalised directional arrows in blue. **c** The geometry of panel (**a)** Blood vessels = red, lymphatic vessels =green. Interstitial tissue not shown .**d** The geometry of panel (**b)**.

8.3.3 Improve Knowledge of Pulmonary Blood Vasculature

Finally, imaging the capillary network and discerning blood vessel geometries by their hierarchal identities are vital for accurate modelling of the vascular system.

To image the capillary network, further antibody testing would be required to identify a candidate which doesn't require harsh tissue pre-treatments for staining success. If this is achieved, although manual segmentation of these structures in the lung would be time-intensive, it would give a better representation of the direct motion of fluid from the arterioles into the interstitium rather than assuming Darcy's law across the capillary bed.

The αSMA staining intensity and area can infer the identity of the larger blood vessel structures as detailed in section 4.3.2. Using this knowledge, Euclidian distance maps could be created from the veins and arteries to identify the smaller unknown blood vessel structures by their continuity and proximity to these larger structures. This knowledge would inform blood flow directionality to

accurately locate the input and output boundaries of the blood vessels in the geometry. In addition, blood pressure modelling would become more accurate as a precise value for blood pressure could be given, dependent on the identity of the vessel.

8.4 Future Work to Improve Current Applications of Methods and Model.

With regards to the preliminary morphological and modelling applications of the current methodology, there was simply not a large enough sample size to make any statically valid conclusions on any of the quantitative studies. Conclusions drawn from the quantitative studies were principally made for hypothesis generation to direct future work.

All analyses performed in the morphology and the modelling chapters would give useful information to the scientific and medical communities if preliminary results can be consolidated. It is easy to say, therefore, that every study should be repeated with hundreds of samples, but naturally, this is impractical. Personally, as the understanding of pulmonary lymphatic biology is in such infancy, I believe that understanding the physiology of the human lung, rather than trying to understand the pathology at the same time should be the short-term focus of future work.

Increasing the samples used or collected from “control” patients would be the first step. Ideally, if new sample biopsies are being actively collected, obtaining information about the harvesting location may give contextual information which could advance modelling applications. Non-peripheral biopsies should also be considered if the harvest location is known.

The qualitative and quantitative morphological methodology and functional modelling should then be repeated to re-assess intra- and inter-sample variability of the anatomically associated lymphatics in the “normal” state. This increased sample size would give more confidence to the quantitative results of the studies. This, in turn, gives more confidence that the following modelling assessment is targeted correctly.

Simulating fluid movement through all VOIs taken from all samples collected would be impractical. However, increasing the sample size from five intralobular VOIs to at least five from each anatomical location would be desired as this data could be used to estimate the fluid drainage from the whole of the secondary lobule. This could be achieved using the current sample size. The importance of modelling blood pressure variability across the lung was well recognised in Chapter 7, an analysis akin to that presented in Chapter 7 should therefore be included in the new study design for each VOI being analysed.

Of course, as outlined in section 3.3.2, there are many more adaptions to the model that could be tested in the future. However, changing, or increasing the complexity of too many factors of a model at once can be detrimental. Not only is it harder to identify where potential errors are in your system, the simulation process takes a lot longer due to high computation requirements. Selective and gradual amendment of the model and model inputs is therefore preferred, therefore including blood pressure heterogeneity within a full geometry comparison study is an appropriate first amendment.

8.5 Using Current Methods as a Blueprint for Future Studies

8.5.1 Human Studies

With some compromise in sample size, arguably any lymphatic network in any soft tissue biopsy could be structurally evaluated in 3D using the imaging methods outlined in this thesis. Also, with the inclusion of image-based modelling, any form of fluid movement within this soft tissue biopsy could be evaluated, including the movement of cells.

To prioritise physiological investigations, elasticity modelling would be an interesting tissue property to incorporate into the current model. Modelling elasticity of the lymphatic vessel walls would be of interest as identifying wall stresses under high fluid load could predict where branching or remodelling may occur. This, alongside possible modelling of cyclic pressure changes in the alveolar wall during respiration, could predict if the bellowing action of ventilation is likely to influence fluid dynamics and tissue fluid clearance in the lung.

Although there have been reasons given above to why physiological investigations should be prioritised, as shown in this thesis, samples can be taken from both healthy and diseased tissue. With consideration of tumour cell behaviours, predictions of metastatic cell migration in the lung through the lymphatic drainage could be made. The influence of fibrotic legions on interstitium fluid permeability in diseases such as idiopathic pulmonary fibrosis could also be investigated. Finally, studies could be made in asthmatic tissue samples to identify the immune cell profile and their 3D recruitment to bronchi in different stages of inflammation.

Although only qualitatively characterised in this thesis in small numbers, it would also be interesting to further characterise and model the lymphatics located within the interlobular septa. These “pre-collecting” lymphatics are thought to function differently from the microlymphatics due to the presence of valves and also seem to be different to equivalent structures in other organs due to their lack of smooth muscle. Modelling the effect of pulmonary ventilation on fluid flow through these vessels would therefore be an exciting proposal to see if it is likely that

mechanical ventilation serves the same purpose as smooth muscle cells for lymph propulsion. Assessing the impact of these vessels and their surrounding structures for secondary lobule fluid balance would also be interesting as these lymphatic vessels are thought to have the intermittent absorbing capacity and are closely associated to veins which have low blood pressure and high osmolarity.

8.5.2 Moving into the Animal Model

The methods presented in this work focus on understanding human pulmonary lymphatics. In most physiological research, the ultimate aim is to forward knowledge of human physiology and pathology, however, sometimes, if basic biological mechanisms are uncertain and it is not possible to quantify them in the human, taking a step back to use animal models is necessary.

To advance my research, I believe it is necessary to use animal models. As obtaining fresh human tissue is time-intensive, animal work can easily be done in parallel to the continuation of human work detailed above.

Animal models critically provide the ability to experimentally determine the dynamic function of the lymphatic system over time rather than relying on probabilities and speculation. The use of animal models also permits access to large sample numbers over short periods of time. It also provides an opportunity for experimentally determining input values for the model simulation and experimentally validating the modelling results. To be able to validate the model will increase confidence in the predictions made for fluid, cell and particulate drainage when used in human studies.

In the mouse, the use of fresh tissue would remove some limitations faced with using fixed and embedded human lung specimens. A systematic assessment of the extent of tissue collapse after harvesting-induced pneumothorax and dehydration-induced tissue shrinkage artefacts could be undertaken. µCT scans of fresh lung tissue *in-situ/ in-vivo* and *ex-vivo* along with scans between each step of the dehydration and embedding protocol could be collected. Comparing the lung volumes at each stage would give a precise assessment of tissue collapse and shrinkage. These artefacts can then be mitigated for by the process detailed in section 8.3.2. To advance this idea further, digital volume correlation algorithms may be able to digitally morph the formalin-fixed paraffin embedded sample geometry back to the in-vivo geometry dimensions. This would compensate for any non-uniform, as well as the uniform tissue collapse or shrinkage.

To use the full methodology presented in Chapters 2 and 3 as a blueprint for the assessment of pulmonary lymphatics structure and function in the animal, a suitable biomarker for LECs in the

animal is essential. Antibodies such as LYVE-1 have been successful for imaging murine LECs in other organ systems, but as in humans, very few are reliably specific for pulmonary LECs. Fortunately, the LEC marker Prox-1 has proved proficient in the mouse during lymphatic development (Choi *et al.*, 2011). In preliminary work, this success has been confirmed in-house using immunofluorescent imaging (see Figure 8.3). The staining is strong, has connectivity between tissue sections, and is in a similar pattern to that expected for pulmonary lymphatics. The methods laid out in Chapter 2 and 3 could now be applied directly to animal tissue.

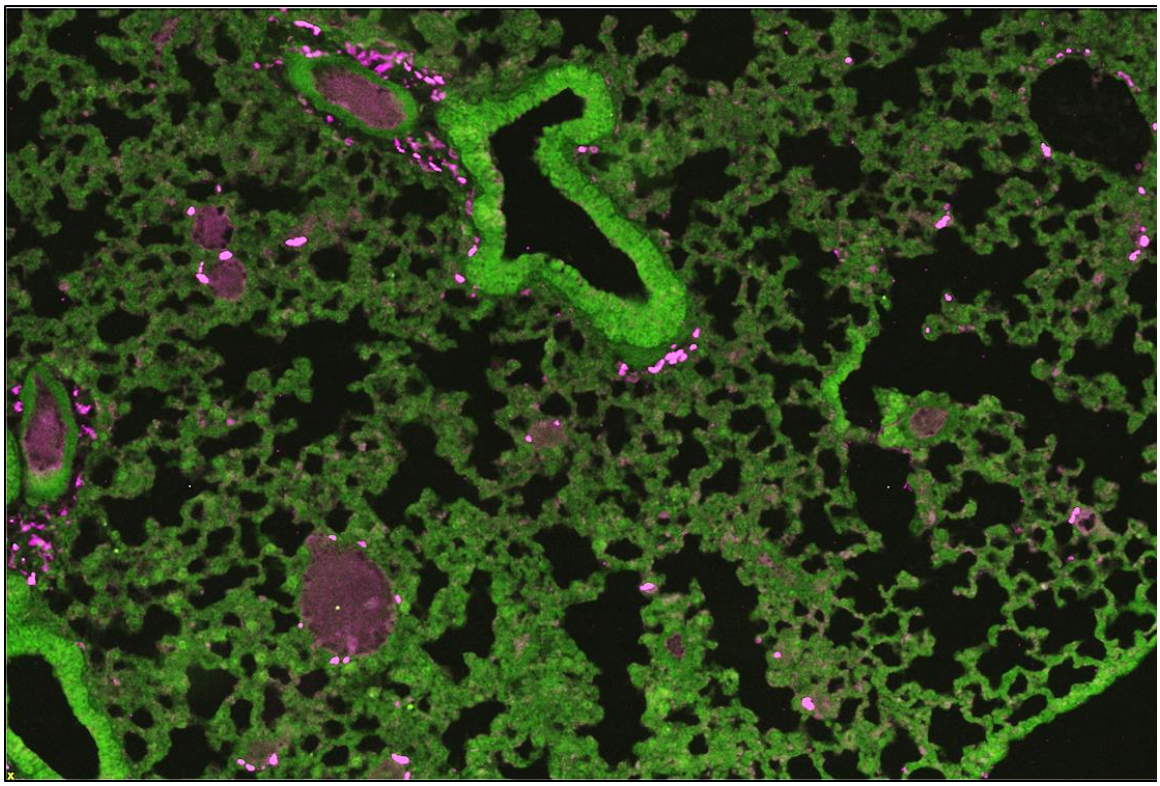

Figure 8.3 Immunofluorescence Staining of Prox-1 in Mouse Lung Prox-1 staining within a 5µm thick tissue section of mouse lung is shown in pink (using secondary antibody tagged with fluorophore alexa 647 nm). Autofluorescence of the tissue is shown in green (fluorescing at a wavelength of ~500 nm). Scale bar shown = 200 µm.

Recent literature suggests lung mechanics are essential for lymph drainage in the murine lung, reflecting the lack of smooth muscle cells on the collecting lymphatics (Reed *et al.*, 2019). By using animal models, lung tissue could be obtained at different stages of the breathing cycle and, with use of the Prox-1 antibody, be put through the workflow presented in this thesis. Morphological assessment would determine the change in lymphatics and associated alveolar geometries at different inspiratory volumes. This will enable image-based modelling to assess if geometrical changes to the lung lymphatics and alveolar pressures throughout the respiratory cycle influence the lymphatic drainage in the murine lung.

Animal studies also permit the use of genetically modified animals. A transgenic mouse strain that expresses fluorescently labelled Prox-1, provides an alternative approach. This mouse model has been used successfully in recent years to image the lymphatics of young and adult mice in 2D (Jakus *et al.*, 2014; Baluk & McDonald, 2018). The main limitation with these transgenic animal strains is that sometimes fluorescence fades after tissue fixation. Previous studies using this mouse model have shown that anti-GFP (green fluorescent protein) antibodies can be used successfully to enhance this fluorescence through standard immunofluorescence protocols (Baluk & McDonald, 2018).

Using the transgenic Prox-1-GPF mouse, the 3D technique of light-sheet fluorescence microscopy could be used to identify lymphatic vessels in the lung rather than the 2D techniques of IHC or Immunofluorescence. This allows for larger volumes of the lung to be analysed and over a shorter timeframe as this technique permits fluorescence imaging across whole lung lobes. This would enable strategic sampling of the lung so non-peripheral components of the lung can be imaged and modelled, and gravitational influences on fluid simulation could be modelled. 3D registration to µCT would still be required as µCT obtains both higher-resolution and isotropic images needed for image-based modelling.

Preliminary data using a whole lung lobe of a mouse shows, if necessary, *in-vivo* antibody administration is compatible with light-sheet microscopy if inherent fluorescence fades after fixation (see Figure 8.4 a and b). This preliminary work used an antibody raised against a biomarker associated with high-level lymphatic vessels and lymph-nodes rather than Prox-1 or GFP, but it still demonstrates these imaging methods are possible. This data also shows the compatibility of light-sheet imaging with µCT imaging and data registration between the two techniques (see Figure 8.4 c, e and f).

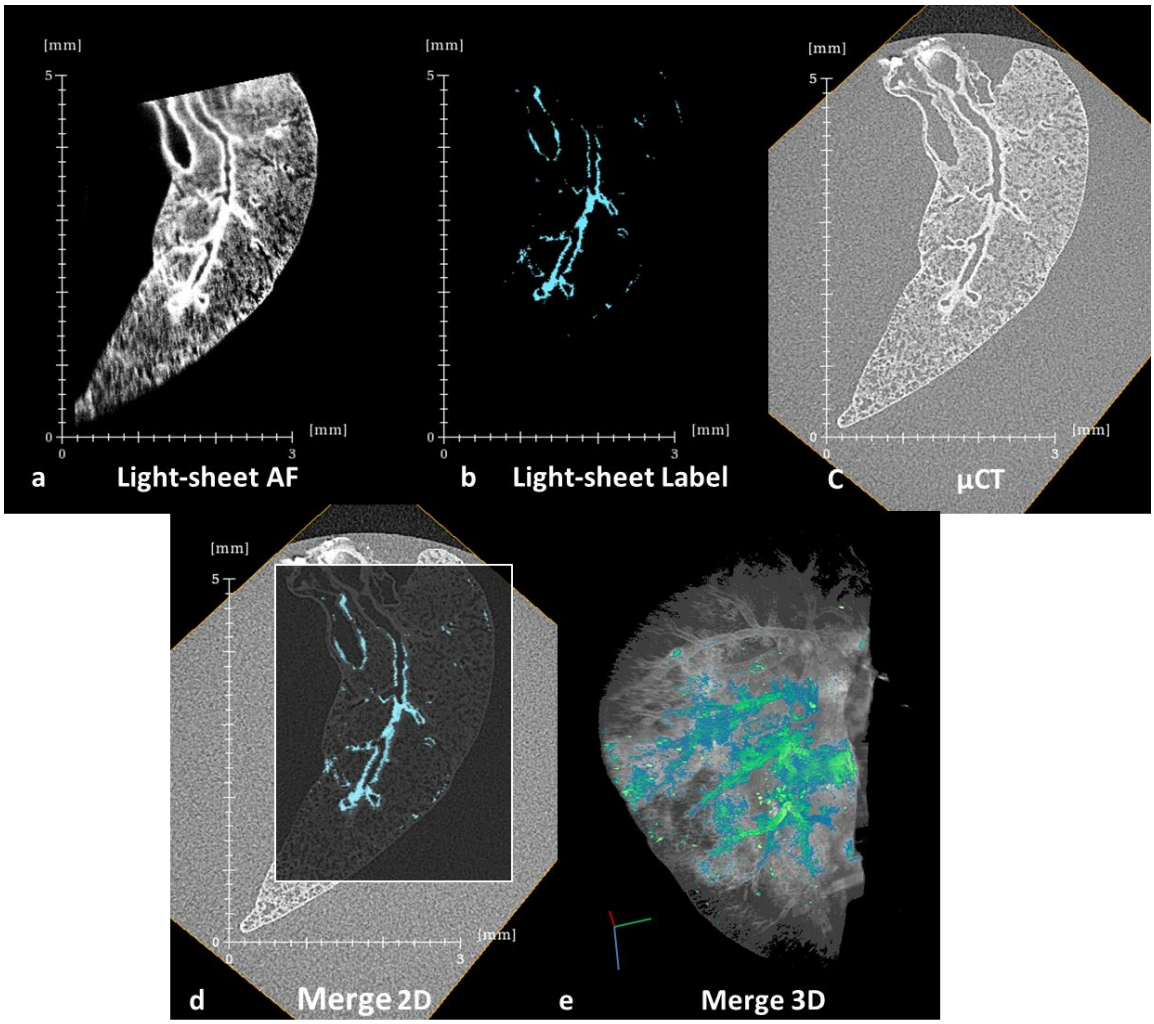

Figure 8.4 Correlation of 3D Light-sheet Fluorescence Data with 3D µCT Imaging in a Mouse Lung a A 2D representative image of high endothelial venule (HEV) immunostaining in mouse lung, with tissue autofluorescence. **b** The processed binary image of HEV immunostaining. **c** 2D slice of 3D µCT data set in the same plane in the tissue as panel **d**. A registered overlay of staining in panel **b** onto panel **c**. **e** 3D volume rendering of the HEV immunostaining (blue) within the µCT volume of the whole left lobe (grey). *The scale bar shows tissue orientation only. The dimensions of the extent of this subsample are: 2.8 mm; 2.6 mm; 5.5 mm in the green, red and blue axes respectively.* Sample courtesy of Stefan Milutinovic, University of Cardiff.

If necessary, antibodies against biomarkers for blood vessels, airways or cells could be used to confirm other structures in the µCT volume using original IHC or immunofluorescence techniques post light-sheet and µCT imaging. Due to poorer image resolution of the light-sheet technique, original 2D IHC or immunofluorescence imaging methods correlated to µCT may still be necessary for peripheral lung studies of microlymphatic networks. Ideally using a protocol which correlated all three techniques would be desirable.

As it can be shown *in-vivo* antibody administration is compatible with light-sheet microscopy and µCT imaging, Quantum dot ©micro-fluorescent tracers should also be compatible. These tracers are inherently fluorescent and are commercially available at sizes (0.1-100 nm diameter) that will pass from the circulatory system into the tissue (Ashton, West & Badea, 2015). Prox-1-GFP mice

could be terminally anaesthetised and injected intravenously with a lymphatic tracer. At four-time points post-injection, mice could be culled, and tissue harvested and imaged. Lightsheet microscopy would determine the pattern of drainage across the whole lung using Quantum dot fluorophore tracers that are easily distinguishable from the Prox1-GFP fluorescence. Euclidean vectors collected by the time point comparison of the light-sheet data would allow for the calculation of lymph flow/ unit time/ unit volume. As lymph flow is an output result of the current model simulation, this data will enable validation of the model or inform what alterations may be needed.

Many more examples of future structural and functional assessment of murine pulmonary lymphatics can be given, particularly if the pathological field is entered. It is hoped that the examples given above demonstrate the vast potential for moving into the murine model whilst human studies are ongoing.

8.6 Evaluation of Research Aims

The aims of this thesis, as laid out in section 1.5, are detailed below:

1. To develop a method for imaging human pulmonary lymphatics and associated structural features in 3D with the use of X-ray μCT and IHC.
2. To design and apply a mathematical model, describing pulmonary physiological processes to real 3D geometries of healthy and diseased human tissue using finite-element modelling techniques.
3. To further current scientific knowledge of peripheral human lung lymphatics by describing 3D morphology of peripheral pulmonary lymphatics in archived biopsies of clinical lung tissue in states of health and disease.
4. To evaluate the effect of structural changes in the pulmonary lymphatics, vasculature and parenchymal geometry on the functional mechanics of pulmonary fluid movement in health and disease.

Points 1 and 2 of this project aims have been achieved and documented in this thesis. This work has also been published in a peer-reviewed journal and as it is open access, it can aid scientists around the world in the future study of human pulmonary lymphatics (Robinson *et al.*, 2019).

With regards to points 3 and 4, as stated in section 8.4, there was simply not a large enough sample size to make any statistically valid conclusions on any of the quantitative characterisation studies. However, accomplishing these aims will be a lifetime or more of work. The work achieved in the last 2 years of work, after point 1 and 2 were accomplished, have started this structural and

functional characterisation. Hypotheses have been generated and plans suggested as to the best direction further advance this work in the future.

8.7 Final Words

I have been writing this thesis during a major global pandemic caused by the novel coronavirus SARS-CoV-2, as termed in February 2020 by the World Health Organisation. Currently, in June 2021, the global infection case number sits just above 180 million and global deaths at 3.89 million with disastrous social-economic impacts forecasted for years if not decades to come. This viral infection results predominantly in respiratory and vascular disease. To consider a multi-cellular vascular system inside the lung has not been fully visualised or quantified before now, let alone functionally assessed, is remarkable. The importance of future scientific focus on understanding the pulmonary lymphatic system, therefore speaks for itself. I am proud to have contributed to the beginning of this scientific venture.

Appendix A **Human Lung Tissue Sample Codes and Clinical Information.**

Pack years = number of years the patient has smoked 1 packet (20) of cigarettes daily

Sample Code	EV090	EV024	EV104	HL088	HL079	EV014	EV020	HL150	HL108	HL106	EV006
Age	75	84	66	31	21	71	70	52	79	77	34
Gender	M	F	M	M	M	F	F	F	M	F	F
Indications for Biopsy	Cancer	Cancer	Cancer	Pneumothorax	Pneumothorax	Cancer	Cancer	Cancer	Cancer	Cancer	Cancer
Type of Resection	Lobectomy	Lobectomy	Lobectomy	Bullectomy	Bullectomy	Wedge resection	Lobectomy	Lobectomy	Lobectomy	Lobectomy	Wedge resection
FEV1	2.96	1.66	2.65			1.36	1.99	1.13	1.33	2.31	
FVC	3.73	2.26	3.36			1.73	2.67	2.68	2.19	2.85	
FEV1/FVC	0.79	0.73	0.79			0.78	0.75	0.42	0.61	0.81	
GOLD status	0	0	0			0	0	3	3	0	
Smoking history	Non	Non	Current	Non	Non	Current	Current	Current	Ex	Ex	Ex
Pack years			10			82	26	36	80		3.8
Years since Quitting							1		16		
Recent infections				N	N	N	N	N	N	N	
History of allergy				Y	N	N	Y	N	N	N	
History of asthma		Y		N	N	Y	N	N	N	N	
Co-morbidities	GORD	Hypertension	Coeliac disease			Diabetes	None	COPD	COPD	Arthritis	
	Hypertension		Meneres disease			Hypertension				Asthma	
	S.C. Carcinoma		Prostate hypertrophy			Hypothyroidism					
	Asbestosis plaques					High cholesterol					
Medications	Metformin,	Frusemide	Combodart			Bendrofluzamethizide	Nicorette	Citalopram	Lansoprazole	Letrozole	Humira
	Glibenclamide	Simvastatin				Ezetimitre			Propranolol	Alendroit	Salazpyrin
		Lansoprazole				Simvastatin			Domperidone		Hydroxychloroquine
		Ramipril				Ramipril			Salbutamol		Piroxicam
		Citalopram				Metformin					Methotrexate
						Allopurinol					Mometason
						Levothyroxine					Isoniazid
						Atenolol					Co-dynamol
Currently on Steroids	N	N	N	N	N	N	N	N	N	N	N

Sample Code	EV003	HL155	HL087	HL101	HL102	HL135	HL093	HL077	HL098	EV027	HL083
Age	63	62	83	63	72	19	31	77	21	69	75
Gender	F	F	F	F	F	M	F	M	M	M	M
Indications for Biopsy	Cancer	Cancer	Cancer	Cancer	Cancer	Pneumothorax	Bronchiectasis	Cancer	Pneumothorax	Cancer	Cancer
Type of Resection	Lobectomy	Lobectomy	Lobectomy	Lobectomy	Lobectomy	Bullectomy	Lobectomy	Lobectomy	Bullectomy	Lobectomy	Lobectomy
FEV1	2.65	2.28	2.1	2.88	1.96		2.67	2.32		1.77	2.02
FVC	3.55	3.05	2.89	3.84	2.64		3.35	2.87		2.18	2.3
FEV1/FVC	0.75	0.75	0.73	0.75	0.74		0.79	0.81		0.81	0.88
GOLD status	0	0	0	0	0		0	0		0	0
Smoking history	Non	Non	Non	Non	Non	Non	Non	Non	Non	Ex	Ex
Pack years										20	
Years since Quitting										28	1
Recent infections		N	N	N	N	N	N	N	N	N	N
History of allergy		Y	N	Y	Y	N	N	N	N	N	Y
History of asthma		N	N	N	N	N	N	N	N	Y	Y
Co-morbidities	Glaucoma	Arthritis			Hypertension		Lupus	Arthritis		Asthma,	
							Thyrotoxicosis	Hypertension			
								Sleep apnea			
Medications	Citalopram	Bendroflumethiazide	Digoxin	Naproxen	Ramipril	Warfarin	Aspirin	Lansoprazole	Seretide		
			Levothyroxine		Candesartan	Carbimazole	Simvastatin	Symbicort	Atrovent		
			Temazepam		Simvastatin	Plaquenil	Atenolol	Spiriva	Ventolin		
			Amiodarone				Lisinopril	Ventolin	Thyroxine		
							Bendroflumethiazide		Bicalutamide		
Currently on Steroids	N	N	N	N	N	N	N	N	Y	Y	Y

M=Male F-Female Y=Yes N=No Category= Control Active Diease COPD

Appendix B **Sample Processing Data Used for Full 3D Analysis**

1 MuVIS (University of Southampton); 2 Nikon Metrology UK.

Sample Code: Control Active COPD	**µCT**		**IHC**			**Sampling**
	Machine	**Isotropic voxel resolution(µm)**	**Subvolume number (sections cut)**	**Primary Antibody**	**Stain Frequency**	**Subvolume (VOI number)**
EV090	Hutch[1]	13.2	1 (200) 2(108)	D240	Every 5th	1(45) 2(43)
				CD31	Every 5th	
				LPmab-21	Every 40th	
				αSMA	Every 40th	
				PCK	Every 40th	
EV024	Med-X [1,2]	6	1(111) 2 (100)	Same as EV090	Same as EV090	1(34) 2(30)
HL088	Med-X [1,2]	8.5	1 (122) 2(120)	LPmab-21	Every 5th	1(27) 2(27)
				CD31	Every 5th	
				D20	Every 40th	
				αSMA	Every 40th	
				PCK	Every 40th	
EV104	Med-X [1,2]	6	1(102) 2(102)	Same as HL088	Same as HL088	1(40) 2(25)
HL079	Med-X [1,2]	5	1(104) 2(110)	Same as HL088	Same as HL088	1(37) 2(34)
EV014	Med-X [1,2]	6	1(101) 2(125)	Same as HL088	Same as HL088	1(30) 2(25)
EV020	Med-X [1,2]	5	1(114) 2(114)	Same as HL088	Same as HL088	1(35) 2(37)
HL106	Med-X [1,2]	5	1(102) 2(102)	Same as HL088	Same as HL088	1(44) 2(40)
HL150	Med-X [1,2]	7.25	1(104) 2(105)	Same as HL088	Same as HL088	1(59) 2(51)
HL108	Med-X [1,2]	6	1(120) 2(120)	Same as HL088	Same as HL088	1(29) 2(26)

Appendix C **FIJI Script -Random ROI Generator Within 2D Area**

```
// Randomly places predefined Regions of Interest completely within
// the boundaries of a larger Region of Interest, measures them,labels them, and puts them into ROI
manager
// Start with opening the image, and drawing the large ROI (MUST be
//smaller than total image).
// Also Open ROI manager

macro "RandomSampleAndMeasureWithinROI [F1]" {
 run("Select None");

 saveSettings();
 original=getTitle();
 setForegroundColor(255,0,0);

 width = getWidth()-63;   // width of the randomly placed ROI
 height = getHeight()-63; // height of the randomly placed ROI
 RoisN =50; // number of ROIs
 trials=1000; //maximum trials to avoid infinite loop

 i=0;
 j=0;

 xa=newArray(RoisN);
 ya=newArray(RoisN);

 run("Duplicate...", "title=Reference");

 selectWindow("Reference");
 run("8-bit"); //makes it greyscale
 run("RGB Color"); //RGB to display colours
 run("Restore Selection");
 run("Make Inverse");
 run("Fill");
 run("Select None");

  while (i<RoisN && j<trials){
     w = 63;
     h = 63;
     x = random()*width;
     y = random()*height;
     j++;
     //Check for pixels with value (255,0,0):
     flag= -1;
     makeRectangle(x, y, w, h);
     //Scanning the rectangle perimeter should be faster than
//scanning the whole box.
     //This is slower, as checks all the points in the box:
     for (xs=x;xs<x+w;xs++){
        for (ys=y;ys<y+h;ys++){
           if (getPixel(xs,ys)==-65536) // pixel is (255,0,0)
              flag=0;
        }
     }
     if (flag==-1){
        xa[i]=x;
```

```
            ya[i]=y;
            run("Fill");
            i++;
        }
    }

  close();
  selectWindow(original);
  setForegroundColor(255,255,0);
  for (j=0;j<i;j++){
    makeRectangle(xa[j], ya[j], w, h);
      roiManager("Add");
      run("Measure");
      run("Label");
  }
 restoreSettings();
 run("Select None");
 run("Jpeg...", "save");
 run("Close");
}
```

Appendix D **Fiji Script: Lymphatic Morphometry Collection**

```
title=getTitle();
selectWindow("ROI Manager");
var roin=roiManager("count");
//Set up of arrays
AvgBranchLength_array = newArray(0);
AvgBranchED_array = newArray(0);
Tortuosity_array = newArray(0);
//Volumepix_array = newArray(0);
Volumeunit_array = newArray(0);
//SurfaceAreapix_array = newArray(0);
SurfaceAreaunit_array = newArray(0);
FractalDimension_array = newArray(0);
BranchNo_array = newArray(0);
JunctionNo_array = newArray(0);
FractalDimension_array = newArray(0);

//calibration of image
var pixelsize=getNumber("Enter pixel size:",0);
var Stacksize=getNumber("Enter Number of Images in the Stack:",0);
run("Properties...", "channels=1 slices="+Stacksize+" frames=1 unit=µm pixel_width="+pixelsize+"
pixel_height="+pixelsize+" voxel_depth="+pixelsize+"");

for(i=0;i<roin;i++){
//Definitions of Variables
        N1=0;
total_BranchNo=0;
total_JunctionNo=0;
N2=0;
total_Branch_length=0;
mean_Branch_length=0;
total_BranchED=0;
mean_BranchED=0;
Tortuosity=0;
N3=0;
//total_Volumepix=0;
total_Volumeunit=0;
//total_SurfaceAreapix=0;
total_SurfaceAreaunit=0;
FractalDimension=0;

//Data analysis of Branch #, Junction #, Branch Length, Branch ED
        selectWindow(title);
        roiManager("Select", i);
        run("Duplicate...", "duplicate");
        namecounter=i+1;
        rename(namecounter);
        VOItitle=getTitle();

        run("Skeletonize (2D/3D)");
        run("Analyze Skeleton (2D/3D)", "prune=none show");
        selectWindow("Results");

//Number of results in first results table
        N1=nResults;
//Calc Sum of Branch # and Junction # iand add to arrays
```

```
		for (a=0; a<nResults(); a++) {
		total_BranchNo= total_BranchNo + getResult("# Branches",a);
		total_JunctionNo= total_JunctionNo + getResult("# Junctions",a);
		}
		BranchNo_array = Array.concat(BranchNo_array, total_BranchNo);
		JunctionNo_array =Array.concat(JunctionNo_array, total_JunctionNo);

//Save raw data as csv file
		selectWindow("Results");
		saveAs("Results","/Users/sr1g12/Desktop/EV090(1)SS1/Lymph_Data_Raw_Results/"+namecounte
r+"Branch.JunctionNo.csv");
		run("Close");

		selectWindow("Branch information");

//Number of results in second results table
		N2 =getValue("results.count");

//Calc Mean of Branch length and ED and add to array
for (a=0; a<N2; a++) {
  total_Branch_length=total_Branch_length+getResult("Branch length",a);
  mean_Branch_length=total_Branch_length/N2;
  total_BranchED= total_BranchED +getResult("Euclidean distance",a);
  mean_BranchED= total_BranchED/N2;
}
		AvgBranchLength_array = Array.concat(AvgBranchLength_array, mean_Branch_length);
		AvgBranchED_array = Array.concat(AvgBranchED_array, mean_BranchED);

//Calc Tortuosity and add to array
		Tortuosity= mean_Branch_length/mean_BranchED;
		Tortuosity_array = Array.concat(Tortuosity_array, Tortuosity);

//Save raw data as csv file
		saveAs("Results","/Users/sr1g12/Desktop/EV090(1)SS1/Lymph_Data_Raw_Results/"+namecounte
r+"tort.csv");
		run("Close");
		selectWindow(VOItitle);
		close();
		selectWindow("Tagged skeleton");
		run("Close")

//Data analysis of Vol SA and FD
		selectWindow(title);
		roiManager("Select", i);
		run("Duplicate...", "duplicate");
		namecounter=i+1;
		rename(namecounter);
		VOItitle=getTitle();
		run("3D Geometrical Measure");
		selectWindow(VOItitle);
		run("Fractal Dimension");
		run("Close");
		selectWindow("Log");
		run("Close");
		selectWindow(""+namecounter+"::segmented");
		close();
//Processing of Vol and SA data per VOI object, exracting FD result from table
		selectWindow("Results");
		N3=nResults;
```

```
		for (a=0; a<nResults(); a++) {
		//total_Volumepix= total_Volumepix + getResult("Volume(pix)",a);
		total_Volumeunit= total_Volumeunit + getResult("Volume(unit)",a);
		//total_SurfaceAreapix= total_SurfaceAreapix + getResult("Surface(pix)",a);
		total_SurfaceAreaunit= total_SurfaceAreaunit + getResult("Surface(unit)",a);
		FractalDimension= getResult("Fractal Dimension",0)+1;
		}
//Adding V, SA And FD prcoessed Data to array

		//Volumepix_array = Array.concat(Volumepix_array, total_Volumepix);
		Volumeunit_array =Array.concat(Volumeunit_array, total_Volumeunit);
		//SurfaceAreapix_array = Array.concat(SurfaceAreapix_array, total_SurfaceAreapix);
		SurfaceAreaunit_array  =Array.concat(SurfaceAreaunit_array , total_SurfaceAreaunit);
		FractalDimension_array = Array.concat(FractalDimension_array, FractalDimension);

//Save raw data as csv file
		saveAs("Results",
"/Users/sr1g12/Desktop/EV090(1)SS1/Lymph_Data_Raw_Results/"+namecounter+"LV.SA.FD.csv");
		selectWindow(VOItitle);
		close();
		selectWindow("Results");
		run("Close");

		/*Array.print(BranchNo_array);
		Array.print(JunctionNo_array);
		Array.print(AvgBranchLength_array);
		Array.print(AvgBranchED_array);
		Array.print(Tortuosity_array);
		Array.print(Volumepix_array);
		Array.print(Volumeunit_array);
		Array.print(SurfaceAreapix_array);
		Array.print(SurfaceAreaunit_array);
		Array.print(FractalDimension_array);*/
}

//writing and saving results table from arrays
if (nResults>=0){
		run("Clear Results");
}
i = nResults;

for(n=0; n<FractalDimension_array.length; n++){
		setResult("VOI", i, i+1);
		setResult("Branch #", i, BranchNo_array[n]);
		setResult("Junction #", i, JunctionNo_array[n]);
		setResult("Avg.Branch Length", i, AvgBranchLength_array[n]);
		setResult("Avg.Branch ED", i, AvgBranchED_array[n]);
		setResult("Tortuosity", i, Tortuosity_array[n]);
		//setResult("Volume(pix)", i, Volumepix_array[n]);
		setResult("Volume(unit)", i, Volumeunit_array[n]);
		//setResult("Surface Area(pix)", i, SurfaceAreapix_array[n]);
		setResult("Surface Area(unit)", i, SurfaceAreaunit_array[n]);
		setResult("Fractal Dimension", i, FractalDimension_array[n]);
		i = nResults;
}
updateResults;
saveAs("Results","/Users/sr1g12/Desktop/EV090(1)SS1/Lymph_Data_Raw_Results/EV090(1)Results.csv");
selectWindow("Results");
run("Close");
```

Appendix E **Model Simulation Times, Errors, and Computer Memory Use**

Simulation Name	**Simulation error in each domain**			**Time to reach solution (hours)**	**Physical Computer memory usage (GB)**
	Pressure (Pa),P	**Lymphatic vessel velocity field ($m.s^{-1}$), $\underline{u}^L$**	**Blood vessel velocity field ($m.s^{-1}$), $\underline{u}^B$**		
2D Starlings. $\Delta\pi$	4.2×10^{-16}	2.7×10^{-4}	6.9×10^{-4}	<1	4
3D Starlings	2.6×10^{-17}	9.0×10^{-4}	3.6×10^{-4}	46	130
Mesh refinement (-50)	7.1×10^{-16}	4.3×10^{-4}	1.8×10^{-4}	3	12
Mesh refinement (-26)	2.3×10^{-16}	7.3×10^{-4}	1.9×10^{-5}	10	22
Mesh refinement (-12)	2.8×10^{-17}	9.2×10^{-4}	2.0×10^{-5}	22	45
Mesh refinement (0)	3.7×10^{-17}	8.7×10^{-4}	8.2×10^{-4}	46	130
Mesh refinement (+12)	8.9×10^{-17}	8.6×10^{-4}	3.1×10^{-4}	64	166
3D Starlings, No Flux B/C, Valve	2.6×10^{-16}	4.0×10^{-4}	7.8×10^{-4}	51	145
Chapters 5 and 6					
EV090(1)12,Cnt,IL	5.7 x10-17	6.2 x10-5	5.5x10-4	43	140
EV090(1)30,Cnt,IL	4.3 x10-17	4.9 x10-4	2.8x10-4	16	132
EV090(1)44,Cnt,IL	1.7 x10-17	4.5 x10-5	6.0x10-4	12	90
HL088(1)7.Cnt,IL	4.4×10^{-17}	8.3×10^{-4}	5.3×10^{-4}	86	137
HL079(2)5,Cnt,IL	2.6×10^{-17}	9.4×10^{-4}	8.5×10^{-4}	107	112
EV090(2)3,Cnt,BVB	1.9×10^{-16}	6.9×10^{-4}	3.5×10^{-4}	31	356
HL088(1)12,Cnt,BVB	4.0×10^{-17}	3.6×10^{-4}	7.7×10^{-4}	145	427
HL079(1)15,Cnt,BVB	9.9×10^{-16}	3.7×10^{-5}	1.6×10^{-5}	194	825
HL079(2)17,Cnt,BVB	9.4×10^{-17}	3.6×10^{-4}	3.1×10^{-4}	165	630
HL106(1)34,Cnt,BVB	5.7×10^{-17}	6.2×10^{-5}	5.2×10^{-4}	147	220
EV090(1)43,Cnt,SP	6.4×10^{-17},	6.6×10^{-4}	5.4×10^{-4}	50	168
HL079(1)13,Cnt,SP	8.9×10^{-16},	7.2×10^{-5}	2.1×10^{-4}	23	120
HL106(1)13,Cnt,SP	7.6×10^{-17},	1.0×10^{-4}	2.8×10^{-4}	67	165
HL088(2)2,Cnt,SP	3.0×10^{-16},	3.6×10^{-4}	6.6×10^{-4}	163	182
HL088(2)5,Cnt,SP	7.3×10^{-16},	4.1×10^{-4}	4.9×10^{-4}	35	158
EV024(2)3,AD,IL	8.4×10^{-16},	$3\ 8 \times 10^{-4}$	6.2×10^{-4}	37	110
EV104(1)39,AD,IL	4.9×10^{-16},	2.7×10^{-4}	1.4×10^{-4}	101	146
EV104(1)13,AD,IL	8.8×10^{-16},	2.8×10^{-4}	9.3×10^{-5}	30	144
EV014(1)14,AD,IL	3.9×10^{-16},	1×10^{-4}	2.2×10^{-4}	88	165
EV020(1)14,AD,IL	3.4×10^{-16},	1.5×10^{-4}	3.5×10^{-4}	38	104
HL150(1)34,COPD,IL	8.4×10^{-16},	8.3×10^{-4}	7.1×10^{-4}	6	74
HL150(1)35,COPD,IL	2.8×10^{-16},	9.5×10^{-4}	2.4×10^{-4}	13	82

HL150(1)55,COPD,IL	4.3 x10^{-16},	7.7 x10^{-4}	8.1 x10^{-4}	6	68
HL150(1)59,COPD,IL	9.4 x10^{-17},	1.7 x10^{-5}	5.8 x10^{-4}	5	54
HL108(2)20,COPD,IL	1.6 x10^{-16},	9.5 x10^{-4}	7.9 x10^{-4}	6	86
Chapter 7					
3D Starlings, No Flux B/C, Valve BP=800Pa	3.3 x10^{-16},	4.1 x10^{-4}	8.6 x10^{-4}	41	138
EV090(1)12,Cnt,IL BP=800Pa	8.3 x10^{-17},	6.1 x10^{-4}	5.8 x10^{-4}	47	118
EV090(1)30,Cnt,IL BP=800Pa	5.7 x10^{-16},	6.8 x10^{-4}	7.9 x10^{-4}	38	94
EV090(1)44,Cnt,IL BP=800Pa	4.9 x10^{-16},	2.7 x10^{-4}	3.8 x10^{-4}	53	120
HL088(1)7.Cnt,IL BP=800Pa	1.4 x10^{-16},	2.2 x10^{-4}	1.9 x10^{-4}	52	114
HL079(2)5,Cnt,IL BP=800Pa	1.9 x10^{-16},	8.5 x10^{-5}	8.7 x10^{-5}	44	98
3D Starlings, No Flux B/C, Valve, ΔK^L	7.8 x10^{-17},	2.0 x10^{-4}	2.3 x10^{-4}	132	122
3D Starlings, No Flux B/C, Valve, ΔK^B	8.0 x10^{-17},	3.1 x10^{-4}	4.5 x10^{-4}	125	116
3D Starlings, No Flux B/C, Valve, Δu^L	9.1 x10^{-17},	5.0 x10^{-4}	5.2 x10^{-4}	166	98
3D Starlings, No Flux B/C, Valve, Δu^B	5.4 x10^{-16}	4.4 x10^{-4}	8.9 x10^{-4}	175	105
3D Starlings, No Flux B/C, Valve,Scaled x2	2.7 x10^{-16}	8.7x10^{-4}	2.7 x10^{-4}	108	137

Appendix F **Lymphatic and Tissue Rendering of Example Subvolumes**

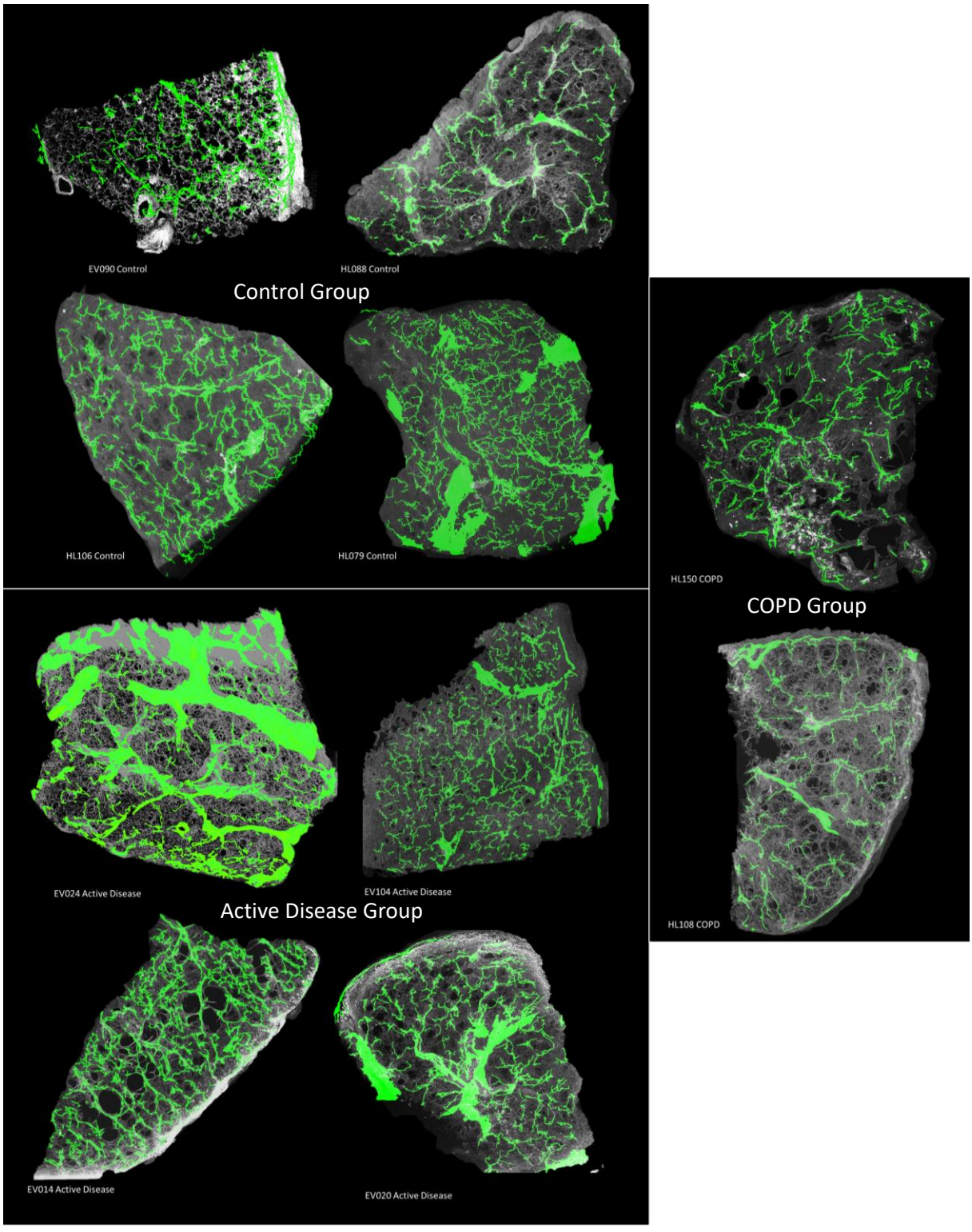

Appendix G **Lymphatic Morphology Variation Within all Samples**

Control Samples

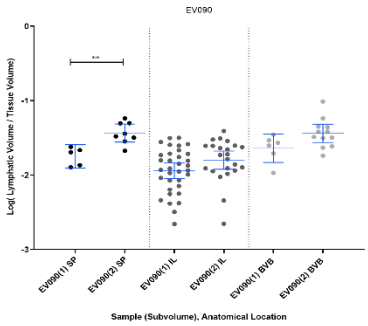

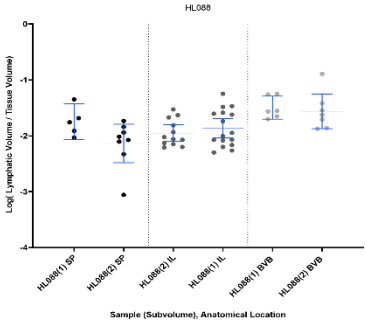

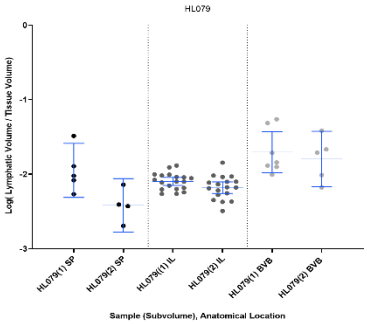

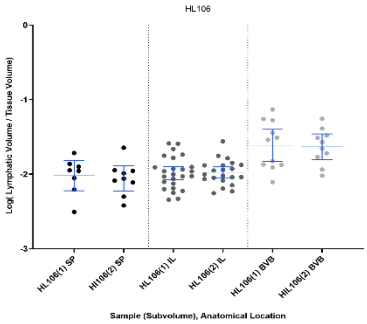

Active Disease Samples

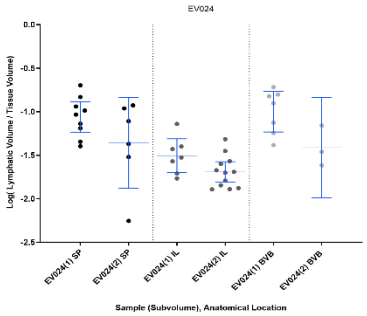

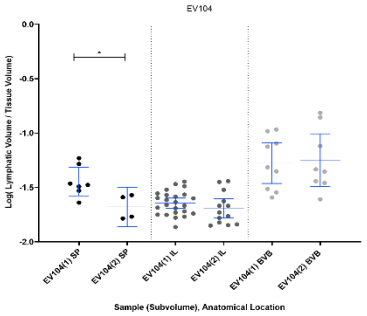

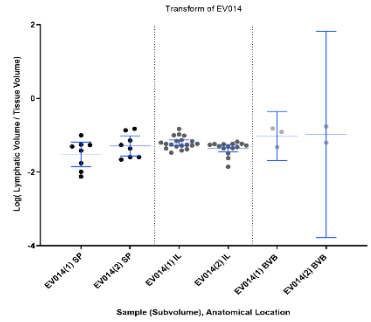

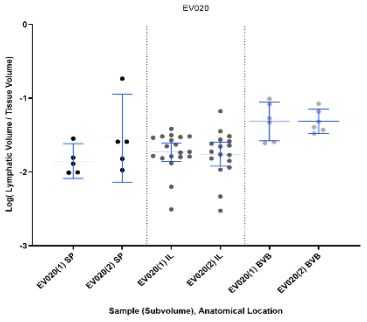

COPD Samples

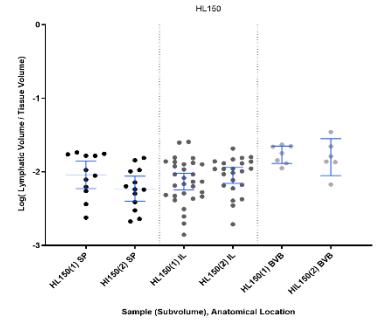

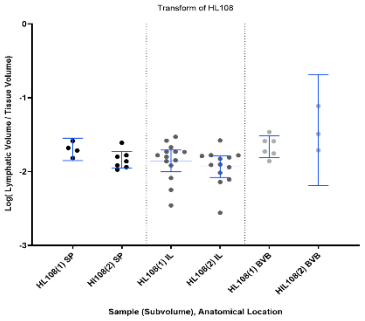

List of References

Alitalo, K., Tammela, T. & Petrova, T. V (2005) Lymphangiogenesis in development and human disease. *Nature*. [Online] 438, 946–953. Available from: doi:10.1038/nature04480.

Allison, B.J., Crossley, K.J., Flecknoe, S.J., Morley, C.J., et al. (2010) Pulmonary hemodynamic responses to in utero ventilation in very immature fetal sheep. *Respiratory Research*. [Online] 11, 1–11. Available from: doi:10.1186/1465-9921-11-111.

Ashton, J.R., West, J.L. & Badea, C.T. (2015) In vivo small animal micro-CT using nanoparticle contrast agents. *Frontiers in Pharmacology*. [Online] 6 (NOV), 1–22. Available from: doi:10.3389/fphar.2015.00256.

Aukland, K. & Reed, R. (1993) Interstitial-lymphatic mechanisms in the control of extracellular fluid volume. *Physiol Rev*. 73(1), 1–78.

Baluk, P., Adams, A., Phillips, K., Feng, J., et al. (2014) Preferential lymphatic growth in bronchus-associated lymphoid tissue in sustained lung inflammation. *American Journal of Pathology*. [Online] 184 (5), 1577–1592. Available from: doi:10.1016/j.ajpath.2014.01.021.

Baluk, P., Fuxe, J., Hashizume, H., Romano, T., et al. (2007) Functionally specialized junctions between endothelial cells of lymphatic vessels. *Journal of Experimental Medicine*. [Online] 204 (10), 2349–2362. Available from: doi:10.1084/jem.20062596 [Accessed: 11 October 2015].

Baluk, P. & McDonald, D.M. (2018) Imaging Lymphatics in Mouse Lungs. *Methods Mol Biol*. [Online] (1846), 161–180. Available from: doi:10.1007/978-1-4939-8712-2.

Baluk, P. & McDonald, D.M. (2008) Markers for microscopic imaging of lymphangiogenesis and angiogenesis. *Annals of the New York Academy of Sciences*. [Online] 1131, 1–12. Available from: doi:10.1196/annals.1413.001.

Baluk, P., Tammela, T., Ator, E., Lyubynska, N., et al. (2005) Pathogenesis of persistent lymphatic vessel hyperplasia in chronic airway inflammation. *Journal of Clinical Investigation*. [Online] 115 (2), 247–257. Available from: doi:10.1172/JCI200522037.

Baxter, L. & Jain, R. (1989) Transport of fluid and macromolecules in tumors: I. role of interstitial pressure and convection. *Microvascular Research*. (37), 77–104.

Benias, P.C., Wells, R.G., Sackey-Aboagye, B., Klavan, H., et al. (2018) Structure and distribution of an unrecognized interstitium in human tissues. *Scientific Reports*. [Online] 8 (1), 1–8. Available from: doi:10.1038/s41598-018-23062-6.

Benoit, J.N., Zawieja, D.C., Goodman, A.H. & Granger, H.J. (1989) Characterization of intact mesenteric lymphatic pump and its responsiveness to acute edemagenic stress. *The American journal of physiology*. 257 (6 Pt 2), 2059–2069.

Bertram, C.. D., Macaskill, C., Jr., M.J.. & Moore, J.E. (2011) Simulation of a Chain of Collapsible Contracting Lymphangions With Progressive Valve Closure. *J Biomech Eng*. [Online] 133 (4), 1–26. Available from: doi:10.1115/1.4002799.

Bhandari, V., Choo-Wing, R., Chapoval, S.P., Lee, C.G., et al. (2006) Essential role of nitric oxide in VEGF-induced, asthma-like angiogenic, inflammatory, mucus, and physiologic responses in the lung. *Proceedings of the National Academy of Sciences of the United States of America*. [Online] 103 (29), 11021–11026. Available from: doi:10.1073/pnas.0601057103.

Boardman, K.C. & Swartz, M.A. (2003) Interstitial flow as a guide for lymphangiogenesis. *Circulation Research*. [Online] 92 (7), 801–808. Available from: doi:10.1161/01.RES.0000065621.69843.49.

Boggon, R.P. & Palfrey, A.J. (1973) The microscopic anatomy of human lymphatic trunks. *Journal of anatomy*. [Online] 114 (Pt 3), 389–405. Available from: http://www.pubmedcentral.nih.gov/articlerender.fcgi?artid=1271452&tool=pmcentrez&rendertype=abstract.

Boon, M., Verleden, S.E., Bosch, B., Lammertyn, E.J., et al. (2016) Morphometric analysis of explant lungs in cystic fibrosis. *American Journal of Respiratory and Critical Care Medicine*. [Online] 193 (5), 516–526. Available from: doi:10.1164/rccm.201507-1281OC.

Botto, L., Beretta, E., Daffara, R., Miserocchi, G., et al. (2006) Biochemical and morphological changes in endothelial cells in response to hypoxic interstitial edema. *Respiratory Research*. [Online] 7, 1–14. Available from: doi:10.1186/1465-9921-7-7.

Boudier, T., Ollion, J., Cochennec, J., Escude, C., et al. (2013) TANGO : a generic tool for high-throughput 3D image analysis for studying nuclear organization. *Bioinformatics*. [Online] 29 (14), 1840–1841. Available from: doi:10.1093/bioinformatics/btt276.

Brandis, K. (2020) *Pulmonary Microcirculation*. 2020. Fluid Physiology.

Bressler, S.B. & Bressler, N.M. (2012) *Age-Related Macular Degeneration: Non-neovascular Early AMD, Intermediate AMD, and Geographic Atrophy*. Fifth Edit. [Online]. Elsevier Inc. Available from: doi:10.1016/B978-1-4557-0737-9.00065-5.

Bullitt, E., Zeng, D., Gerig, G., Aylward, S., et al. (2005) Vessel Tortuosity and Brain Tumor Malignancy: A Blinded Study. *Acad Radiol*. [Online] 12 (10), 1232–1240. Available from: doi:10.1038/jid.2014.371.

Burrowes, K.S., Swan, A.J., Warren, N.J. & Tawhai, M.H. (2008) Towards a virtual lung: Multi-scale, multi-physics modelling of the pulmonary system. *Philosophical Transactions of the Royal Society A: Mathematical, Physical and Engineering Sciences*. [Online] 366 (1879), 3247–3263. Available from: doi:10.1098/rsta.2008.0073.

Busse, M., Müller, M., Kimm, M.A., Ferstl, S., et al. (2018) Three-dimensional virtual histology enabled through cytoplasm-specific X-ray stain for microscopic and nanoscopic computed tomography. *Proceedings of the National Academy of Sciences*. [Online] 115 (10), 2293–2298. Available from: doi:10.1073/pnas.1720862115.

Carragher, D.M., Rangel-Moreno, J. & Randall, T.D. (2008) Ectopic lymphoid tissues and local immunity. *Seminars in Immunology*. [Online] 20 (1), 26–42. Available from: doi:10.1016/j.smim.2007.12.004.

Casley-Smith, J.R. (1975) A theoretical support for the transport of macromolecules by osmotic flow across a leaky membrane against a concentration gradient. *Microvascular Research*. [Online] 9 (1), 43–48. Available from: doi:10.1016/0026-2862(75)90050-3.

Casley-Smith, J.R. (1979) 'Prelymphatics'. In: H. Malek, P. Bartos, V. Weissleder (ed.). *Lymphology*. Stuttgart, Georg Thieme Publishers. pp. 17–21.

Casley-Smith, J.R. (1980) The Fine Structure and Functioning of Tissue Channels and Lymphatics. *Lymphology*. 13, 117–183.

Casley-Smith, J.R. (1976) The functioning and interrelationships of blood capillaries and lymphatics. *Experientia*. [Online] 32 (1), 1–12. Available from: doi:10.1007/BF01932595.

Cho, C.H., Koh, Y.J., Han, J., Sung, H.K., et al. (2007) Angiogenic role of LYVE-1-positive macrophages in adipose tissue. *Circulation Research*. [Online] 100 (4). Available from: doi:10.1161/01.RES.0000259564.92792.93.

Choi, I., Chung, H.K., Ramu, S., Lee, H.N., et al. (2011) Visualization of lymphatic vessels by Prox1-promoter directed GFP reporter in a bacterial artificial chromosome-based transgenic mouse. *Blood*. [Online] 117 (1), 362–365. Available from: doi:10.1182/blood-2010-07-298562.

Clark, A.R., Kumar, H. & Burrowes, K. (2017) Capturing complexity in pulmonary system modelling. *Proc IMechE Part H:J Engineering in Medicine*. [Online] 231 (5), 355–368. Available from: doi:10.1177/0954411916683221.

Comparini, L. (1962) Precollettori linfatici. *Biol. Latina.* (15), 1–15.

Cooper, L.J., Heppell, J.P., Clough, G.F. & Roose, T. (2016) An Image-Based Model of Fluid Flow Through Lymph Nodes. *Bulletin of Mathematical Biology*. [Online] 78(1), 52–57. Available from: doi:10.1007/s11538-015-0128-y.

Coxson, H.O., Rogers, R.M., Whittall, K.P., D'Yachkova, Y., et al. (1999) A quantification of the lung surface area in emphysema using computed tomography. *American Journal of Respiratory and Critical Care Medicine*. [Online] 159 (3), 851–856. Available from: doi:10.1164/ajrccm.163.6.16362b.

Cueni, L.N. & Detmar, M. (2008) The lymphatic system in health and disease. *Lymphatic research and biology*. [Online] 6 (3–4), 109–122. Available from: doi:10.1089/lrb.2008.1008.

Dahlgren, M.W. & Molofsky, A.B. (2019) Adventitial Cuffs: Regional Hubs for Tissue Immunity. *Trends in Immunology*. [Online] 40 (10), 877–887. Available from: doi:10.1016/j.it.2019.08.002.

Danielsen, M. & Ottesen, J.T. (2001) Describing the pumping heart as a pressure source. *Journal of theoretical biology*. [Online] 212 (1), 71–81. Available from: doi:10.1006/jtbi.2001.2348.

Davis, J.M., Hyjek, E., Husain, A.N., Shen, L., et al. (2013) Lymphatic endothelial differentiation in pulmonary lymphangioleiomyomatosis cells. *J Histochem Cytochem*. [Online] 61 (8), 580–590. Available from: doi:10.1369/0022155413489311.

Dellacà, R.L., Zannin, E., Sancini, G., Rivolta, I., et al. (2008) Changes in the mechanical properties of the respiratory system during the development of interstitial lung edema. *Respiratory Research*. [Online] 9, 1–9. Available from: doi:10.1186/1465-9921-9-51.

Deserranno, D., Kassemi, M. & Thomas, J.D. (2007) Incorporation of myofilament activation mechanics into a lumped model of the human heart. *Annals of Biomedical Engineering*. [Online] 35 (3), 321–336. Available from: doi:10.1007/s10439-006-9234-1.

Diedrich, K.T., Roberts, J.A., Schmidt, R.H., Kang, C.K., et al. (2011) Validation of an arterial tortuosity measure with application to hypertension collection of clinical hypertensive patients. *BMC Bioinformatics*. [Online] 12 (SUPPL. 10), S15. Available from: doi:10.1186/1471-2105-12-S10-S15.

Dixon, J.B., Raghunathan, S. & Swartz, M.A. (2009) A tissue-engineered model of the intestinal lacteal for evaluating lipid transport by lymphatics. *Biotechnology and Bioengineering*. [Online] 103 (6), 1224–1235. Available from: doi:10.1002/bit.22337.

Doube, M., Kłosowski, M., Arganda-Carreras, I., Cordeliéres, F., et al. (2010) BoneJ: free and extensible bone image analysis in ImageJ. *Bone*. 47, 1076–1079.

Dougherty, R. & Kunzelmann, K.-H. (2007) Computing Local Thickness of 3D Structures with ImageJ. *Microscopy and Microanalysis*. [Online] 13 (S02), 1678–1679. Available from: doi:10.1017/S1431927607074430.

Drake, R.E., Allen, S.J., Katz, J., Gabel, J.C., et al. (1986) Equivalent circuit technique for lymph flow studies. *Am J Physiol Heart Circ Physiol*. 251 (5), H1090-1094.

Drake, R.E., Dhother, S., Oppenlander, V.M. & Gabel, J.C. (1996) Lymphatic pump function curves in awake sheep. *Am. J. Physiol. Regulatory Integr. Comp. Physiol.* 270, 486–488.

Drake, R.E., Weiss, D. & Gabel, J.C. (1991) Active lymphatic pumping and sheep lung lymph flow. *J Appl Physiol*. 71 (1), 99–103.

Dudak, J., Zemlicka, J., Karch, J., Patzelt, M., et al. (2016) High-contrast X-ray micro-radiography and micro-CT of ex-vivo soft tissue murine organs utilizing ethanol fixation and large area photon-counting detector. *Scientific Reports*. [Online] 6 (July), 1–9. Available from: doi:10.1038/srep30385.

Ebina, M. (2008) Remodeling of airway walls in fatal asthmatics decreases lymphatic distribution; beyond thickening of airway smooth muscle layers. *Allergology international*. [Online] 57 (2), 165–174. Available from: doi:10.2332/allergolint.O-07-497.

Ebina, M., Shibata, N., Ohta, H., Hisata, S., et al. (2010) The Disappearance of Subpleural and Interlobular Lymphatics in Idiopathic Pulmonary Fibrosis. *Lymphatic Research and Biology*. [Online] 8 (4), 199–207. Available from: doi:10.1089/lrb.2010.0008.

Effros, R.M. & Parker, J.C. (2009) Pulmonary vascular heterogeneity and the Starling hypothesis. *Microvascular Research*. [Online] 78 (1), 71–77. Available from: doi:10.1016/j.mvr.2009.03.004.

Eisenhoffer, J., Elias, R.M. & Johnston, M.G. (1993) Effect of outflow pressure on lymphatic pumping in vitro. *The American journal of physiology*. 265 (1 Pt 2), R97-102.

El-Chemaly, S., Malide, D., Zudaire, E., Ikeda, Y., et al. (2009) Abnormal lymphangiogenesis in idiopathic pulmonary fibrosis with insights into cellular and molecular mechanisms. *Proceedings of the National Academy of Sciences of the United States of America*. 106 (10), 3958–3963.

Elhay, S. & Casley-Smith, J.R. (1976) *Mathematical Model of the Initial Lymphatics*. 140, 121–140.

Erbertseder, K., Reichold, J., Flemisch, B., Jenny, P., et al. (2012) A coupled discrete/continuum model for describing cancer-therapeutic transport in the lung. *PLoS ONE*. [Online] 7 (3), 1–17. Available from: doi:10.1371/journal.pone.0031966.

Erdmann, a. J., Vaughan, T.R., Brigham, K.L., Woolverton, W.C., et al. (1975) Effect of increased vascular pressure on lung fluid balance in unanesthetized sheep. *Circulation Research*. [Online] 37 (3), 271–284. Available from: doi:10.1161/01.RES.37.3.271.

Faight, E.M., Verdelis, K., Zourelias, L., Chong, R., et al. (2017) MicroCT analysis of vascular morphometry: A comparison of right lung lobes in the SUGEN/hypoxic rat model of pulmonary arterial hypertension. *Pulmonary Circulation*. [Online] 7 (2), 522–530. Available from: doi:10.1177/2045893217709001.

Favre, C.J., Mancuso, M., Maas, K., McLean, J.W., et al. (2003) Expression of genes involved in vascular development and angiogenesis in endothelial cells of adult lung. *American Journal of Physiology-Heart and Circulatory Physiology*. 285 (5), H1917–H1938.

Flannery, B.P., Deckman, H.W., Roberge, W.G. & Amico, K.L.D. (1987) Three-Dimensional X-ray Microtomography. *Science*. 237, 1439–1444.

Fleischner, F.G. (1967) The butterfly pattern of acute pulmonary edema. *Am. J. Cardiol.* 20, 39–46.

Folarina, A.A., Konerding, M.A., Timonen, J., Nagl, S., et al. (2010) Three-Dimensional Analysis of Tumour Vascular Corrosion Casts using Stereoimaging and Micro- Computed Tomography. *Microvascular Research*. [Online] 80 (1), 89–98. Available from: doi:10.1016/j.mvr.2010.03.007.THREE-DIMENSIONAL.

Földi, M., Földi, E., Strößenreuther, R.H.K. & Kubic, S. (2006) *Földi's Textbook of Lymphology: For Physicians and Lymphedema Therapists.* Second edi. Munich, Urban and Fischer.

Fujiwara, M., Sawada, M., Kasuya, A., Matsushita, Y., et al. (2014) Measurement of cutaneous lymphatic flow rates in patients with skin cancer: Area extraction method. *Journal of Dermatology*. [Online] 41 (6), 498–504. Available from: doi:10.1111/1346-8138.12506.

Fukushima, M., King, L.S., Kang, K.H., Banerjee, M., et al. (1990) Lung mechanics and airway reactivity in sheep during development of oxygen toxicity. *Journal of Applied Physiology*. [Online] 69 (5), 1779–1785. Available from: doi:10.1152/jappl.1990.69.5.1779.

Galie, P. & Spilker, R.L. (2009) A two-dimensional computational model of lymph transport across primary lymphatic valves. *Journal of biomechanical engineering*. [Online] 131 (11), e-111004. Available from: doi:10.1115/1.3212108.

Gashev, A.A., Davis, M.J. & Zawieja, D.C. (2002) Inhibition of the active lymph pump by flow in rat mesenteric lymphatics and thoracic duct. *The Journal of physiology*. [Online] 540, 1023–1037. Available from: doi:10.1113/jphysiol.2001.016642.

Gefen, A., Elad, D. & Shiner, R.J. (1999) Analysis of stress distribution in the alveolar septa of normal and simulated emphysematic lungs. *Journal of Biomechanics*. [Online] 32 (9), 891–897. Available from: doi:10.1016/S0021-9290(99)00092-5.

Gluecker, T., Capasso, P., Schnyder, P., Gudinchet, F., et al. (1999) Clinical and radiologic features of pulmonary edema. *Radiographics.* 19, 1507–1531.

Gonzalez, R.F. & Dobbs, L.G. (1998) Purification and analysis of RTI40, a type I alveolar epithelial cell apical membrane protein. *Biochimica et Biophysica Acta*. 1429, 208–216.

Granger, D.N., Mortillaro, N.A. & Taylor, A.E. (1977) Interactions of intestinal lymph flow and secretion. *American Journal of Physiology*. [Online] 232 (1). Available from: doi:10.1152/ajpendo.1977.232.1.e13.

Grotberg, J.B. (2011) Respiratory fluid mechanics. *Physics of Fluids*. [Online] 23 (2), 1–15. Available from: doi:10.1063/1.3517737.

Guyton, A.C. & Hall, J.E. (2010) *Guyton and Hall Textbook of Medical Physiology*. Guyton Physiology. 12th edition. Philadelphia PA, Elsevier Health Sciences.

Haagensen, C.. (1972) The General Anatomy of the Lymphatic system. In: *The Lymphatics in Cancer*. Philadelphia PA, W.B Saunders Company. pp. 22–40.

Haitao, S., Ning, L., Lijun, G., Fei, G., et al. (2011) Fractal dimension analysis of MDCT images for quantifying the morphological changes of the pulmonary artery tree in patients with pulmonary hypertension. *Korean Journal of Radiology*. [Online] 12 (3), 289–296. Available from: doi:10.3348/kjr.2011.12.3.289.

Hall, B.Y.J.G., Morris, B. & Woolley, G. (1965) Intrinsic Rhythmic propulsion of lymph in the Unanaesthetized Sheep. *J. Physiol*. 180, 336–349.

Han, H.C. (2012) Twisted blood vessels: Symptoms, etiology and biomechanical mechanisms. *Journal of Vascular Research*. [Online] 49 (3), 185–197. Available from: doi:10.1159/000335123.

Hansen-Flaschen, J.H., Lanken, P.N. & Pietra, G.G. (1986) Effect of 100% O2 on passage of uncharged dextrans from blood to lung lymph. *Journal of Applied Physiology*. [Online] 60 (5), 1797–1809. Available from: doi:10.1152/jappl.1986.60.5.1797.

Helmberger, M., Pienn, M., Urschler, M., Kullnig, P., et al. (2014) Quantification of tortuosity and fractal dimension of the lung vessels in pulmonary hypertension patients. *PLoS ONE*. [Online] 9 (1). Available from: doi:10.1371/journal.pone.0087515.

Heppell, C., Richardson, G. & Roose, T. (2013) A Model for Fluid Drainage by the Lymphatic System. *Bulletin of Mathematical Biology*. [Online] 75 (1), 49–81. Available from: doi:10.1007/s11538-012-9793-2.

Heppell, C., Roose, T. & Richardson, G. (2015) A Model for interstitial drainage through a Sliding Lymphatic Valve. *Bulletin of Mathematical Biology*. [Online] 1–37. Available from: doi:10.1007/s11538-015-0078-4.

Hogan, R.D. & Unthank, J.L. (1986) Mechanical control of initial lymphatic contractile behavior in bat's wing. *Am. J. Physiol.* 251, 357–363.

Hogg, J.C., Chu, F., Utokaparch, S., Woods, R., et al. (2004) The Nature of Small-Airway Obstruction in Chronic Obstructive Pulmonary Disease. *N Engl J Med*. 350 (26), 2645–2653.

Hogg, J.C., Mcdonough, J.E., Sanchez, P.G., Cooper, J.D., et al. (2009) Micro – Computed Tomography Measurements of Peripheral Lung Pathology in Chronic Obstructive Pulmonary Disease. *Proc Am Thorac Soc*. [Online] 6, 546–549. Available from: doi:10.1513/pats.200905-029DS.

Hogg, J.C., McDonough, J.E. & Suzuki, M. (2013) Small Airway Obstruction in COPD. *CHEST Journal*. [Online] 143 (5), 1436. Available from: doi:10.1378/chest.12-1766.

Hsia, C.C., Hyde, D.M. & Weibel, E.R. (2016) Lung Structure and the Intrinsic Challenges of Gas Exchange. *Compr Physiol.* 6(2), 827-95.

Huo, Y. & Kassab, G.S. (2012) Intraspecific scaling laws of vascular trees. *Journal of the Royal Society Interface*. [Online] 9 (66), 190–200. Available from: doi:10.1098/rsif.2011.0270.

Jackson, D.G. (2004) Biology of the lymphatic marker LYVE-1 and applications in research into lymphatic trafficking and lymphangiogenesis. *Apmis*. [Online] 112 (7–8), 526–538. Available from: doi:10.1111/j.1600-0463.2004.apm11207-0811.x.

Jakus, Z., Gleghorn, J.P., Enis, D.R., Sen, A., et al. (2014) Lymphatic function is required prenatally for lung inflation at birth. *Journal of Experimental Medicine*. [Online] 211 (5), 815–826. Available from: doi:10.1084/jem.20132308.

Jin, Z.G., Ueba, H., Tanimoto, T., Lungu, A.O., et al. (2003) Ligand-independent activation of vascular endothelial growth factor receptor 2 by fluid shear stress regulates activation of endothelial nitric oxide synthase. *Circulation Research*. [Online] 93 (4), 354–363. Available from: doi:10.1161/01.RES.0000089257.94002.96.

Johnson, J.T., Hansen, M.S., Wu, I., Healy, L.J., et al. (2006) Virtual histology of transgenic mouse embryos for high-throughput phenotyping. *PLoS Genetics*. [Online] 2 (4), 471–477. Available from: doi:10.1371/journal.pgen.0020061.

Johnson, L.A., Prevo, R., Clasper, S. & Jackson, D.G. (2007) Inflammation-induced uptake and degradation of the lymphatic endothelial hyaluronan receptor LYVE-1. *Journal of Biological Chemistry*. [Online] 282 (46), 33671–33680. Available from: doi:10.1074/jbc.M702889200.

Jones, A.S., Milthorpe, B.K. & Howlett, C.R. (1994) Measurement of microtomy induced section distortion and its correction for 3-dimensional histological reconstructions. *Cytometry*. [Online] 15 (2), 95–105. Available from: doi:10.1002/cyto.990150203.

Jones, M.G., Fabre, A., Schneider, P., Cinetto, F., et al. (2016) Three-dimensional characterization of fibroblast foci in idiopathic pulmonary fibrosis. *JCI Insight*. [Online] 1 (5), 1–11. Available from: doi:10.1172/jci.insight.86375.

Jones, R.T. (1968) Blood Flow. *Annual Review of Fluid Mechanics*. 1, 223–244.

Kahn, H.J., Bailey, D. & Marks, A. (2002) *Monoclonal Antibody D2-40 , a New Marker of Lymphatic Endothelium , Reacts with Kaposi ' s Sarcoma and a Subset of Angiosarcomas*. 15 (4), 434–440.

Kaipainen, A., Korhonen, J., Mustonen, T., Dumontt, D., et al. (1995) Expression of the fms-like tyrosine kinase 4 gene becomes restricted to lymphatic endothelim during development. *Proc.Natl.Acad.Sci USA*. 92 (April), 3566–3570.

Kambouchner, M. & Bernaudin, J. (2009) Intralobular Pulmonary Lymphatic Distribution in Normal Human Lung Using D2-40 Antipodoplanin Immunostaining. *The Journal of Histochemistry & Cytochemistry*. 57 (7), 643–648.

Kaneko, M.K., Nakamura, T., Honma, R., Ogasawara, S., et al. (2017) Development and characterization of anti-glycopeptide monoclonal antibodies against human podoplanin, using glycan-deficient cell lines generated by CRISPR/Cas9 and TALEN. *Cancer Medicine*. [Online] 6 (2), 382–396. Available from: doi:10.1002/cam4.954.

Kantor, B., Jorgensen, S.M., Lund, P.E., Chmelik, M.S., et al. (2002) Cryostatic micro-computed tomography imaging of arterial wall perfusion. *Scanning*. 24 (4), 186–190.

Kato, S., Shimoda, H., Ji, R.-C. & Miura, M. (2006) Lymphangiogenesis and expression of specific molecules as lymphatic endothelial cell markers. *Anatomical science international*. 81 (2), 71–83.

Katsamenis, O.L., Olding, M., Warner, J.A., Chatelet, D.S., et al. (2019) X-ray Micro-Computed Tomography for Nondestructive Three-Dimensional (3D) X-ray Histology. *American Journal of Pathology*. [Online] 189 (8), 1608–1620. Available from: doi:10.1016/j.ajpath.2019.05.004.

Keeley, V. (2006) The use of lymphoscintigraphy in the management of chronic oedema. *Journal of Lymphoedema*. 1 (1), 42–57.

Khimchenko, A., Deyhle, H., Schulz, G., Schweighauser, G., et al. (2016) NeuroImage Extending two-dimensional histology into the third dimension through conventional micro computed tomography. *NeuroImage*. [Online] 139, 26–36. Available from: doi:10.1016/j.neuroimage.2016.06.005.

Kim, D., Deerinck, T.J., Sigal, Y.M., Babcock, H.P., et al. (2015) Correlative stochastic optical reconstruction microscopy and electron microscopy. *PLoS ONE*. [Online] 10 (4), 1–20. Available from: doi:10.1371/journal.pone.0124581.

Koo, H.K., Vasilescu, D.M., Booth, S., Hsieh, A., et al. (2018) Small airways disease in mild and moderate chronic obstructive pulmonary disease: a cross-sectional study. *The Lancet Respiratory Medicine*. [Online] 6 (8), 591–602. Available from: doi:10.1016/S2213-2600(18)30196-6.

Krouskop, T., Newell, P.J. & Reddy, N. (1975) Biomechanics of a lymphatic vessel. *Blood Vessels.* 12, 261–278.

Kulkarni, R.M., Herman, A., Ikegami, M., Greenberg, J.M., et al. (2011) Lymphatic ontogeny and effect of hypoplasia in developing lung. *Mechanisms of Development*. 128 (1–2), 29–40.

Kumar, H., Vasilescu, D.M., Yin, Y., Hoffman, E.A., et al. (2013) Multiscale imaging and registration-driven model for pulmonary acinar mechanics in the mouse. *Journal of Applied Physiology*. [Online] 114 (8), 971–978. Available from: doi:10.1152/japplphysiol.01136.2012.

Kurbel, S., Kurbel, B., Belovari, T., Maric, S., et al. (2001) Model of interstitial pressure as a result of cyclical changes in the capillary wall fluid transport. *Medical Hypotheses*. 2 (57), 161–166.

Landis, E.N. & Keane, D.T. (2010) X-ray microtomography. *Materials Characterization*. [Online] 61 (12), 1305–1316. Available from: doi:10.1016/j.matchar.2010.09.012.

Lauweryns, J.M. & Baert, J.H. (1977) Alveolar clearance and the role of the pulmonary lymphatics. *The American review*

of respiratory disease. 115 (4), 625.

Leak, L. V. & Burke, J.F. (1968) Ultrastructural Studies on the Lymphatic Anchoring Filaments. *The Journal of Cell Biology*. [Online] 36 (1), 129–149. Available from: doi:10.1083/jcb.36.1.129 [Accessed: 21 October 2015].

Leak, L. V. & Jamuar, M.P. (1983) Ultrastructure of Pulmonary Lymphatic Vessels. *The American review of respiratory disease*. 128, 59–65.

Leak, L. V (1976) The structure of lymphatic capillaries in lymph formation. *Fed. Proc.* 35, 1863–187.

Lewandowski, E., O Connor, B., Bertagnolli, A., Tinoco, A., et al. (2016) Screening and diagnosis of depression in adolescents in a large HMO. *Psychiatr Serv.* [Online] 93 (4), 292–297. Available from: doi:10.1016/j.contraception.2015.12.017.Women.

Litzlbauer, H.D., Korbel, K., Kline, T.L., Jorgensen, S.M., et al. (2010) Synchrotron-based Micro-CT Imaging of the Human Lung Acinus. *Anat Rec.* [Online] 293 (9), 1607–1614. Available from: doi:10.1002/ar.21161.Synchrotron-based.

Loukas, M., Bellary, S.S., Kuklinski, M., Ferrauiola, J., et al. (2011) *The Lymphatic System : A Historical Perspective*. 816, 807–816.

Lutfi, M.F. (2017) The physiological basis and clinical significance of lung volume measurements. *Multidisciplinary Respiratory Medicine*. [Online] 12 (1), 1–12. Available from: doi:10.1186/s40248-017-0084-5.

Macdonald, A.J., Arkill, K.P., Tabor, G.R., Mchale, N.G., et al. (2008) Modeling flow in collecting lymphatic vessels: one-dimensional flow through a series of contractile elements. *Am J Physiol Heart Circ Physiol*. [Online] 295, 305–313. Available from: doi:10.1152/ajpheart.00004.2008.

Mandelbrot, B. (1967) How long is the coast of Britain? Statistical self-similarity and fractional dimension. *Science*. [Online] 156 (3775), 636–638. Available from: doi:10.1126/science.156.3775.636.

Mansel, R.E. (2000) History , Present Status and Future of Sentinel Node Biopsy in Breast Cancer. *Acta Oncologica*. [Online] 39 (3), 265–268. Available from: doi:10.1080/028418600750012998.

Mansoor, A., Bagci, U., Foster, B., Xu, Z., et al. (2015) Segmentation and image analysis of abnormal lungs at CT: Current approaches, challenges, and future trends. *Radiographics*. [Online] 35 (4), 1056–1076. Available from: doi:10.1148/rg.2015140232.

Maran, A., Khosla, S., Riggs, B.L., Zhang, M., et al. (2003) Measurement of gene expression following cryogenic µ-CT scanning of human iliac crest biopsies. *Journal of Musculoskeletal Neuronal Interactions*. 3 (1), 83–88.

Marchetti, C., Poggi, P., Clement, M.G., Aguggini, G., et al. (1994) Lymphatic capillaries of the pig lung: TEM and SEM observations. *Anat Rec.* 238 (3), 368–373.

Margaris, K.N. & Black, R. a (2012) Modelling the lymphatic system : challenges and opportunities. *J R Soc Interface*. [Online] 9 (69), 601–612. Available from: doi:10.1098/rsif.2011.0751.

Martin, B.A., Reymond, P., Novy, J., Baledent, O., et al. (2012) A coupled hydrodynamic model of the cardiovascular and cerebrospinal fluid system. *AJP: Heart and Circulatory Physiology*. [Online] 302 (7), H1492–H1509. Available from: doi:10.1152/ajpheart.00658.2011.

McDonough, J.E., Yuan, R., Suzuki, M., Seyednejad, N., et al. (2012) Small-Airway Obstruction and Emphysema in Chronic Obstructive Pulmonary Disease. *N Engl J Med*. [Online] 365 (17), 1567–1575. Available from: doi:10.1056/NEJMoa1106955.Small-Airway.

Mcelroy, M.C. & Kasper, M. (2004) The use of alveolar epithelial type I cell-selective markers to investigate lung injury

and repair. *Eur Respir J*. [Online] 24, 664–673. Available from: doi:10.1183/09031936.04.00096003.

Mega, M.S., Chen, S.S., Thompson, P.M., Woods, R.P., et al. (1997) Mapping histology to metabolism: Coregistration of stained whole-brain sections to premortem PET in Alzheimer's disease. *NeuroImage*. [Online] 5 (2), 147–153. Available from: doi:10.1006/nimg.1996.0255.

Mendoza, E., Schmid-Schönbein, G.W. & Schmid-Schonbein, G.W. (2003) A Model for Mechanics of Primary Lymphatic Valves. *Journal of Biomechanical Engineering*. [Online] 125 (3), 407–414. Available from: doi:10.1115/1.1568128.

Meyer, E.C. & Ottaviano, R. (1974) Right lymphatic duct distribution volume in dogs. Relationship to pulmonary interstitial volume. *Circulation Research*. [Online] 35 (2), 197–203. Available from: doi:10.1161/01.RES.35.2.197.

Michel, C.C. & Curry, F.E. (1999) Microvascular permeability. *Physiological Reviews*. [Online] 79 (3), 703–761. Available from: doi:10.1152/physrev.1999.79.3.703.

Michel, R.P., Meterissian, S. & Poulsen, R.S. (1986) Morphometry of the distribution of hydrostatic pulmonary oedema in dogs. *British Journal of Experimental Pathology*. 67 (6), 865–877.

Miller, M.J., Mcdole, J.R. & Newberry, R.D. (2010) Microanatomy of the intestinal lymphatic system. *Annals of the New York Academy of Sciences*. 1207, 1–11.

Miserocchi, G., Negrini, D. & Gonano, C. (1990) Direct measurement of interstitial pulmonary pressure in in situ lung with intact pleural space. *Journal of Applied Physiology*. [Online] 69 (6), 2168–2174. Available from: doi:10.1152/jappl.1990.69.6.2168.

Miserocchi, G., Negrini, D., Passi, A. & De Luca, G. (2001) Development of lung edema: interstitial fluid dynamics and molecular structure. *News in physiological sciences : an international journal of physiology produced jointly by the International Union of Physiological Sciences and the American Physiological Society*. 16 (April), 66–71.

Missbach-Guentner, J., Pinkert-Leetsch, D., Dullin, C., Ufartes, R., et al. (2018) 3D virtual histology of murine kidneys - high resolution visualization of pathological alterations by micro computed tomography. *Scientific Reports*. [Online] 8 (1), 1–14. Available from: doi:10.1038/s41598-018-19773-5.

Moledina, S., De Bruyn, A., Schievano, S., Owens, C.M., et al. (2011) Fractal branching quantifies vascular changes and predicts survival in pulmonary hypertension: A proof of principle study. *Heart*. [Online] 97 (15), 1245–1249. Available from: doi:10.1136/hrt.2010.214130.

Molthen, R.C., Karau, K.L. & Dawson, C.A. (2004) Quantitative models of the rat pulmonary arterial tree morphometry applied to hypoxia-induced arterial remodeling. *Journal of Applied Physiology*. [Online] 97 (6), 2372–2384. Available from: doi:10.1152/japplphysiol.00454.2004.

Mori, M., Andersson, C.K., Graham, G.J., Löfdahl, C.-G., et al. (2013) Increased number and altered phenotype of lymphatic vessels in peripheral lung compartments of patients with COPD. *Respiratory research*. 14, 65.

Moriondo, A., Mukenge, S. & Negrini, D. (2005) Transmural pressure in rat initial subpleural lymphatics during spontaneous or mechanical ventilation. *American journal of physiology. Heart and circulatory physiology*. [Online] 289, H263–H269. Available from: doi:10.1152/ajpheart.00060.2005.

Müller, A.M., Hermanns, M.I., Skrzynski, C., Nesslinger, M., et al. (2002) Expression of the Endothelial Markers PECAM-1, vWf, and CD34 in Vivo and in Vitro. *Experimental and Molecular Pathology*. [Online] 72 (3), 221–229. Available from: doi:10.1006/exmp.2002.2424.

Müller, L.O., Leugering, G. & Blanco, P.J. (2016) Consistent treatment of viscoelastic effects at junctions in one-dimensional blood flow models. *Journal of Computational Physics*. [Online] 314, 167–193. Available from:

doi:10.1016/j.jcp.2016.03.012.

Negrini, D. & Del Fabbro, M. (1999) Subatmospheric pressure in the rabbit pleural lymphatic network. *Journal of Physiology*. 520 (3), 761–769.

Negrini, D., Moriondo, A. & Mukenge, S. (2004) Transmural Pressure During Cardiogenic Oscillations in Rodent Diaphragmatic Lymphatic Vessels. *Lymphatic Research and Biology.* 2 (2), 69–81.

Negrini, D. & Passi, A. (2007) Interstitial matrix and transendothelial fluxes in normal lung. *Respiratory Physiology and Neurobiology*. 159 (3), 301–310.

Newman, V., Gonzalez, R.F., Matthay, M.A. & Dobbs, L.G. (2000) A Novel Alveolar Type I Cell – Specific Biochemical Marker of Human Acute Lung Injury. *Am J Respir Crit Care Med*. 161, 990–995.

Nisimaru, Y. (1982) Summary of our studies concerning the structure and function of lymphatic-system. *Hiroshima J. Med. Sci.* 31, 145–160.

O'Shaughnessy, T.C., Ansari, T.W., Barnes, N.C. & Jeffery, P.K. (1997) Inflammation in bronchial biopsies of subjects with chronic bronchitis: Inverse relationship of CD8+ T lymphocytes with FEV1. *American Journal of Respiratory and Critical Care Medicine*. [Online] 155 (3), 852–857. Available from: doi:10.1164/ajrccm.155.3.9117016.

Ogasawara, S., Kaneko, M.K., Price, J.E. & Kato, Y. (2008) Characterization of Anti-podoplanin Monoclonal Antibodies: Critical Epitopes for Neutralizing the Interaction Between Podoplanin and CLEC-2. *Hybridoma*. [Online] 27 (4), 259–267. Available from: doi:10.1089/hyb.2008.0017.

Ohhashi, T., Azuma, T. & Sakaguchi, M. (1980) Active and passive mechanical characteristics of bovine mesenteric lymphatics. *Am. J. Physiol.* 239, 88–95.

Ohtani, O. (2008) Organistation and Developmental Aspects of Lymphatic Vessels. *Arch Histol Cytol*. 71, 1–22.

Oki, H., Ogasawara, S., Kaneko, M.K., Takagi, M., et al. (2015) Characterization of Monoclonal Antibody LpMab-3 Recognizing Sialylated Glycopeptide of Podoplanin. *Monoclonal Antibodies in Immunodiagnosis and Immunotherapy*. [Online] 34 (1), 44–50. Available from: doi:10.1089/mab.2014.0087.

Oliver, G. & Detmar, M. (2002) The rediscovery of the lymphatic system : old and new insights into the development and biological function of the lymphatic vasculature. *Genes and Development*. [Online] (901), 773–783. Available from: doi:10.1101/gad.975002.GENES.

Olszewski, W.L. (1991) *Lymph Stasis.Pathology, Diagnosis and Treatment*. CRC Press.

Olszewski, W.L. & Engeset, A. (1980) Intrinsic contractility of prenodal lymph vessels and lymph flow in human leg. *American Journal of Physiology - Heart and Circulatory Physiology*. [Online] 8 (6), 775–783. Available from: doi:10.1152/ajpheart.1980.239.6.h775.

Pabst, R. (2004) The periarterial space in the lung: Its important role in lung edema, transplantation, and microbial or allergic inflammation. *Pathobiology*. [Online] 71 (6), 287–294. Available from: doi:10.1159/000081723.

Palestini, P., Calvi, C., Conforti, E., Botto, L., et al. (2002) Composition, biophysical properties, and morphometry of plasma membranes in pulmonary interstitial edema. *American Journal of Physiology - Lung Cellular and Molecular Physiology*. [Online] 282 (6 26-6), 1382–1390. Available from: doi:10.1152/ajplung.00447.2001.

Pan, W., Michelle, C., Roux, L.E., Levy, S.M., et al. (2010) The Morphology of the Human Lymphatic Vessels in the Head and Neck. *Clinical Anatomy*. [Online] 661, 654–661. Available from: doi:10.1002/ca.21004.

Parker, J.C., Crain, M., Grimbert, F., Rutili, G., et al. (1981) Total lung lymph flow and fluid compartmentation in

edematous dog lungs. *Journal of Applied Physiology Respiratory Environmental and Exercise Physiology*. [Online] 51 (5), 1268–1277. Available from: doi:10.1152/jappl.1981.51.5.1268.

Parker, J.C., Falgout, H.J., Grimbert, F.A. & Taylor, A.E. (1979) The effect of increased vascular pressure on albumin-excluded volume and lymph flow in the dog lung. *Circulation Research*. [Online] 45 (6), 440–450. Available from: doi:10.1161/01.RES.47.6.866.

Parker, J.C., Ryan, J. & Taylor, A.E. (1984) Plasma-lymph albumin kinetics, total lymph flow, and tissue hematocrit in normally hydrated dog lungs. *Microvascular Research*. [Online] 28 (2), 254–269. Available from: doi:10.1016/0026-2862(84)90021-9.

Pula, B., Witkiewicz, W., Dziegiel, P. & Podhorska-Okolow, M. (2013) Significance of podoplanin expression in cancer-associated fibroblasts: A comprehensive review. *International Journal of Oncology*. [Online] 42 (6), 1849–1857. Available from: doi:10.3892/ijo.2013.1887.

Pullinger, D.B. & Florey, W.H. (1935) Some observations on the structure and functions of lymphatics: their behaviour in local oedema. *Br J Exp Pathol*. 16, 49–61.

Pusztaszeri, M.P., Seelentag, W. & Bosman, F.T. (2006) Immunohistochemical Expression of Endothelial Markers CD31, CD34, von Willebrand Factor, and Fli-1 in Normal Human Tissues. *Journal of Histochemistry & Cytochemistry*. [Online] 54 (4), 385–395. Available from: doi:10.1369/jhc.4A6514.2005.

Quick, C.M., Venugopal, A.M., Dongaonkar, R.M., Laine, G., et al. (2008) First-order approximation for the pressure-flow relationship of spontaneously contracting lymphangions. *American journal of physiology Heart and circulatory physiology*. [Online] 294 (5), H2144-9. Available from: doi:10.1152/ajpheart.00781.2007.

Quick, C.M., Venugopal, A.M., Gashev, A.A., Zawieja, D.C., et al. (2007) Intrinsic pump-conduit behavior of lymphangions. *American journal of physiology. Regulatory, integrative and comparative physiology*. [Online] 292 (4), R1510-8. Available from: doi:10.1152/ajpregu.00258.2006.

Rabe, K.F., Hurd, S., Anzueto, A., Barnes, P.J., et al. (2007) Global strategy for the diagnosis, management, and prevention of chronic obstructive pulmonary disease: GOLD executive summary. *American Journal of Respiratory and Critical Care Medicine*. [Online] 176 (6), 532–555. Available from: doi:10.1164/rccm.200703-456SO.

Rahbar, E. & Moore, J.. J. (2011) A model of a radially expanding and contracting lymphangion. *J Biomech*. 44 (6), 1001–1007.

Randolph, G.J., Ivanov, S., Zinselmeyer, B.H. & Scallan, J.P. (2017) The Lymphatic System: Integral Roles in Immunity. *Annu. Rev. Immunol.* [Online] 35, 31–52. Available from: doi:10.1016/j.gde.2016.03.011.

Rangel-Moreno, J., Hartson, L., Navarro, C., Gaxiola, M., et al. (2006) Inducible bronchus-associated lymphoid tissue (iBALT) in patients with pulmonary complications of rheumatoid arthritis. *Journal of Clinical Investigation*. [Online] 116 (12), 3183–3194. Available from: doi:10.1172/JCI28756.

Rausch, S.M.K., Haberthür, D., Stampanoni, M., Schittny, J.C., et al. (2011) Local strain distribution in real three-dimensional alveolar geometries. *Annals of Biomedical Engineering*. [Online] 39 (11), 2835–2843. Available from: doi:10.1007/s10439-011-0328-z.

Reddy, N.P. (1974) *A discrete model of the lymphatic system.* Texas A&M University, TX.

Reddy, N.P. & Kesavan, S.K. (1989) Low Reynolds number liquid propulsion in contracting tubular segments connected through valves. *Mathematical and Computer Modelling*. [Online] 12 (7), 839–844. Available from: doi:10.1016/0895-7177(89)90138-6.

Reddy, N.P., Krouskop, T.A. & Newell, P.H.J. (1977) A computer model of the lymphatic system. *Comput Biol Med.* 7(3), 181-97.

Reddy, N.P. & Patel, K. (1995) A mathematical model of flow through the terminal lymphatics. *Medical Engineering & Physics*. [Online] 17 (2), 134–140. Available from: doi:10.1016/1350-4533(95)91885-K.

Reed, H.O., Wang, L., Sonett, J., Chen, M., et al. (2019) Lymphatic impairment leads to pulmonary tertiary lymphoid organ formation and alveolar damage. *Journal of Clinical Investigation*. [Online] 129 (6), 2514–2526. Available from: doi:10.1172/JCI125044.

Robinson, S.K., Ramsden, J.J., Warner, J. & Lackie, P.M. (2019) Correlative 3D Imaging and Microfluidic Modelling of Human Pulmonary Lymphatics using Immunohistochemistry and High- resolution μ CT. *Scientific Reports*. [Online] 9 (6415), 1–14. Available from: doi:10.1038/s41598-019-42794-7.

Roose, T. & Swartz, M.A. (2012) Multiscale modeling of lymphatic drainage from tissues using homogenization theory. *Journal of Biomechanics*. [Online] 45 (1), 107–115. Available from: doi:10.1016/j.jbiomech.2011.09.015.

Roselli, R.J., Coy, S.R. & Harris, T.R. (1987) Models of lung transvascular fluid and protein transport. *Annals of biomedical engineering*. [Online] 15 (2), 127–138. Available from: http://www.ncbi.nlm.nih.gov/pubmed/3592323.

Rovenska, E. (2011) Lymphatic vessels : Structure and Function. *IMAJ*. 13, 762–768.

Rubenstein, D.A., Yin, W. & Frame, M.D. (2015) *Biofluid Mechanics*. Second Edi. Oxford, Elsevier Inc.

Sabin F.R (1902) On the origin of the lymphatic system from the veins, and the development of the lymph hearts and thoracic duct in the pig. *Am.J.Anat*. 1, 367–389.

Sacchi, G., Weber, E., Aglian, M., Raffaelli, N., et al. (1997) The structure of superficial lymphatics in the human thigh: Precollectors. *Anatomical Record*. [Online] 247 (1), 53–62. Available from: doi:10.1002/(SICI)1097-0185(199701)247:1<53::AID-AR8>3.0.CO;2-G.

Saccomano, M., Albers, J., Tromba, G., Dobrivojević Radmilović, M., et al. (2018) Synchrotron inline phase contrast μCT enables detailed virtual histology of embedded soft-tissue samples with and without staining. *Journal of Synchrotron Radiation*. [Online] 25 (4), 1153–1161. Available from: doi:10.1107/S1600577518005489.

Sarkar, M., Niranjan, N. & Banyal, P.K. (2017) Mechanisms of hypoxemia. *Lung India : official organ of Indian Chest Society*. 34 (1), 47–60.

Scallan, J., Huxley, V.H., Korthuis, R.. & San, R. (2010) The Lymphatic Vasculature. In: *Capillary Fluid Exchange: Regulation, Functions, and Pathology.* Morgan & Claypool Life Sciences. p.

Scavelli, C., Weber, E., Aglianò, M., Cirulli, T., et al. (2004) Lymphatics at the crossroads of angiogenesis and lymphangiogenesis. *Journal of anatomy*. [Online] 204 (6), 433–449. Available from: doi:10.1111/j.0021-8782.2004.00293.x.

Schacht, V., Dadras, S.S., Johnson, L.A., Jackson, D.G., et al. (2005) Up-Regulation of the Lymphatic Marker Podoplanin, a Mucin-Type Transmembrane Glycoprotein, in Human Squamous Cell Carcinomas and Germ Cell Tumors. *The American Journal of Pathology*. [Online] 166 (3), 913–921. Available from: doi:10.1016/S0002-9440(10)62311-5.

Schacht, V., Ramirez, M.I., Hong, Y.-K., Hirakawa, S., et al. (2003) T1alpha/podoplanin deficiency disrupts normal lymphatic vasculature formation and causes lymphedema. *The EMBO journal*. [Online] 22 (14), 3546–3556. Available from: doi:10.1093/emboj/cdg342.

Schindelin, J., Arganda-Carreras, I., Frise, E., Kaynig, V., et al. (2012) Fiji: an open-source platform for biological-image

analysis. *Nat Methods*. (9:), 676 – 682.

Schmid-Schönbein, G. (1990) Mechanisms causing initial lymphatics to expand and compress to promote lymph flow. *Arch Histol Cytol.* 53, 107–114.

Schneider, J.P. & Ochs, M. (2014a) Alterations of mouse lung tissue dimensions during processing for morphometry: A comparison of methods. *American Journal of Physiology - Lung Cellular and Molecular Physiology*. [Online] 306 (4), 341–350. Available from: doi:10.1152/ajplung.00329.2013.

Schneider, J.P. & Ochs, M. (2014b) Alterations of mouse lung tissue dimensions during processing for morphometry: A comparison of methods. *AJP: Lung Cellular and Molecular Physiology*. [Online] 306 (4), L341–L350. Available from: doi:10.1152/ajplung.00329.2013.

Schraufnagel, D.E. (2010) Lung lymphatic anatomy and correlates. *Pathophysiology : the official journal of the International Society for Pathophysiology / ISP*. [Online] 17 (4), 337–343. Available from: doi:10.1016/j.pathophys.2009.10.008 [Accessed: 16 October 2015].

Schulte-Merker, S., Sabine, A. & Petrova, T. V. (2011) Lymphatic vascular morphogenesis in development, physiology, and disease. *Journal of Cell Biology*. [Online] 193 (4), 607–618. Available from: doi:10.1083/jcb.201012094.

Scott, A.E., Vasilescu, D.M., Seal, K. a. D., Keyes, S.D., et al. (2015) Three Dimensional Imaging of Paraffin Embedded Human Lung Tissue Samples by Micro-Computed Tomography. *Plos One*. [Online] 10 (6), e0126230. Available from: doi:10.1371/journal.pone.0126230.

Senter-zapata, M., Patel, K., Bautista, P.A., Griffin, M., et al. (2016) The Role of Micro-CT in 3D Histology. *Pathobiology*. [Online] 83, 140–147. Available from: doi:10.1159/000442387.

Sera, T., Uesugi, K., Yagi, N. & Yokota, H. (2015) Numerical simulation of airflow and microparticle deposition in a synchrotron micro-CT-based pulmonary acinus model. *Computer Methods in Biomechanics and Biomedical Engineering*. [Online]. 18 (13) pp.1427–1435. Available from: doi:10.1080/10255842.2014.915030.

Sera, T., Yokota, H., Tanaka, G., Uesugi, K., et al. (2013) Murine pulmonary acinar mechanics during quasi-static inflation using synchrotron refraction-enhanced computed tomography. *Journal of Applied Physiology*. [Online] 115 (2), 219–228. Available from: doi:10.1152/japplphysiol.01105.2012.

Sheilds, J.W. (2001) The High Points in the History of Lymphology 1602-2001. *Lymphology*. 34, 51–68.

Skandalakis, J.E. (2007) Anatomy of the lymphatics. *Surgical oncology clinics of North America*. 16 (1), 1–16.

Smedby, O., Hogman, N., Nilsson, S., Erikson, U., et al. (1993) Two-dimensional Tortuosity of the Superficial Femoral Artery in Early Atherosclerosis. *J Vas Res*. 30, 181–191.

Sodi, A., Guarducci, M., Vauthier, L., Ioannidis, A.S., et al. (2013) Computer assisted evaluation of retinal vessels tortuosity in Fabry disease. *Acta Ophthalmologica*. [Online] 91 (2), 113–119. Available from: doi:10.1111/j.1755-3768.2012.02576.x.

Sozio, F., Rossi, A., Weber, E., Abraham, D.J., et al. (2012) Morphometric analysis of intralobular, interlobular and pleural lymphatics in normal human lung. *Journal of Anatomy*. [Online] 220 (4), 396–404. Available from: doi:10.1111/j.1469-7580.2011.01473.x.

Srinivasan, R.S., Dillard, M.E., Lagutin, O. V., Lin, F.J., et al. (2007) Lineage tracing demonstrates the venous origin of the mammalian lymphatic vasculature. *Genes and Development*. [Online] 21 (19), 2422–2432. Available from: doi:10.1101/gad.1588407.

Starling, E.H. (1896) On the Absorption of Fluids from the Connective Tissue Spaces. *The Journal of Physiology*. [Online] 19, 312–326. Available from: doi:10.1063/1.1740489.

Di Stefano, A., Turato, G., Maestrelli, P., Mapp, C.E., et al. (1996) Airflow limitation in chronic bronchitis is associated with T-lymphocyte and macrophage infiltration of the bronchial mucosa. *American Journal of Respiratory and Critical Care Medicine*. [Online] 153 (2), 629–632. Available from: doi:10.1164/ajrccm.153.2.8564109.

Stump, B., Cui, Y., Kidambi, P., Lamattina, A.M., et al. (2017) Lymphatic changes in respiratory diseases: more than just remodeling of the lung? *Am J Respir Cell Mol Biol*. [Online] 1, 1–30. Available from: doi:10.1152/japplphysiol.01616.2005.

Sugihara-Sekim, M. & Fu, B. (2005) Blood flow and permeability in microvessels. *Fluid Dynamic Research*. 37, 82–132.

Sunagawa, K., Maughan, W.L., Burkhoff, D. & Sagawa, K. (1983) Left ventricular interaction with arterial load studied in isolated canine ventricle. *American Journal of Physiology - Heart and Circulatory Physiology*. [Online] 14 (5), 773–780. Available from: doi:10.1152/ajpheart.1983.245.5.h773.

Swabb, E., Wei, J. & Gullino, P. (1974) Diffusion and convection in normal and neoplastic tissues. *Cancer Res*. 53 (34:), 2814–2822.

Swartz, M. (2001) The physiology of the lymphatic system. *Advanced Drug Delivery Reviews*. [Online] 50 (1–2), 3–20. Available from: doi:10.1016/S0169-409X(01)00150-8 [Accessed: 13 October 2015].

Sweet, D., Jiménez, J., Chang, J., Hess, P., et al. (2015) Lymph flow regulates collecting lymphatic vessel maturation in vivo. *Journal of Clinical Investigation*. [Online] 125 (8), 2995–3007. Available from: doi:10.1172/JCI79386DS1 [Accessed: 12 October 2015].

Ta-Chih, L. & Kashyap, R.L. (1994) Building Skeleton Models via 3-D Medial Surface Axis Thinning Algorithms. *Graphical Models and Image Processing*. 56 (6), 462–478.

Tanabe, N., Vasilescu, D.M., Kirby, M., Coxson, H.O., et al. (2018) Analysis of airway pathology in COPD using a combination of computed tomography and histology. *Eur Respir J*. [Online] 51, 1–10. Available from: doi:10.1183/13993003.01245-2017.

Taylor, A.. (1981) Capillary Fluid Filtration. *Circulation research*. [Online] 49 (3), 557–574. Available from: doi:10.1161/CIRCRESAHA.119.315412.

Tretbar, L., Morgan, L.C., Lee, B.B., Simonian, J.S., et al. (1992) *Lymphedema: diagnosis and treatment*. Berlin, Germany, Springer.

Trzewik, J., Mallipattu, S.K., Artmann, G.M., Delano, F. a, et al. (2001) Evidence for a second valve system in lymphatics: endothelial microvalves. *FASEB*. [Online] 15 (10), 1711–1717. Available from: doi:10.1096/fj.01-0067com.

Tyrrell, C., Mckechnie, S.R., Beers, M.F., Mitchell, T.J., et al. (2012) Differential alveolar epithelial injury and protein expression in pneumococcal pneumonia expression in pneumococcal pneumonia. *Experimental Lung Research*. [Online] 38, 266–276,. Available from: doi:10.3109/01902148.2012.683321.

Vasilescu, D.M., Knudsen, L., Ochs, M., Weibel, E.R., et al. (2012) Optimized murine lung preparation for detailed structural evaluation via micro-computed tomography. *J Appl Physiol*. [Online] (2), 159–166. Available from: doi:10.1152/japplphysiol.00550.2011.

Venugopal, A.M., Stewart, R.H., Laine, G. a, Dongaonkar, R.M., et al. (2007) Lymphangion coordination minimally affects mean flow in lymphatic vessels. *American journal of physiology. Heart and circulatory physiology*. [Online] 293 (2), H1183–H1189. Available from: doi:10.1152/ajpheart.01340.2006.

Venugopal, A.M., Stewart, R.H., Laine, G.A. & Quick, C.M. (2010) Nonlinear Lymphangion Pressure-Volume Relationship Minimizes Edema. *American Journal of Physiology. Heart and Circulatory Physiology*. [Online] 299 (3), H876–H882. Available from: doi:10.1152/ajpheart.00239.2009.

Verleden, S.E., Vasilescu, D.M., Willems, S., Ruttens, D., et al. (2014) The site and nature of airway obstruction after lung transplantation. *American Journal of Respiratory and Critical Care Medicine*. [Online] 189 (3), 292–300. Available from: doi:10.1164/rccm.201310-1894OC.

Vogelmeier, C.F., Criner, G.J., Martinez, F.J., Anzueto, A., et al. (2017) Global strategy for the diagnosis, management, and prevention of chronic obstructive lung disease 2017 report. *American Journal of Respiratory and Critical Care Medicine*. [Online] 195 (5), 557–582. Available from: doi:10.1164/rccm.201701-0218PP.

Vreim, C.E., Ohkuda, K. & Staub, N.C. (1977) Proportions of dog lung lymph in the thoracic and right lymph ducts. *Journal of Applied Physiology Respiratory Environmental and Exercise Physiology*. [Online] 43 (5), 894–898. Available from: doi:10.1152/jappl.1977.43.5.894.

Watz, H., Breithecker, A., Rau, W.S. & Kriete, A. (2005) Micro-CT of the Human Lung: Imaging of Alveoli and Virtual Endoscopy of an Alveolar Duct in a Normal Lung and in a Lung with Centrilobular Emphysema—Initial Observations1. *Radiology*. [Online] 236 (3), 1053–1058. Available from: doi:10.1148/radiol.2363041142.

Wilting, J., Papoutsi, M., Christ, B., Nicolaides, K.H., et al. (2002) The transcription factor Prox1 is a marker for lymphatic endothelial cells in normal and diseased human tissues. *The FASEB Journal*. 10, 1271–1273.

Yamashita, M., Iwama, N., Date, F., Chiba, R., et al. (2009) Characterization of lymphangiogenesis in various stages of idiopathic diffuse alveolar damage. *Human Pathology*. [Online] 40 (4), 542–551. Available from: doi:10.1016/j.humpath.2008.06.031.

Yang, Y. & Oliver, G. (2014) Development of the mammalian lymphatic vasculature. *Journal of Clinical Investigation*. [Online] 124 (3), 888–897. Available from: doi:10.1172/JCI71609.

Yao, L.C., Baluk, P., Srinivasan, R.S., Oliver, G., et al. (2012) Plasticity of button-like junctions in the endothelium of airway lymphatics in development and inflammation. *American Journal of Pathology*. [Online] 180 (6), 2561–2575. Available from: doi:10.1016/j.ajpath.2012.02.019.

Zawieja, D.C. (2009) Contractile physiology of lymphatics. *Lymphatic research and biology*. [Online] 7 (2), 87–96. Available from: doi:10.1089/lrb.2009.0007.

Zysk, A.M., Garson, A.B., Xu, Q., Brey, E.M., et al. (2012) Nondestructive volumetric imaging of tissue microstructure with benchtop x-ray phase-contrast tomography and critical point drying. *Biomedical Optics Express*. [Online] 3 (8), 1924. Available from: doi:10.1364/BOE.3.001924.